9-24-2018

FIELD INSTRUMENTATIONS AND NUMERICAL ANALYSIS OF GEOSYNTHETIC REINFORCED SOIL – INTEGRATED BRIDGE SYSTEM (GRS-IBS)

allam ardah
Louisiana State University and Agricultural and Mechanical College, aardah2@lsu.edu

FIELD INSTRUMENTATIONS AND NUMERICAL ANALYSIS OF GEOSYNTHETIC REINFORCED SOIL – INTEGRATED BRIDGE SYSTEM (GRS-IBS)

A Dissertation

Submitted to the Graduate Faculty of the
Louisiana State University and
Agricultural and Mechanical College
in partial fulfillment of the
requirements for the degree of
Doctor of Philosophy

in

The Department of Civil and Environmental Engineering

by
Allam I. S. Ardah
B.S., AN-Najah National University, 2007
M.S., Louisiana State University, 2015
December 2018

Acknowledgments

Without the support, guidance and encouragement of many people, this dissertation would not have been possible. First of all, I would like to thank my dissertation committee who has wholeheartedly given me inspiration, advice and guidance from the beginning until the completion of this dissertation. It is such a great honor to have them as my advisors.

I owe my deepest gratitude to Professor Dr. Murad Abu-Farsakh, my advisor, for his valuable advice and for sharing his extraordinary experiences from the beginning of my research. Professor Abu-Farsakh has helped me how to think and look at soil reinforcement principles and problems with great wisdom. With intuition and great care, he pointed out substantial issues that I had missed to ensure the fullest development of my intellectual maturity and growth as a scholar.

I am deeply indebted to Professor Dr. George Z. Voyiadjis, my co-advisor, for his stimulating suggestions, his enduring support and his steady belief in me. Taking many courses with him in my first year inspired me to master my education in this field.

I am deeply grateful to Professor Dr. Louay Mohammad, Dr. Shengli Chen, and Dr. Darrell J Henry, the faculty members who contributed to this work by accepting to serve in my PhD committee.

There are many people who are behind this success and whose contribution in many ways lead to the completion of this dissertation. My sincere gratitude goes to all staff of Louisiana State University (LSU) and Louisiana Transportation Research Center (LTRC). I would like to specially thank Dr. Zhongjie Zhang, Kevin Gaspard, Gavin Gautreau, Dr. Ahmad Souri, Dr. Qiming Chen, Dr. Milad Saghebfar, Dr. Firouz Rosti, Md H Rahman and Ayan Mehrotra for their unconditional help and support.

Last but not least, I would like to express my greatest appreciation to my parents, siblings, and wife: Ismail (your memory will be eternal), Iqbal, Azzam, Rawand, Husam, Mahmoud, Ahmad, Amal, Naser, Mona, Ghena, Mona Jr, Bashar, Abed, Aya, Ismail Jr and to all of my uncles and cousins, especially my cousin, Dr. Mahmoud (your memory will always be with me).

Contents

Abstract

Geosynthetic reinforced soil (GRS) is a special soil with geosynthetic fabric closely stacked in layers as soil stabilization and considered an alternative design method to the conventional bridge support technology. In this research study, a field case study of Maree Michel bridge, which is located in Route LA 91 Vermilion Parish in Louisiana, was instrumented with six different types of instrumentations to monitor the performance of GRS-IBS bridge abutment and to develop 2D and 3D finite element models. The instrumentations include Shape Acceleration Array (SAA), earth pressure cells, strain gauges, piezometers, and thermocouples. Additionally, surveying was conducted at the bridge surface upon the completion of the construction. Two and three-dimensional finite elements (FE) computer program PLAXIS 2016 was chosen to model the GRS abutment. First, the FE simulation is performed for the case study, in which the FE models were verified using the results of field monitoring program. A comprehensive parametric study was then conducted to evaluate the effect of different design variables on the performance of the GRS-IBS.

Based on the results of parametric study, the relationship between the reinforcement spacing and the reinforcement strength on the behavior of the GRS-IBS performance was evaluated. The results indicated that the reinforcement spacing has a higher impact than the reinforcement strength on the performance of GRS-IBS for a reinforcement spacing equal or greater than 0.2 m (8 in.), and similar impact for reinforcement spacing less than 0.2 m (8 in.). An analytical model was developed to calculate the required tensile strength of GRS-IBS abutment based on the composite behavior of the closely reinforcement soil. The equations were verified by using field measurements and by the results of the finite element (FE) method of analysis. The results of the analytical model were also compared with the current design procedure adopted by the Federal Highway Administration (FHWA). Finally, the FE analysis demonstrated that the

possible potential failure envelope of the GRS-IBS abutment was found to be a combination of a punching shear failure at the top and Rankine failure surface at the bottom, in which the failure envelope is developed under the inner edge of the footing and extending vertically downward to intersect with the Rankine active failure surface.

Chapter One
Introduction

1.1. Geosynthetic Reinforced Soil-Integrated Bridge System

The use of geosynthetics to reinforce walls, slopes and embankment have been used for many years (e.g., Allen et al., 1992). The Geosynthetic Reinforced Soil Walls (GRS) and Mechanically Stabilized Earth Walls (MSE) have advantages over the traditional concrete walls due to the ease of construction, cost saving, and reduction in construction time. In addition to the support of the self-weight of the backfill soil, the GRS or MSE walls can support the roadway structures and traffic loads (Abu-Hejleh et al., 2000a,b; Adams, 1997, 2002; Ketchart and Wu, 1997).

A relatively new use of this system is in bridge application [Geosynthetic Reinforced Soil Integrated Bridge System (GRS-IBS)], which can help reduce both the bridge construction time and cost. The GRS-IBS usually includes a GRS abutment, a GRS integrated approach, and a reinforced soil foundation (FHWA, 2015). In the GRS-IBS, the reinforcement tensions and soil stresses are assembled in a different way than the case of mechanically stabilized earth walls, support small surcharge loads. Distinctions must be made between the MSE walls and GRS walls; researchers have found that the reinforcement spacing plays a significant role in the performance and carrying capacities of the GRS-IBS (e.g., Adams, 1997, 2002; Wu and Pham, 2013; Adams et al., 2007a,b,c, 2011, 2014; Zheng and Fox, 2016). Compared to MSE walls, the closely reinforced soils ($\leq$ 0.3 m) result in a relatively constant lateral earth pressure at the facing. Wu (2007a) introduced the "bin pressure" concept to estimate the lateral earth pressure of tightly reinforced soils at the facing. He found that the lateral earth pressure is much smaller than those calculated by Rankine and Coulomb theories.

Three limit states for bridge foundations have been defined by the AASHTO LRFD Bridge Design Specifications (2014), which are strength, abnormal, and service limits (Nicks et al., 2016). The strength limit state of GRS has been studied with a closed-form semi-empirical equation proposed and validated to predict bearing resistance that required reinforcement strength for these closely-spaced systems (Wu and Pham, 2013; Adams et al., 2011a,b, 2014). The service limit state for the GRS abutments mainly includes vertical settlement, reinforcement strain, and lateral deformation. To empirically measure the load-deformation behavior of the GRS walls, the Federal Highway Administration (FHWA) recommended conducting a GRS performance test (PT), known as mini-pier experiments (Adams et al., 2011a). The mini-pier experiments simulate the proposed project with the same backfill materials, reinforcement, facing block, and reinforcement spacing. The results of this experiment are used to develop a methodology to predict the in-service performance of GRS abutments, including the maximum lateral deformation based on the postulate of zero volume change [(i.e., the volume lost due to settlement is equal to the volume gained due to lateral deformation (Adams et al., 2002, Adams et al., 2011a, 2015)]. This method can provide reasonable approximations of settlements and lateral deformation of in-service GRS abutments (Adams et al., 2011b). However, though the mini-pier mimics the actual GRS wall in terms of backfill materials, reinforcement materials and spacing, and facing block, distinction must be made between the performance test experiments and the actual GRS wall in terms of foundation type.

The first documented use of alternating layers of geosynthetic (or GRS) was in the early of 1970's when the US forest services used non-woven geotextile to build wrapped faced walls (Burrito walls) in the steep mountain terrain for logging roads (Berg et al., 1998). By using lightweight concrete modular blocks rather than securing the blocks to the reinforcement with connections as in Mechanically Stabilized Earth (MSE) wall system, the Colorado Department of

Transportation (CDOT) developed a low-cost generic wall system in which the concrete facing blocks were frictionally connected to the GRS mass, in which the interface between the blocks and the geosynthetic provided the required friction to resist block movement. The FHWA refined the CDOT method to account for vertical load-bearing applications, resulting in the development of the GRS abutments, followed by Geosynthetic Reinforced Soil-Integrated Bridge System (GRS-IBS). Later in the mid-1990's, the Turner-Fairbank Highway Research Center in Mclean, Virginia, built a full-scale experiment to demonstrate the load bearing capacity of reinforced soil (Adams, 1997). Several factors have been triggered that caused the increasing use of GRS-IBS system including cost savings, fast construction techniques, the ability to tolerate large differential settlement and good seismic performance without structural distress. These advantages have brought attention to the concept and genuine interest has developed to promote and use this technology (Adams et al., 2007; Kost et al., 2014; Talebi et al., 2014).

Compared to the typical systems involving the use of deep foundations to support bridge structures, using the geosynthetic-reinforced systems affords the ability to alleviate the "bump at the bridge" problem caused by differential settlements between the bridge abutment and the approaching roadway. When GRS walls were first introduced, a metallic skin was used at their face to retain the backfill soil. Later, precast concrete panels replaced the metallic skin in the Reinforced Earth system. Many types of GRS retaining walls were introduced after the Reinforced Earth system. They were constructed by the wrapped-around method (Bell et al., 1975), with the geosynthetic layers used to retain the backfill soil at the wall face. However, geosynthetic materials are vulnerable to fires and deteriorate when exposed to ultraviolet light. In addition, walls with wrapped around facing are less attractive. Thus, different facings such as vegetation, timber, and shotcrete were used in some applications (e.g., Rimoldi, 1997).

The GRS-IBS design consists of three main components: reinforced soil foundation (RSF), GRS abutment, and integrated approach. The GRS abutment is constructed using well-compacted backfill soil and closely spaced geosynthetic reinforcement (usually $< 0.3m$) to provide support for the bridge. The bridge seat (bearing bed) is a thin layer consisting of wrapped-face GRS fill. Double reinforcement is incorporated underneath the bridge seat to provide additional support for the bridge load. Concrete bridge structures are placed directly on top the bridge seat, whereas steel bridge girders are placed on a concrete pad. To create a smooth transition, minimize differential settlement, and to alleviate the bridge bump, the approach roadway, which consists of a wrapped-face GRS fill, is integrated with the bridge (i.e., no joint).

When compared to conventional GRS walls, the GRS abutments are subjected to much larger surcharge loads and, as such, allowable bearing pressure in which the deformations are important issues for design. To predict the ultimate bearing capacity of GRS abutments, the FHWA provides analytical and empirical design methods with the corresponding allowable bearing pressure calculated using a factor of safety (Adams et al., 2011a, b). The FHWA analytical design method was developed by Wu et al., (2013) to incorporate the reinforcement spacing, the confinement caused by facing rigidity, aggregate size, tensile strength, and backfill soil friction angle. The FHWA empirical design method is based on an experimentally determined vertical stress-strain relationship that is obtained from performance tests (i.e., GRS mini-pier loading tests) conducted using project-specific geosynthetic reinforcement and backfill soil. According to the FHWA guidelines, the ultimate bearing capacity is determined at 5% vertical strain and a maximum allowable bearing pressure of 200 kPa for GRS abutments (Berg et al., 2009; Adams et al., 2011a).

Helwany et al., (2003) investigated the effects of the foundation soil on the behavior of GRS bridge abutments. The study was conducted by the FE analysis using the computer program DACSAR. They studied the effects of different foundation soils on the performance of a GRS-IBS abutment. Their FE analysis indicated that the performance of GRS-IBS bridge abutments was significantly affected by the behavior of the foundation soil, ranging from dense sand to medium clay. They found out that the abutment displacements of loose and medium dense sand foundations can be up to three times greater than the dense sand foundation, under the same loading from the superstructure. Though these displacements were considered tolerable according to the criterion suggested by Wahls (1990), attention should be made to these displacements when conducting the mini-pier tests.

Numerical methods such as finite element or finite difference techniques are now extensively used for analyzing the behavior of Geosynthetic Reinforced Soil (GRS) walls (e.g., Liu, 2012; Liu et al., 2011; Rowe and Ho, 1998; Bathurst et al., 2005). When compared with laboratory experiments and field measurements, the numerical methods have many advantages including obtaining more comprehensive results, investigating the effects of different loading conditions and studying the effect of different variables and parameters, which are difficult or costly to achieve in laboratory and field tests. Numerical methods help to better understand the performance of these reinforced soil structures and thus, they can be considered as new steps in the optimization of design methods (e.g., Helwany et al., 1999; Ho and Howe, 1996). Two-dimensional numerical modeling studies have been conducted for GRS abutments under static loading (Helwany et al., 2003, 2007; Wu et al., 2006a, b; Fakharian and Attar, 2007; Zheng et al., 2014, 2015a, b; Zheng and Fox, 2014) and the results of these studies showed that the reinforcement spacing, relative compaction of backfill soil, reinforcement stiffness, and bridge load have significant effects on the

performance of GRS abutments (Helwany et al., 2007; Zheng and Fox, 2014). The preceding numerical studies have focused on 2D analysis of GRS abutments, with much less analysis conducted with 3D analysis.

Many numerical studies have been conducted on the behavior of a free-standing GMSE walls (e.g., Christopher et al., 1990; Adib et al., 1990; Ling et al., 1995; Ho and Rowe 1996; Ling and Leshchinsky, 1996; Leshchinsky and Vulova, 2001; Holtz and Lee, 2002; Guler et al., 2007; Huang et al., 2011, 2013, 2014; Mirmoradi and Ehrlich, 2014a,b; Mellas et al., 2015; Rahmouni et al., 2016). A few numerical studies were conducted recently to evaluate the composite behavior of the GRS-IBS (e.g., Wu et al., 2006a, 2006b, 2014; Liu, 2015; Zheng and Fox, 2016, 2017; Ardah et al., 2017). Wu et al. (2006a) conducted a finite element analysis to investigate the allowable bearing pressure on bridge sills over a GRS abutment with flexible facing. They performed 72 case analyses in their study for various geometric and materials properties: footing type and width, soil strength and stiffness, reinforcement spacing, and foundation stiffness. Their results showed that the effect of reinforcement spacing on the performance of the GRS in terms of lateral deformation, sill settlement, and allowable bearing capacity is significant. They also found out that the integrated footing performs better than the isolated footings in terms of footing settlement. Wu et al. (2014) developed a finite element model to investigate the composite behavior of closely spaced reinforcement soil. They conducted a FE parametric study to investigate the effect of the reinforcement spacing, reinforcement stiffness, and soil stiffness on the volume change behavior (soil dilation). They found that the inclusion of geosynthetic will serve to suppress the soil dilation and lead to a stronger soil and zero volume change assumption, which has been adopted by the FHWA for estimating the lateral deformation of GRS abutment. Zheng and Fox (2016) investigated the performance of GRS abutments under static loading conditions using the

finite-difference analysis. Their model was verified using the field measurement of the Founders/Meadows GRS bridge abutment. The results of their numerical simulation were in good agreement with the field measurements during the construction process and after the bridge was open to traffic loading. A corresponding FE parametric study indicated that the reinforcement spacing, the backfill compaction, and the bridge load have significant influence on the lateral facing deformations and bridge footing settlement for the GRS abutments. They also found out that the horizontal restraining forces from the bridge span have a pronounced influence on the GRS abutment deflections. Zheng and Fox (2017) conducted another parametric study to investigate the effect of reinforcement stiffness, bearing bed reinforcement, height of the bridge abutment, and bridge load on the lateral deformations and bridge seat settlement. They found out that the reinforcement stiffness, bridge load, and the abutment height are the most significant factors on the performance of the GRS-IBS under static loading. It was noticed that the abutment vertical strain decreases with increasing the abutment height due to higher stress conditions and larger soil stiffness for taller abutments.

1.2 Problem statement

Bridges are wearing down due to traffic and age. On an annual basis, more than 3 trillion vehicle miles of travel occur over bridges in the US, with 223 billion miles of that travel occurring in trucks. Truck miles have nearly doubled in the past 20 years and are projected to grow steadily, adding significantly more loads to the already heavily traveled bridge system. Overall, freight volumes will grow from 16 billion tons at 2008 to 31 billion by 2025, with trucks continuing to carry approximately 60 percent of that tonnage on the nation's highways and bridges. Not only have traffic volumes increased dramatically, but the nation's bridges also are aging. The Interstate Highway System building boom from the mid-1950s to the mid-1970s led to the greatest bridge-

building period in history. Many of those structures are approaching 50 years old and represent a sizeable need for additional investment—no matter how diligently they have been maintained. Nearly one in four bridges needs repairs or reconstruction, and the average age of America's bridges is 43 years; seven years shy of the maximum age for which most are designed, according to the report, titled "Bridging the Gap". Based on the report from the American Association of State Highway and Transportation Officials, the nation has a generation of Baby Boomer Bridges, constructed in the 1950s and 1960s, that need major repair or replacement. Usually built to last 50 years, the average bridge in this country is 43 years old. While safe to travel, almost one in four bridges is either structurally deficient and in need of repair, or functionally obsolete and too narrow for today's traffic volumes.

With approximately 600,000 bridges in use in the U.S. One of the solutions to reduce the construction cost and accelerate the construction time is developing and adopting alternative abutment construction method technologies such as GRS-IBS that is considered a great solution for small single span bridge (length $\leq$140 ft), which is around 90% of the total bridges in use in the USA. According to the FHWA and U.S. states report that the GRS-IBS reduces project costs from 25 to 60%, depending on the application. GRS-IBS can be built and completed within weeks instead of months with a typical crew for construction the GRS abutment consists of four to five workers.

Geosynthetic reinforced soil (GRS) is considered an internally supported system (composite) due to the close reinforcement spacing. Recently, analytical methods were developed to predict the ultimate capacity of the GRS; however, these analytical methods have to be verified or modified. The FE numerical method provides a feasible alternative to field experiments to study the aspects of the problem and evaluate the effects of different design parameters on the performance of the GRS-IBS abutments. The method allows modeling 2-D and 3-D problems,

studying different cases, different geometries, and evaluating the effect of reinforcement spacing and reinforced stiffness on the creation of composite system. Moreover, the output from FE analysis includes many important lab/field variables such as deformations, stresses, strains, and internal forces, which are difficult to obtain from experiments.

1.3 Objectives

The objectives of the study are:

1. Investigate the in-service performance of GRS-IBS behavior through a well instrumented field project.

2. Develop and verify a 2D FE model of the instrumented case study bridge using the results of the dead and live loads.

3. Develop a 3D FE model and compare the results with the 2D FE results.

4. Perform comprehensive parametric study to investigate the effects of abutment height H, span length L_{span}, reinforcement spacing S_v, and reinforcement stiffness, EA, internal friction angle, ϕ, length of reinforcement, Lr, width of reinforcement soil footing, B_{RSF}, secondary reinforcement, setback distance, a_b, subgrade soil conditions, bearing width, b, and effect of differential settlement.

5. Develop an analytical model to calculate the required tensile strength of GRS-IBS abutment based on the composite behavior of the closely reinforcement soil.

6. Determine the potential failure surface of GRS-IBS abutment that coincide with locus of the maximum tensile force throughout the reinforcement layers to evaluate the pullout capacity and required reinforcement length.

1.4 Research scope

This study is focused on using the 2-D and 3-D FE method to simulate the composite behavior of GRS-IBS system. The constitutive model for the backfill material is selected to account for the nonlinearity, soil dilation, and stress dependent behavior. The interface friction is simulated using Mohr-Columb constitutive model. Linear elastic constitutive model was selected to simulate the geosynthetic and facing block. The results discuss the influence of closely spaced reinforcement effect on the behavior of the GRS-IBS system as compared to the Mechanically Stabilized Earth (MSE) walls. Also, the results of 2-D FE model are compared with the results of 3-D FE. The 2D FE model is used to study the effects of abutment height H, span length L_{span}, reinforcement spacing S_v, and reinforcement stiffness, EA, internal friction angle, ϕ, length of reinforcement, Lr, width of reinforcement soil footing, B_{RSF}, secondary reinforcement, setback distance, a_b, subgrade soil conditions, bearing width, b, and effect of differential settlement on the performance of GRS-IBS.

1.5 Outline

The outline for this dissertation is as following; Chapter 2 presents literature review for the previous work on GRS walls for both experimental and numerical. Chapter 3 presents the results of field instrumentation and monitoring. Chapter 4 presents the methods used in the FE modeling and the constitutive models. Chapter 5 presents FE simulation for the Maree Michel case study at the end of construction and dead load behavior, and simulation of truck load using 2D & 3D FE methods of analysis. Chapter 6 presents the results of the parametric study. Chapter 7 presents the analytical model to calculate the reinforcement strength of GRS-IBS abutment. Chapter 8 presents the conclusions and recommendations.

Chapter Two
Literature Review

2.1 Introduction

It is a well-known fact that soil is weak in tension and relatively strong in compression and shear. In a reinforced soil, the soil mass is reinforced by incorporating an inclusion (or reinforcement) that is strong in tensile resistance. Through soil-reinforcement interface bonding, the reinforcement restrains lateral deformation of the surrounding soil, increases its confinement, reduces its tendency for dilation, and consequently increases the stiffness and strength of the soil mass. Many studies have been conducted on the behavior of GRS structures; however, the interactive behavior between soil and reinforcement in a GRS mass has not been fully elucidated.

Researchers and engineers have realized that reinforcement spacing appears to play a much greater role than reinforcement strength in the performance of a GRS wall. Researchers at the Turner-Fairbank Highway Research Center have conducted a series of full-scale experiments (Adams, 1997; Adams, et al., 2007) in which a weak reinforcement at small spacing and a strong reinforcement (with several times the strength of the weak reinforcement) at twice the spacing were load-tested. The former was found to be much stronger than the latter. An in-depth study on the relationship between reinforcement spacing and reinforcement stiffness/strength regarding their effects on the behavior of a GRS mass is of critical importance to the design of GRS structures and is urgently needed.

GRS-IBS is a form of accelerated bridge construction that lowers cost, slashes construction time, improves durability, and increases safety—all at the same time. GRS-IBS technology uses alternating layers of compacted granular fill material and fabric sheets of geotextile reinforcement to provide support for the bridge. GRS-IBS also provides a smooth transition from the bridge onto

the roadway and alleviates the "bump at the bridge" problem caused by uneven settlement between the bridge and approaching roadway. The technology offers unique advantages in the construction of small bridges, including:

• Reduced construction time and cost, with costs reduced 25 to 60 percent from conventional construction methods.

• Easy to build with common equipment and materials; easy to maintain because of fewer parts.

• Flexible design that is easily modified in the field for unforeseen site conditions, including utilities, obstructions, existing structures, variable soil conditions, and weather.

The GRS technology has been used in a variety of applications such as retaining walls, slope stability, embankment construction, roadway support, rock fall barriers, and load-bearing foundations. Building a GRS mass involves three simple steps. First, lay a row of facing blocks. Second, add a layer of compacted fill to the height of the facing blocks (8 in.). Next, add a layer of geosynthetic fabric. Each layer of geosynthetic is extended between the rows of blocks to frictionally connect the block to the GRS mass. This 1-2-3 process is repeated until the desired wall height is achieved. The construction of the GRS mass should then follow two simple rules. First, thin layers of granular fill materials should be well compacted. Second, the reinforcement should be placed in closely spaced layers.

Geosynthetic reinforced soil technology (GRS) was first used in the United States in the 1970's by U.S. Forest Service (USFS). USFS used plain non-woven geotextiles to build GRS wall to support logging roads in steep mountain terrain. Shortly after the construction of GRS walls by USFS, Colorado Department of Transportation (CDOT) began constructing GRS walls in some of the interstate expansion projects. Later in 1994, Colorado Transportation Institute published a design and construction manual for construction of low cost retaining walls. This manual presents

guidelines for three types of GRS walls: wrapped-faced geotextile-reinforced retaining wall, timber-faced geosynthetic-reinforced wall, and modular block geosynthetic-reinforced wall (Wu 2007a).

GRS has a variety of applications in civil engineering such as culverts, rockfall barriers, walls, bridge piers, and bridge abutments. Over the last few years, the use of GRS technology for bridge abutments has received considerable attention. Geosynthetic Reinforced Soil Integrated Bridge System (GRS-IBS) is the coined name for a GRS wall and bridge system that was developed as part of the "Bridge of the Future" initiative by the Federal Highway Administration (FHWA) (Adams et al., 2011a). GRS-IBS is a cost effective and efficient solution for low volume, single span bridges. Furthermore, GRS-IBS can be used under a variety of foundation soil conditions. Another advantage of GRS-IBS is the elimination of the "bump" at the end of the bridge. This is due to the improved performance of these systems in regard to differential settlement.

GRS-IBS typically consists of three main components: reinforced soil foundation (RSF), abutment, and integrated approach (Figure 2.1). The RSF is built from compacted granular aggregate wrapped with geosynthetic. The RSF is placed under the GRS abutment to provide more support and increase the bearing capacity. In addition, RSF prevents water from collecting underneath the abutment. The GRS abutment is composed of compacted backfill and layers of geosynthetic reinforcement. Typically, spacing of geosynthetic layer decrease underneath the integrated approach. Usually, GRS abutments consist of three sides: the abutment face wall and two wing walls. In some cases, an abutment can be made by one or none of the wing walls, but it must have the facing element. The facing element is flexible wall built from articulated units that are not rigidly attached to each other. The purpose of facing element in GRS-IBS is to protect

abutment from outside weathering. Facing wall is not a structural element. The approach is also constructed with GRS to transition to the bridge.

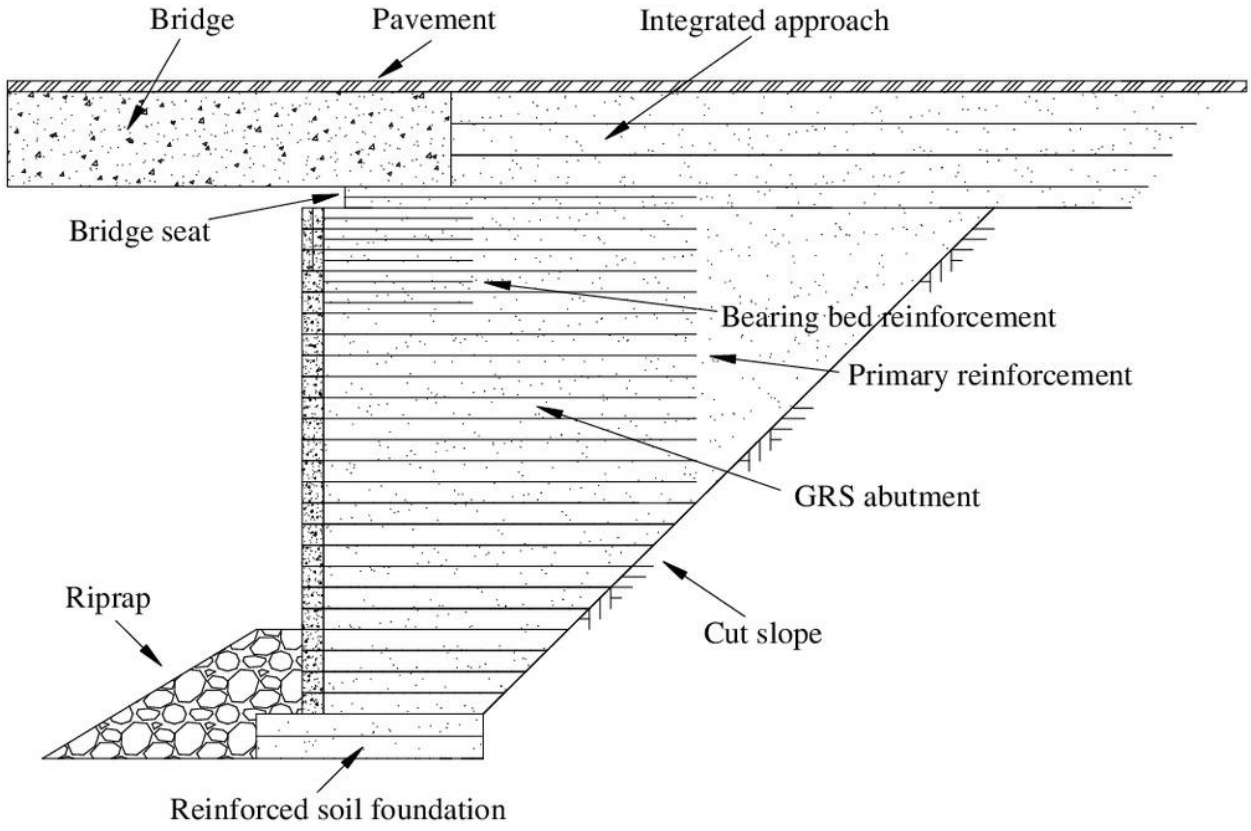

Figure 2.1. Typical GRS-IBS Cross Section

In 2010, GRS-IBS was made an Every Day Counts (EDC) initiative, which was prompted by the poor state of bridges in the U.S. Many of the 600,000 bridges in the U.S. have structural deficiencies. Of these bridges, the vast majority are single span bridges no more than 90 feet in length. Currently the demand for repair and future construction of bridges does not align with government budgets. Therefore, a new efficient system is required so that more bridges can be rehabilitated and constructed at low cost. GRS-IBS is a possible solution for this dilemma (Adam et al., 2011).

2.2 Mechanics of Geosynthetic Reinforced Soil

Reinforced soil is the technique where tensile elements are placed in the soil to improve stability and control deformation. To be effective, the reinforcements must intersect potential failure surfaces in the soil mass. Strains in the soil mass generate strains in the reinforcements, and in turn, tensile loads in the reinforcements. These tensile loads act to restrict soil movements and thus impart additional shear strength. This results in the composite soil/reinforcement system having greater shear strength than the soil mass alone. Several mechanisms by which geosynthetic reinforcement contributes to the increase in strength and/or stiffness of soil have been proposed. Among them, two mechanisms involve quantitative evaluation of the reinforcing effects, apparent cohesion, and apparent confining pressure (Schlosser and Long 1974, and Yang 1972). Recently, Wu et al., (2014) proposed a new mechanism, where presence of closely spaced geosynthetic is said to suppress the soil dilation.

2.2.1 Concept of apparent cohesion

Based on this concept, presence of reinforced layer increases the principal stress at failure with an apparent cohesion (C_R). As shown in Mohr stress diagram in Figure 2.2, the principle stress at failure increased from σ_1 to σ_{1R}. A study by Yang (1972) shows that the ϕ value is not changed by using reinforcement as long as slippage at the soil-reinforcement interface did not occur.

2.2.2 Concept of increase of apparent confining pressure

Another method to explain the mechanism of reinforced soil is concept of increase of apparent confining pressure. In this concept, axial strength of reinforced soil increases due to increase of confining pressure. As illustrated in Figure 2.3, with increase of confining pressure ($\Delta\sigma_{3R}$), the axial strength of unreinforced soil (σ_1) increases to σ_{1R}. The strength of reinforced soil can be

measured by triaxial test. Schlosser and Long (1974) suggested the following equation to calculate apparent cohesion of reinforced soil (C_R) based on the concept of apparent confining pressure.

$$C_R = \frac{T_f \sqrt{K_p}}{2S_v}$$

where T_f is tensile strength of reinforcement and S_v is vertical spacing of reinforcement and K_p is coefficient of passive earth pressure. This equation is based on the assumption that the increase in strength of reinforcement has the same effect as a proportional decrease in vertical spacing on strength of GRS mass. However, some studies reject this assumption (Wu et al., 2013).

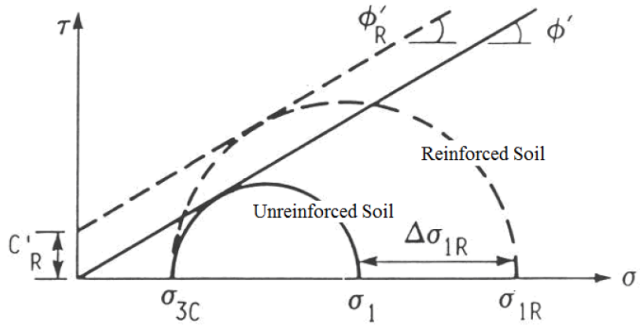

Figure 2.2. Concept of Apparent Cohesion due to the presence of Reinforcement (Scholosser and Long, 1974)

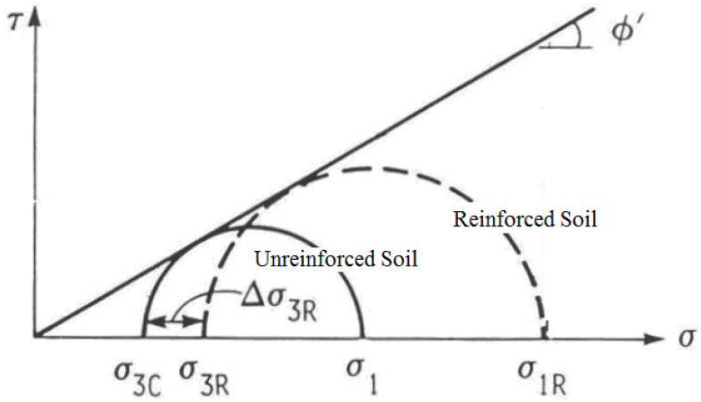

Figure 2.3. Concept of Apparent Confining Pressure due to the presence of Reinforcement (Wu et al. 2013)

2.2.3 Concept of Suppression of Soil Dilation

Loose granular soil contracts when subjected to shear stress. Under the shear stress, soil particles fall into the voids between the particles and cause contraction. On the other hand, the volume of dense granular soil increases when subjected to shear stress. The curve mark as test 1 in Figure 2.4 shows the stress-strain and volume behavior of unreinforced compacted fill material. In granular material, usually small contraction occurs before volumetric strain reaches maximum compressive volumetric strain. Then, particles roll past other particles and cause dilation which increases volume of soil sample. Figure 2.5a illustrate the dilative behavior of dense granular soil.

Presence of reinforcement can restrict dilation of soil. Strains in the soil mass, through soil-reinforcement interface friction, generate tensile strains in the reinforcements and stretch them. Stretched geosynthetics form enclosed boundaries which tend to suppress dilation of the soil. This behavior is illustrated by Figure 2.4b, where two adjacent reinforcement sheets in tension are said to restrain soil particles enclosed between them from rolling past other soil particles. Wu et al. (2014) used the angle of dilation as a quantitative measure of the degree of reinforcing effect of a GRS mass. A study by Wu et al. (2014) shows that soil particle sizes, reinforcement spacing, and reinforcement stiffness have significant effect on the behavior of GRS mass in terms of dilation.

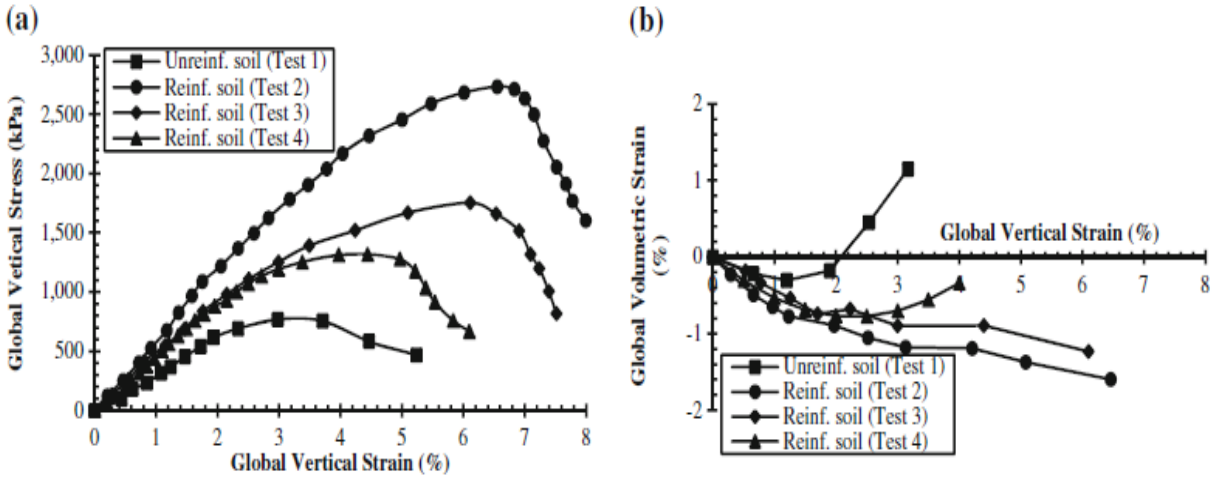

Figure 2.4. Behavior of Unreinforced and Reinforced Soil Masses: (a) Stress-Strain and (b) Volume Change (Wu et al., 2014)

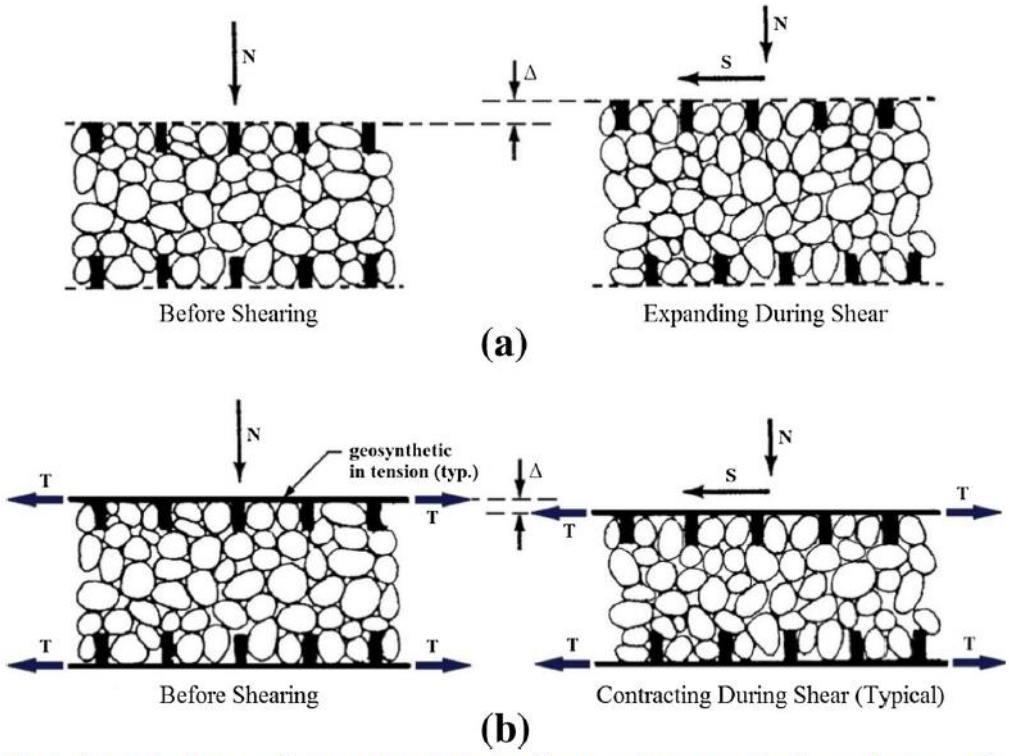

Figure 2.5. Schematic Diagrams of Volume Change Behavior of Compacted Granular Soil: (a) Unreinforced Soil and (b) Reinforced Soil (Wu et al 2014)

2.3 Difference Between GRS and MSE Structures

For many years, the geosynthetic reinforced structures had been considered to be a simple subset of mechanically stabilized earth (MSE) structures. However, there are many fundamental engineering differences between MSE and GRS (VanBuskirk, 2010).

The horizontal reinforcements are spaced and connected to the rigid face throughout the height of the wall, with the primary design considerations being vertical distance between layers of reinforcement, strength of the reinforcements themselves, and connection strength between the reinforcements and the rigid face (Elias et al., 2001). Triaxial test results show that the addition of reinforcement results in increased peak strength, larger axial strain at failure, and reduced or limited post-peak loss of strength (Elton and Patawaran, 2005). Although MSE walls use reinforcements within the soil mass, MSE walls are technically classified as externally stabilized walls because the explicit purpose of the reinforcements is to prevent deformation of the wall face and current design standards ignore the soil-reinforcement interaction (Wu, 2001). GRS walls are an example of internally stabilized walls and are different than MSE walls. The concept of reinforced soil is not new; evidence of reinforcing soil for stability can traced back as early as the construction of the Great Wall of China (Bradley and VanBuskirk, 2010). Although the theory of reinforcing soil remains the same, GRS uses new technology that provides improvements over other reinforced soil walls such as MSE walls. GRS walls are constructed using well-compacted soil between closely spaced reinforcement layers (VanBuskirk, 2010). The close spacing between reinforcement layers allows the face of GRS walls to be flexible, non-rigid and non-load bearing (Wu, 2007b).

A primary difference is that the reinforcement layers are spaced differently. Vertical space between reinforcement layers in GRS is less than MSE. Layers of reinforcement are typically

spaced 6-10 inches in GRS structures while MSE layers are usually spaced 24 inches. The reinforcement material is also different. GRS reinforcement can be built by any geosynthetic and most commonly with a geotextile or geogrid fabric while MSE reinforcement can be any type of reinforcement like steel or geosynthetic. The connection between the reinforcement and the facing on GRS structures is frictional. The facing blocks sit directly on the reinforcing geosynthetic and are held in place purely by the friction between the reinforcement and concrete block. By contrast, with MSE structures, the face is providing external support (confinement) to the soil and must be mechanically connected to the reinforcement through devices such as shear pins, lips, or keys (FHWA website). Difference in construction results in fundamental design and performance differences between these two technologies. These performance difference, as reported by VanBuskirk (2010), are summarized next.

Soil mass and reinforce layers in MSE structures are considered as one component and designed similar to tied-back wall systems. The stabilization is designed with a given strength and spacing to resist the theoretical loading which would have been imposed by the nonstabilized soil, while GRS treats the soil and the reinforcement in a composite manner. The tightly spaced reinforcements in GRS structures imparts an elevated confining stress on soil and influence the fundamental particle-to-particle interaction of the soil.

Another fundamental difference of GRS and MSE is function of facing wall. A facing unit in MSE is provided to resist the loading imposed by the soil between the embedded tensile elements. The reinforcement is secured to the facing units to hold the facing in place. The facing units within the GRS are purely a construction aid and a façade for the wall face as the facing only needs to resist construction-induced compaction loads. Figure 2.6 illustrates this fundamental difference between these two technologies. Reinforce layer in MSE is attached to two masses

which have a tendency to move apart. The main function of reinforcement layer in this case is to keep them together. On the other hand, the main function of geosynthetic in GRS is to carry tensile loads.

GRS mass usually shows higher strength due to suppression of dilation. In order to develop a shear plane in a compact or dense granular soil, the soil particles need to dilate so they can move past adjacent particles. If this does not happen, the strength of the soil mass approaches that of the aggregate. Reinforcement layer in soil mass restricts soil dilation within the surrounding soil. By decreasing the reinforcement spacing to a set distance, the zones of influence of the reinforcement on the soil mass can begin to overlap and become stiffer and stronger. Within a properly designed and constructed GRS, the fabric spacing would be sufficiently close such that the fabric resists dilation of the soil particles.

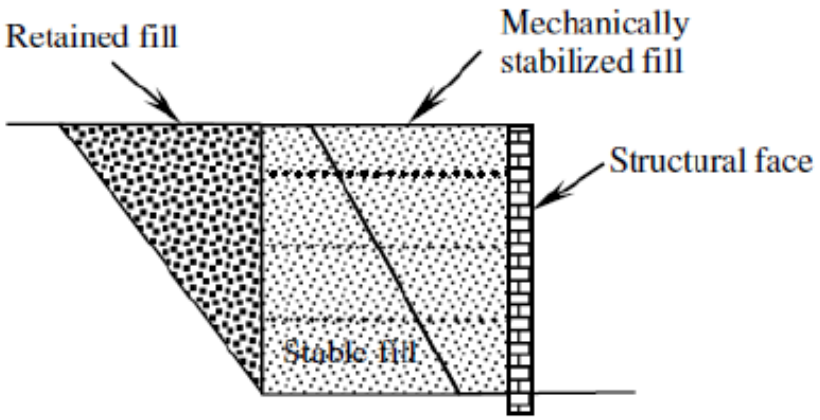

a)

Figure 2.6. Difference between MSE and GRS Technology: (a) MSE Technology and (b) GRS Technology (VanBuskirk, 2010)

(Figure cont'd)

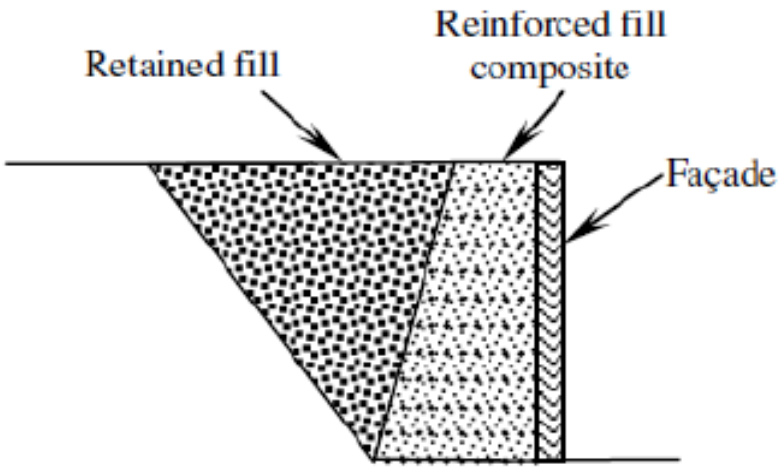

b)

The existence of reinforcing layer increases the later resistance of soil mass due to compaction. By compaction, lateral stresses developed within the soil. After removal of compactor, the vertical stress returns to normal. However, a portion of the elevated lateral stresses remains in reinforced mass as a result of reinforcement layer. These locked-in stresses increase the lateral resistance within the soil mass by providing an apparent increase in confining pressure. The level of lock-in stresses would be increased by reducing the reinforcement spacing. Therefore, this phonemenon is more significant in GRS masses with tightly space reinforcement than MSE walls.

2.4 Numerical studies

Correct numerical modeling offers the possibility to investigate the influence of a wide range of geometry and component material properties on structure performance. A challenge faced by modelers has been the treatment of the elastic-plastic properties of polymeric reinforcement materials and the interactions between reinforcement layers, soil and structural facings.

Advanced numerical methods hold promise as a design and research tool to investigate the entire response of reinforced soil retaining walls. An advantage of related computer codes is that appropriate constitutive models for polymeric materials and soils can also be implemented. Furthermore, numerical models can be used to carry out parametric analysis of the influence of wall geometry, facing type and mechanical properties of the constituent materials on wall behavior. Calibrated numerical models can also be used to extend the database of carefully instrumented field or laboratory-scale structures and hence contribute to the development of rational design methods based on conventional concepts of earth pressure theory.

Helwany et al. (1999) used the program DACSAR and calibrated their finite element model against the measured response of the *Denver Test Wall* (Figure 2.7). The nonlinear soil model proposed by Duncan et al. (1980) was used to model the soil. A good agreement between the model simulation and the triaxial test results was obtained, as indicated in Figure 2.8. The stress-strain behavior of the geotextile reinforcement and the timber facing was simulated as linear elastic. They obtained satisfactory agreement between the measured results of facing lateral displacement and reinforcement strain and results from the finite element simulation. Helwany et al. (1999) carried out parametric analysis to investigate the effects of wall height, backfill type and reinforcement stiffness on wall response using three different geosynthetic reinforcements and sixteen different backfills in the analysis of three different wall configurations. They concluded that backfill type has the most profound effect on the behavior of the GRS retaining wall. They found that the stiffness of the geosynthetic reinforcement has an important influence on wall displacement response when the backfill shear strength and stiffness are low. Helwany et al. developed a series of design charts for selection of backfill type and reinforcement stiffness to meet code requirements for the performance of reinforced soil wall systems.

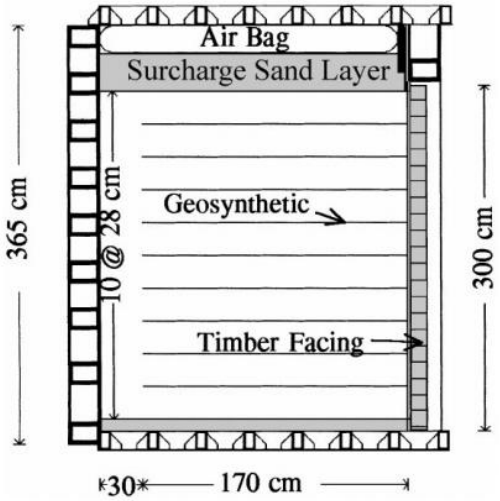

Figure 2.7. Schematic diagram of Denver Wall.

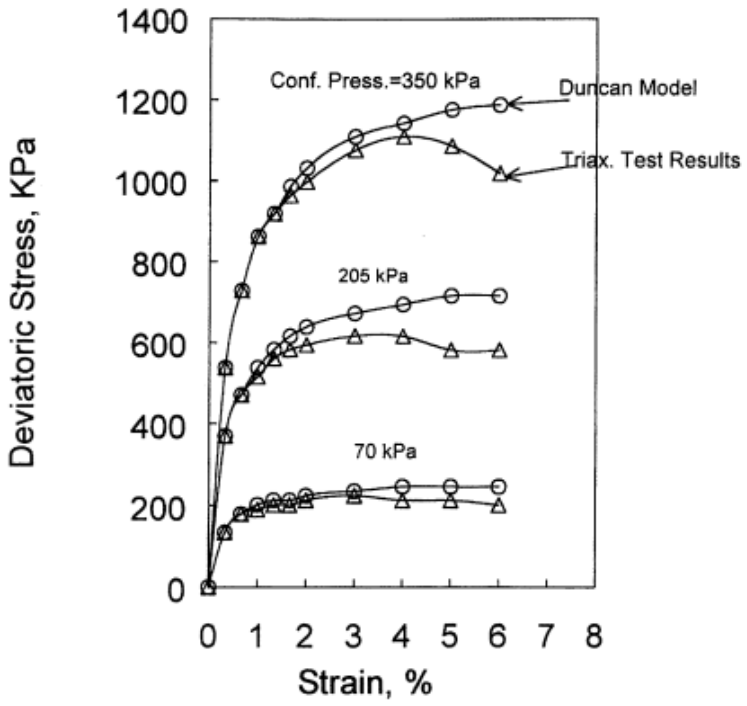

Figure 2.8. Triaxial compression test results for Ottawa sand

Walters et al. (2000) used the program FLAC to calibrate the reinforced retaining walls constructed at Royal Military Collage of Canada (RMCC) (Figure 2.9). They used the hyperbolic model proposed by Duncan et al. (1980) with Mohr-Columb failure criteria and non-associated

flow rule to represent the soil elastic response. Walters et al. (2000) found good agreement between the measured wall response and predicted values from the FLAC program. However, the numerical results were very sensitive to the choice of interface properties assigned to the discrete block units during simulated construction.

Chou and Wu (1993) used finite element program DACSAR to analyze the lateral pressure of a GRS wall. They simulate lateral earth pressure of GRS wall along three planes: the wall face, the back of the reinforced zone, and the plane along which the maximum tension load occurred in the reinforcement. Results of this study is shown in Figure 2.10. As is seen in Figure 2.10, the load at the wall face was very low in comparison to the other planes and nearly constant with depth except near the base of the wall where the foundation partially restrains the facing movement (Wu 2007b). The results of this study indicated that lateral earth pressure on the facing wall does not follow the Rankine or Coulomb earth pressure theories which indicate an increase in lateral earth pressure with depth. Authors claimed that in well-designed GRS wall there is no need for structural wall (Wu, 2007a).

Ketchart and Wu (2001) developed a finite element model using SSCOMPPC program to compare the stress distribution in soil mass with and without reinforcement. The wide-width strength of reinforcement layer was 70 kN/m and the reinforcement spacing was 0.3 m. Figures 2.11, 2.12 and 2.13 present the vertical, horizontal, and shear stress distributions, respectively, at a vertical load of 6 kN. As seen in these figures, the vertical stress distribution for reinforced and unreinforced samples is almost same. However, horizontal and shear stress distribution of reinforced sample is different from unreinforced specimen. The horizontal stresses were almost uniform in unreinforced specimen. The largest horizontal stress occurred near the reinforcement and reduced with the increasing distance from the reinforcement. The shear stress in unreinforced

specimen was negligible. In reinforced specimen, some shear stresses occurred near the reinforcement layer. Increase in the horizontal and shear stresses near the reinforcement result in an increase of minor principal stress. Stiffness and shear strength of the soil were subsequently increased by increasing minor principal stress. The largest increase of minor principal stress occurred near the reinforcement and reduced with the increasing distance from the reinforcement.

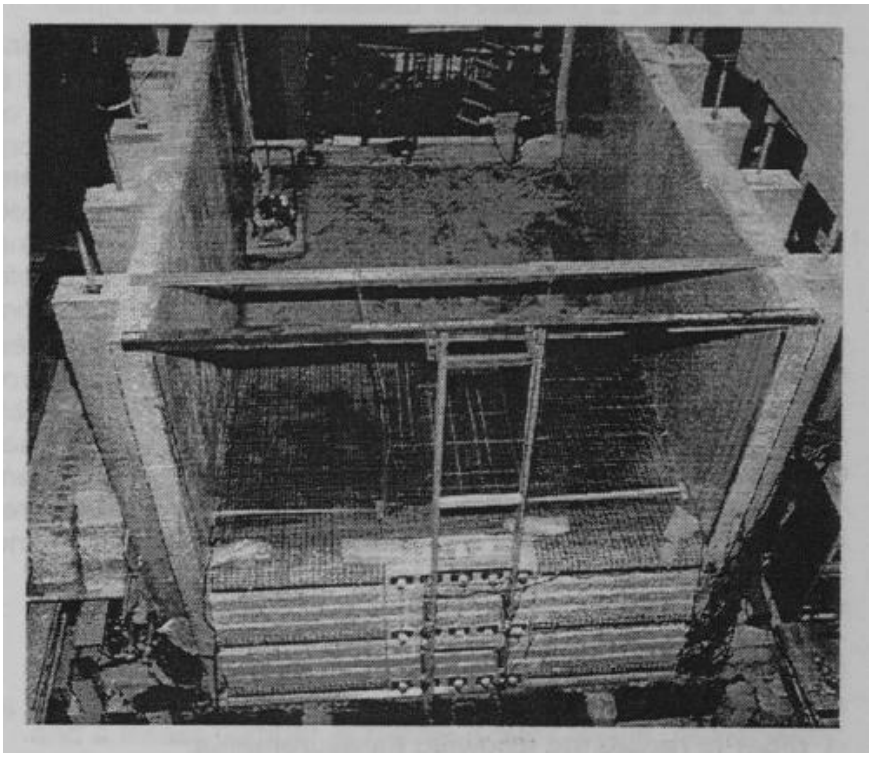

Figure 2.9. Geosynthetic reinforced retaining wall at RMCC.

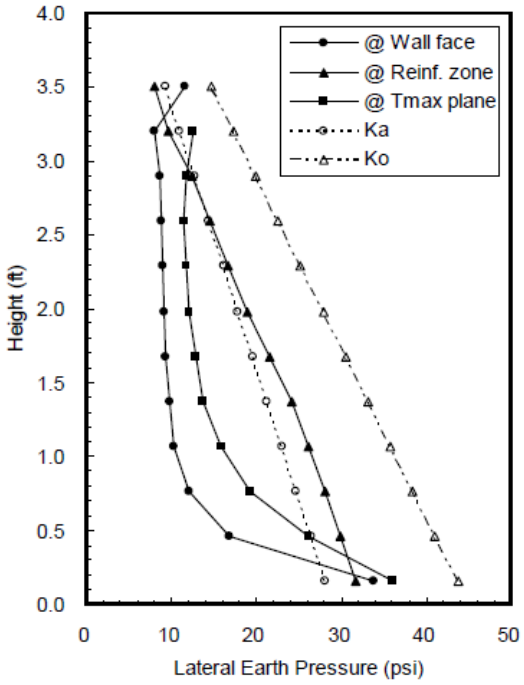

Figure 2.10. Lateral Earth Pressure of a GRS Wall (Chou and Wu, 1993)

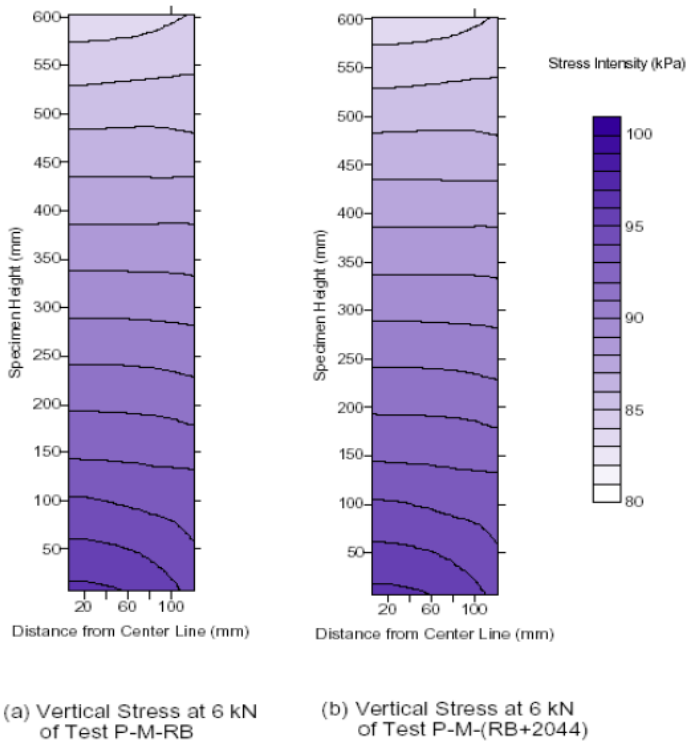

Figure 2.11. Vertical Stress Distribution at 6-kN Vertical Load: (a) With and (b) Without Reinforcement (Ketchart and Wu, 2001)

Helwany et al. (2003) used DACSAR program to study the effects of foundation soil, ranging from loose sand to stiff clay, on the performance of a GRS abutment. Authors used field measurement values from Founders/Meadows Bridge to verify their numerical model. Results show that using dense sand as foundation soil results in lower abutment settlement compared to loose and medium-dense sand. Figure 2.14 shows the effects of the foundation soil on the behavior of the GRS wall and abutment. Figure 2.14 illustrates a gradual change in settlement between the bridge deck and roadway.

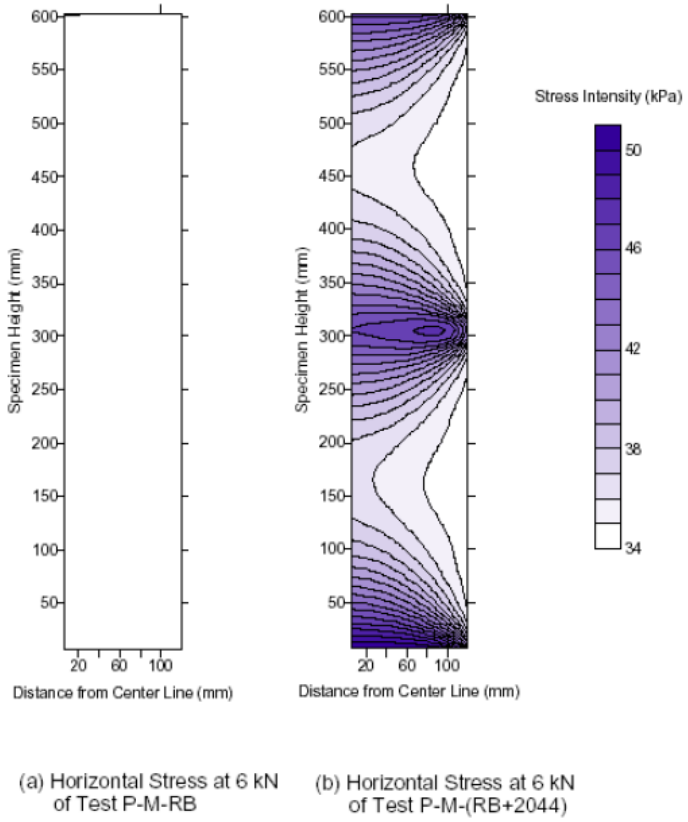

Figure 2.12. Horizontal Stress Distribution at 6-kN Vertical Load: (a) With and (b) Without Reinforcement (Ketchart and Wu 2001)

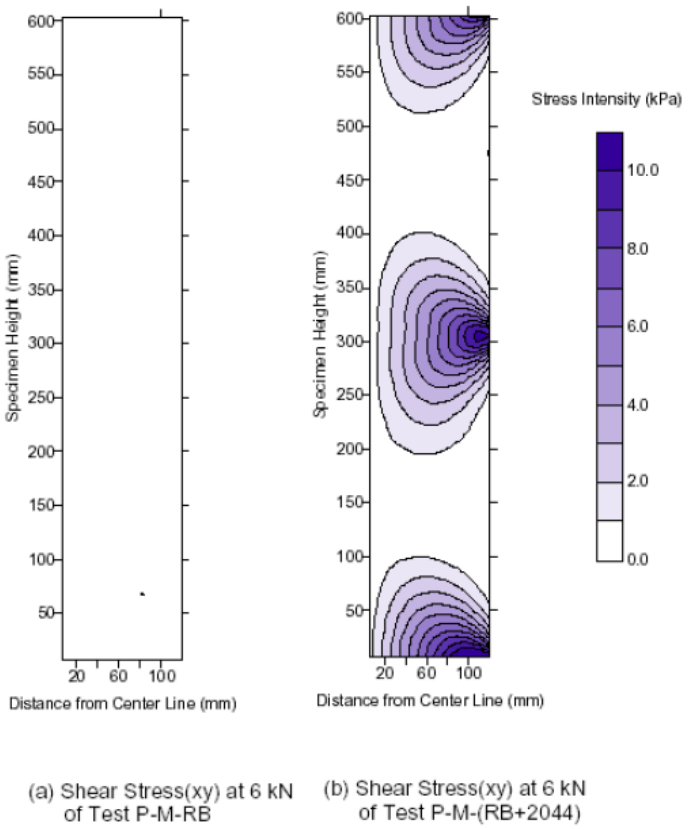

Figure 2.13. Shear Stress Distribution at 6-kN Vertical Load: (a) With and (b) Without Reinforcement (Ketchart and Wu, 2001)

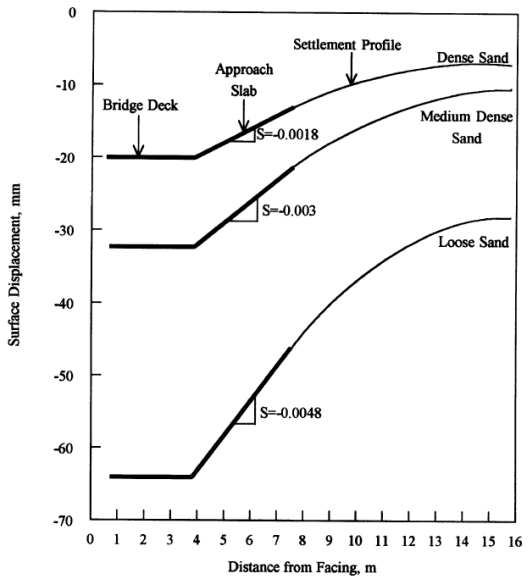

Figure 2.14. Bridge Approach Settlement after Load Application (Helwany et al., 2003).

Hatami and Bathurst (2005) developed a numerical model to predict the response of geosynthetic-reinforced soil modular block retaining walls during construction. The backfill and facing modular blocks were modeled with continuum zones. The reinforcement layers were modeled with structural (cable) elements. Figure 2.15 shows the numerical grid used for the segmental retaining walls. They compared the predicted wall response results from the plane-strain numerical models with the measured responses of three 3.6 m high test walls constructed with sand backfill and different geogrid reinforcement stiffness and spacing. The numerical simulation was carried out using the finite-difference-based program, FLAC. They used a homogeneous, isotropic, nonlinear elastic–plastic material with Mohr–Coulomb failure criterion and dilation angle (non-associated flow rule) to model the compacted backfill soil. They found that accurately predicting the response of the walls, which were constructed with a stiff facing column, required a technique to account for compaction-induced stresses in the soil. A transient 8 kPa vertical pressure was applied to the backfill surface at each stage during the simulation of wall construction. They found also that the magnitude of the horizontal compliance at the toe of the facing column has a major influence on wall response. They observed that a simple elastic–plastic soil model is sufficient for predicting wall deformation, footing reaction response, and peak strain values in reinforcement layers for strains of <1.5% provided that suitably selected values for the constant elastic modulus and Poisson's ratio for the sand backfill soil are used. However, they observed that using nonlinear elastic– plastic soil models giving a better fit to the measured data because the linear elastic–plastic model they used was shown to predict a contiguous zone of plasticity through the reinforced soil zone that was not consistent with measured results and because of the stress level dependency of granular soils, the selection of a suitable single-value elastic modulus is problematic.

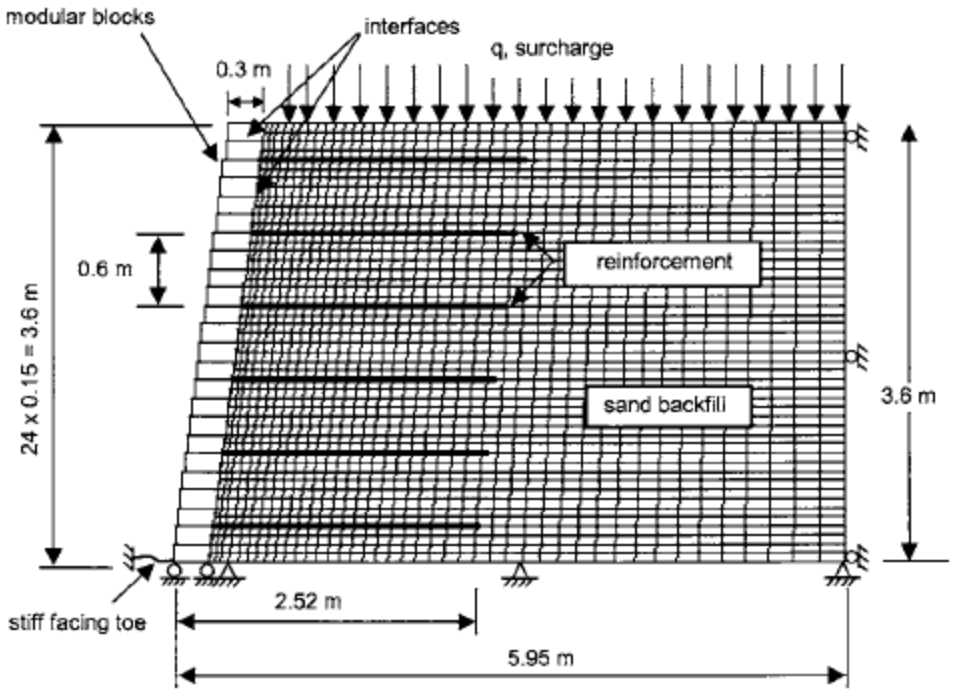

Figure 2.15. Details of numerical grid

Wu et al. (2006b) developed a finite element model to investigate the allowable bearing capacity of GRS abutments with flexible facing. This study was conducted by a finite element code DYNA3D/LS-DYNA. The sill, modular facing blocks, approach slab, and geosynthetic reinforcement were simulated by an elastic material model. A geologic cap model was used to capture the dilation and time dependency of the backfill material. The model evaluated by comparing the analytical results with measured data from five instrumented full-scale experiences, namely; the spread footing experiments by Briaud and Gibbens, the spread footing experiments on reinforced sands by Adams and Collin, the FHWA Turner-Fairbank GRS bridge pier, the Garden experiment of GRS abutments in France, and the NCHRP full-scale GRS abutment loading experiments. There was significant agreement between the model and measured data. A series of analysis was performed to examine the load carrying capacity of GRS abutment for various

geometric conditions and material properties. Authors recommended a bearing capacity based on limiting displacement and shear strain criterion.

Helwany et al. (2007) developed two finite element models, a plane strain and a three-dimensional model, using DYNA3D. The plane strain model had much less degree of freedom which makes this model run much faster than three-dimensional model. Calculated lateral displacements of the facing, at the end of construction and at an applied sill pressure of 200 kPa from plane strain model was similar to those obtained using the three-dimension model. Therefore, authors used the plane strain model to conduct a parametric study on properties of GRS abutment. Helwany et al. (2007) used the same cap soil model as Wu et al. (2006b) did. The behavior of geosynthetic reinforcement was simulated by elastoplastic model with failure. In this model, the geosynthetic reinforcement loses its tensile capability immediately after failure. The penalty type element was used to model interface between the modular blocks and reinforcement, and between the blocks and backfill soil. The Interface elements allows sliding with friction and separation. Results of Parametric analysis showed that stiffness and spacing of reinforcement layer have a significant effect on the vertical displacement at the abutment. The increase in vertical displacement by increasing spacing was more significant when applied pressure increased. Moreover, friction angle of backfill material effected vertical displacement, however it was not as significant as effect of geosynthetic stiffness and spacing.

The composite behavior of internally supported reinforced soil, the Geosynthetic Reinforced Soil walls (GRS), has advantages over the traditional concrete walls due to the ease of construction, cost saving, and construction time. In addition to the support of the self-weight of the backfill soil, the GRS walls can support the roadway structures and traffic loads (Abu-Hejleh et al., 2000; Adams, 1997; Ketchart, 1997; Adams et al., 2002, 2007). A relatively new use of this

system is in bridge application [Geosynthetic Reinforced Soil-Integrated Bridge System (GRS-IBS)], which can help reduce both the bridge construction time and cost (e.g., Saghebfar et al., 2017a, 2017b; Abu Farsakh et al., 2016; Liu, 2015; Hoffman and Wu, 2015; Yarivand et al., 2017). The GRS-IBS usually includes a GRS abutment, bearing bed reinforced zone, GRS integrated approach, and a reinforced soil foundation (Adams et al., 2011). The GRS-IBS can be used to integrate the bridge structure with the approaching road to create a jointless bridge system. Two versions of GRS-IBS are defined by the FHWA, one version uses steel girders with either a CIP footing or a precast sill. Another version of GRS-IBS uses adjacent concrete box beams supported directly on the GRS abutment without a concrete footing.

Many numerical studies have been conducted on the behavior of a free-standing GMSE walls (e.g., Christopher et al., 1990; Adib et al., 1990; Ling et al., 1995; Ho and Rowe 1996; Ling and Leshchinsky, 1996; Leshchinsky and Vulova, 2001; Holtz and Lee, 2002; Guler et al., 2007; Huang et al., 2011, 2013, 2014; Mirmoradi and Ehrlich, 2014a,b; Mellas et al., 2015; Rahmouni et al., 2016). A few numerical studies were conducted recently to evaluate the composite behavior of the GRS-IBS (e.g.,Wu et al., 2006a, 2014; Liu, 2015; Zheng and Fox, 2016, 2017; Abu-Farsakh et al. 2017,2018; Ardah et al., 2017). Wu et al. (2006a) conducted a finite element analysis to investigate the allowable bearing pressure on bridge sills over a GRS abutment with flexible facing. They performed 72 case analysis in their study for various geometric and materials properties: sill type and width, soil strength and stiffness, reinforcement spacing, and foundation stiffness. Their results showed that the effect of reinforcement spacing on the performance of the GRS in terms of lateral deformation, sill settlement, and allowable bearing capacity is significant. They also found that the integrated sill performs better than the isolated sills in terms of sill settlement. Wu et al. (2014) developed a finite element model to investigate the composite

behavior of closely spaced reinforcement soil. They conducted a FE parametric study to study the effect of the reinforcement spacing, reinforcement stiffness, and soil stiffness on the volume change behavior (soil dilation). They found that the inclusion of geosynthetic will serve to suppress the soil dilation and lead to a stronger soil and zero volume change assumption, which has been adopted by the FHWA for estimating the lateral deformation of GRS abutment. Zheng and Fox (2016) investigated the performance of the GRS abutments under static loading conditions using the finite-difference analysis. Their model was verified using the field measurement of the Founders/Meadows GRS bridge abutment. The results of their numerical simulation were in good agreement with the field measurements during the construction process and after the bridge was open to traffic loading. A corresponding FE parametric study indicates that the reinforcement spacing, the backfill compaction, and the bridge load have significant influence on the lateral facing deformations and bridge footing settlement for the GRS abutments. They also found that the horizontal restraining forces from the bridge span have a pronounced influence on the GRS abutment deflections. Zheng and Fox (2017) conducted another parametric study to investigate the effect of reinforcement stiffness, bearing bed reinforcement, height of the bridge abutment, and bridge load on the lateral deformations and bridge seat settlement. They found that the reinforcement stiffness, bridge load, and the abutment height are the most significant factors on the performance of the GRS-IBS under static loading. It was noticed that the abutment vertical strain decreases with increasing the abutment height due to higher stress conditions and larger soil stiffness for taller abutments.

Many numerical studies have been conducted on the behavior of the GRS-IBS and free-standing GRS walls under different loading conditions, bridge load, reinforcement spacing, reinforcement strength, and different soil properties (e.g., Hatami and Bathurst, 2000, 2005, 2006;

Huang et al., 2007, 2009, 2010; Wu et al., 2014; Adams et al., 2011; Mirmoradi and Ehrlich, 2014a; Zheng and Fox, 2017; Ambauen et al., 2015; Talebi et al., 2017; Ahmadi and Bezuijen, 2018; Sadat et al., 2018). Hatami and Bathurst (2005) developed a numerical model to predict the response of geosynthetic-reinforced soil modular block retaining walls during construction and under working stress. The performance was simulated with the finite-difference-based Fast Lagrangian Analysis of Continua (FLAC) program. Their numerical model accounts for staged construction of the segmental retaining walls, including backfill compaction and incremental lateral displacement of the modular facing during construction. They pointed out that the soil elastic modulus value (Ke) inferred from triaxial testing of the wall sand was 2.25 times lower than the value required to fit plane-strain laboratory testing of the same soil and to match numerical simulation results with measured wall response features. Bathurst et al. (2006) investigated the influence of the facing type on the reinforcement load using two fully instrumented full-scale walls constructed at Royal Military Collage of Canada (RMCC) (e.g., Bathurst et al., 2000; Bathurst et al., 2001). The walls were identical except one was constructed with flexible wrapped facing and the other with stiff facing. They found that the peak reinforcement load in case of flexible wrapped facing is three and a half times higher than the stiff facing at the end of construction and two times higher at the end of loading. Their results demonstrate that the facing type plays a significant role in the reinforcement load value. They also pointed out the importance of conducting the lower strain-rate tests because it is well known that the load–strain response of PP geogrid reinforcement products is sensitive to rate of loading as was documented in literature (e.g., Yeo, 1985; Walters et al., 2000).

Wu et al. (2014) developed a finite element model to investigate the composite behavior of closely spaced reinforcement soil. They conducted a FE parametric study to study the effect of

the reinforcement spacing, reinforcement stiffness, and soil stiffness on the volume change behavior (soil dilation). They found that the inclusion of geosynthetic will serve to suppress the soil dilation and lead to a stronger soil and zero volume change assumption, which has been adopted by the FHWA for estimating the lateral deformation of GRS abutment. Zheng and Fox (2017) conducted another parametric study to investigate the effect of reinforcement stiffness, bearing bed reinforcement, height of the bridge abutment, and bridge load on the lateral deformations and bridge seat settlement. They found that the reinforcement stiffness, bridge load, and the abutment height are the most significant factors on the performance of the GRS-IBS under static loading. It was noticed that the abutment vertical strain decreases with increasing the abutment height due to higher stress conditions and larger soil stiffness for taller abutments.

However; only one case study was conducted by Kost et al. (2015) to describe the behavior of the GRS-IBS subjected to differential settlements. The differential settlement between the bridge abutment and the approach embankment might be caused by compressible foundation soils or scour. Scour can be defined as the erosion caused by the water of the soil surrounding the bridge abutment or foundation. For more information about the scour causes, design, and evaluation, the reader can refer to (Arneson et al., 2012). A relatively small differential movement produces the common "bump at the end of the bridge," which is unpleasant and often hazardous to the motoring public (Zhang and Hu, 2007). Kost et al. (2015) conducted a field-scale experiment to examine the response of the GRS abutment to differential settlement. Their experiment lacked integrated approach; instead, a surcharge loading was applied on top of the GRS abutment. The differential settlement was assumed to be located under the edges of the GRS abutment. A 200 mm differential settlement between the edges was assumed under an 83.8 kPa surcharge loading. They found that a GRS abutment can tolerate a relatively large differential settlement under service loading

conditions. Review of literature showed that the allowable differential settlement (bump) at the intersection between the bridge span and the approach roadway should range between 15-30 mm (e.g., Zaman et al., 1993). Stark et al. (1995) and Long et al. (1998) considered that a differential settlement of 50-70 mm would create a serious riding comfort issue.

2.5 GRS Design Criteria

The most commonly used design method for reinforced soil slopes (RSS) and MSEW in the U.S. is the "FHWA LRFD MSE Wall Design Manual" published in 2009. This method is often called the "FHWA Simplified Procedure". This method was adopted as the standard design guidance by AASHTO in 2014. The "FHWA Simplified Procedure" is the state of practice referenced for highway projects involving MSE and RSS. The design guidance is very comprehensive and provides guidelines to select, design, construct, and maintain MSE and RSS structures. The design guidance covers a wide range of reinforcement types, including geosynthetics. Additionally, design examples and equations are provided for bridge loading conditions imposed on an abutment wall. However, the code does not incorporate the defining characteristics of GRS technology, specifically the close reinforcement spacing (Berg et al., 2009).

In general, there is two different methodologies for designing of GRS systems: the tie back wedge approach (GMSE wall design) and composite design approach (GRS-IBS). The first approach is very comprehensive and covers various types of reinforcement (i.e. with steel or geosynthetic reinforcement). The primary application of GRS structures designed with this approach is highway projects involving mechanically stabilized earth and reinforced soil slopes. Examples of tie back wedge design approaches are FHWA LRFD MSE Wall Design Manual, AASHTO LRFD Bridge Design Specifications and the FHWA Mechanically Stabilized Earth Walls Design and Construction Guidelines (Zornberg et al., 2014). The second method was

developed specially for GRS-IBS bridge (Adam et al., 2011). This method reduces the conservatism of first approach for closely-spaced geosynthetic reinforced soil. This method is explained briefly in next section.

The other differences between the two methods have been described in a number of publications (Nicks et al., 2013; Zornberg et al., 2014). The GRS- IBS design method is mainly focused on design of GRS abutment structures and it does not sufficiently cover design details of wing walls and walls supporting embankment (Zornberg et al 2014). The GMSE wall design was mainly developed for free standing structures such as footing supporting bridge, and wall supporting embankment slopes. The fundamental difference of decoupling the bridge from the supporting structure in the latter case does not account for the confining effect of the bridge on the wall and the composite strength that develops in the reinforced soil mass. It also does not consider the restraining effect of the bridge on the wall in the GRS-IBS system, which will significantly decrease lateral movement during loading.

Some researchers proposed modifications and revisions to the GMSE design method regarding the design and construction of GRS walls. Wu (2001) suggested four modifications to AASHTO guidelines included:

- lateral earth pressure on wall facing was proposed to be simulated by a “bin pressure” diagram on the wall facing of segmental GRS walls instead of the Rankine active earth pressure,
- cumulated long-term reduction factor was proposed, which depends on backfill type and placement conditions, reinforcement spacing, and polymer type of the reinforcement,

- truncated reinforcement length at wall base was proposed where excavation is needed as it is impractical to have full design length reinforcement. Yet, the external stability has to be checked when truncated base is adopted, and
- embedment depth (measured from the leveling pad to the grade in front of the wall) is not necessary for GRS walls.

Chapter Three
Case Study (Maree Michel Bridge)

Recognizing the potential benefits of using GRS-IBS for local bridges, the Louisiana Department of Transportation and Development (LA DOTD) decided to build GRS-IBS abutments for one single-span bridge at Maree Michel bridge site. The Maree Michel bridge is located in Route LA 91 Vermilion Parish. The new bridge is a replacement for an existing bridge that was nearing the end of its design life. The existing bridge was a 7.3 m by 18 m treated timber trestle, which was replaced by a 19.8 m steel girder span bridge Figure 3.1. The new GRS-IBS bridge had the same general footprint area as the previous bridge, carrying two lanes of traffic. The Average Daily Traffic (ADT) count on the bridge in 2013 was about 375, and it was estimated to be 450 vehicles in 2033.

For proper design of the GRS-IBS, several site exploration tests consisting of boreholes, soil sampling, and associated laboratory soil testing were performed to determine the foundation soil conditions. Soil borings were drilled from the ground surface elevation of the existing bridge prior to its removal, which is similar to the elevation of the constructed GRS-IBS, to a depth of 30.5 m below the surface. Filed exploration indicates that the foundation soil predominantly consists of high plasticity clay (CH) according to Unified Soil Classification method. Laboratory testing of representative soil samples indicated that wet in-place density ranged from 1.74 to 1.76 g/cm^3, natural moisture content ranged from 23% to 49%, liquid limit (LL) ranged from 45% to 84%, and the plasticity index (PI) ranged from 35% to 56%. The geosynthetic used was a woven polypropylene geotextile with an ultimate tensile strength of 80 kN/m and tensile strength at 2% strain of 17 kN/m. The groundwater table was encountered at about 1.5 m below the existing ground surface.

(a)

(b)

Figure 3.1. Maree Michel GRS-IBS Bridge: a) top view, and b) side view

The maximum height of the GRS abutment is approximately 4.8 m from the bottom of the reinforced soil foundation (RSF) to the road pavement, the width of the abutment is 13 m, and the girder span is 22 m. The overall width of the bridge superstructure is 9.1 m. This bridge was built with seven steel girders, and its GRS abutments were constructed using locally available materials. The width of the beam seat bearing area on each abutment was determined to be 1.5 m using the

FHWA design procedure. The vertical space between the reinforcement layers of GRS was 20 cm. However, for the top 5 layers of abutment, secondary reinforcement was added in the middle of each layer to increase the load carrying capacity.

The three primary materials for GRS construction are a high-quality granular fill, geosynthetic reinforcement, and facing elements. For this project, the abutment's structural fill consisted of an open-graded crushed rock with a maximum particle size of 12.7 mm and less than 5% passing the No. 16 (1.19 mm) sieve. The aggregate had a maximum dry density of 2.13 g/cm^3 and an angle of internal friction (ϕ) of 50.9^o based on large-size direct shear test. The backfill material was compacted to a minimum of 95% of the maximum dry density according to ASHTO-T-99. In the bearing bed and beam seat the backfill material was compacted to 100% of the maximum dry density. Small hand operated compaction equipment was used to compact the backfill materials. The RSF was constructed with the same backfill material as the abutment. The reinforcement for the abutment and the RSF consisted of woven polypropylene geotextile with an ultimate tensile strength of 70 kN/m. Facing elements consisted of nominal 203-mm by 203-mm by 406-mm concrete masonry units (CMUs) with a compressive strength of 27.6 MPa.

The design of the GRS abutment was performed using the Geosynthetic Reinforced Soil Integrated Bridge System Interim Implementation Guide (*Adams et al. 2011*). The factor of safety (F.S.) for the different types of failure modes are as follows: F.S. against sliding = 1.5; F.S. against bearing failure = 2.5; F.S. against global failure = 1.5; tolerable vertical strain = 0.5% wall height; and tolerable lateral strain = 1.0% bearing width.

The construction of the instrumented abutment began in April 6, 2015 and was completed on April 28, 2015. After the abutment construction is completed, seven steel girders were placed on

May 5, 2014. Due to weather condition and extensive rains, the construction of integrated approach slab was complete on July 27, 2015 and the bridge was opened to traffic on October 2015.

3.1 Instrumentation

In order to monitor and evaluate the performance of the in-service GRS-IBS abutment, various types of instrumentations were installed in south abutment of Maree Michel Bridge (Figure 3.2). An instrumentation plan was developed to measure the load-associated and environment-associated responses and the performance of the GRS-IBS abutments (Figure 3.3). The primary measurements were the vertical and horizontal deformations near the front wall, settlements due to the soil foundation and the GRS-IBS backfill, the stresses and distribution of stresses in the GRS-IBS abutments and below reinforced soil foundation, and the distribution of strains along the geosynthetic reinforcements. Additionally, the pore water pressure and temperature were monitored by piezometers and thermocouples. Six different types of instrumentations were used to monitor the GRS-IBS bridge abutment: Shape Acceleration Array (SAA), earth pressure cells, strain gauges, piezometers, and thermocouples. Additionally, surveying was conducted at the bridge surface upon the completion of the construction.

The SAA was used to measure the GRS-IBS abutment deformations and settlement because of its reliability and successful applications for other geotechnical structures (Abdoun et al. 2008). The SSA consists of an array of triaxial accelerometers based on the micro-electromechanical system (MEMS) technology. The SSA measures the three-dimensional accelerations and deformations at each sensor node. Two vertical SAAs was installed at the center of abutment, 0.6 m behind the face of the wall and 3 m behind wall. The bottom of vertical SAAs was located 0.6 m below the reinforced soil foundation, while the top of SAAs was leveled with the backfill surface. The vertical SAAs measured the lateral deformations throughout the depth of the GRS-

IBS abutment. Additionally, two sets of horizontal SAAs were installed at the location of 0.9 m behind the face of wall; one at 0.3 m below the reinforced soil foundation (RSF) and one at the top layer of the abutment. The end of horizontal SAAs was attached to settlement plates. Survey of settlement plates was used to adjust the SAA readings. The vertical SAAs have a segment length of 0.3 m between sensors. Since the horizontal profile of the GRS-IBS abutment settlement is expected to be approximately symmetric, the horizontal SAAs need less sensor nodes and have a segment length of 0.5 m. The measured deformations by the SAAs were used to evaluate the serviceability performance of the GRS-IBS abutment, particularly with respect to the settlements and the lateral deformation near the face wall. Measurements from the SAAs installed horizontally underneath the RSF represent the settlements of the soil foundation, while the measurement from the other horizontal SAA at the top of the GRS-IBS represent the overall settlement of the abutment. The difference between the two horizontal SAAs is the vertical deformations within the GRS-IBS abutment. The vertical deformation of the GRS-IBS abutment was used to calculate the strain of the GRS-IBS abutment and to verify against the tolerable limit. On the other hand, measurements from the SAA installed vertically was used to verify the lateral deformation of the GRS-IBS abutment.

Measurements from the pressure cells were used to examine the bearing pressure underneath the bridge girders as well as the distribution of the stresses in the GRS-IBS abutment. Hydraulic type earth pressure cells with semiconductor transducer (Geokon 4800) were used to measure the vertical and the horizontal stresses. These pressure cells are capable of measuring both static and dynamic stresses. A total of 12 earth pressure were installed in the GRS-IBS abutment at different locations. Three pressure cells were installed underneath the reinforced soil foundation (RSF) to measure the distribution of the vertical total pressure. Three pressure cells were installed behind

the face wall to measure the horizontal total pressure. Six pressure cells were installed in the bearing reinforcement zone at the level 16 and 19 to measure the distribution of the total vertical pressure within the bearing zone. Calibration of each pressure cell was performed in the laboratory. Vertical pressure ranges from 0 to 55 kPa were applied on the top of pressure cells in a load-controlled condition. The loads were applied using a loading plate of larger diameter than the cell diameter attached to thin rubber to ensure uniform pressure distribution above the surface of the pressure cell.

A total of three piezometers with semiconductor type transducer were installed to measure the developed pore water pressure. Along with the measurement of total stresses from earth pressure cells, the measurement of pore water pressure can be used to examine the effective stresses in the GRS-IBS abutment. The three piezometers were installed at the bottom, one-third and two-third of the height from the bottom of the GRS-IBS abutment, respectively.

Electrical resistance-type/foil-type strain gauges were installed onto the geosynthetic reinforcements to measure the developed strains along the geosynthetic layers. The reinforcement tensile forces developed in the geosynthetic reinforcement can be estimated from the strain measurements and the elastic modulus of the geosynthetic materials. A total of 55 strain gauges were installed on five geosynthetic layers in the abutment (see Figure 2d).

a) Horizontal SAA

b) Pressure cell

c) Piezometer

d) Strain gauges

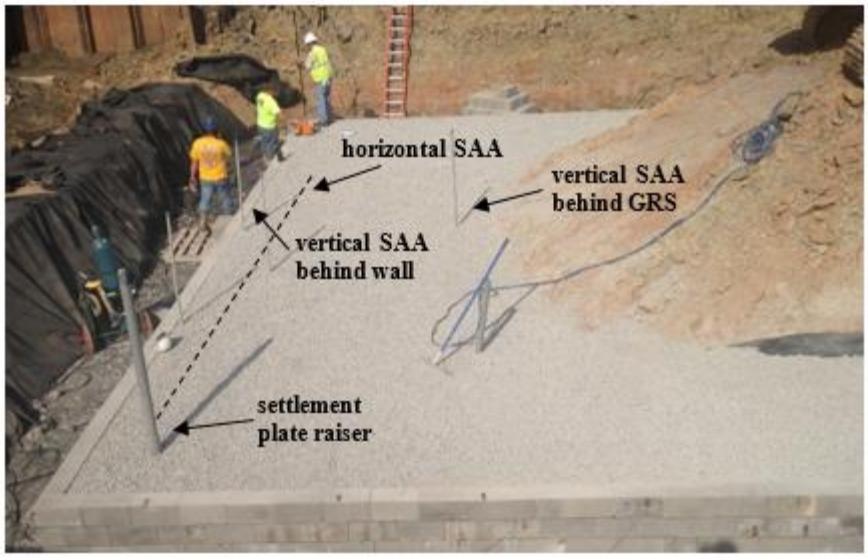

e) Settelment plate and SAAs

Figure 3.2. Example of GRS-IBS instrumentations.

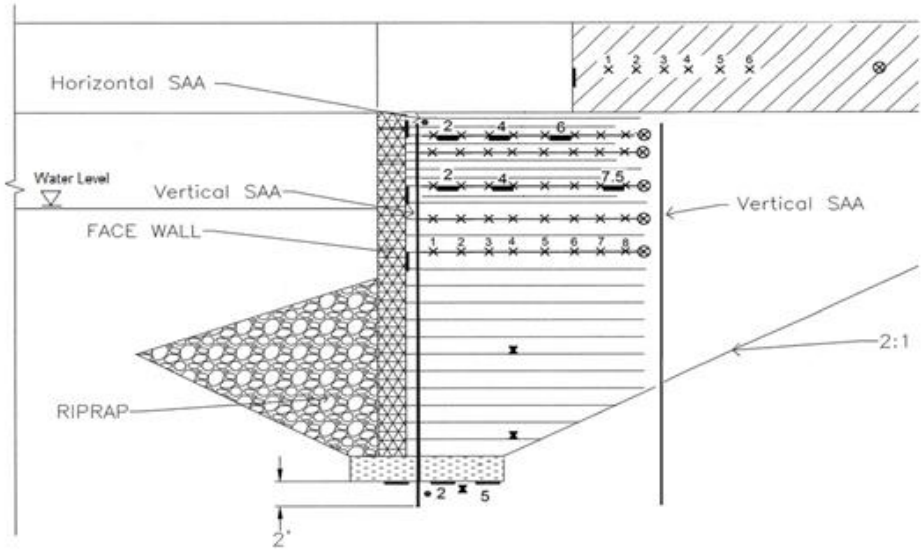

(a) Arrangement of Instrumentations in the GRS abutment section view

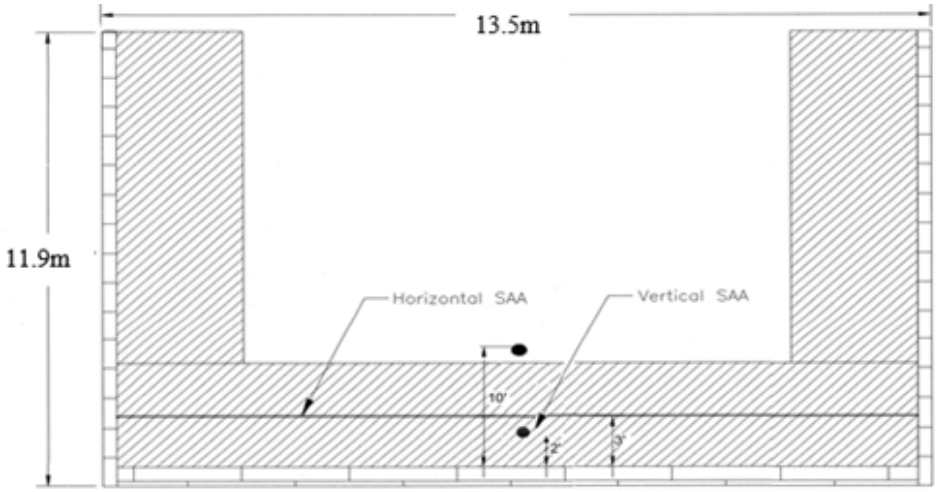

(b) Arrangement of Instrumentations in the GRS abutment plan

Figure 3.3. Instrumentation plan

3.2 Performance Monitoring

3.2.1 Settlement and Deformation Measurements

The GRS-IBS abutment is expected to experience settlements and deformations along with the construction progress and time. The deformation characteristic of the GRS-IBS abutment is a

critical indicator of the performance of the GRS-IBS abutment for internal and external stability, particularly the deformations near the facing wall. The bridge deformation was monitored, started shortly after the beginning of construction (04/08/2015) to about four months after open to traffic (10/6/2015). Figure 3.3 shows the settlement profile of soil foundation measured during and after the construction. As expected, the maximum settlement was increased with lift placement, with more movements occurred near the center of abutment than the corners.

The maximum deformation of the soil foundation as well as the GRS abutment is illustrated in Figure 3.4a. Figure 3.4b shows the construction time schedule of the abutment layers. It took 18 days of construction time to complete GRS abutment. The foundation soil settlement increase was fast at the early stage of construction; however, the rate of increase in settlement decreased with time. The maximum deformation of the abutment was significantly less than the design value of 20 mm. Measuring the deformation of abutment began five days following the end the abutment construction (4/29/2015). Figure 3.4 clearly shows the settlement due to the weight of the concrete deck. The bridge was opened to traffic on 10/6/2015, but this is not apparent in the settlement record. The deformation on the top abatement, from when the bridge was opened to traffic (7.9 mm on 10/6/2015) until one month after that (8.4 mm on 11/2/2015), was 0.5 mm. Compared to the increase in deformation from 4.4 mm five days after end of abutment construction to 7.1 mm after casting the concrete deck on the steel girders, the settlement after open to traffic is minimal. The deformation measurements indicate that the maximum total settlements across the GRS abutment one month after trafficking was less than 9 mm. About 70% of abutment deformation was due to settlement of foundation soil and less than 30% of total deformation experienced within the abutment and RSF. Small amount of deformation in the GRS can prove that closely placed reinforcement can reduce and suppress dilation of soil mass. Majority of backfill deformations

occurred by end of GRS construction (4/28/2015), which did not increase significantly with time. Overall, the GRS abutment performed satisfactory during the construction in terms of settlement and deformation measurements. The vertical strain of bridge abutment can be calculated by dividing the vertical deformation of GRS mass to the height of wall. The maximum vertical strain of 0.2 percent was observed which is significantly less than tolerable limit of 0.5 percent as stated by FHWA.

Figures 3.5a and 3.5b present the lateral movements or deformations of the abutment at locations of 0.6 and 3 m behind the facing wall, respectively. The positive value of deformation indicates movement toward the wall and the negative value indicates deformation away from the wall. These figures demonstrate that the maximum lateral movement occurred near the top of the wall. Following the construction of bridge abutment, the facing wall experienced some appreciable outward (away from backfill) lateral displacements. After placing the steel girders (5/8/2015), the lateral movement close to the wall significantly increased from 0.25 mm (measured after completing the construction of GRS abutment on 4/28/2015) to 2.3 mm. The measured lateral movement behind the GRS mas is very small and in the direction away from the wall. The maximum measured lateral movement was 0.4 mm at the top one third of the abutment mass.

The FHWA consider a zero-volume change in the GRS mass to predict the lateral displacement of the abutment face wall. By assuming the volume lost at the top of abutment due to settlement equal to the volume gained at the face due to lateral deformation, FHWA provides the following equation to estimate the maximum lateral displacement (D_L):

$$D_L = \frac{2b_{q,vol}D_v}{H} \quad (1)$$

where *bq,vol* is the width of the load along the top of the wall including the setback, *Dv* is the vertical settlement in the GRS mass, and *H* is the wall height. The lateral strain can be measured

by dividing lateral displacement to the width of the load. Table 3.1 provides the theoretical values and measurements of lateral displacement and strain during the monitoring period. In general, the theoretical method under predicts the lateral movement of facing wall. The difference between measurement and theoretical values was more significant during the construction of bridge, however, after open the bridge to traffic (10/6/2015), the difference between the predicted and measured lateral deformations and strains were decreased. FHWA assumes a triangular lateral deformation and uniform vertical deformation and restricts the horizontal strain at the facing by 1.0%. Still, the measured strains during the monitoring period were significantly less than the FHWA criteria.

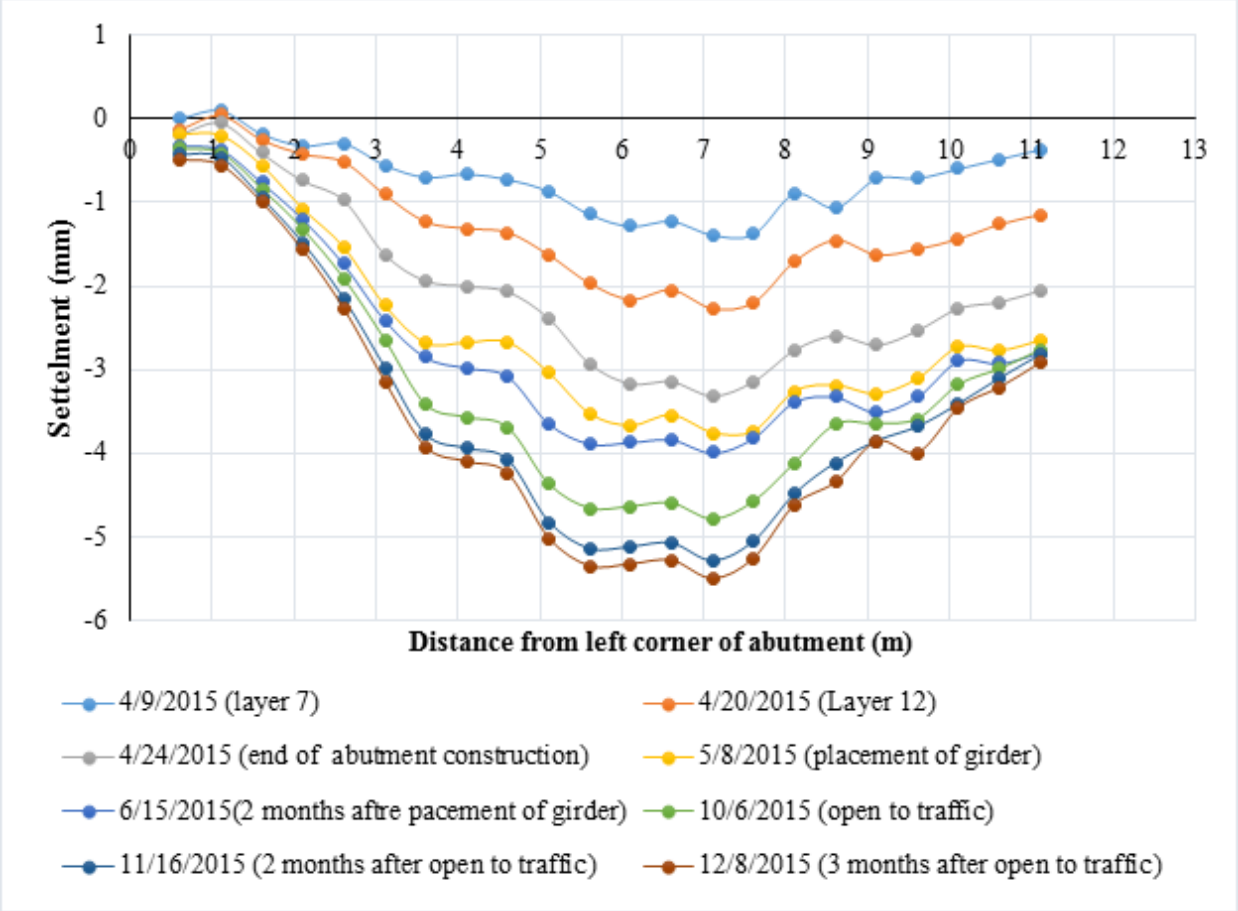

Figure 3.4. Settlement profile of soil foundation.

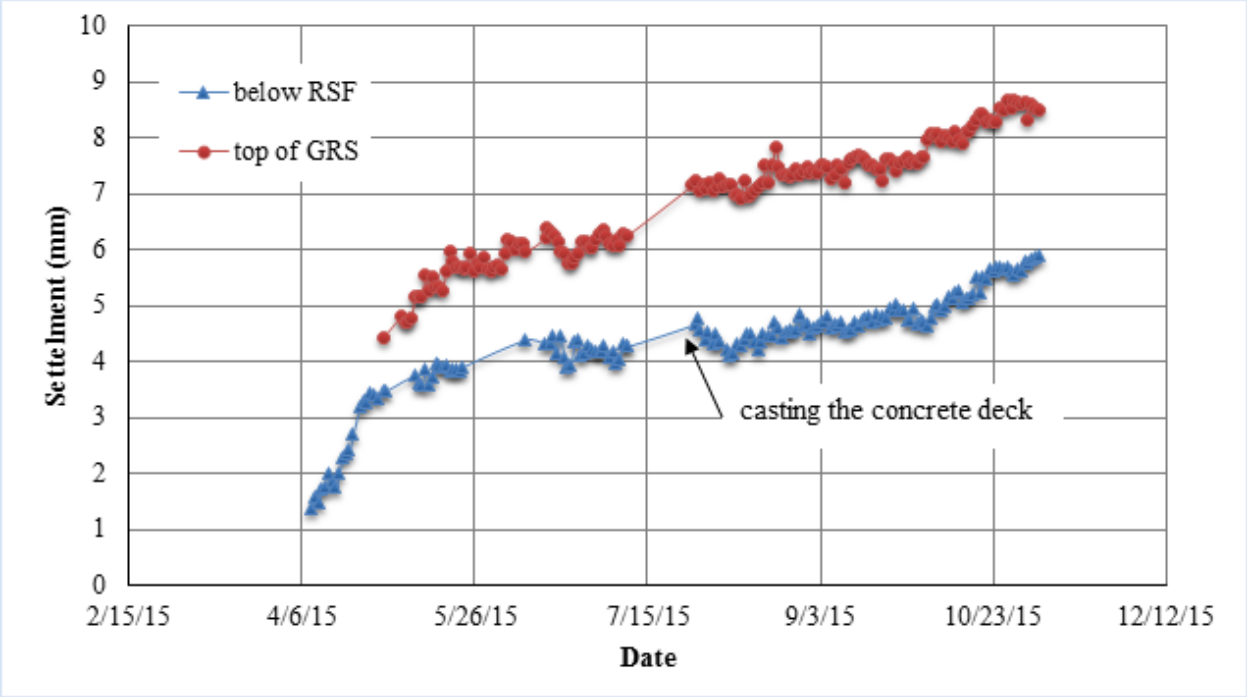

Figure 3.5. Settlement and vertical deformation during the construction of GRS abutment.

3.2.2 Measurement of Soil Stresses

Figure 3.6 shows the measured vertical pressure at different elevations during and after the construction of GRS-IBS abutment. As expected, higher pressure was observed at lower levels of the abutment. The maximum vertical pressure of 115 kPa was measured below the RSF after bridge opened to the traffic. Figure 3.7 shows that at the certain level, the vertical pressures from behind the wall up to 1.8 m away from wall are generally very close. However, the pressure cell located at 2.3 m away from wall on layer 16 shows significantly lower value than the pressure cell close to the wall. The measured vertical earth pressure at the end of abutment construction was compared to the theoretical values for verification. The theoretical value was calculated by multiplying the heights of the backfill above the cells by the average unit weight of backfill. The calculated theoretical pressure at the level below RSF, level 16 and level 19 are 84 kPa, 16 kPa, and 7 kPa, respectively, which compare well with the measured values at the end of abutment construction.

In overall, the maximum measured vertical pressure below the girders was less than FHWA bearing stress restriction of 192 kPa. The horizontal total pressure on the wall was measured by pressure cells attached vertically behind the wall. Three pressure cells were installed behind the facing wall on layers 13, 17 and 20 of the GRS abutments. Figure 8 depicts the measurements of the horizontal pressures. The maximum horizontal pressure was observed in the lower level (layer 13), which is about two times the measured horizontal pressures at upper layers. The higher value at layer 13 can be attributed to the reinforcement spacing. The addition of secondary reinforcement in the top 5 layers of abutment decreases the reinforcement spacing from 20 to 10 cm. The measured horizontal pressures were used later in this paper to calculate thrust force on the facing wall.

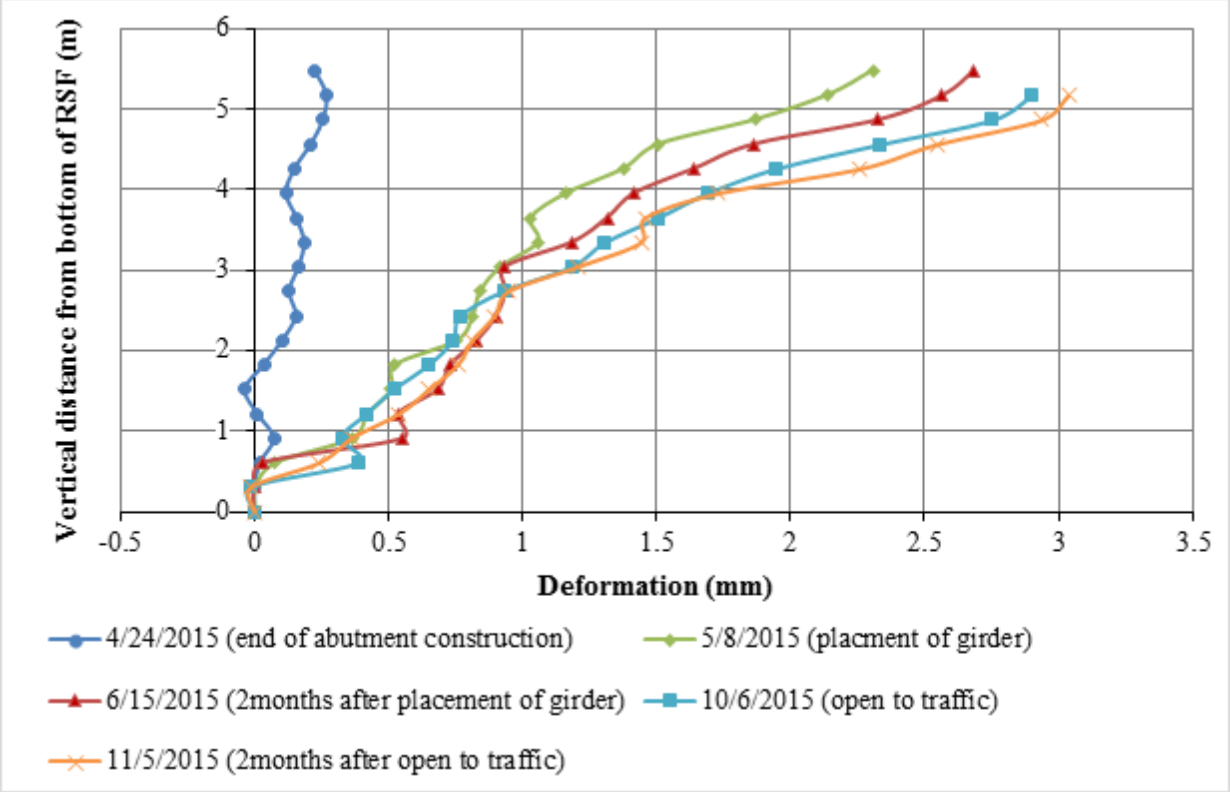

Figure 3.6. Lateral movements of the abutment close to facing wall.

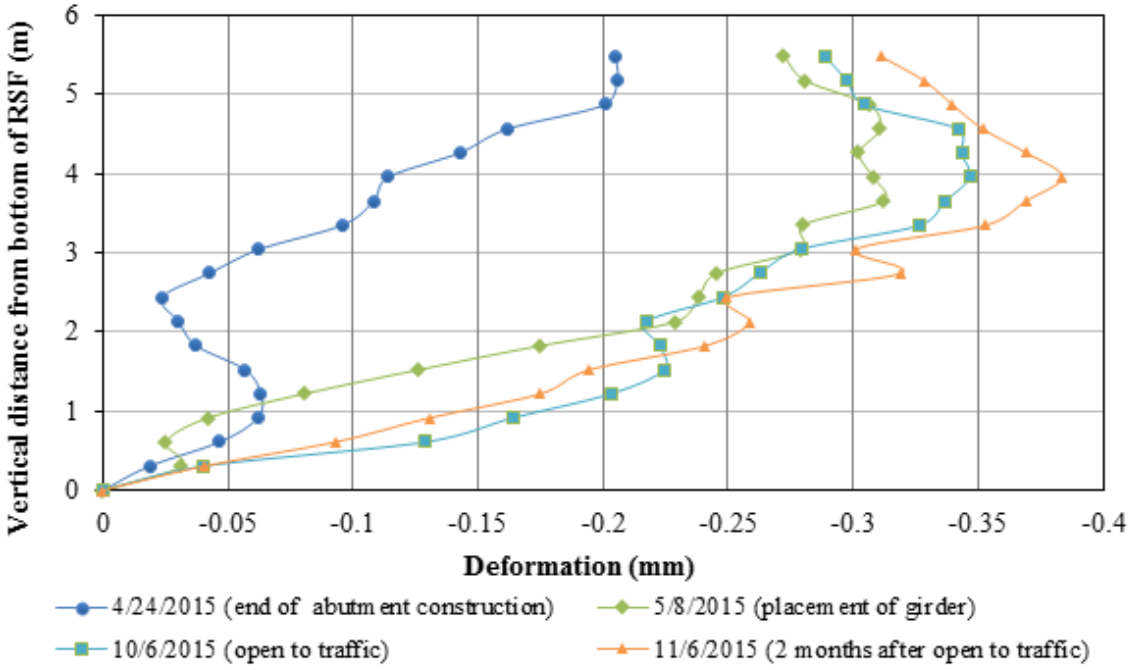

Figure 3.7. Lateral movements behind GRS mass.

Table 3.1. Comparison between predicted and measured lateral deformation of facing wall

Date	**Vertical settlement in abutment (mm)**	**Maximum lateral displacement (mm)**		**Maximum lateral strain**	
		Measurement	**Theory**	**Measurement**	**Theory**
5/8/2015	1.5	2.2	1.35	0.12%	0.07%
6/15/2015	1.9	2.7	1.67	0.14%	0.09%
10/6/2015	2.81	2.9	2.47	0.15%	0.13%
11/5/2015	2.79	3.0	2.46	0.16%	0.13%

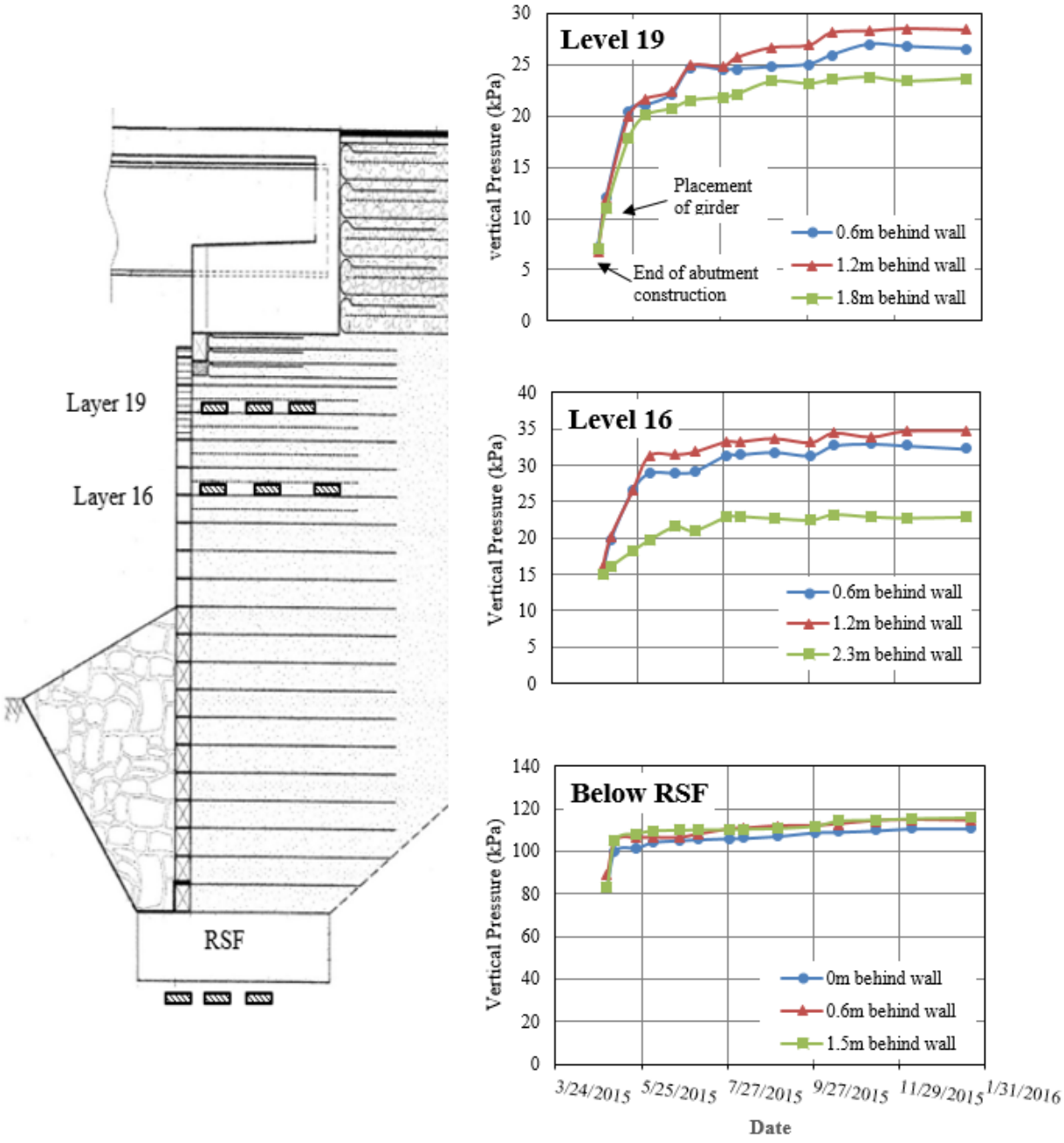

Figure 3.8. Measurement of vertical pressures.

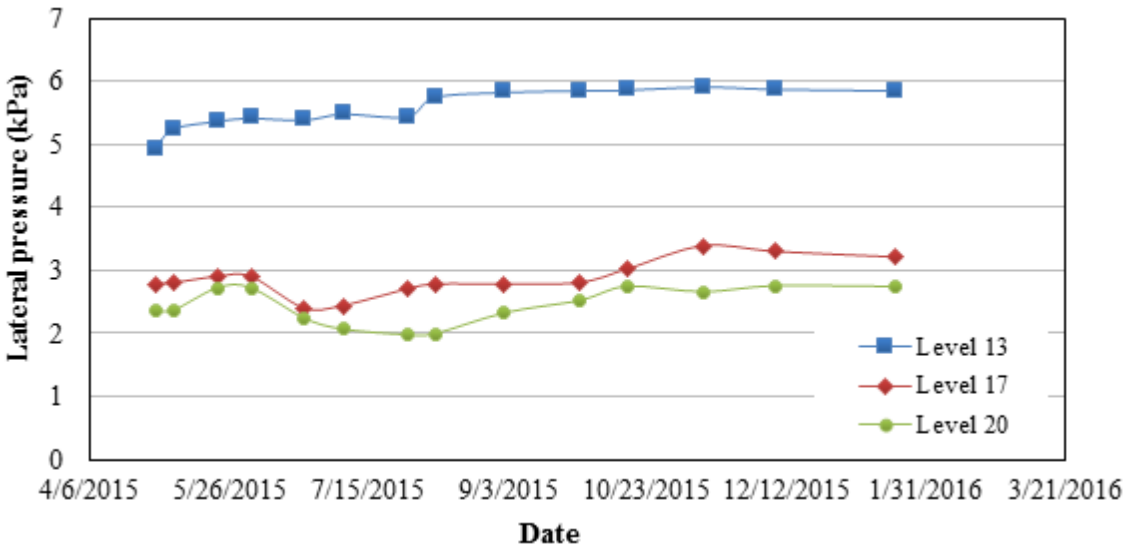

Figure 3.9. Measurements of lateral pressures on the wall.

3.2.3 Strain Measurements along Geosynthetics

Electrical resistance-type/ foil-type strain gauges were installed onto the geosynthetic reinforcements to measure the developed strains along the geosynthetics. A total of 55 strain gauges were installed on five different geotextile layers few weeks before the construction of GRS. 40 out of 55 strain gauges were installed along the centerline of the abutment and the rest 15 strain gauges were installed at one foot offset from the centerline for redundancy. The installation locations of strain gauges were arranged in a fashion such that strain gauge measurements would be able to capture the strain distributions. The extensive instrumentation of geosynthetics provides the opportunity to quantify the mobilized tensile reinforcement forces and the distribution of the tensile strain along geosynthetics that help to identify the critical load bearing zone for internal stability.

The strain measurements of abutment reinforcements for selected layers are shown in Figure 3.11. The figure presents the strain distribution along the reinforcements at different layers and the locus of maximum strains in the abutment. Before placement of the steel girders, the

maximum strain was observed at lower levels. However, after placement of the steel girders (5/8/2015), the maximum strain spikes on the upper layers of abutment. During the construction period, the maximum strain of 1.2% was observed at Level 19, which is less than the maximum strain of 2% specified by the FHWA (*14*).

3.2.4 Thrust Force against the Wall Face

FHWA design method assumes that in a GRS structure, there is no thrust on the wall face due to surcharge or bridge loads. Therefore, this method does not consider the connection strength in the design of the GRS-IBS and consider a relatively constant earth pressure with depth at the wall face. When the reinforcement is capable of restraining lateral deformation of the soil immediately above and below it, the lateral earth pressure from the reinforced soil mass becomes independent of the wall height, surcharge or bridge loads. This occurs because the reinforcement, not the wall face, acts to restrain lateral deformation of the soil. The validity of this assumption behavior is strongly dependent on the reinforcement spacing.

Figure 3.12 presents the measured thrust force on the wall face with time. These values were calculated from the vertical pressure cells that were attached against the inside face of the wall at layers 13, 17 and 20. The maximum measured force at the lower level (layer 13) of abutment was less than 250 N, while the maximum measured thrust forces in the upper layers of abutment (layers 17 and 20) were less than this value. The presence of secondary reinforcement layer within the upper 5 layers of the GRS mass (layers 16-20) reduced the reinforcement spacing and consequently the thrust force against the wall, in addition to lower overburden pressure. Less than 14% change in thrust force was observed during the monitoring period, which can prove the validation of the FHWA (Adams et al., 2011a) assumptions.

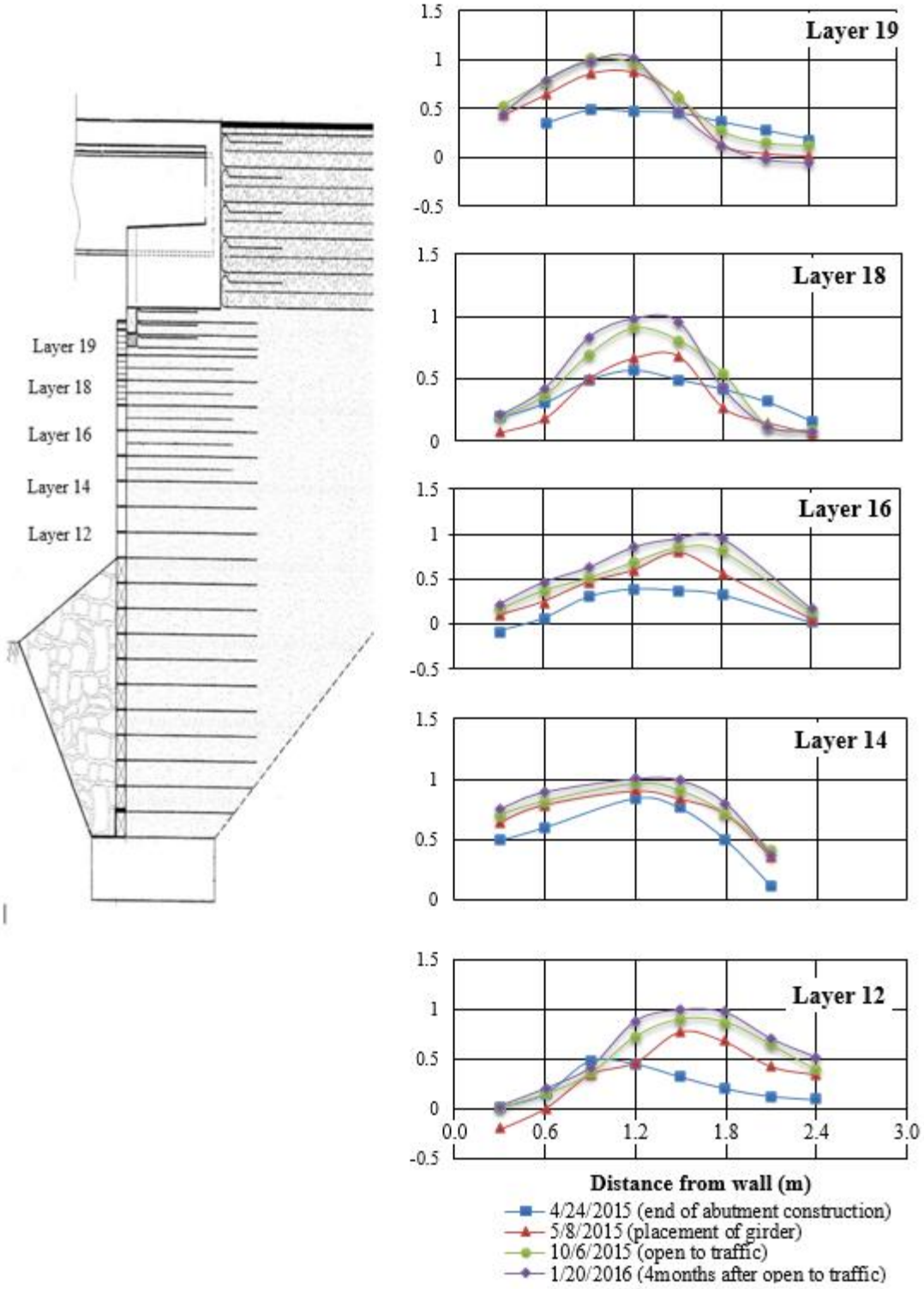

Figure 3.10. Measurement of strain distribution along geosynthetics.

Wu et al. (2007b) suggested that the lateral pressure distribution between reinforcement layers is based on the bin pressure concept. They developed an equation to calculate the thrust force that is only a function of reinforcement spacing and the strength parameter of fill material. This dependency is demonstrated in the following relationship:

$$F_{bin} = 0.72\gamma k_a {s_v}^2 \quad (2)$$

where F_{bin} = the thrust force against the wall face from bin theory, γ = unit weight of fill material, k_a =coefficient of active earth pressure, and s_v =reinforcement spacing.

The comparison of the theoretical and measured thrust values are illustrated in Figure 3.11. The results indicate that the load predicted by the pressure theory were close to the measured thrust loads at layer 13 with 20 cm reinforcement spacing before placement of the girder. However, the bin pressure theory under predicts the load at the layer 17 and 20 with reduced reinforcement spacing. The theoretical thrust values at the layers with 10 cm reinforcement spacing are about half the thrust values measured using the vertical pressure cells.

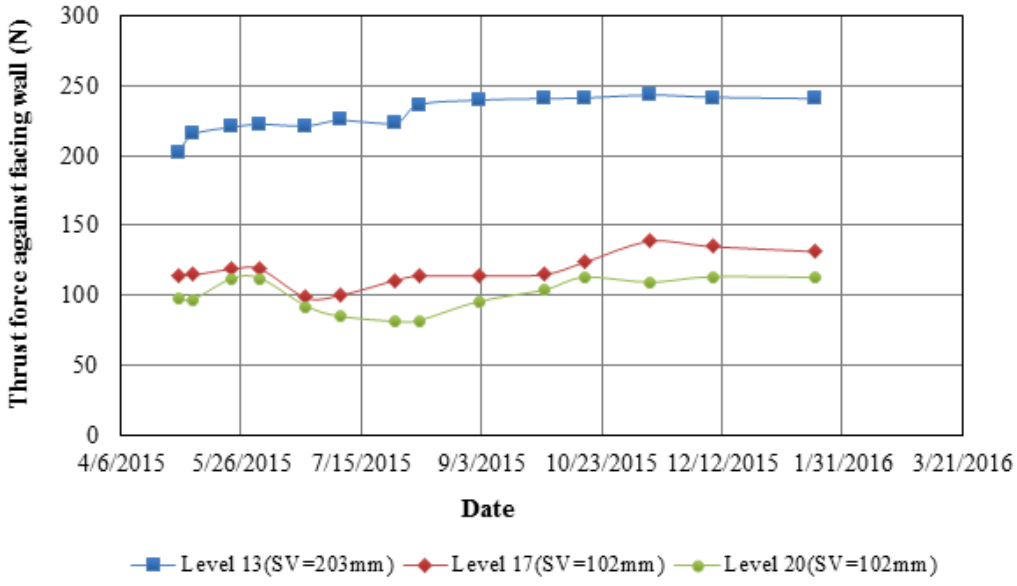

Figure 3.11. Measured thrust force at various stages of construction

Chapter Four
Finite Element Modeling Methodology

4.1 Finite element method

The finite element (FE) method is used in this study to simulate composite behavior of GRS-IBS under dead and live load. This method allows modeling and analyzing complex engineering problems that are not possible to solve using traditional methods. Some of the advantages of the FE method are:

- Include a linear or nonlinear material response,
- Include more than one material type in the same problem
- Include surface to surface interaction between materials
- Solve static or dynamic problems
- Perform parametric studies
- Theoretically, no limits for the problem size

However, the FEA method is not without fault and a bad assessment due to an inferior element selection or an inaccurate load selection can result in all kinds of failures. This directs us to the most paramount and significant principle of finite element methods: ‘Garbage In-Garbage Out’. Essentially, this principle states that the finite element method can generate any results that the design engineer desires.

As a result, it is the responsibility of the user to completely comprehend the real properties of the component to be analyzed and how they would interact with the environment in real life conditions, i.e. water forces would be applied to it or its movement once it is assembled.

For the current study, the choice of two and three-dimensional FE is necessity based. The geosynthetic-backfill interaction is essentially for composite behavior in which the reinforcement spacing surrounding backfill materials influence the composite behavior of the GRS-IBS in interest.

The components of the FE modeling can be summarized as:

- Problem geometry
- Materials constitutive model
- Loads
- Boundary conditions
- Interface behavior.

These components are described in detail in the following sections.

4.1.1 Geometry

The first step in the FE simulation is the model geometry and is considered the basis for creating the FE mesh for the object. The input geometry for the current study has two main parts: GRS-IBS part, and soil body part (Figure 4-1). The GRS wall part is composed of the reinforcement (geotextile) and a set of compacted backfill materials (19 layers). The dimensions of the GRS wall model follow the Maree Michel bridge located on Route LA 91 Vermilion Parish as described below in the geometry Figure 4.1. The reinforcement spacing will vary throughout the study parts and will be mentioned later in the parametric study section. The soil body can be treated as single layer or multiple layers. The dimensions of the soil body vary depending on the pile to pile spacing and are determined by finding the least dimension at which the deformation in the boundary

elements is negligible. The soil is represented by a fourth-order 15-noded triangle element to describe the stress-deformation behavior.

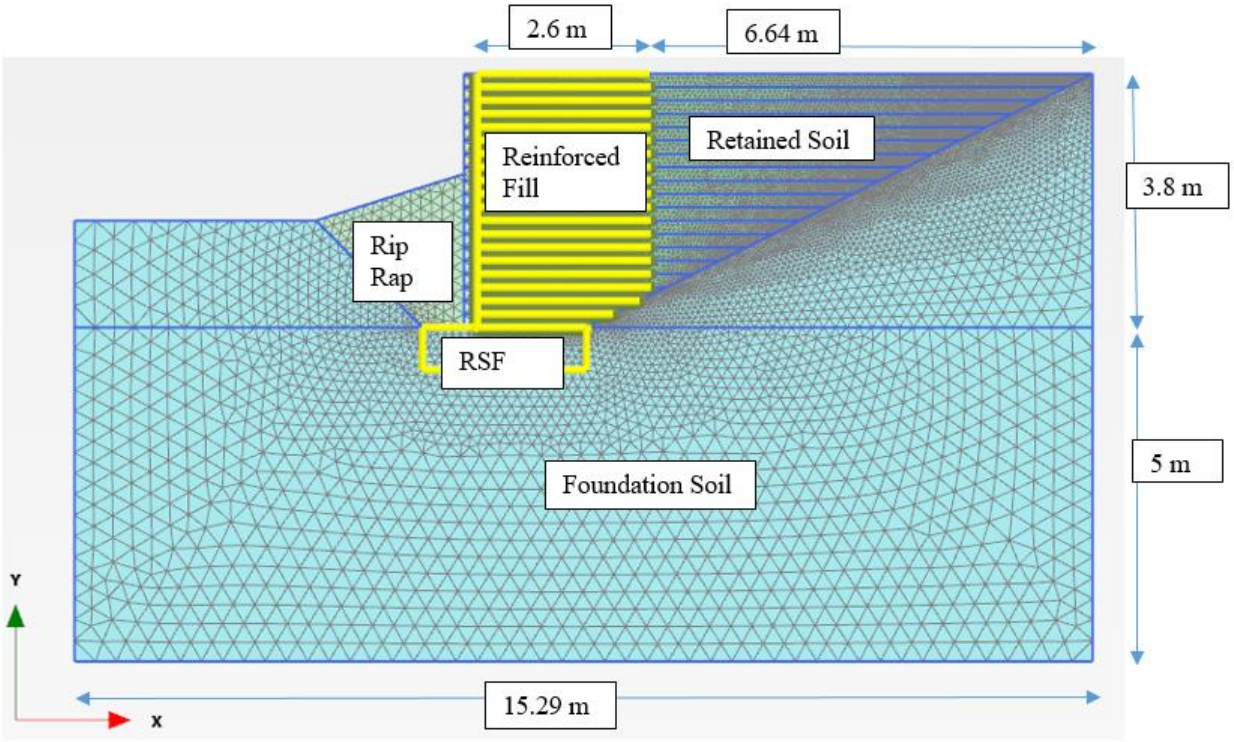

Figure 4.1. GRS-IBS and soil body geometries

4.1.2 Load

Two types of load are applied in the FE model: gravity load, and vertical static load. In the initial state, the gravity load (i.e. the soil body self-weight and the initial stresses). A special procedure is necessary to generate or to calculate the initial stresses within the soil body. As the name implied, initially only the original soil body is in existence, therefore, all the structural elements and geometry changes, e.g.: backfilling, excavation, all structural elements must not be activated. Engineers, very often, directly go through the so called k_o procedure to generate the initial water pressure and the initial effective stresses of the ground. The k_o procedure calculates the stresses within the soil body by the following simple equations:

$$\sigma_{h0} = k_0 \sigma_{v0} \quad \text{.....4.1}$$

where σ_{ho} is the horizontal earth pressure at rest, k_o is the coefficient of earth pressure at rest, σ_{vo} is the effective vertical overburden pressure. This procedure is correct only when all the geometry of the ground surface, the ground layers, and the ground water table are horizontal. Where the ground surface, the subsoil layer, or the ground water level is not horizontal, the k_o procedure will lead to the existence of unbalance forces or non-equilibrium of initial forces within the soil body, which are obviously not correct. In such cases, to maintain equilibrium, there should be shear stresses developed within the soil body. Therefore, the k_o procedure should not be used; instead a gravity loading procedure, where the shear stresses are calculated should be chosen. By default, the earth gravity acceleration, g, is set to 9.8 m/s^2 and the direction of the gravity coincides with the negative y-axis. The vertical static load, the dead and live load, is applied at the top of the GRS-IBS as a uniform distributed load and the direction coincides with the negative y-axis as well, as shown in Figure 4.2.

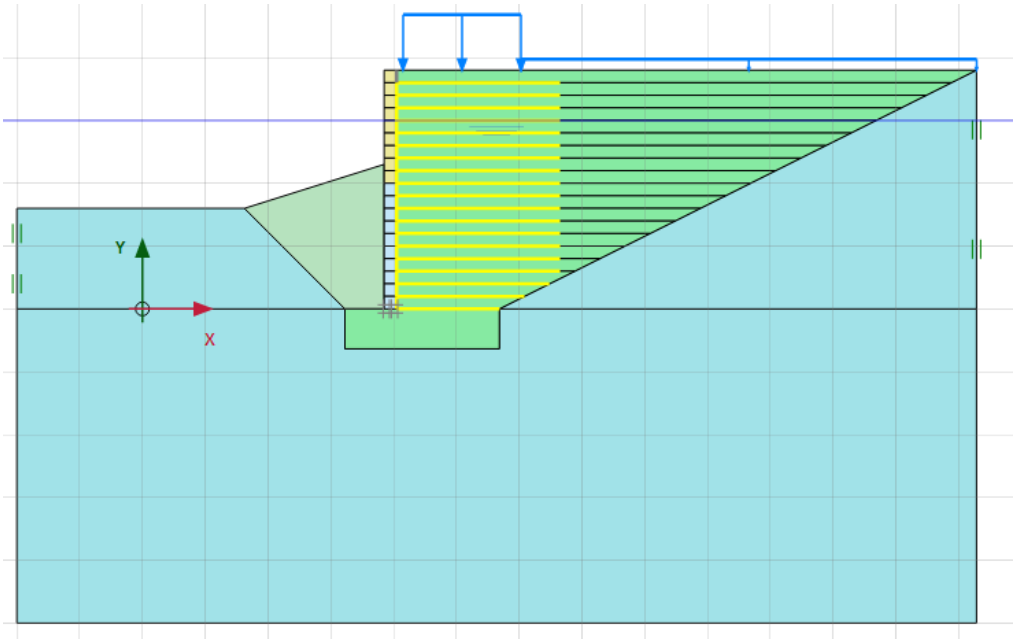

Figure 4.2. Direction of Dead and live load

4.1.3 Boundary Conditions

The global static equilibrium in the FE model is enforced by applying boundary conditions. Roller-type boundary conditions are used on the sides of the soil body and fixed-type boundary conditions are used at the bottom of the soil body as shown in see Figure 4-3. For three-dimensional FE models, a roller-type boundary condition restrains the displacement in one direction and rotations in the other two directions and the fixed-type boundary condition restrain the displacement in two directions and rotations in the other direction. For example, a roller-type boundary condition in the x-direction restrains the displacement in the x direction and rotations in the y- and z- directions.

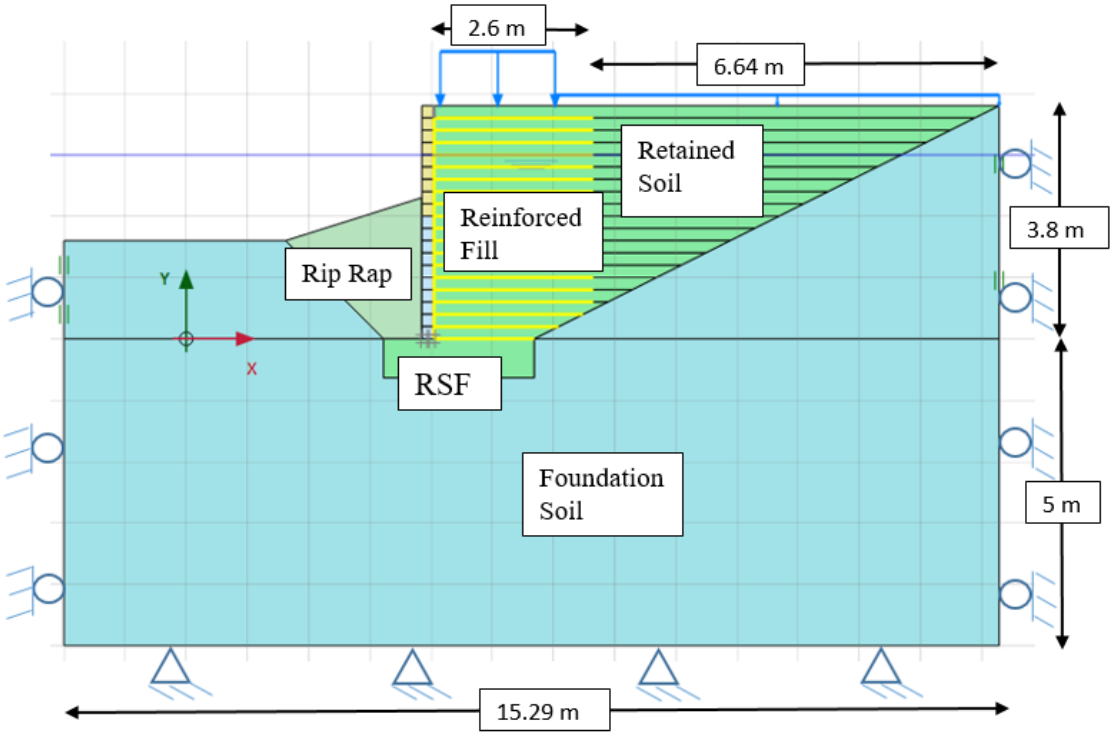

Figure 4.3. Locations of the applied boundary conditions

4.1.4 Geosynthetic-Soil Interface behavior

The choice of structure element to simulate soil reinforcement and soil–structure interaction details for numerical modelling of geosynthetic reinforced soil (GRS) walls can have a significant influence on numerical outcomes. PLAXIS has two options to model the reinforcement (beam and

geogrid element). PLAXIS program uses the linear elastic Mohr–Coulomb interface model to simulate the mechanical behavior of the interface between dissimilar materials. Two options are available to model soil–structure interaction in advanced numerical models: (a) interface elements with zero thickness to transfer shear and normal stresses from the soil to the structure; and (b) continuum elements with finite thickness. The focus of this study is on interface elements with zero thickness that are available in PLAXIS. By using an interface, node pairs are created at the interface of structure and soil. From a node pair, one node belongs to the structure and the other node belongs to the soil. The interaction between these two nodes consists of two elastic-perfectly plastic springs, one elastic-perfectly plastic spring to model the gap displacement and one elastic-perfectly plastic spring to model slip displacement. Also see the connectivity plot in Figure 4.4 of a soil-structure connection with and without interface. Note: for a clear display in the connectivity plot the node pairs are drawn with a certain spacing in between where actually in the calculation kernel the two nodes have the same coordinates (PLAXIS 2D 2016).

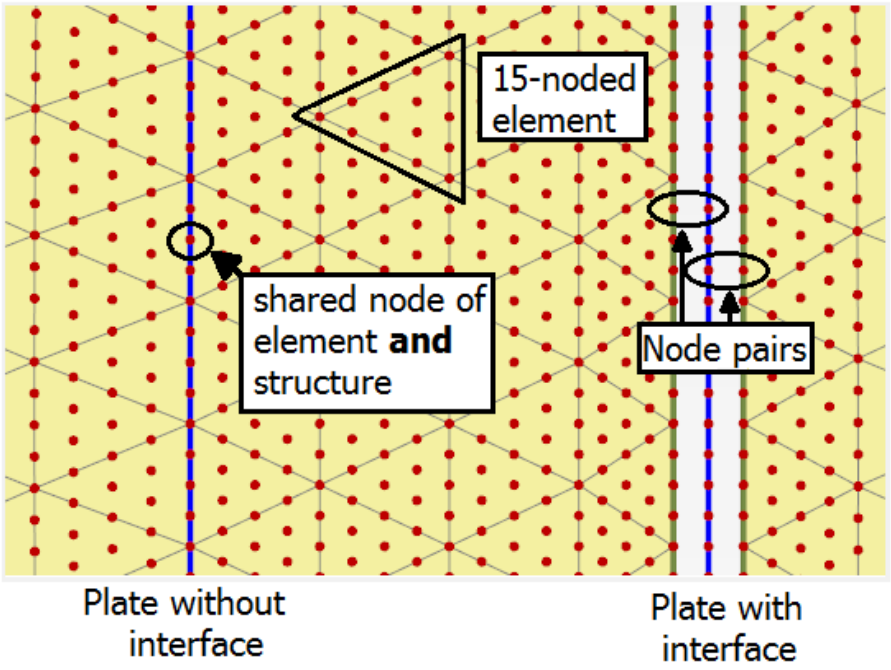

Figure 4.4. Interface Connectivity plot (PLAXIS)

Interfaces using linear elastic model with Mohr-coulomb failure criterion have properties of friction angle, dilation angle, cohesion, Young's modulus (E_i), Poisson's ratio (v_i), and tensile strength. These values can be set using a reduction factor ($R_i \leq 1.0$) applied to the soil materials (the default value is R_i = 1.0, i.e. a fully-bonded interface). The interface value properties are described in the following equations adopted from PLAXIS 2D 2016.

$$c_i = R_i c_i \quad \text{..... 4.2}$$

$$\tan\varphi_i = R_i \tan\varphi_i \quad \text{..... 4.3}$$

$$\Psi_i = \begin{bmatrix} 0 & R_i < 1.0 \\ \Psi_{soil} & R_i = 1.0 \end{bmatrix} \quad \text{..... 4.4}$$

$$G_i = R_i^2 G_{soil} \quad \text{..... 4.5}$$

$$v_i = 0.45 \quad \text{..... 4.6}$$

$$E_i = 2G_i(1 + v_i) \quad \text{..... 4.7}$$

$$E_{oed,i} = 2G_i\left(\frac{1-v_i}{1-2v_i}\right) \quad \text{..... 4.8}$$

$$\sigma_{t,i} = R_i \sigma_{t,i} \quad \text{..... 4.9}$$

where $c_i, \varphi_i, \Psi_i, G_i, v_i, \sigma_{t,i}\ and\ E_i$ are the cohesion, friction angle, dilation angle, shear modulus, Poisson's ratio, tensile strength, and Young's modulus of the surrounding soil, respectively. The strength properties and the R_{inter} value of the relevant material set is directly controlling the level at which (plastic) slipping occurs. By default, these parameters are taken from the material set of the surrounding soil cluster. However, it is also possible to directly appoint a material set to the interface without changing the properties of the soil cluster and thus allows for direct control of the strength properties (and thus the interface strength).

4.2 Constitutive models

Soil and rock tend to behave in a highly non-linear way under load. This no-linear stress-train behavior can be modeled at several levels of sophistication. Clearly, the number of model parameters increases with the level of sophistication. PLAXIS supports different models to simulate the behavior of soil. The models and their parameters that have been used are discussed in details below:

Material	Constitutive Model
Backfill Soil	Hardening Soil Model
Subgrade Soil	Mohr-Coulomb Model
Geosynthetic and Facing Block	Linear Elastic

4.2.1 Backfill Material

The soil (backfill) nonlinear behavior is modeled using the elastoplastic hardening soil model (HSM). The hardening soil was developed under the framework of the theory of plasticity. In this model, a stress-dependent stiffness is using to calculate the total strains, which is different for both loading and unloading/ reloading. An isotropic hardening is assumed, depending on the plastic volumetric and shear strains. An associated flow rule is assumed for the cap hardening and non-associated flow rule is assumed when related to frictional hardening.

The formulation and verification of the Hardening Soil Model was explained by Schanz et al. (1999) and Brinkgreve (2002) in detail. The stress–strain relationship is assumed to be a hyperbolic curve due to the primary loading in the HSM. The hyperbolic function, as given by Kondner (1963), for the drained triaxial test can be formulated as

$$\varepsilon_1 = \frac{q_a}{2E_{50}} \frac{q}{q_a - q}, \quad for\ q < q_f \qquad \text{.....4.10}$$

where ε_1 is the axial strain, and q is the deviatoric stress. The ultimate deviatoric stress (q_f) is defined as

$$q_f = \frac{6sin\emptyset'}{3-sin\emptyset'}(\sigma_3' + c'cot\emptyset') \quad \text{.....4.11}$$

and the quantity (q_a) is

$$q_a = \frac{q_f}{R_f} \quad \text{.....4.12}$$

where q_f : the ultimate deviatoric stress at failure, which is derived from the Mohr–Coulomb failure criterion involving the strength parameters c' and $\emptyset'$.

q_a : the asymptotic value of the shear strength.

R_f : the failure ratio.

Figure 4.5 shows the hyperbolic relationship of stress and strain in primary loading. A total of 10 input parameters are required in the Hardening Soil Model, as tabulated in Table 2.

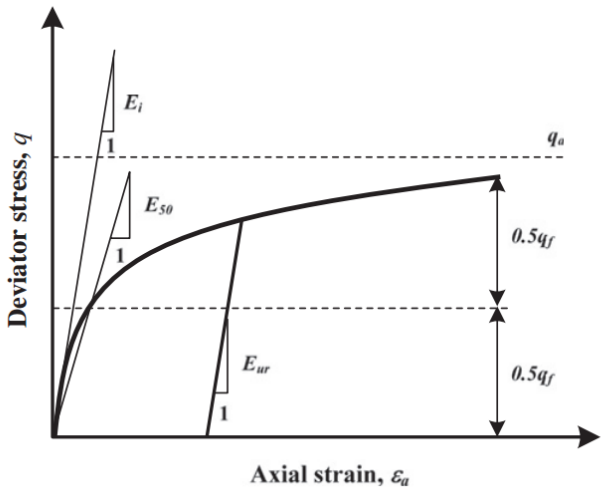

Figure 4.5. Hyperbolic stress–strain relationship in primary loading for a standard drained triaxial test (Schanz et al., 1999).

Table 4.1. Hardening soil model input parameters.

Parameter	Description	Parameter evaluation
$\emptyset^{'}$	Internal friction angle	Mohr-Coulomb
$c^{'}$	Cohesion	Mohr-Coulomb
R_f	Failure ratio	$(\sigma_1 - \sigma_3)/(\sigma_1 - \sigma_3)_{ult}$
Ψ	Dilatancy angle	Function of $\varepsilon_a \; and \; \varepsilon_v$
E_{50}^{ref}	Reference secant stiffness from drained triaxial test	y-intercept in $\log\left(\frac{\sigma_3}{p^{ref}}\right) - \log(E_{50}) \; space$
E_{oed}^{ref}	Reference tangent stiffness form oedometer primary loading	y-intercept in $\log\left(\frac{\sigma_1}{p^{ref}}\right) - \log(E_{oed}) \; space$
E_{ur}^{ref}	Reference unloading/reloading stiffness	y-intercept in $\log\left(\frac{\sigma_3}{p^{ref}}\right) - \log(E_{ur}) \; space$
m	Exponential power	Slope of trend line in
v_{ur}	Unloading/reloading Poisson's ratio	0.2 (default setting)
K_0^{nc}	Coefficient of earth pressure at rest	$1 - \sin\emptyset^{'}$ (default setting)

The stress–strain behavior of soil and rock for primary loading is highly non-linear. The parameter E_{50} is a confining stress dependent stiffness modulus for primary loading. E_{50} is used instead of the initial modulus E_0 for small strain which, as a tangent modulus, is difficult to determine experimentally, and is given as

$$E_{50} = E_{50}^{ref}\left(\frac{c^{'} cos\emptyset^{'} - \sigma_3^{'} \sin\emptyset^{'}}{c^{'}\cos\emptyset^{'} + p^{ref}\sin\emptyset^{'}}\right)^m \quad \ldots\ldots\ldots\

$$E_{ur} = E_{ur}^{ref}\left(\frac{c^{`}\cos\emptyset^{`} - \sigma_3^{`}\sin\emptyset^{`}}{c^{`}\cos\emptyset^{`} + p^{ref}\sin\emptyset^{`}}\right)^m \quad \text{.....4.14}$$

where:

E_{ur}^{ref} is a reference stiffness modulus for unloading/reloading corresponding to the reference stress p_{ref}. (In PLAXIS, p^{ref} = 100 kN/m^2 and E_{ur}^{ref} equal to $3E_{50}^{ref}$). The shear hardening yield function is given as:

$$f_s = f^{`} - \gamma^p \quad \text{.....4.15}$$

$$f^{`} = \frac{q_a}{E_{50}}\left[\frac{(\sigma_1^{`} - \sigma_3^{`})}{q_a - (\sigma_1^{`} - \sigma_3^{`})}\right] - \frac{2(\sigma_1^{`} - \sigma_2^{`})}{E_{ur}} \quad \text{.....4.16}$$

where:

$\sigma_1^{`}\ and\ \sigma_3^{`}$: major and minor effective principal stresses

E_{50} : 50% secant modulus

γ^p : plastic shear strain

$$\gamma^p \approx \varepsilon_1^p - \varepsilon_2^p - \varepsilon_3^p = 2\varepsilon_1^p - \varepsilon_v^p \approx 2\varepsilon_1^p \quad \text{.....4.17}$$

where:

$\varepsilon_1^p, \varepsilon_2^p\ and\ \varepsilon_3^p$: plastic strains

ε_v^p : volumetric strain

It can be seen that the triaxial moduli ($E_{50}^{ref}\ and\ E_{ur}^{ref}$) are parameters that control the shear hardening yield surfaces. In addition to the shear hardening yield surfaces, the cap yield surfaces are also used in the HSM. These cap yield surfaces are related to the plastic volumetric strain measured in the isotropic compression condition. Fig. 4.6 shows the shear hardening and the cap yield surfaces in the HSM for soil with no cohesion.

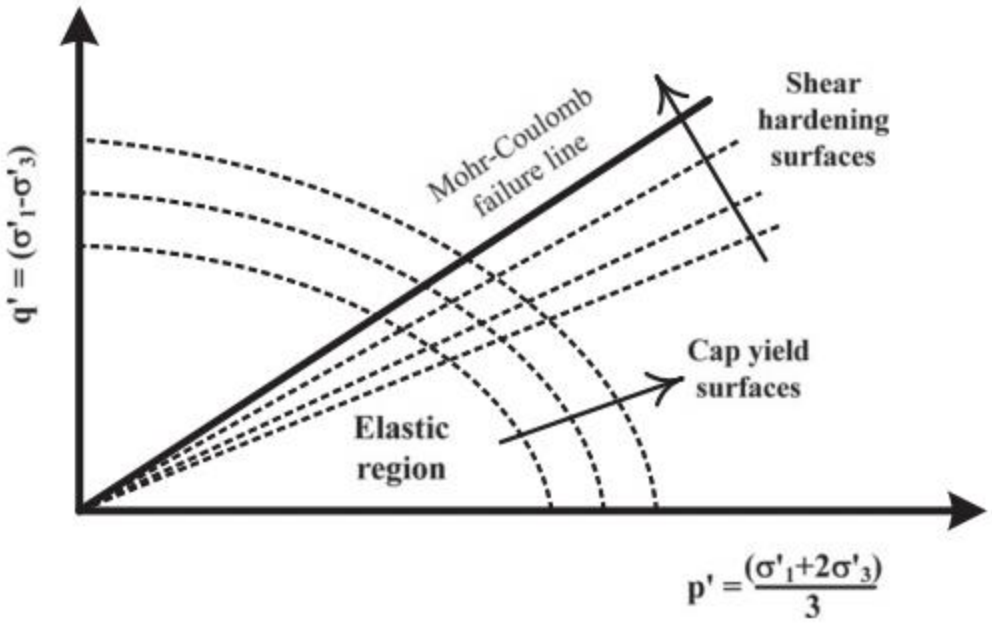

Fig. 4.6. Shear hardening and cap yield surfaces in the Hardening Soil Model (Schanz et al., 1999).

Another input parameter, the reference oedometer modulus (E_{oed}^{ref}), is used to control the magnitude of the plastic strains that originate from the yield cap (ε_v^{pc}). In a similar manner to the triaxial moduli, the oedometer modulus (E_{oed}) obeys the stress dependency law:

$$E_{oed} = E_{oed}^{ref}\left(\frac{c` cos\emptyset` - \sigma_1` sin\emptyset`}{c` cos\emptyset` + p^{ref} sin\emptyset`}\right)^m \quad \text{.....4.18}$$

The cap yield function is given as:

$$f^c = \frac{q^2}{\alpha^2} + p^2 - p_p^2 \quad \text{.....4.19}$$

where:

p_p : pre-consolidation stress

$$p = \frac{-(\sigma_1+\sigma_2+\sigma_3)}{3} \quad \text{.....4.20}$$

$$q^2 = \sigma_1 + (\delta - 1)\sigma_2 - \sigma_3 \quad \text{.....4.21}$$

$$\delta = \frac{(3+sin\emptyset`)}{(3-sin\emptyset`)} \quad \text{.....4.22}$$

The magnitude of the yield cap is determined by the isotropic pre-consolidation stress p_p.The hardening law, which relates the pre-consolidation pressure (p_p) to the volumetric cap-strain (ε_v^{pc}), can be expressed as

$$\varepsilon_v^{pc} = \frac{\beta}{1-m}\left(\frac{p_p}{p^{ref}}\right)^{1-m} \quad \text{.....4.23}$$

where ε_v^{pc} is the volumetric cap strain, which represents the plastic volumetric strain in isotropic compression. In addition to the constants m and pref, which have been discussed earlier, there is another model constant β. Both α and β are cap parameters, but PLAXIS does not adopt them as input parameters. Instead, their relationships can be expressed as:

$\alpha = K_0^{nc}$ (by default $K_0^{nc} = 1 - \sin\emptyset$`) ……..4.24

$\beta = E_{oed}^{ref}$ (by default, $E_{oed}^{ref} = E_{50}^{ref}$) ……....4.25

Figure 4.7 shows the ellipse shape cap surface in the *p*–*q* plane.

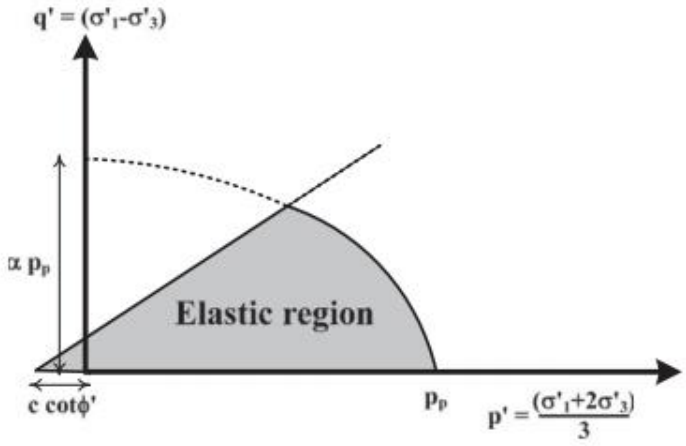

Figure 4.7. Yield surface of the Hardening Soil Model in q-p0 plane (Schanz et al., 1999)

Chapter Five
Finite Element Modeling 2D

5.1 Introduction

In this chapter, a plane strain FE analysis was developed and verified using the results from the field monitoring of the fully-instrumented GRS-IBS bridge abutment at Maree Michel Bridge in Louisiana. The PLAXIS 2D 2016 was selected for the numerical analysis of this study. In the FE model, the soil and the facing block were represented by a plane strain fourth-order 15-noded triangle element to describe the stress-deformation behavior. The geotextile was represented by a special tension 5-noded elements (note that the geotextile elements are automatically taken to be compatible with the soil element type) to describe the axial forces. The Interface between the backfill soil and geosynthetic was simulated using joints elements to model the soil-structure interface behavior, which is represented by 5 pair joint element (also compatible with the soil element) to simulate the thin zone of intense shearing at the contact between the geotextile and the surrounding soil.

PLAXIS 2D 2016 also offers a linear elastic model with Mohr–Coulomb failure criterion option to simulate the mechanical behavior of the interface between dissimilar materials by using a reduction factor ($R_i \leq 1.0$) applied to the soil material when defining soil property values (R_i = 1.0, for a fully-bonded interface). Hence, the interface property values are directly related to the mechanical properties of the soil forming the interface (e.g. $C_i = R_i * C_{soil}$). These interfaces have properties of friction angle, cohesion, dilation angle, tensile strength, Young's modulus (E), and Poisson's ratio (ν). Laboratory and in-situ testing were conducted to evaluate the soil parameters. The geotextile and facing block properties were provided from the manufacture. A summary of the parameters used in FE modeling is provided in Table 5.1.

Figures 5.1. presents the FE mesh for the GRS-IBS of Maree Michel Bridge abutment (252932 nodes and 30229 elements). Mesh sensitivity was first carried out to select the proper size of FE mesh that is not affecting the FE results. A fixed boundary condition was applied at the bottom of the FE model. A roller boundary conditions was used on both sides of the FE model. The total height of the GRS-IBS wall is 3.8 m from the top of the RSF and was divided into twenty layers to simulate the field construction process by using the staged construction mode in PLAXIS 2D 2016, which allows for simulation of construction and excavation processes. A 63 kPa distribution load at the top and bottom of each soil layer was applied during the staged construction process to simulate the soil compaction. This approach is based on the procedure introduced by Dantas (2004) and Morrison et al. (2006) to consider the induced stress on the backfill soil due to compaction, which was also adopted later by Ehrlich and Mirmoradi (2013), Mirmoradi and Ehrlich (2014 a,b) and Riccio et al. (2014).

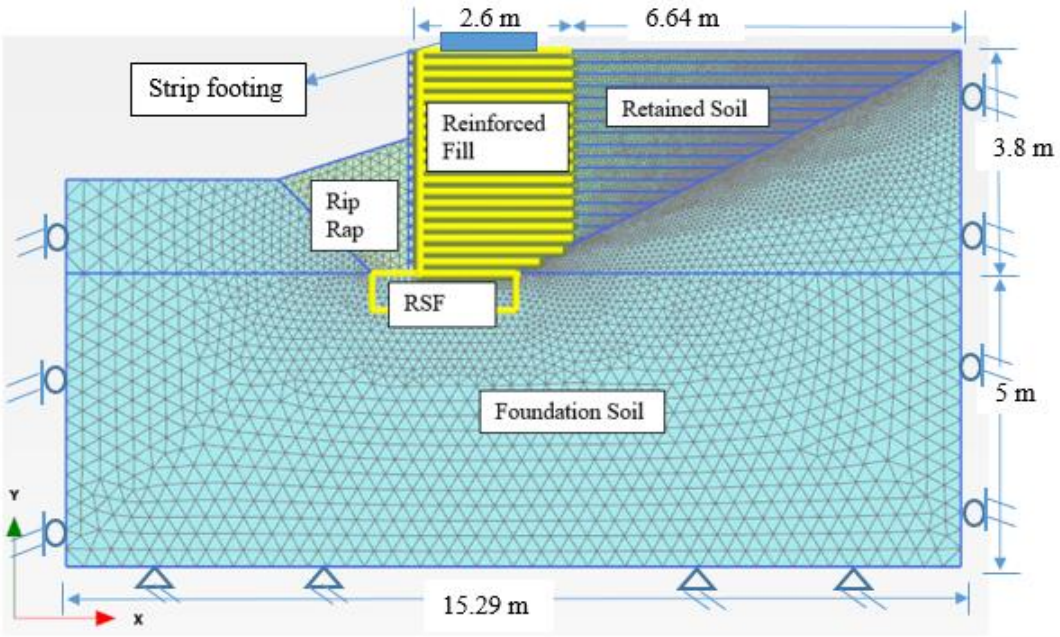

Figure 5.1. FE Mesh of the GRS-IBS and locations of the applied boundary conditions

5.2 Results and Discussion (Two-Dimensional Finite Element (2D-FE) Model)

5.2.1 Introduction

This chapter presents the results of a finite element (FE) numerical analysis that was developed to simulate the fully-instrumented geosynthetic reinforced soil integrated bridge system (GRS-IBS) at the Maree Michel bridge in Louisiana. Four different loading conditions were considered in this paper to evaluate the performance of GRS-IBS abutment due to dead loading, tandem axle truck loading, service loading, and abnormal loading. The two-dimensional FE computer program PLAXIS 2D 2016 was selected to model the GRS-IBS abutment. The hardening soil model proposed by Schanz et al. (1999) that was initially introduced by Duncan-Chang (1980) was used to simulate the granular backfill materials; a linear-elastic model with Mohr-Coulomb frictional criterion was used to simulate the interface between the geosynthetic and backfill material. Both the geosynthetic and the facing block were modeled using linear elastic model. The Mohr-Coulomb constitutive model was used to simulate the foundation soil. The FE numerical results were compared with the field measurements of monitoring program, in which a good agreement was obtained between the FE numerical results and the field measurements. The range of maximum reinforcement strain was between 0.4% and 1.5%, depending on the location of the reinforcement layer and the loading condition. The maximum lateral deformation at the face was between 2 and 9 mm (0.08% to 0.4% lateral strain), depending on the loading condition. The maximum settlement of the GRS-IBS under service loading was 10 mm (0.3% vertical strain), which is about two times the field measurements (~5 mm). This is most probably due to the behavior of over consolidated soil caused by the old bridge. The axial reinforcement force predicted by FHWA (2012) design methods were 1.5 - 2.5 times higher than those predicted by the FE analysis and the field measurements, depending on the loading condition and reinforcement

location. However, the interface shear strength between the reinforcement and the backfill materials predicted by Mohr-Coulomb method was very close to those predicted by the FE.

5.2.2 Objective

The primary objective of this FE numerical analysis is to develop a model that is capable of simulating the GRS-IBS system under service loading conditions. The results of the FE analysis were verified using the field measurements of the fully-instrumented GRS-IBS system at the Maree Michel Bridge in Louisiana. The FE model were then used to simulate the service loading and the abnormal loading conditions.

5.2.3 Finite Element Numerical Model

Plane strain FE analysis was developed and verified using the results from the field monitoring of the fully-instrumented GRS-IBS bridge abutment at Maree Michel Bridge, in Louisiana. The PLAXIS 2D 2016 was selected for the numerical analysis of this study. In the FE model, the soil and the facing block were represented by a plane strain fourth-order, 15-noded triangle elements to describe the stress-deformation behavior. The geotextile was represented by a special tension 5-noded elements to describe the axial forces (note that the geotextile elements are automatically taken to be compatible with the soil element type). The interface between the backfill soil and geosynthetic was simulated using joint elements to model the soil-structure interface behavior, which is represented by 5-pair joint element (also compatible with the soil element) to simulate the thin zone of intensely shearing at the contact between the geotextile and the surrounding soil.

PLAXIS 2D 2016 offers a range of constitutive models including the second order hyperbolic elastoplastic hardening soil model (Schanz et al., 1999) that was selected to simulate the behavior of granular backfill materials in this study. The hardening model implies friction hardening to

model the plastic shear strain in deviatoric loading and cap hardening to model the plastic volumetric strain in primary compression. The model is also capable of simulating the soil dilation, non-linear stress-strain behavior of the backfill soil, stress dependency, and unloading-reloading behavior. The formulation and verification of the Hardening Soil Model (HSM) was explained by Schanz et al. (1999) and Brinkgreve (2002) in detail.

PLAXIS 2D 2016 also offers a linear elastic model with the Mohr–Coulomb failure criterion option to simulate the mechanical behavior of the interface between dissimilar materials by using a reduction factor ($R_i \leq 1.0$) applied to the soil material when defining soil property values (R_i = 1.0, meaning the interface should not have a reduced strength with respect to the strength of the surrounding soil). Hence, the interface property values are directly related to the mechanical properties of the soil forming the interface (e.g. $C_i = R_i * C_{soil}$). These interfaces have properties of friction angle, cohesion, dilation angle, tensile strength, Young's modulus (E), and Poisson's ratio (ν).

The backfill material was a crushed diabase open-graded aggregate soil with a maximum particle size of 19 mm. Three triaxial tests were conducted to evaluate the stiffness of the backfill materials at confining pressures of 207 kPa, 345 kPa, and 483 kPa. The soil specimen was 15.24 cm in diameter and 30.48 cm in height. Figure 5.2 presents the stress-strain curve for the backfill materials. Three large direct shear tests were conducted to evaluate the strength of the backfill materials at normal stresses of 48 kPa, 120 kPa, and 192 kPa. The soil specimen was $30.48 \times 30.48 \times 15.24$ cm. The peak stress was found to be 83.5 kPa, 144 kPa, and 260 kPa for the previous normal stresses, respectively. The dilation angle was estimated using (Bolton, 1986);

$$\phi_p = \phi_{cv} + 0.8\psi$$

where: ϕ_p = peak friction angle = 51°; ϕ_{cv} = critical state friction angle = 34°; ψ = dilation angle.

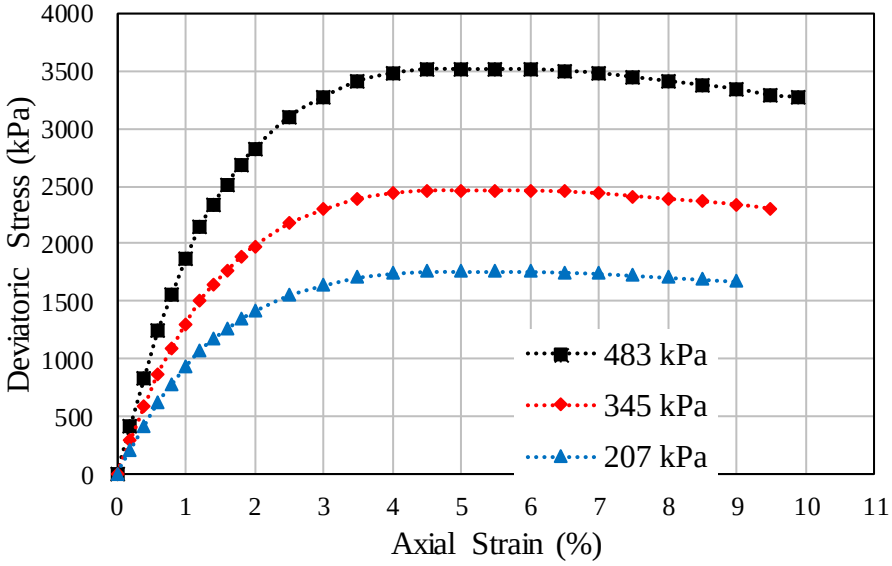

Figure 5.2. Stress-Strain Curves of Backfill at 18 kN/m3 Dry Density

A cone penetration test (CPT) was conducted to evaluate the foundation soil properties. The geotextile and facing block properties were provided from the manufacturer (note that the strain-rate in the field is less than the strain-rate described in the ASTM D 4595, which is 10% strain min^{-1}). However, as the manufacturer does not provide the axial stiffness parameter, which is the only input parameter required to model the geotextile as elastic, the axial stiffness of geotextiles was calibrated from laboratory experiment test data). A summary of the parameters used in FE modeling is provided in Table 1.

Figures 5.1 presents the FE mesh for the GRS-IBS of the Maree Michel Bridge abutment (252932 nodes and 30229 elements). Mesh sensitivity was first carried out to select the proper size of FE mesh that is not affecting the FE results. A fixed boundary condition was applied at the bottom of the FE model. A roller boundary conditions was used on both sides of the FE model.

The dimensions of the soil body are determined by finding the least dimension at which the deformation in the boundary elements is negligible.

Table 5.1. Material Properties

Category	Description
Facing Block	Linear elastic model; E = 3×10^7 kPa,; γ=12.5 kN/m^3; dimensions, 40.64×20.32×20.32 cm; Poisson's ratio, ν = 0
Geotextile	Linear elastic perfectly plastic model; Tensile strength @ 2% = 13×17 kN/m, Tensile strength @ 5% = 35×40 kN/m; Tult = 80 kN/m; reinforcement spacing = 0.2 m; Axial stiffness, EA= 600 kN/m.
Backfill Material	Hardening soil model; dry unit weight, γ_d= 18 kN/m /m^3; wet unit weight, γ_t=19 kN/m /m^3; cohesion, c =20 kPa; friction angle, ϕ =51°; dilation angle Ψ=21°; E_{50}^{ref}=34,000 kPa, E_{ur}^{ref}= 103,200 kPa, E_{oed}^{ref}=26,400, ν= 0.2; power, m = 0.5
Foundation Soil	Soil model, Mohr-Coulomb model; dry unit weight, γ_d= 15.2 kN/m^3; wet unit weight, γ_w=18.65 kN/m^3; cohesion, c=17.7 kPa; ϕ= 27°; E =30000 kPa; ν= 0.2.
Interface (backfill and geotextile)	Linear elastic with Mohr-Coulomb failure criterion; adhesion, c=8.6 kPa; interface friction angle δ=40.4°
Interface (block and geotextile)	Linear elastic with Mohr-Coulomb failure criterion; cohesion, c=7 kPa; friction angle ϕ=34°
Riprap[a]	Linear elastic model, E[b] = 50 MPa; γ = 22 kN/m^3; ν = 0.25

[a]30 lb riprap was used with spherical diameter = 0.155 m. [b]For riprap, use E_{50}= $0.5E_i$. According to Duncan and Chang (1970), $E_i=K_m p_a\,(\sigma_3 / p_a)^n$, where K_m and n=initial tangent modulus coefficient and exponent, respectively, p_a=atmospheric pressure, and σ_3=minor principal stress which is estimated to be $\sigma_v(1+2K_0)/3$, σ_v = vertical effective stress at mid depth of layer and K_o = at-rest earth pressure coefficient. For gravels, the highest value of $K_m\cong$2, 500 (Duncan et al. 1980). For riprap, use K_m = 3, 500 and n= 0.4.

The total height of the GRS-IBS wall is 3.8 m from the top of the RSF and was divided into 20 layers to simulate the field construction process by using the staged construction mode in PLAXIS 2D 2016, which allows for simulation of construction and excavation processes. A 63 kPa distribution load at the top and bottom and exposed faces of each soil layer was applied during the staged construction process to simulate the soil compaction. This approach is based on the

procedure introduced by Dantas (2004) and Morrison et al. (2006) to consider the induced stress on the backfill soil due to compaction, which was also adopted later by Ehrlich and Mirmoradi (2013), Mirmoradi and Ehrlich (2014 a, b), and Riccio et al. (2014).

5.2.4 Results and Discussion

Four different loading cases were considered in this study: (a) end of bridge construction, which is equal to the total dead loads on the abutment (case 1 = 100 kPa); (b) truck loading, which is equal to the total dead loads and the load of a dump truck (case 2 = 130 kPa); (c) service loading, which is equal to the total dead loads and the bridge live loads (case 3 = 177 kPa); and (d) abnormal loading, which is equal to the total dead loads and three times the service loading (case 4 = 331 kPa) (note that abnormal loading is totally hypothetical loading assuming a linear elastic behavior for the reinforcement under these loading). The equivalent roadway live load was considered 12 kPa and the equivalent roadway dead load was 18 kPa. The field measurements during monitoring of the GRS-IBS at the Maree Michel bridge were used to verify the FE model, and then the verified FE model was used to generate the vertical and lateral deformations, horizontal and vertical earth pressures, the axial force and strain in the reinforcement, and the interface shear strength between the reinforcement and backfill materials due to the four loading cases.

5.2.5 Vertical and Lateral Deformations

According to FHWA (2012), the vertical strain deformation should be less than 0.5% of the abutment height. The maximum lateral deformation at the face can be calculated using the assumption of the composite behavior of properly constructed GRS-IBS mass such that the reinforcement and soil strain extend laterally together (FHWA, 2012). With that being said and assuming a zero-volume change in the GRS-IBS abutment due to vertical loading, the lateral strain

according to FHWA (2012) is two times the vertical strain and should be less than 1% of the abutment height.

Figure 5.3 presents the comparison profiles of the lateral deformations at the face of the GRS-IBS wall determined from FE analysis at the end of abutment construction and the end of bridge construction and field measurements. It can be seen that there is a good agreement between the field measurements and FE numerical results. The maximum lateral deformation was found to be 0.5 mm and 2 mm for the end of abutment construction and at the end of bridge construction, respectively. It is interesting to notice that these results are much lower than the FHWA (Adams et al., 2011a) recommendations (less than 1%, 20.8 mm for the width of the load along the top of the wall including the setback which is equal to 2.08 m).

Figure 5.4 presents the comparison profiles of the settlement distribution under the RSF predicted by FE analysis at the end of abutment construction and the end of bridge construction and field measurements. The maximum footing settlement due to service load and abnormal load are 10 mm (0.3%) and 23 mm (0.6%), which is acceptable for both the service load and for the abnormal load according to FHWA (2012) recommendations since the field measurements are lower than those predicted by the FE analysis and this is most probably due to the over consolidated soil caused by the old bridge.

Figure 5.5 presents the lateral deformation profile of the GRS-IBS wall face, which shows that the maximum lateral deformations are 0.5, 2, 2.5, 4, and 9 mm at the end of abutment construction, the end of bridge construction, the truck loading, the service loading, and abnormal loading, respectively.

5.2.6 Horizontal and Vertical Stresses

Figure 5.6 presents the profile comparison of the lateral stress at the face of the GRS-IBS abutment wall predicted by the FE analysis and the field measurements at the end of bridge construction. The figure also presents the lateral stresses predicted by FE analysis for the truck loading, service loading, and abnormal loading. It can be noted that the lateral earth pressure at the face of the GRS-IBS wall is somehow uniform with depth and much less than the lateral earth pressure estimated by Rankine method as in the case of MSE walls, which is in agreement with the composite behavior of closely reinforced soil as demonstrated by (Adams et al., 2014). The maximum lateral earth pressure was found to be 5 kPa, 8 kPa, 10 kPa, 12 kPa, and 25 kPa for Case 1, Case 2, Case 3, and Case 4, respectively. The composite behavior of the GRS-IBS wall plays an important role in reducing the lateral earth pressure at the face as shown in Figure 5.6. The presence of closely reinforcement in a soil mass has proved to reduce the lateral stresses when subjected to vertical loading because the reinforcement is capable of restraining the lateral deformation of the soil around it (Wu, 2014).

For instance, the active lateral earth pressure at the facing would be 15 kPa for backfill material having internal friction angle 51° (using the MSE design criteria where the internal friction angle is capped at 40°) and 87 kPa after adding 331 kPa to the GRS-IBS abutment using Rankine method without reinforcement, which is used for MSE wall design criteria. For the purpose of comparison, the theoretical active earth pressure using Rankine method for Case 1 loading is also presented in Figure 5.6 to give the reader an indication of the major differences between the internally (GRS-IBS) and externally (MSE) supported structure.

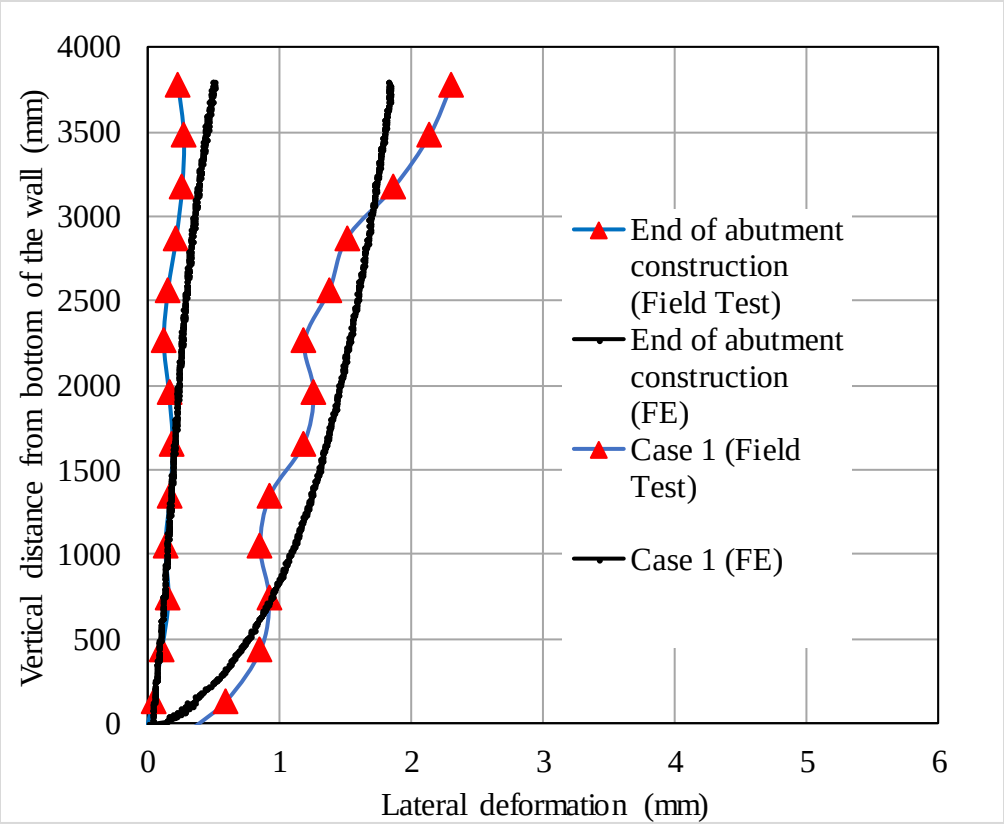

Figure 5.3. Measurement of lateral deformation profiles along the wall face

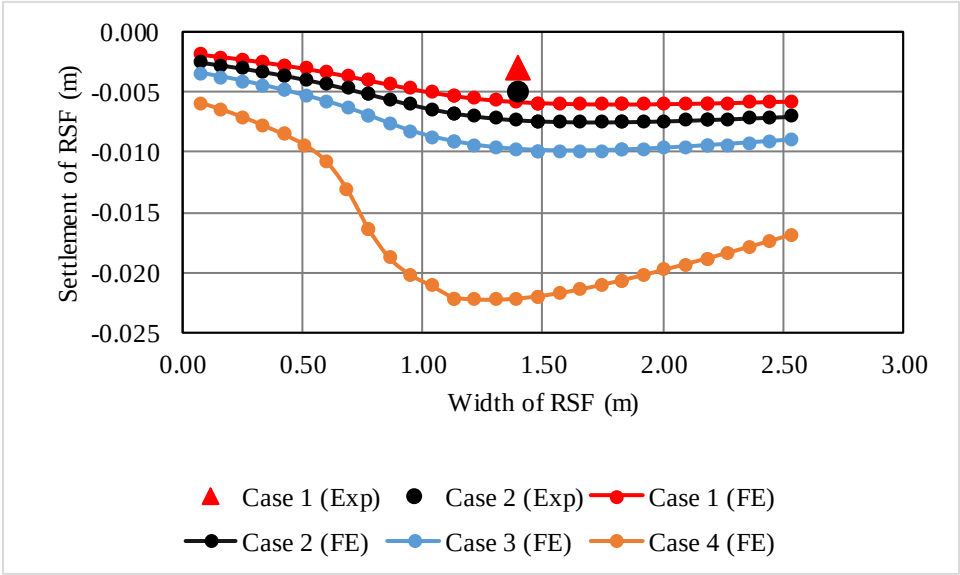

Figure 5.4. Measurement of RSF settlement distribution

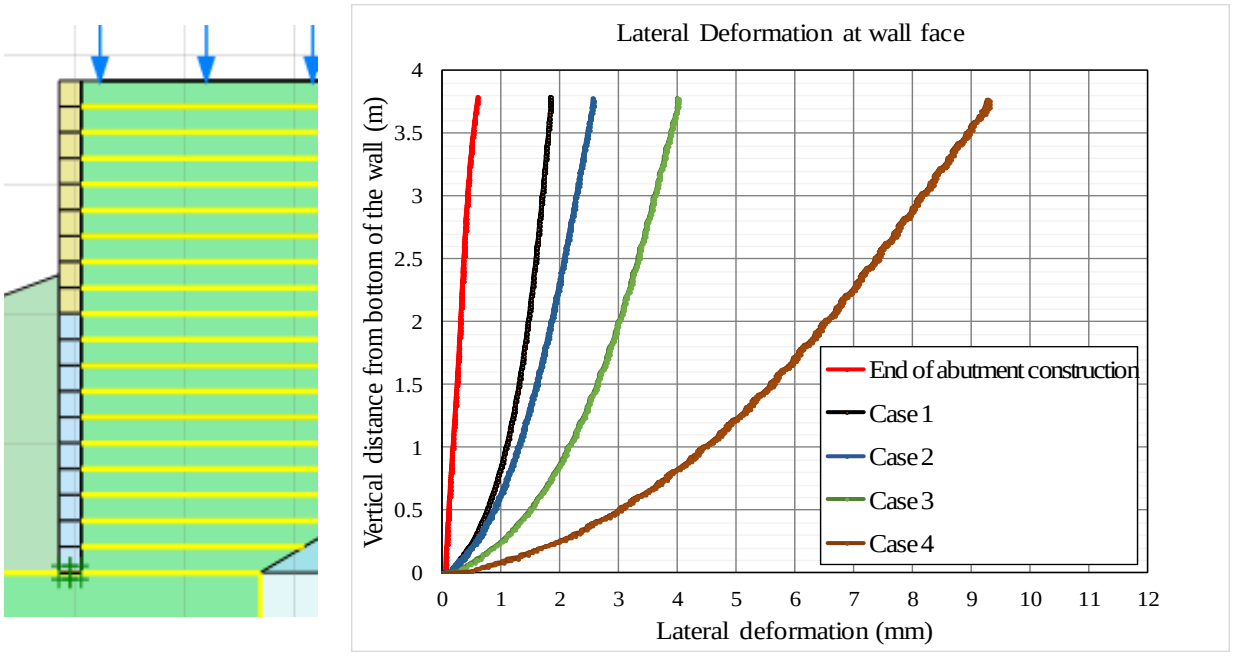

Figure 5.5. Prediction of lateral deformation distribution along the face after at different loading using FE analysis

Figure 5.7 presents the predicted vertical stresses at different layers at the end of bridge construction, truck loading, service loading, and abnormal loading for the upper third of GRS-IBS abutment. The distribution of the stresses changes with the depth. A symmetrical stress distribution was noted in layer 19 and 18 right under the footing and a biased stress distribution toward the facing was noted in layers 16, 14, and 12. The symmetrical stress distribution right under the footing can be explained due to the short distance between these layers and the strip footing.

5.1.7 Reinforcement Strain Distribution and Axial Force

For the purpose of comparison and verification, the distribution strain of geotextile reinforcement obtained from the FE analysis were compared with those obtained from field strain measurements at the end bridge construction (Case 1) as presented in Figure 5.8. It can be noted that the maximum

strains predicted by the FE analysis are a little lower than the measured strains in the field, which researchers believe are in good agreement and within the acceptable range.

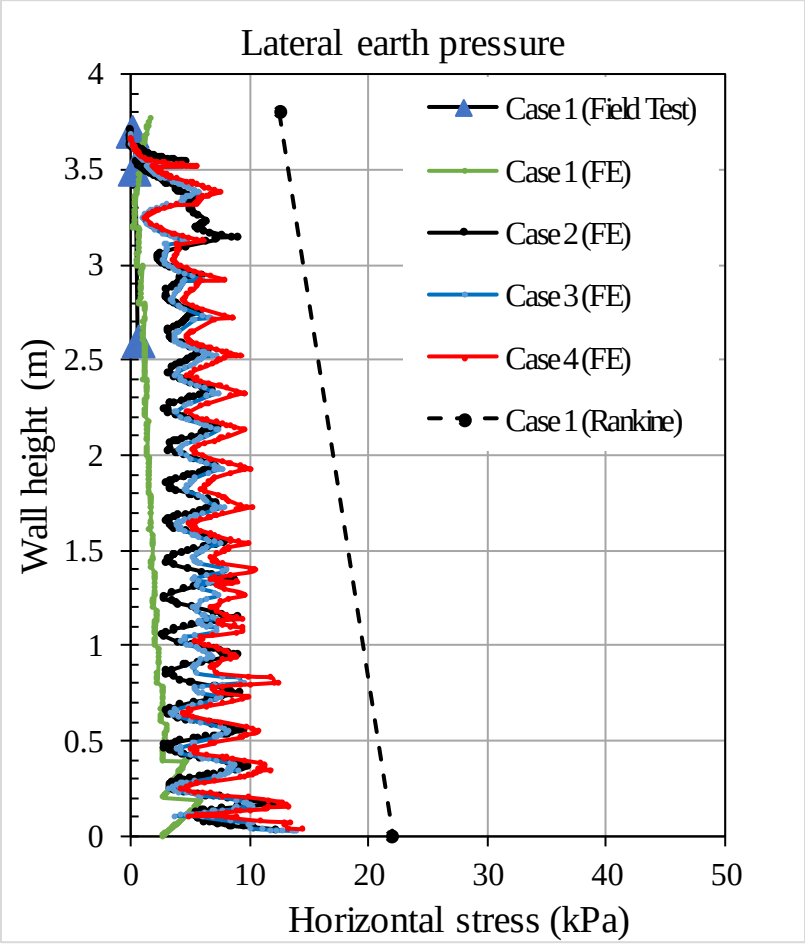

Figure 5.6. Measurement of lateral earth pressure distribution at the GRS-IBS abutment face

Figure 5.9 presents the predicted strains generated by the FE analysis for the end of bridge construction, truck loading, service loading, and abnormal loading. The highest reinforcement strain was found to be 1.5% for abnormal loading (331 kPa), while the lowest strain was 0.4% at the end of abutment construction. The maximum strain for the service loading is 1.2%. The strain predicted by the FE analysis were close for the top two geotextile layers (layers 18 and 16) and slightly increases in the fourth and fifth layer from the top (layer 14). It can be seen that the locus of maximum strain was varied with depth. The maximum strain at the top four layers were located

at about 20% of the reinforcement length from the wall face and then moved to about 40% for the next six layers, and finally, the location goes back up to about 10% for the remaining lower eight layers mainly due to the presence of rip rap as described in Figure 5.10.

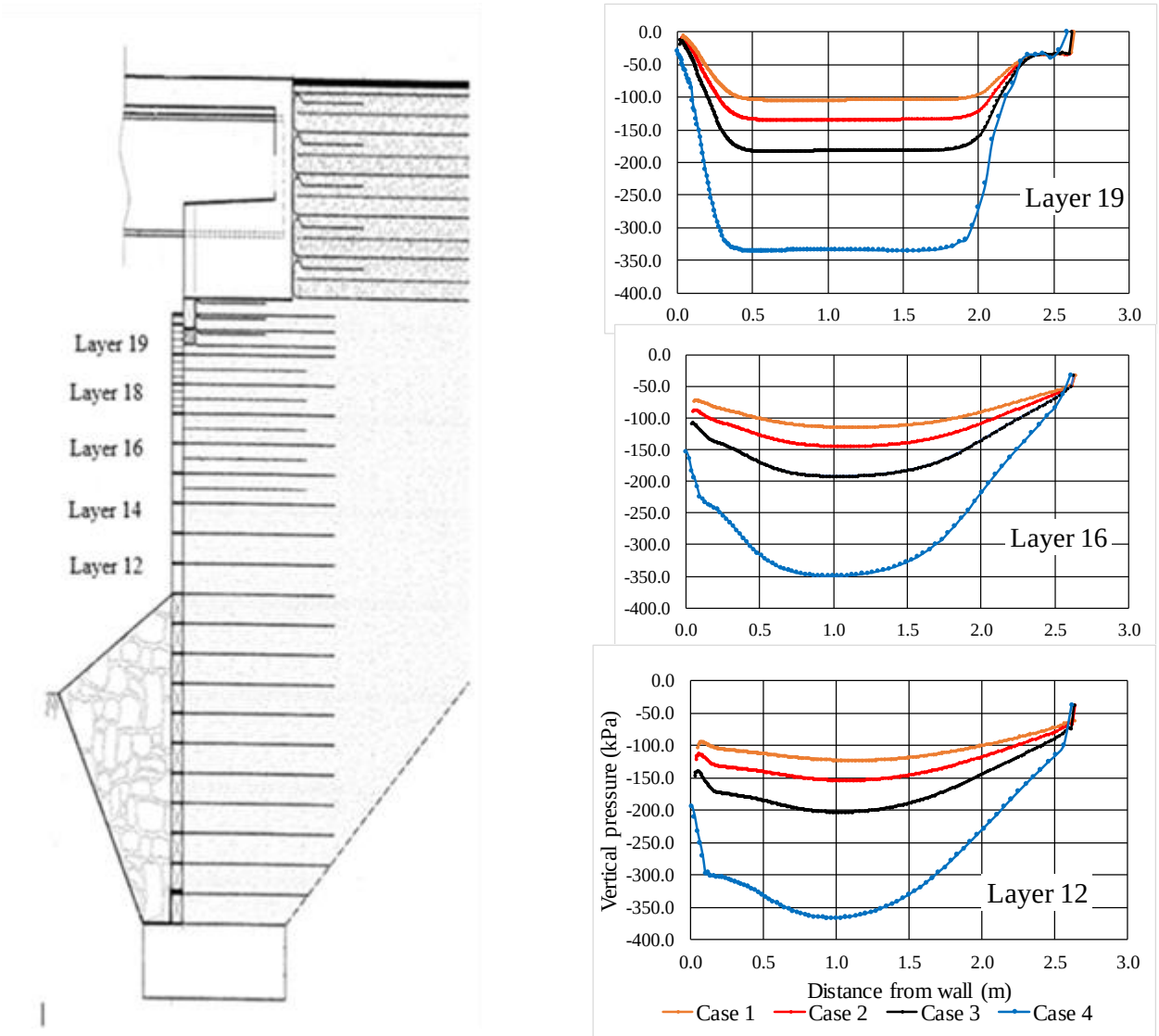

Figure 5.7**.** Measurement of vertical stress distribution at different layers in the GRS abutment

Table 5.2 compares the axial force in the reinforcement and the interface shear stress between the reinforcement and backfill materials as predicted by the FE analysis, the FHWA (2012) method and Mohr-Coulomb analytical methods for the service loading and the abnormal loading.

It can be seen in Table 5.2 that the strength of the geotextile reinforcement predicted by the FHWA method are 1.5-2.5 times higher than those predicted by the FE analysis, depending on the loading condition and reinforcement location. It should be noted that the FHWA method is a design guideline that have built-in safety factors and conservatism, and therefore it is expected that the predictions by FHWA would be higher than the results of FE analysis. It was noted that the deviation decreases with increase in the loading. The highest predicted axial force is 9.6 kN/m and 14.4 kN/m for the service loading and the abnormal loading, respectively. Note that the axial forces remain constant through the entire GRS-IBS abutment in all different loading cases except for case 4 (abnormal loading), which explains the main difference between the internally supported structures (GRS-IBS) and externally supported structures (MSE walls) as the axial forces in the latter (MSE walls) increases with depth according to the conventional Rankine or Coulomb method. It also can be seen that the axial force in the double reinforcement in the top third (layers 12-18) predicted by the FE analysis is closer to those predicted by the FHWA analytical method for both cases.

It was also noted in Table 5.2 that the interface shear stress predicted by the FE analysis is very close to those predicted by Mohr-Coulomb analytical method which indicates the use of 0.8 as an interface friction value that was found between the reinforcement and backfill using the direct shear test is accurate.

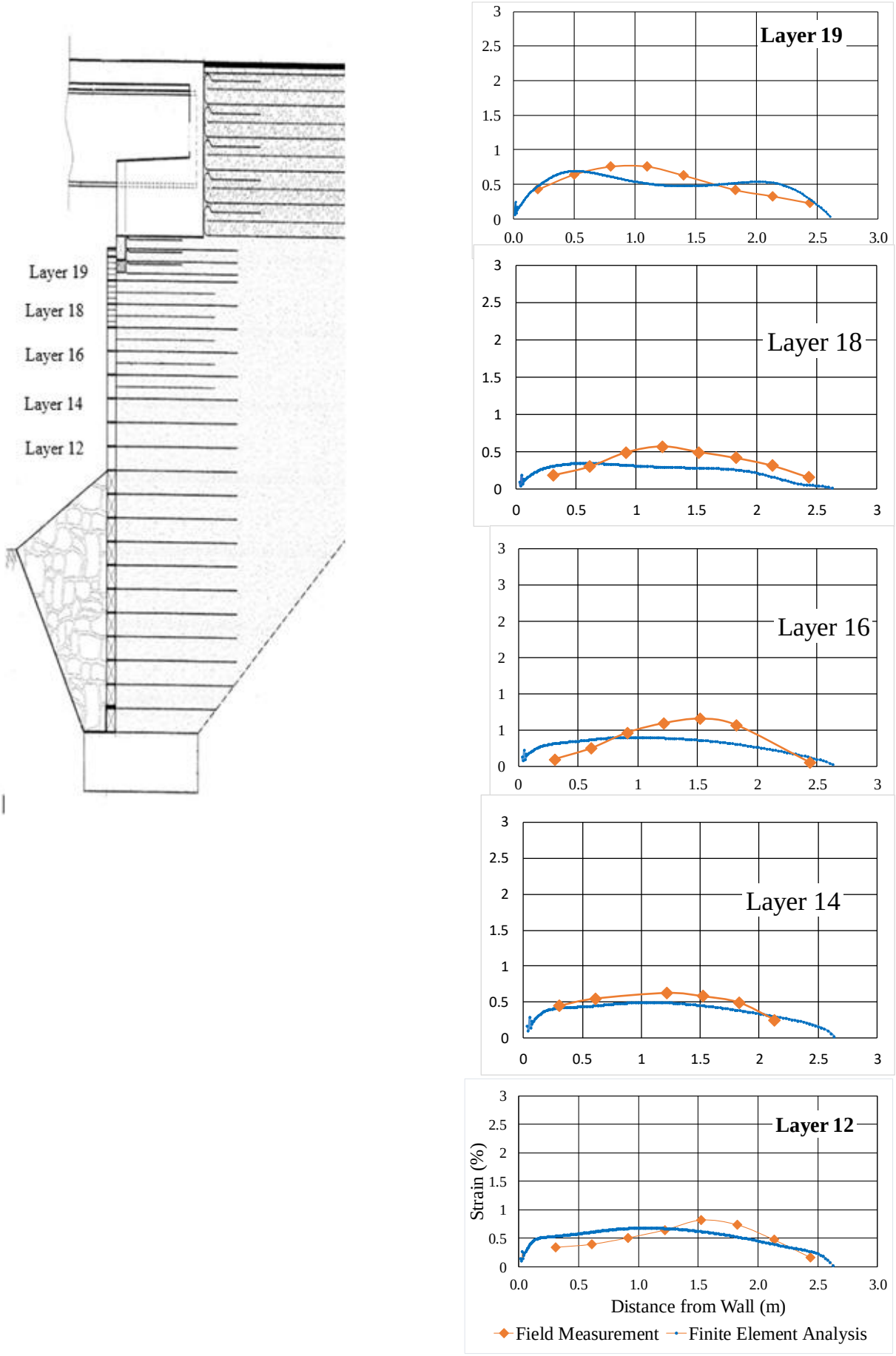

Figure 5.8. Measurement of strain distribution along geosynthetics for Case 1

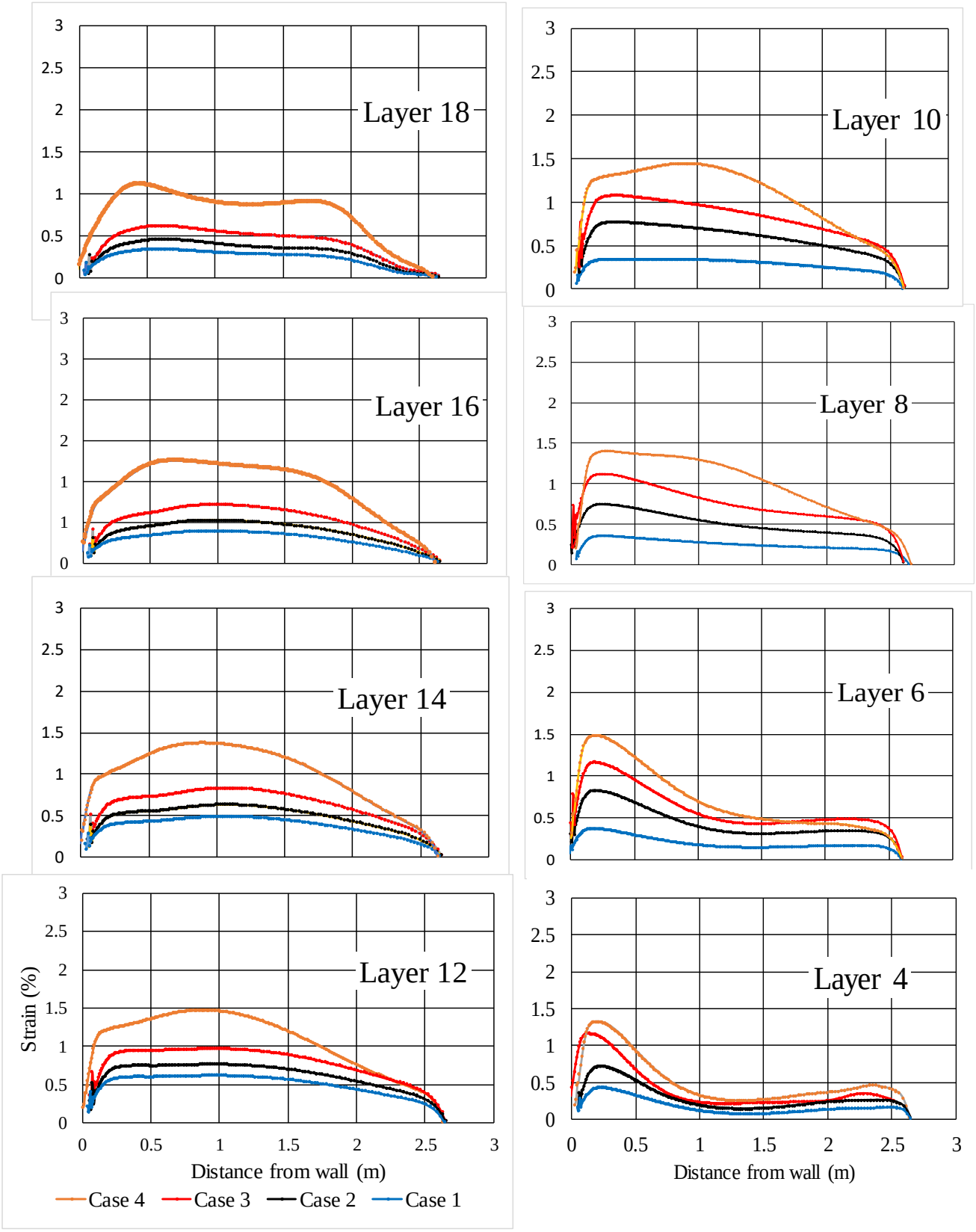

Figure 5.9. Measurement of strain distribution along geosynthetics for the four cases of loading

Table 5.2. Axial force in the reinforcement and the interface shear stress

Layer #	Case 3				Case 4			
	Max Axial Force FE (kN/m)	Max Axial Force FHWA (kN/m)	Max Shear Stress FE (kPa)	Max Shear Stress Analytical (kPa)	Max Axial Force FE (kN/m)	Max Axial Force FHWA (kN/m)	Max Shear Stress FE (kPa)	Max Shear Stress Analytical (kPa)
1	5.3	9.9	315	303	10.8	12.0	622	542
2	4.8	9.8	272	265	9.9	12.1	529	446
3	4.5	9.8	254	248	9.2	12.2	431	411
4	4.3	9.8	243	237	8.9	12.3	412	392
5	4.1	9.8	235	228	8.7	12.5	398	378
6	4	9.8	230	222	8.4	12.7	388	368
7	3.9	9.9	225	216	8.3	12.9	378	358
8	3.8	9.9	219	210	8.2	13.2	378	358
9	3.9	10.0	214	203	8.2	13.5	367	346
10	4.1	10.2	208	196	8.5	13.9	358	336
11	4.2	10.4	208	195	8.9	14.4	354	331
12	4.1	10.6	209	189	8.8	15.0	356	331
13	3.9	10.9	211	194	8.3	15.7	360	332
14	**3.7**	**5.6**	**213**	**194**	**8.2**	**8.2**	**363**	**334**
15	**3.5**	**5.9**	**214**	**193**	**7.6**	**8.7**	**366**	**335**
16	**3.4**	**6.0**	**212**	**191**	**7.3**	**9.3**	**368**	**334**
17	**3.2**	**6.3**	**208**	**188**	**7.1**	**9.8**	**365**	**332**
18	**3.0**	**6.3**	**204**	**185**	**6.7**	**9.8**	**360**	**328**

Bold: double reinforcement (layer 12-19)

Figure 12 presents the comparison between the location of maximum strain envelope with depth obtained from FE analysis for cases 1 and 2 and those obtained from field measurements. The figure also presents the location of maximum strain envelope with depth obtained from FE analysis for other loading cases (3 and 4). The FE analysis demonstrates that the maximum strain location is load dependent, i.e., by increasing the applied load, the maximum strain location moves toward the GRS-IBS abutment face. It is also noted that the presence of rip-rap (2 m from the bottom of the GRS-IBS abutment) affects the maximum strain location for the bottom

reinforcement layers due to the lateral pressure that is created by the rip-rap in front of the GRS-IBS abutment.

For the purpose of comparison between the MSE wall and GRS-IBS design philosophies, the Rankine active failure surface envelope through the reinforced soil slopes (i.e., $45° + \phi/2$) is also drawn in Figure 5.10. It can be seen that the active failure assumption is not valid for the case of GRS-IBS abutment (internally supported structure due to the composite behavior of closely reinforcement) and that the failure envelope extends beyond this assumption up to 40% extra. In MSE walls, the reinforcements extend beyond the assumed active failure surface, and their reinforcement mechanism is considered to be tension-resistant tieback (fully bonded to the facing structure) for the assumed failure wedge. This analysis is commonly referred to as tieback wedge analysis, while in GRS-IBS the reinforcement mechanism is not considered as a tieback. Instead it is considered to be part of a composite material due to the interaction between closed spaced reinforced and backfill material.

Figure 5.11 depicts the relative shear stress τ_{rel} as determined from FE analysis for the GRS-IBS under service loading (Case 3) and abnormal loading (Case 4), respectively, which gives an indication of the proximity of the stress to the failure envelope. τ_{rel} is defined as:

$$\tau_{rel} = \frac{\tau_{mob}}{\tau_{max}^{'}}$$

where $\tau_{max}^{'}$ is the maximum projected value of shear stress where the Mohr's circle is expanded to touch the Coulomb failure envelope while keeping the center of Mohr's circle constant, which is different than the shear strain at failure τ_{ult}, and τ_{mob} is the maximum value of shear stress (i.e., the radius of the Mohr stress circle).

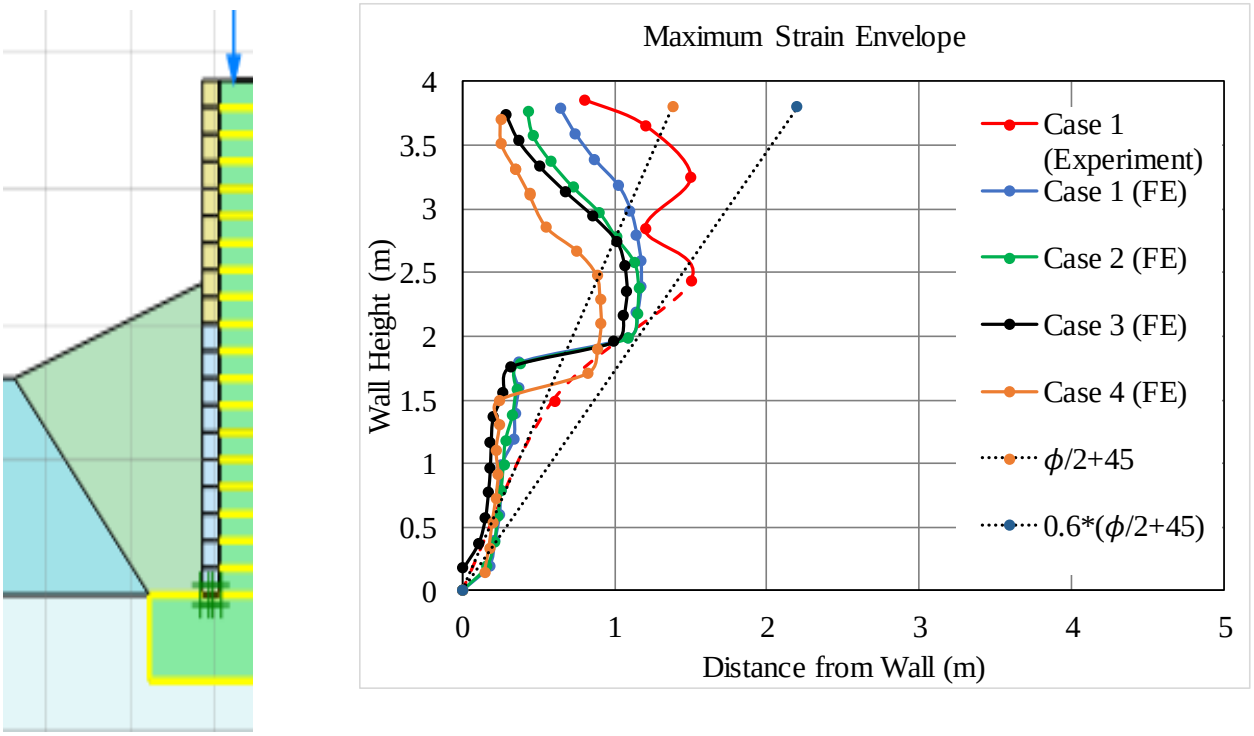

Figure 5.10. Maximum strain envelope for field and FE results at different loading.

It can be seen that the maximum relative shear stress envelope is consistent with the previous discussions as with increasing the applied load on top of the GRS-IBS abutment, the failure envelope slopes less. It is also noted that the reinforced zone is subject to higher shear stress as compared to the retained soil, which indicates that potential critical failure surface lies within the reinforced zone with a slope of about $(\frac{\phi}{2} + 45°)$*0.6 up to 3 m from the top of the RSF, then moves toward the wall.

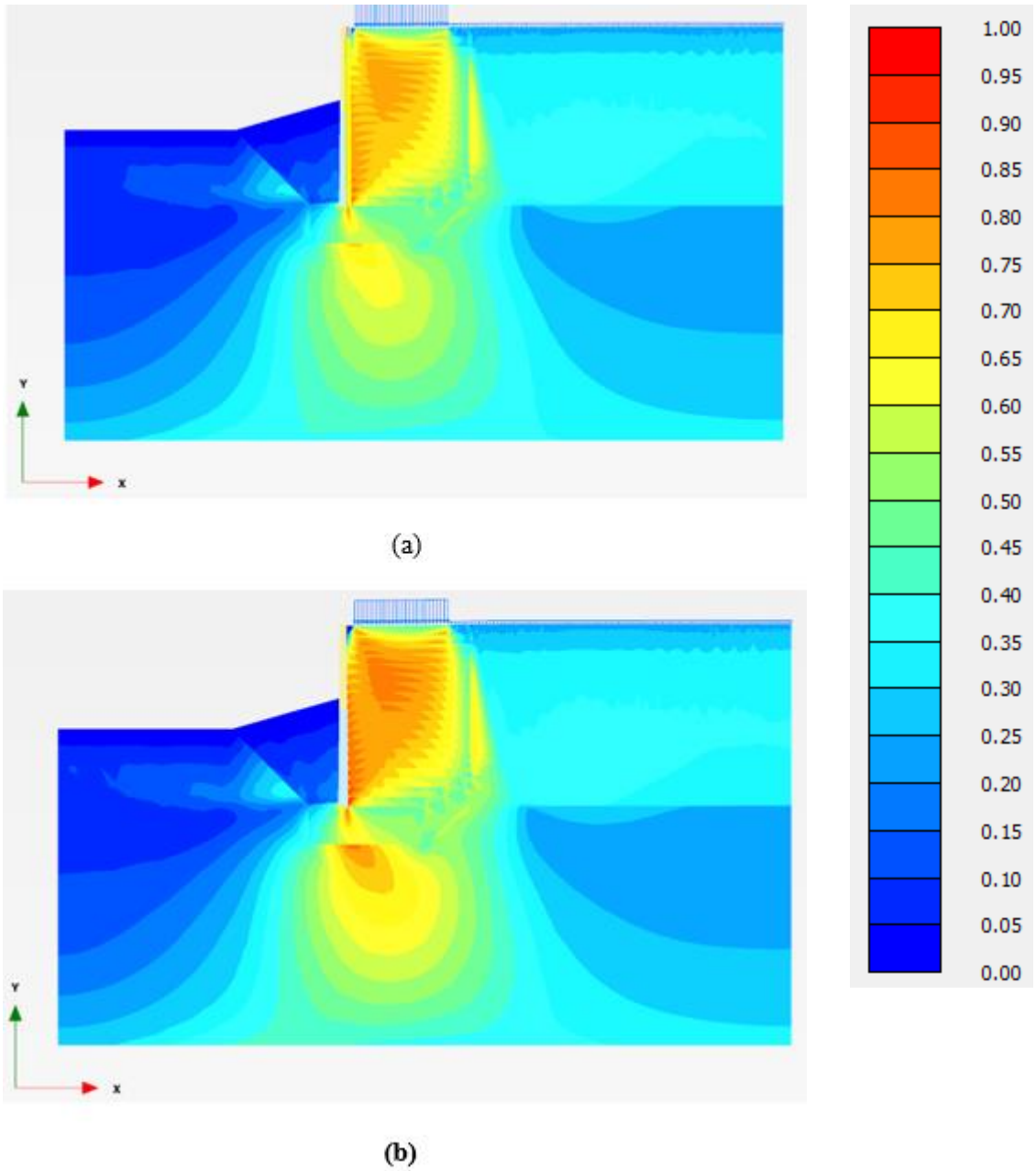

Figure 5.11. The relative shear stress τ_{rel} as determined from FE analysis for the GRS-IBS under service loading: a) Case 3 and b) abnormal loading Case 4

5.2.7 Strain distribution and vertical pressure distribution under RSF

Figure 5.12a presents the strain distribution along the geotextile reinforcement under the RSF and Figure 5.12b compares the vertical pressure distribution under the RSF between the field test measurement and the FE analysis at the end of the bridge construction (Case 1). It can be seen that

vertical pressure distribution under the RSF as predicted by the FE analysis is very close to those measured in the field. Figure 5.12b also presents the vertical pressure distribution for the truck loading (Case 2), service loading (Case 3), and abnormal loading (Case 4) as predicted by the FE analysis. Figure 5.12a shows that the maximum reinforcement strain is less than half of the strain developed in reinforced layers within the GRS-IBS abutment, with 0.16% and 0.72% values obtained for the service load (Case 3) and the abnormal load (Case 4), respectively. It can be seen that the maximum vertical pressure under the RSF is very close to those values under the bridge footing in the top third of the GRS-IBS abutment. Figure 5.12 demonstrates that the shape of reinforcement strain distribution and the vertical pressure distribution are different than those shown in Figures 5.8 and 5.9 in the GRS-IBS abutment, with the peak values located immediately below the GRS-IBS wall facing and decreases in both directions as shown in Figure 14.

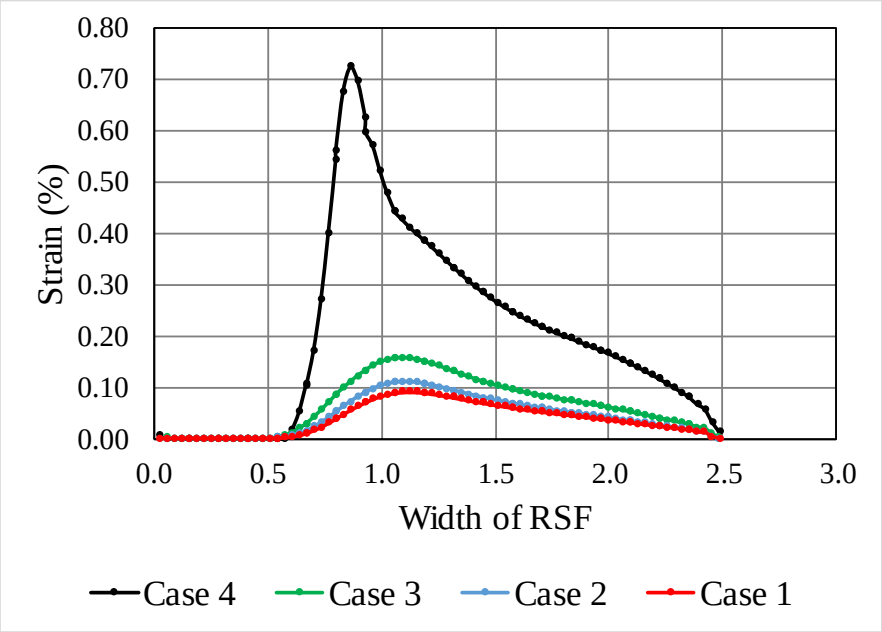

(a)

Figure 5.12**.** (a) Strain distribution along RSF reinforcement strain, (b) vertical stress distribution below RSF

(Figure cont'd)

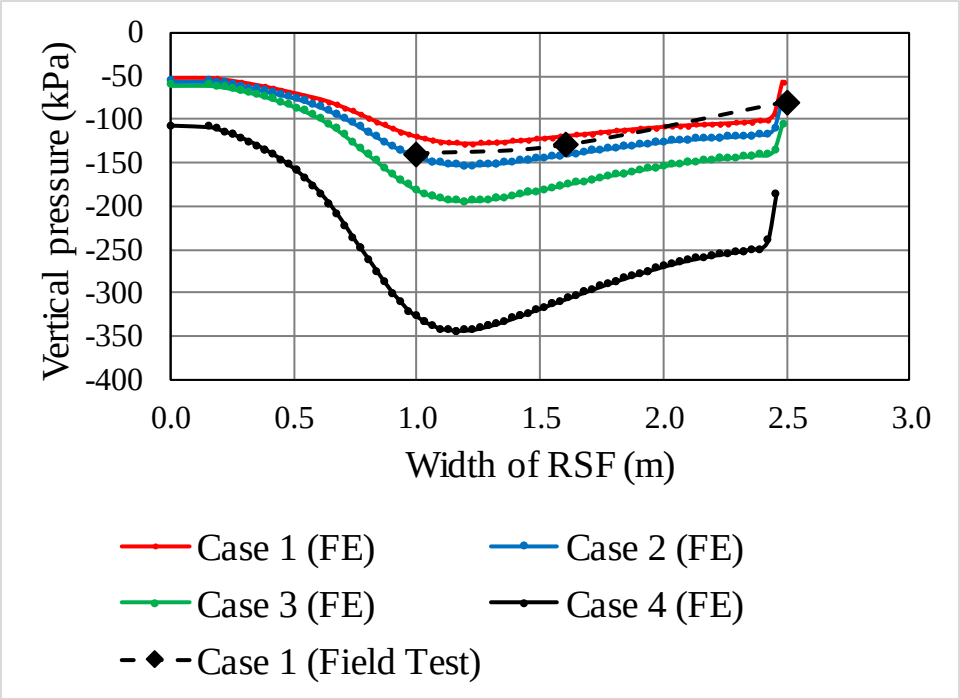

(b)

5.2.8 Sensitivity Analysis

Sensitivity analysis was carried out to evaluate the influence of individual parameters on the displacement of the GRS wall behavior at the end of construction to better understand the effect of each individual parameter on the behavior of geosynthetic reinforced wall. Sensitivity analysis study the effects that varying the input parameters will have on the output values (Saltelli, et al., 2008). In this paper, Secant stiffness (E_{50}^{ref}) and friction angel (φ) of the backfill materials, tensile strength of the geotextile (EA_1), and friction angel (φ), Cohesion (C) and Young's modulus (E) of the soil foundation were chosen to evaluate the influence of each individual parameter on the GRS wall in terms of horizontal and vertical displacement. Three points were selected at the face of the GRS wall on top, in the middle, and at the bottom to conduct the sensitivity analysis. Table 2 shows the selected parameters and their minimum and maximum values that were chosen for the

sensitivity analysis. The ranges were chosen at ± 10% of the actual parameters. For more information about the theory sensitivity analysis refer to the Scientific Manual PLAXIS 2D 2016.

Table 5.3. Sensitivity Analysis Parameters

Material	Parameter	Reference	Minimum	Maximum
Back fill	E_{50}^{ref}	52000 kPa	46800 kPa	57200 kPa
Back fill	φ	50 °	45 °	55 °
Geotextile	EA_1	1200	1080	1320
Foundation	E	30000 kPa	27000 kPa	33000 kPa
Foundation	φ	27 °	24.3 °	29.7 °
Foundation	c	20 kPa	18 kPa	22 kPa

Figures (5.13-5.17) provides a comparison between the results of lateral and vertical deformation at the wall face at the top, middle, and bottom of the face, respectively. The results indicate that the foundation soil stiffness is the primary variable affecting the wall displacements in y-direction and the backfill friction angle is the primary variable affecting the wall displacements in x-direction at the top of the wall. The foundation soil properties have a minor affect on the lateral deformation of the GRS wall at the face at the middle and top of the wall. However, the properties of foundation soil have the major impact along with the friction angle of the backfill materials on both directions at the bottom of the wall. The stiffness of the foundation affects the vertical deformation the most at the top of the wall and decreases down to the bottom of the wall where the strength of the backfill materials has the major influence on the lateral displacement at the top of the wall and decreases down to the bottom of the wall. It was noted that the properties of the foundation soil (especially the stiffness of the foundation soil) have a major influence (up to 50% on average) on the vertical deformation of the geosynthetic reinforced wall compared to the back fill and geosynthetic materials.

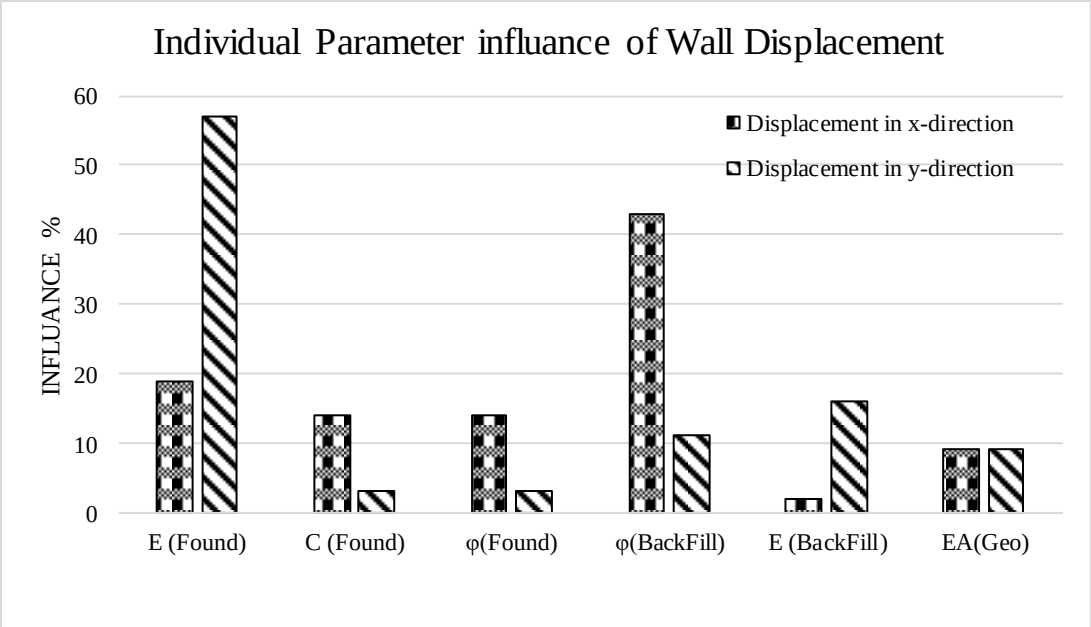

Figure 5.13. Effects of individual Parameters on the displacement in x and y direction at the wall face at the top of the wall

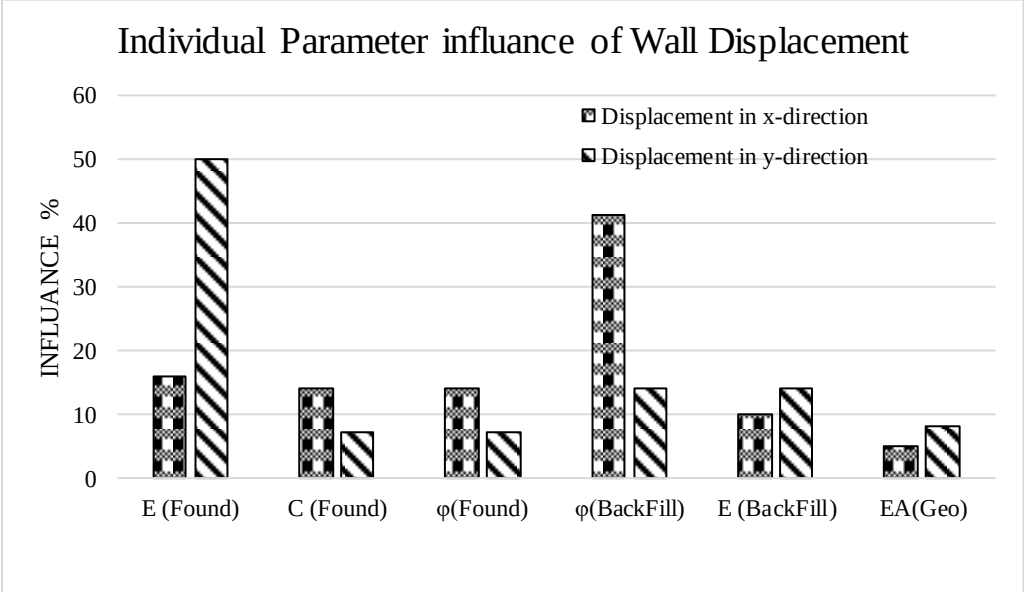

Figure 5.14. Effects of individual Parameters on the displacement in x and y direction at the wall face at the middle of the wall

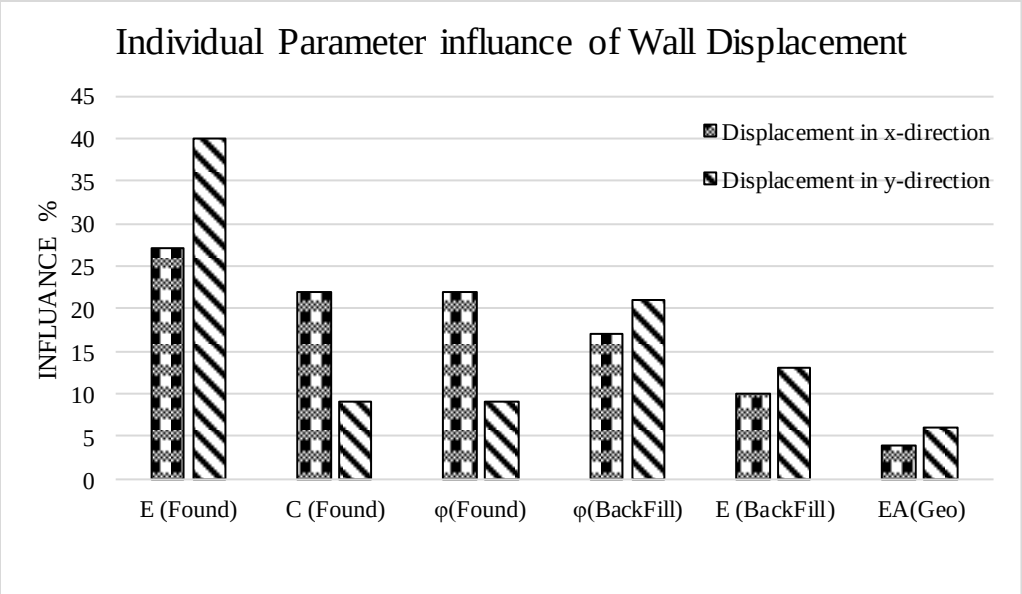

Figure 5.15. Effects of individual Parameters on the displacement in x and y direction at the wall face at the bottom of the wall NOTE: in the chart, change influance to influence

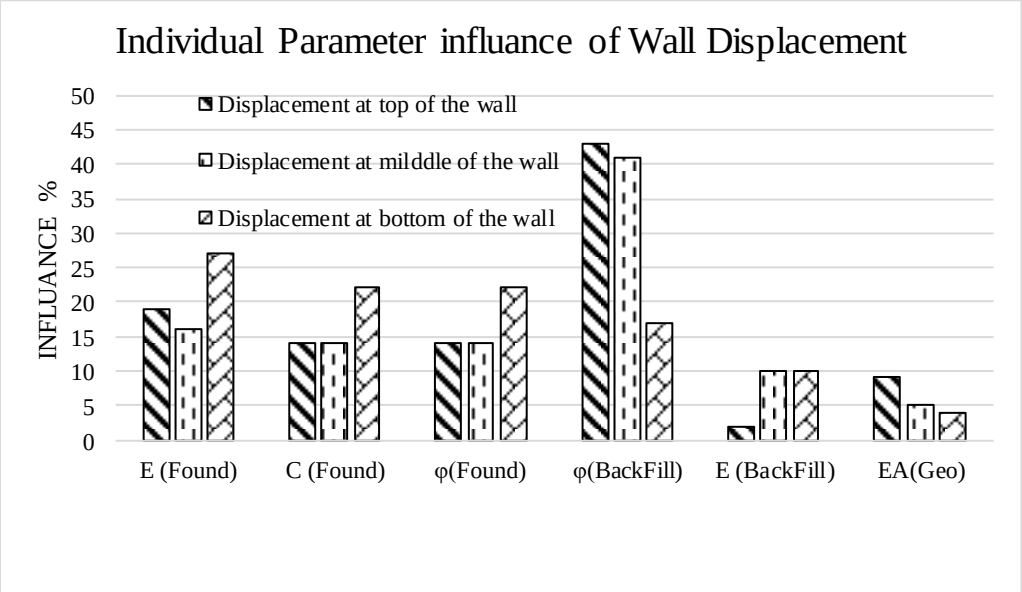

Figure 5.16. Effects of individual Parameters on the displacement in x direction at the wall face at the top, middle, and bottom of the wall Change influance to influence

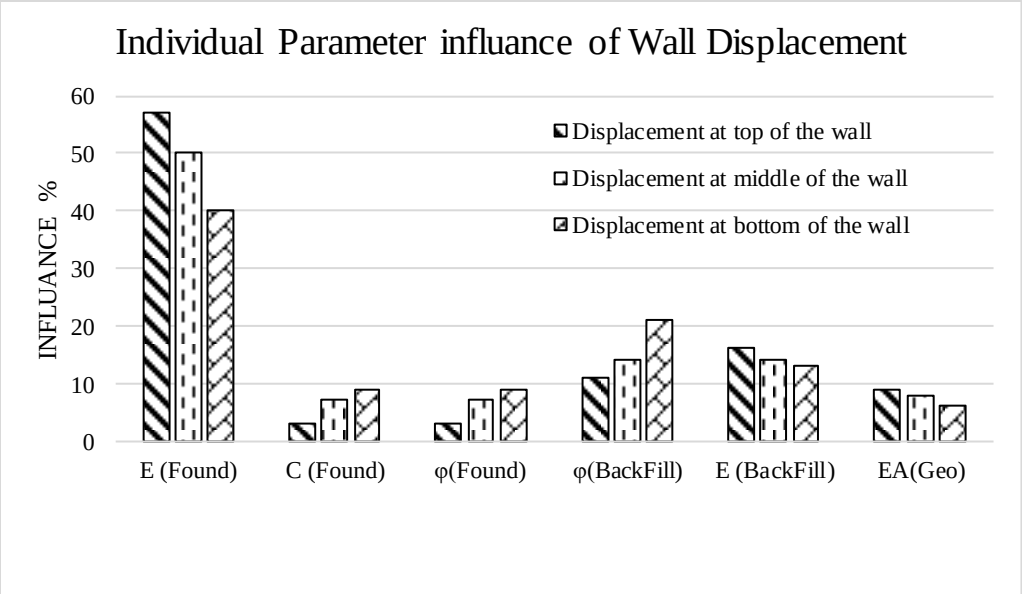

Figure 5.17. Effects of individual Parameters on the displacement in y direction at the wall face at the top, middle, bottom of the wall Change influance to influence

5.3 Three-Dimensional Finite Element (2D-FE) Model

5.3.1 Introduction

In this section, a three-dimensional (3D) Finite Element (FE) analysis was developed to simulate the fully-instrumented geosynthetic reinforced soil integrated bridge system (GRS-IBS) at Maree Michel bridge in Louisiana. The 3DFE computer program PLAXIS 3D 2016 was selected to simulate the GRS-IBS behavior under different loading conditions. The second order-hyperbolic elasto-plastic soil model proposed by Schanz et al., (1999) was used to simulate the granular backfill materials. The soil-structure interaction was simulated using zero thickness interface elements, in which the interface shear strength is governed by Mohr-Coulomb failure criterion. Three different loading conditions were considered in this study: a) at the end of bridge construction (Case 1); b) surface loading (Case 2); and c) at abnormal loading (Case 3), which is equal to the dead load of the bridge structure plus three times the service loading. The predicted results were compared with the field measurements at the end of bridge construction. Moreover,

the predicted results of the 3D-FE analysis were compared with those predicted using the 2D-FE analysis. A good agreement was obtained between the 3D-FE and 2D-FE numerical results and the field measurements. The predicted results using the 3D-FE showed that the range of maximum reinforcement strain under service loading ranges between 0.6% and 1.5%, depending on the location of the reinforcement layer. The maximum lateral deformation at the face was between 3 mm (0.07% lateral strain) under service load case and 7 mm (0.3% lateral strain) for abnormal load case. The maximum settlement of the GRS-IBS due to the service loading was 9 mm (0.3% vertical strain). The axial reinforcement forces predicted by FHWA (2012) design methods are compared with those predicted by the 3D-FE and 2D-FE analysis and the results showed that the FHWA analytical method is 1.5-2.5 times higher than those predicted by the FE analysis, depending on the loading condition and reinforcement location.

5.3.2 Objective

The objective of this section is to develop and verify a 3D-FE numerical method that is capable of simulating the performance of GRS-IBS system under different loading conditions. The results of the 3D-FE model were compared and verified with measured horizontal and vertical deformations, reinforcement strain distribution, and horizontal and vertical pressures of a fully-instrumented GRS-IBS system at Maree Michel Bridge in Louisiana. The results of the 3D-FE model were also compared with the results of 2D-FE model. The 3D-FE model was then used to simulate service loading and the abnormal loading conditions.

5.3.3 Finite Element Numerical Model

A three-dimensional FE model was developed and verified by using the measured results from the field monitoring of the fully-instrumented GRS-IBS bridge abutment at Maree Michel Bridge in

Louisiana. For the numerical analysis of this study, PLAXIS 3D 2016 was selected to simulate the three-dimensional behavior of GRS-IBS system. In the FE model, the soil was represented by 10-node tetrahedral elements to simulate the stress-strain behavior. To simulate the axial force along the geotextile, Plaxis offers a special tension 6-node triangular surface elements with three transional degrees of freedom per node (U_x,U_y, and U_z) to represent the geosynthetic materials (note that the geotextile elements are compatible with the soil element type). The interfaces between the geotextile and the backfill material and the facing blocks were simulated using joint elements to model the soil-structure interface behavior, which is represented by 10-node interface element (also compatible with the soil element) to simulate the thin zone of intense shearing at the contact between the geotextile and the surrounding geomaterial.

The second order hyperbolic elastoplastic hardening soil model (Schanz et al., 1999), which is a built-in constitutive model in PLAXIS 3D 2016, was selected to simulate the granular backfill material in this study. The hardening soil model (HSM) implies friction hardening to model the plastic shear strain in deviatoric loading and cap hardening to model the plastic volumetric strain in primary compression. The HSM is also capable of simulating the non-linear stress-strain behavior of the backfill soil, stress dependency, soil dilation, and unloading-reloading behavior. For more details about the formulation and verification of the Hardening Soil Model (HSM), the reader can refer to Schanz et al. (1999) and Brinkgreve (2002). A built-in linear elastic model with Mohr–Coulomb failure criterion model was selected to simulate the mechanical behavior of the interface between the backfill material and geotextile and the facing blocks by applying a reduction factor ($R_i \leq 1.0$) to the backfill material when defining soil property values ($R_i = 1.0$, for a fully-bonded interface). The interface property values are directly related to the mechanical properties of the backfill forming the interface (e.g. $C_i = R_i * C_{soil}$). These interfaces

have properties of friction angle, dilation angle, cohesion, Young's modulus (E), tensile strength, and Poisson's ratio (ν).

A summary of the parameters used in 3D-FE modeling is provided in Table 2. Soil parameters were evaluated using the laboratory and in-situ testing. The geotextile and facing block properties were provided from the manufacturer.

Figures 5.18. presents the FE mesh for the GRS-IBS of Maree Michel Bridge abutment (326270 nodes and 193983 elements). Mesh sensitivity was first carried out to select the proper size of FE mesh that is not affecting the FE results. For the purpose of comparison, 2D-FE analysis was also conducted using the same parameters and dimensions.

To simulate the field construction process, PLAXIS offers a staged construction mode, which enables a realistic simulation of construction and excavation processes by activating and deactivating cluster of elements and load applications. To take into account the induced stress on the backfill soil due to soil compaction, a 63 kPa distribution load were applied at the top and bottom of each soil layer during the staged construction process according to the procedure introduced by Dantas (2004) and Morrison et al. (2006), which was also adopted later by Ehrlich and Mirmoradi (2013), Mirmoradi and Ehrlich (2014 a,b) and Riccio et al. (2014).

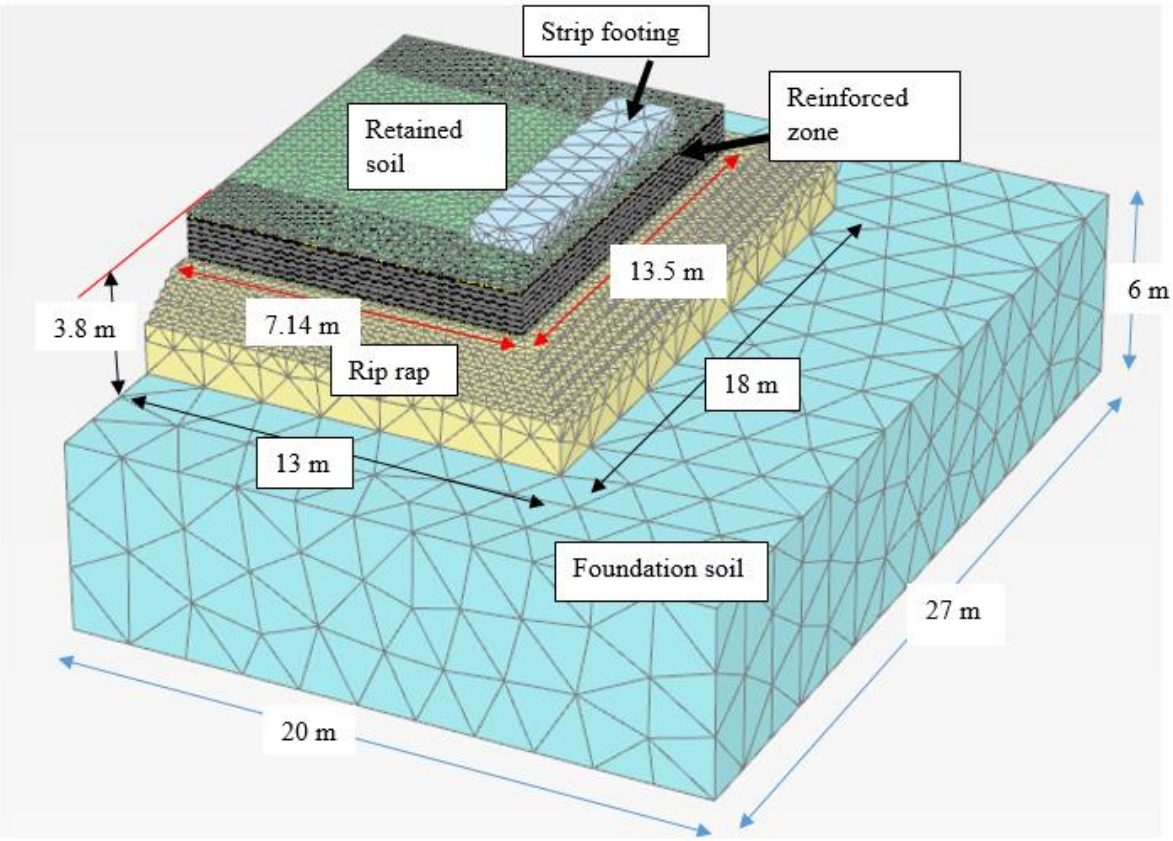

Figure 5.18. FE Mesh of the GRS-IBS and locations of the applied boundary conditions

5.3.4 Results and Discussion

In this section, a comprehensive FE analyses in terms of reinforcement strain, lateral and vertical deformation, and horizontal and vertical pressure were carried out to evaluate the performance of the GRS-IBS system at Maree Micheal bridge. Results of 3D-FE analysis were compared with field measurements during monitoring program and with 2D-FE analysis. Three different loading conditions were considered in this study: at the end of bridge construction (Case 1), which is equal to the dead load of the bridge structure; service loading (Case 2), which is equal to the dead load of the bridge structure plus the equivalent live traffic load; and at abnormal loading (Case 3), which is equal to the dead load of the bridge structure plus three times the traffic loading.

5.3.5 Lateral and Vertical Deformation

According to FHWA (2012), the lateral facing deformation can be determined by conducting a performance test, in which the materials used in the performance test are the same materials to be used in constructing the GRS-IBS abutment. The vertical strain deformation (settlement of GRS-IBS abutment) can be calculated by multiplying the vertical strain from the performance test by the total height of the GRS-IBS abutment, which should be less than 0.5% of the abutment height. In order to determine the maximum lateral deformation at the face, a zero-volume change is assumed in the GRS-IBS abutment due to vertical loading. The FHWA (2012) defined the lateral strain to be two times the vertical strain and should be less than 1% of the abutment height.

Figures 5.19 and 5.20 depict the results of vertical and lateral deformations of the GRS-IBS due to the abnormal loading (Case 3). It can be seen that the reinforced-zone (GRS-IBS abutment) experienced the most vertical and lateral deformations due to the applied load from steel girders. A zero or very low deformation occurs behind the reinforced-zone.

The profiles of lateral deformations at the face of the GRS-IBS wall determined using the 3D-FE and 2D-FE analyses at the end of abutment construction and the end of bridge construction were compared with field measurements as shown in Figure 5.21. It can be seen that the prediction results by the 2D-FE and 3D-FE analyses are very close to each other and are in a good agreement with the field measurements. It was also noted that the 3D-FE analysis predicts a little lower lateral deformation than the 2D-FE analysis. The maximum lateral deformations predicted using the 3D-FE analyses were found to be less than 0.5 mm and 2 mm at the end of abutment construction and at the end of bridge construction, respectively.

The 3D-FE model was used to predict the lateral deformation profile of the GRS-IBS wall face for the three loading conditions (Case 1, 2, & 3) as presented in Figure 5.22, which shows that the

maximum lateral deformations are 2, 3, and 7 mm at the end of bridge construction (case 1), the service loading (case 2), and abnormal loading (case 3), respectively. With the exception of case 3 (abnormal loading), the predicted maximum lateral deformations are less than the values recommended by the FHWA (Adams et al., 2011a).

Since the GRS-IBS abutment is built using granular materials, most of the vertical deformation within the abutment occurs immediately after adding the load. Distinguish must be made here between the GRS-IBS abutment vertical deformation and the settlement of underlying foundation soils (RSF). With that being said, the comparison profiles of the settlement distribution under the RSF predicted using the 2D-FE and 3D-FE analyses at the end of abutment construction and the end of bridge construction and the comparison with the field measurements are presented in Figure 5.23 in both the cross-section direction and the longitudinal direction. The maximum footing settlement due to service load (case 2) and abnormal load (case 3) are 10 mm (0.3%) and 23 mm (0.6%), which is acceptable for the service load but not acceptable for the abnormal load according to FHWA (2012) recommendations.

5.3.6 Strain distribution under RSF

Figure 5.24a compares the predicted 2D-FE and 3D-FE strain distributions along the geotextile reinforcement under the RSF in the cross-section direction; and Figure 5.24b presents the predicted 3D-FE strain distribution along the geotextile reinforcement under the RSF in the longitudinal direction. Figure 5.24a shows that the maximum reinforcement strain predicted by both the 2D-FE and the 3D-FE analysis are very close in magnitude but with a little different in the location of those maximum strains.

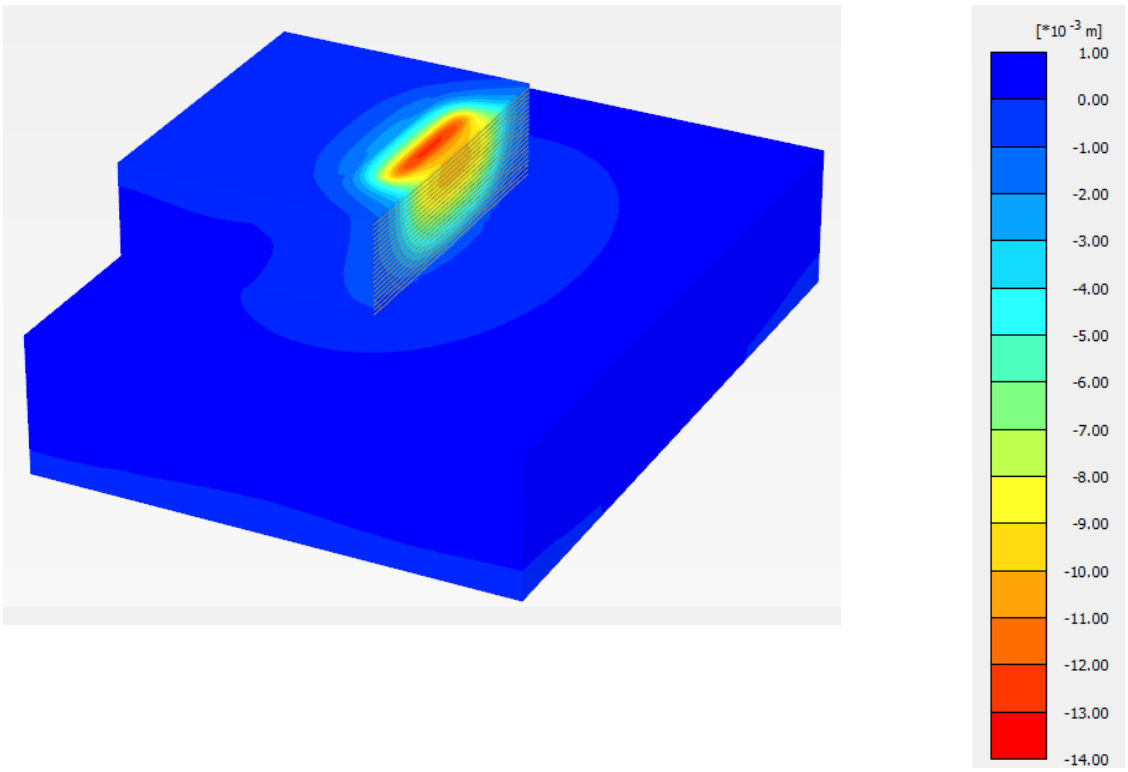

Figure 5.19. Settlement of GRS-IBS due to abnormal loading (Case 3).

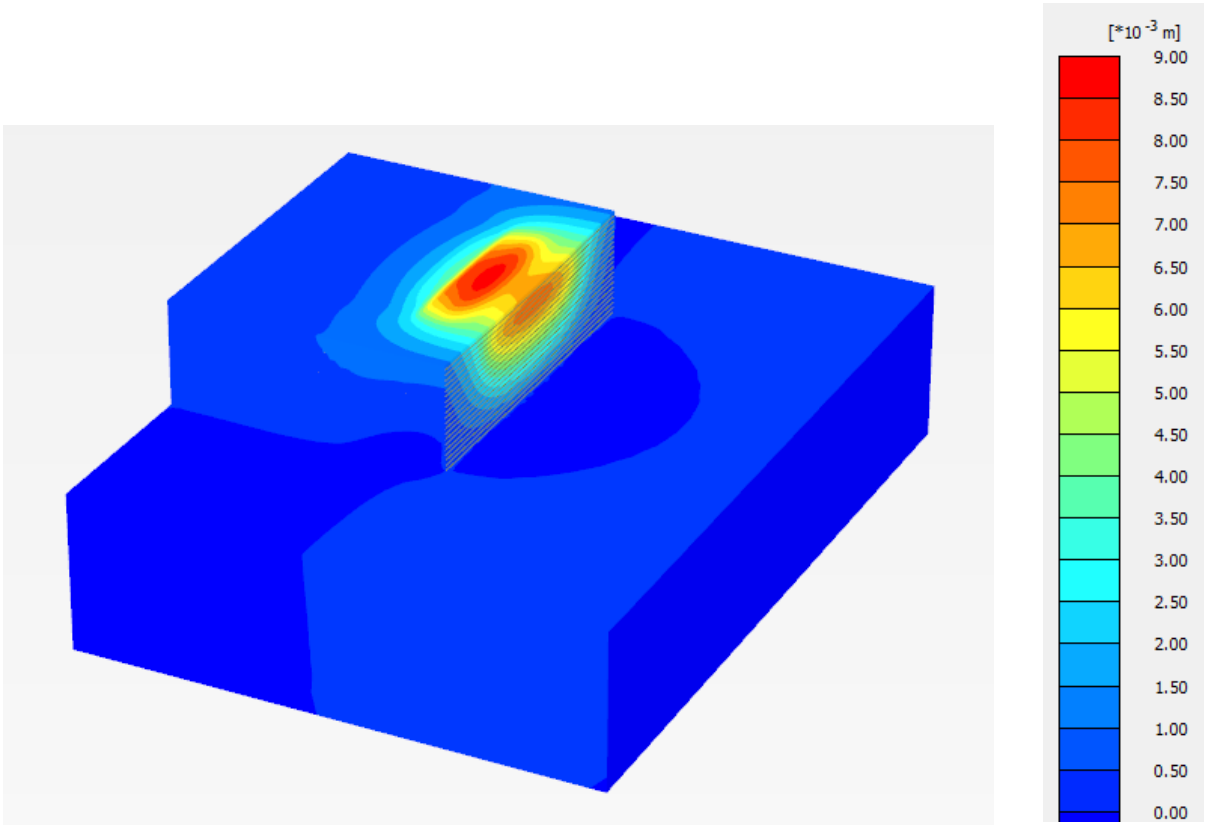

Figure 5.20. lateral deformation of GRS-IBS due to abnormal loading (Case 3).

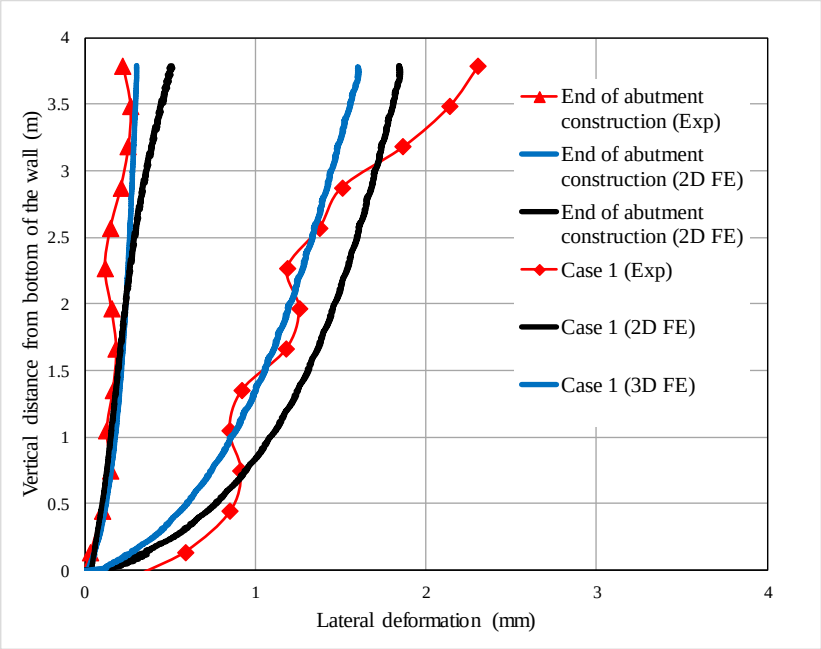

Figure 5.21. Measurement of lateral deformation profiles along the wall face.

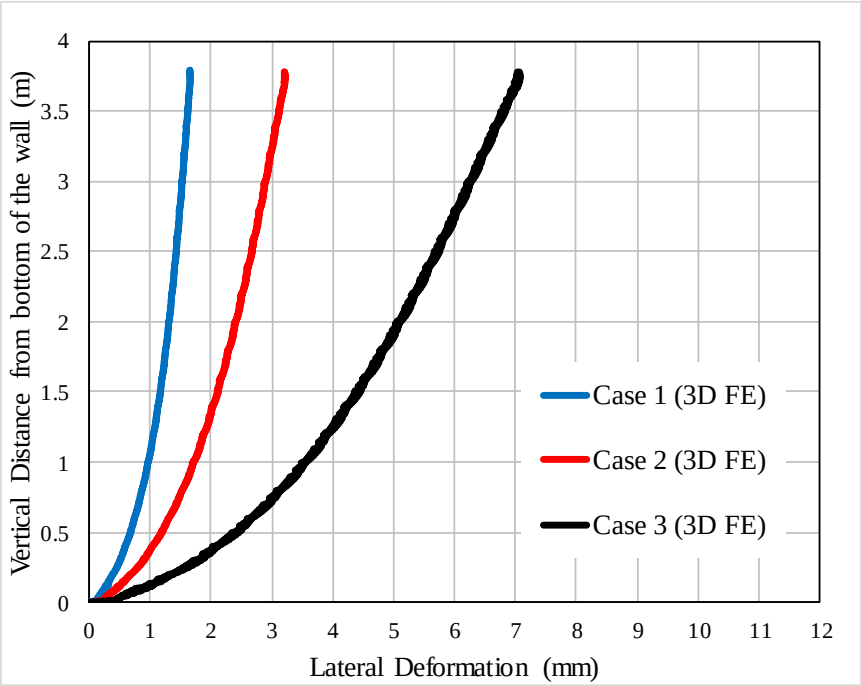

Figure 5.22. 3D-FE prediction of lateral deformation profile along the face at different loading conditions

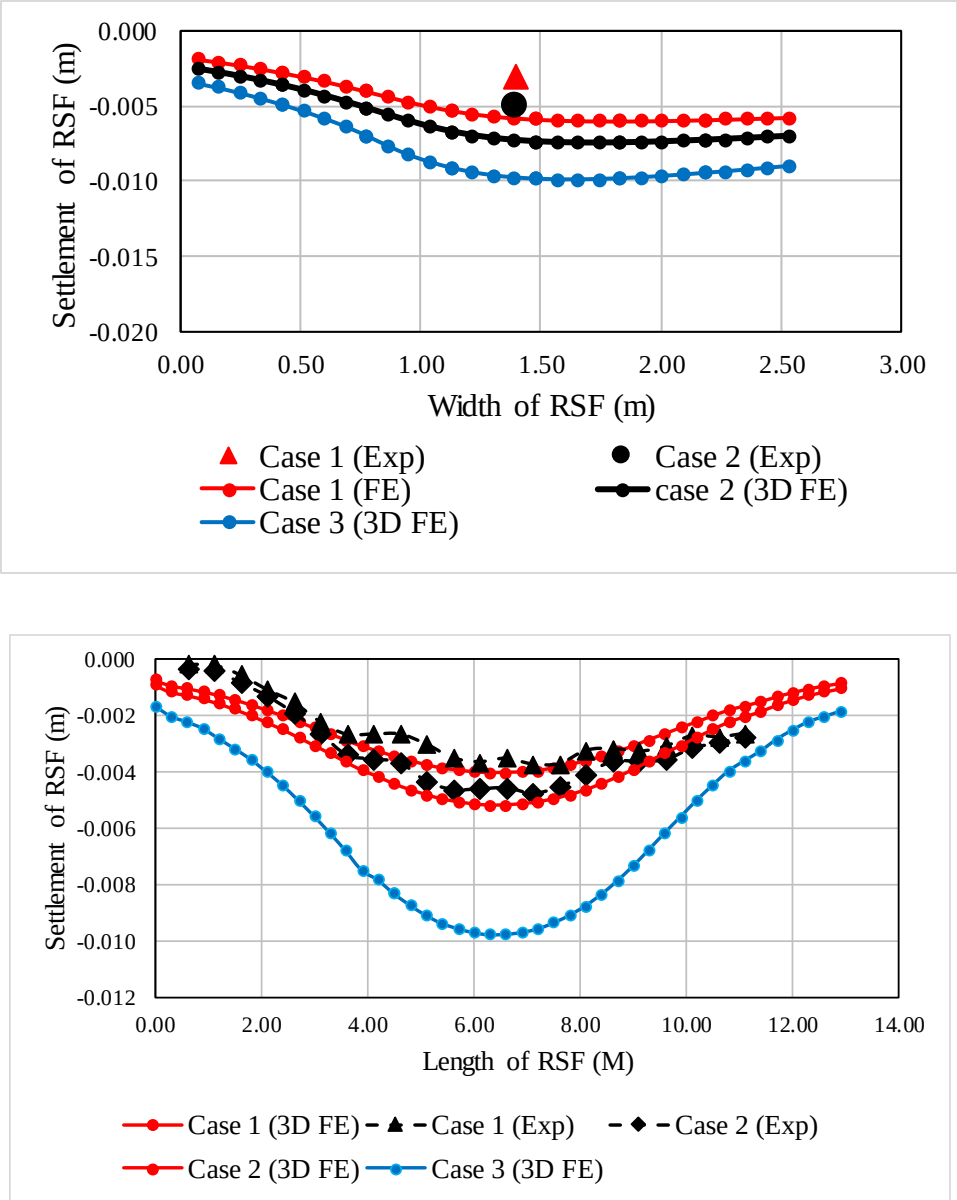

Figure 5.23. Measurement of RSF settlement distribution.

Strains values of 0.16% and 0.72% were obtained for the service load (Case 2) and the abnormal load (Case 3), respectively. The shapes of distribution of reinforced strains under the RSF are different than those reinforcements within the GRS-IBS abutment as will be discussed later.

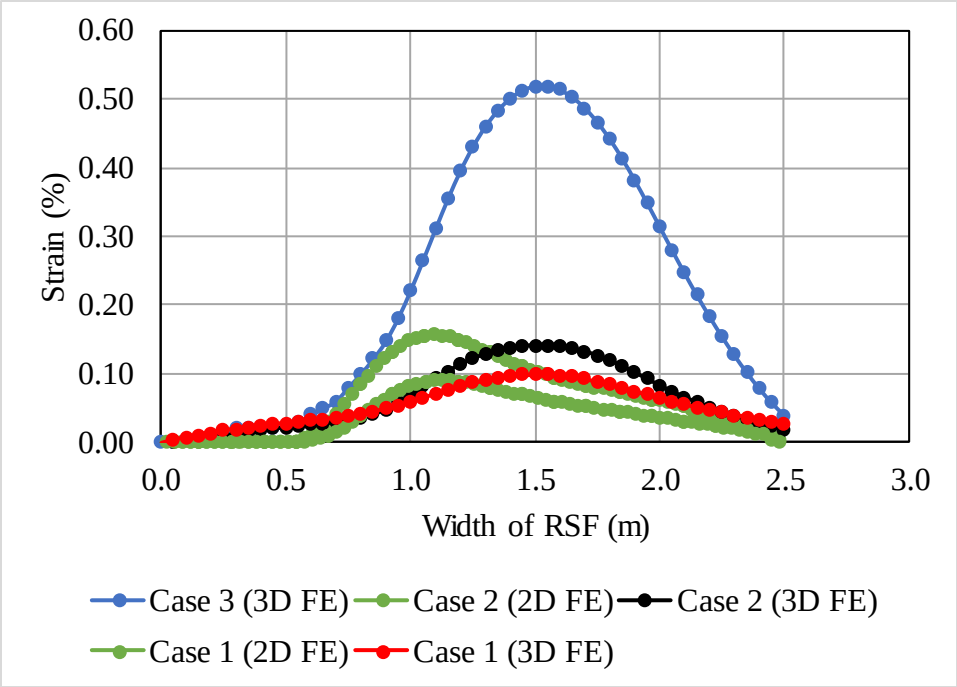

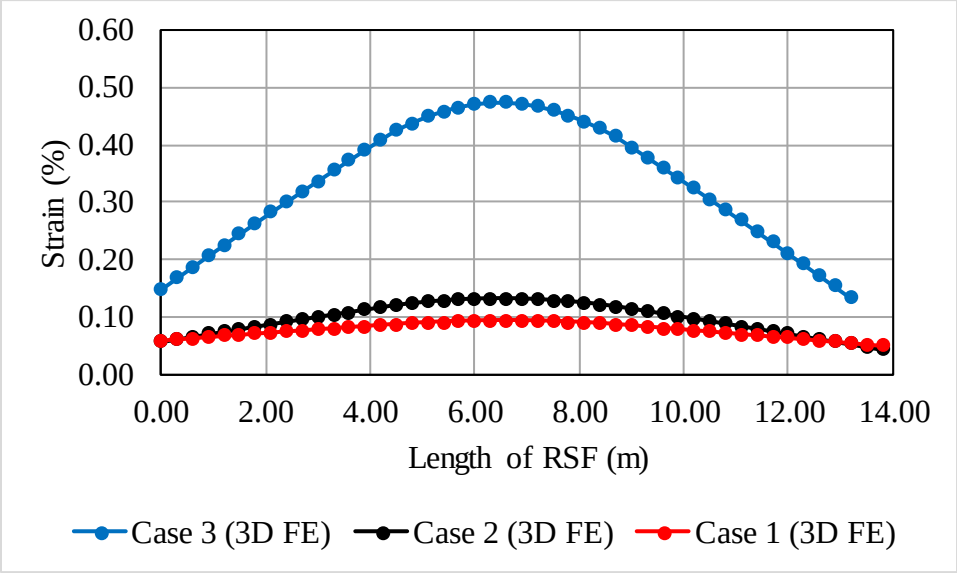

Figure 5.24. Strain distribution along RSF reinforcement strain

5.3.7 Vertical and Lateral Stresses within GRS Abutment

Figures 5.25&26 present the vertical stresses distribution under three different loading conditions along the cross-section and longitudinal direction of GRS-IBS, respectively. It was noted that the vertical stresses in the longitudinal direction are symmetrically distributed under the applied loads. On the other hand, the vertical stresses along the cross-section direction are biased toward the front wall face direction as it is expected. It is also noted that the distribution of vertical stresses for the top five to six layers are very close within the bearing bed zone under the same loading conditions.

Figure 5.27a presents the comparison between the lateral pressures on the wall face predicted using the 3D-FE and 2D-FE analyses and the field measurements at the end of bridge construction (case 1); and Figure 5.27b presents the predicted lateral pressures using the 3D-FE analyses for three different loading cases (case 1, 2, and 3). It can be seen that there is a good agreement between both the 3D-FE and the 2D-FE analyses and the field measurements. For the purpose of comparison, the lateral stresses as predicted by Rankine method is also presented in Figures 5.27a and 5.27b. It was noted that the predicted and measured lateral pressure are much less than the Rankine lateral earth pressure. This is mainly attributed to the composite behavior of closely-spaced reinforced layers.

Wu (2001) proposed the bin pressure theory to evaluate the performance of the GRS walls in terms of lateral facing pressure, in which the smaller reinforcement spacing results in significant

reduction in lateral earth pressure on the face. The FE analysis and the field measurements results showed the main difference between the MSE walls and GRS in terms of lateral earth pressure. In the MSE walls, the current design methods use Rankine or Coulomb lateral earth pressure theories which assume the stresses on the wall-face increases linearly with depth. Obviously, this is not valid in case of GRS (internally supported structure).

5.3.8 Reinforcement Strain Distribution and Axial Force

For the purpose of comparison and verification, the distribution strain of geotextile reinforcement obtained from the 3D-FE analysis were compared with those obtained from the 2D-FE analysis and from the field strain measurements at the end bridge construction (Case 1) as shown in Figure 5.28. It can be noted that the maximum strains predicted by the 3D-FE and 2D-FE analysis are very close to each other in the plain strain direction, which are slightly lower than the measured strains in the field. The figures demonstrate that the shape of reinforcement strain distribution is different than those in the GRS-IBS abutment in Figure 28, with the peak values are located immediately below the GRS-IBS wall facing and decreases in both directions. Figure 5.29 presents the predicted strains generated by the 3D-FE analysis in the cross-section direction at the end of bridge construction (Case 1), service loading (Case 2), and abnormal loading (Case 3). The highest reinforcement strain was found to be 1.6% for abnormal loading (331 kPa) in layer number 12; while the lowest strain was 0.4% at the end of bridge construction in layer number 18. The maximum strain for the service loading is 1.2%. The strain predicted by the 3D-FE analysis were close for the top three geotextile layers (layers 18, 16, and 14) within the bearing bed zone and slightly increases in the fifth layer from the top (layer 12).Figure 5.30 presents the predicted strains generated by the 3D-FE analysis in the longitudinal-direction, It can be seen that the maximum

strains predicted by the 3D-FE analysis in the longitudinal direction are distributed symmetrically in which the highest values are located under the strip footing and decreases toward the edges.

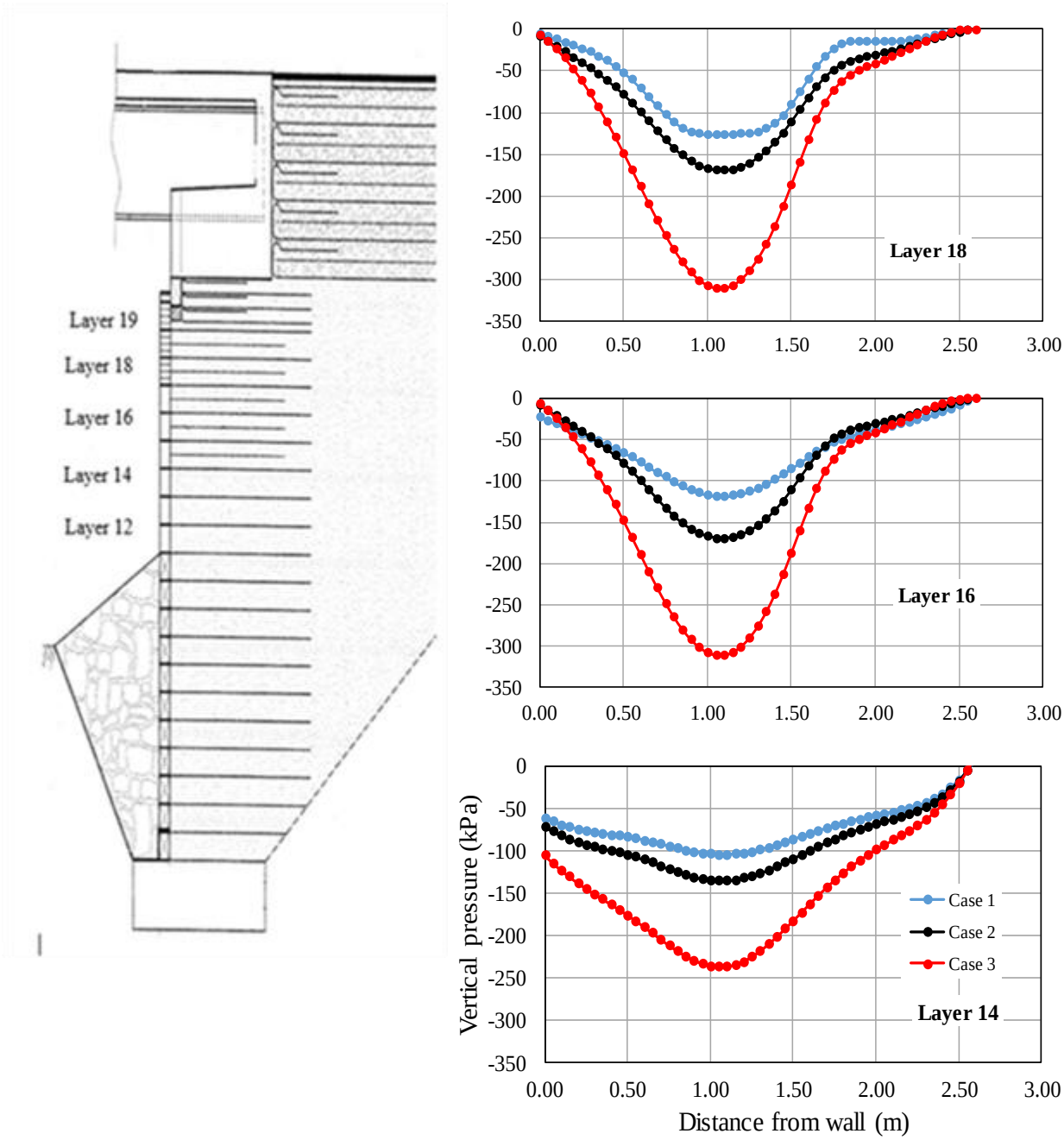

Figure 5.25. Measurement of vertical stress distribution along cross-section at different layers in the GRS abutment.

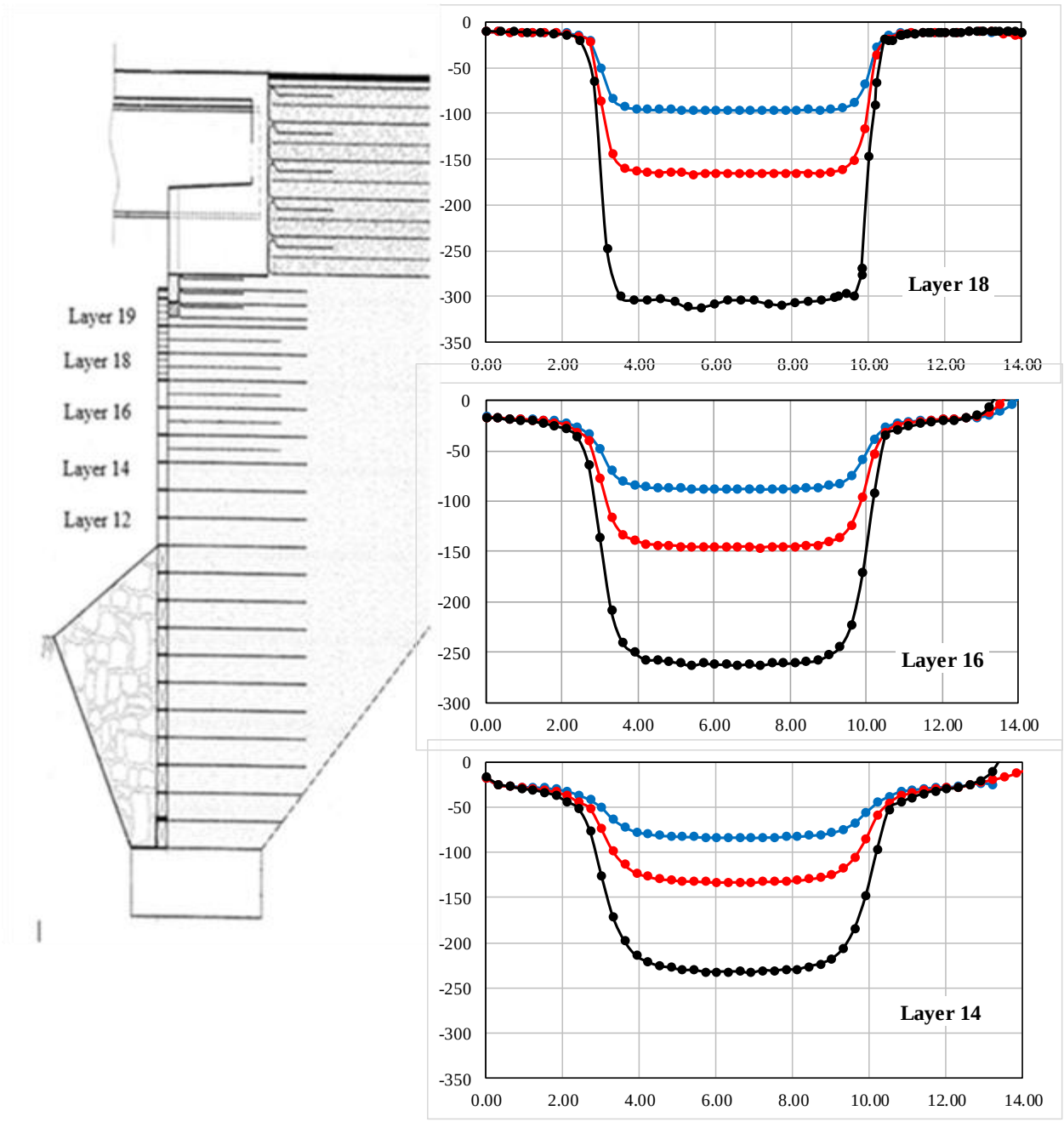

Figure 5.26. Measurement of vertical stress distribution along longitudinal-section at different layers in the GRS abutment.

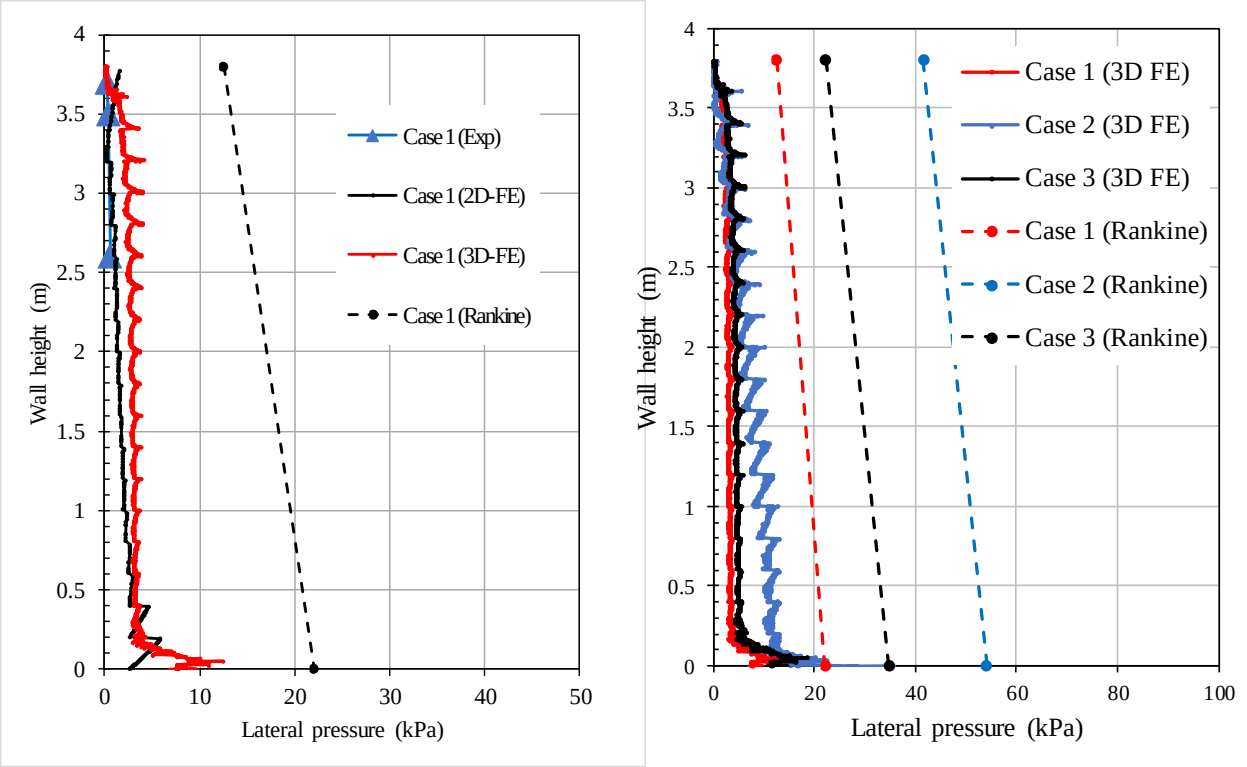

(a) under service load (b) under different load conditions

Figure 5.27. Comparison of lateral pressures on wall face a) under service load, and b) under different load conditions.

Table 2. compares the interface shear stress between the reinforcement and backfill materials as predicted by the 2D-FE and 3D-FE analysis and estimated using the Mohr-Coulomb (Eq. 1) analysis method for the service loading (Case 2) and the abnormal loading (Case 3). The table also compares between the axial force in the reinforcement predicted by the 2D-FE and 3D-FE analyses and the estimated values by the FHWA (Adams et al., 2011a) method (Eq. 2) for the same cases.

$$\tau_{max} = c_a + \sigma_n \tan\delta \quad \text{..... (1)}$$

where :

τ_{max} : Maximum interface shear stress at interface; σ_n : Normal stress; δ : Interal friction angle of backfill

$$T_{req} = \left[\frac{\sigma_h}{0.7^{\left(\frac{S_v}{6d_{max}}\right)}} \right] S_v \quad \text{..... (2)}$$

where:

T_{req}: Required reinforcement strength; σ_h : Lateral earth pressure; S_v: Reinforcement spacing; d_{max} : maximum grain size of backfill which is 19.05 mm in this study.

It can be seen in Table 2 that the axial forces in the geotextile reinforcement predicted by 2D-FE and 3D-FE analysis are within $\pm$ 10%. It was also noted that the highest deviation comes from the bottom layers where the maximum reinforcement strain strains are less than 1% for the service loading. For the purpose of comparison, the predicted axial forces by the FE analysis were also compared with the FHWA analytical method. It was noted that the axial forces in the geotextile reinforcement predicted by the values estimated by the FHWA analytical method are 1.5-2.0 times higher than those predicted by 2D-FE and 3D-FE analysis, depending on the loading condition and reinforcement location. It was noted that the deviation also decreases with increasing the loading. The highest predicted axial force by FHWA method is 10.9 kN/m and 15.7 kN/m for the service loading and the abnormal loading, respectively. On the other hand, the highest predicted axial forces by 3D-FE analysis for the same layer are 5.6 kN/m and 8.2 kN/m for the service loading and the abnormal loading, respectively. The coresponding predicted values by 2D-FE are 3.9 kN/m and 8.3 kN/m for for the service loading and the abnormal loading, respectively. The predicted axial forces remain almost constant through the entire GRS-IBS abutment for all different loading cases. This explains the main difference between the internally supported structures (GRS-IBS) and the externally supported structures (MSE walls) as the axial forces in the later (MSE walls) increases with depth according to the conventional Rankine or Coulomb methods. The results

support the assumption by Adams et al. (2011a) that the facing is not a structural element but it is rather aesthetic component.It was also noted in Table 2 that the interface shear stresses predicted by the 2D-FE and 3D-FE analyses are very close to each other and to those predicted by Mohr-Coulomb analytical method, which indicates that using coffeicent of interface ($\mu = 0.8$) as an interface friction value that was obtained between the reinforcement and backfill from the direct shear test is accurate.

Figure 5.31 presents the comparison between the location of maximum strain envelope with depth obtained from the 3D-FE and the 2D-FE analysis for cases 2 and 3 and those obtained from field measurements for case 1. The FE analysis demonstrates that both the 3D-FE and 2D-FE analyses can predict the location of maximum strain for the upper half of GRS-IBS abutment. However, it was noted that the location of maximum strain varies between the 3D-FE and 2D-FE for the lower half where the rip-rap is located, and this is might due to the 3D boundary effects. The figure demonstrates that the locations of maximum strain is load dependent, i.e., by increasing the applied load, the location of maximum strain moves toward the GRS-IBS abutment face.

Distinguish must be made here between the MSE wall (externally supported structure due to the tension resistant tieback) and the GRS-IBS (internally supported structure due to the composite behavior of closely reinforcement) design philosophies. The most used methods for MSE wall are Coherent Gravity Method (AASHTO,1996) and Tie Back Wedge Method (AASHTO, 1996). According to Coherent Gravity Method, the failure wedge is determined by assuming a bi-linear envelope of the maximum axial forces, in which three points are required to draw the failure envelope (H, 0.3H), (H/2,0.3H), and (0,0) as shown in Figure 5.31. On the other hand, the failure envelope in the Tie Back Wedge Method can be drawn according to Rankine active failure surface envelope through the reinforced soil slopes (i.e., $45° + \phi/2$), which is also

drawn in Figure 5.31. As the FE analyses and field measurements results indicated in Figure 5.31, both methods fail to predict the failure assumption for the case of GRS-IBS abutment. The failure envelope extends beyond the Coherent Gravity Method assumption up to 33% extra, in which the three points are required to draw the failure envelope; (H, 0.4H), (H/2,0.4H), and (0,0) as shown in Figure 5.31. In MSE walls design criteria, the reinforcements extend beyond the assumed active failure surface, and their reinforcement mechanism is considered to be tension-resistant tieback (fully bonded to the facing structure) for the assumed failure wedge. This analysis is commonly referred to as tieback wedge analysis; while in the GRS-IBS the reinforcement mechanism is not considered as a tieback instead it is considered to be part of a composite material due to the interaction between closed spaced reinforced and backfill material.

Figure 5.31 presents the predicted distribution of the shear strain using the 3D-FE analyses for the service loading condition (Case 2). The figure shows that the maximum shear strain occurs directly below the strip footingat the bottom center of the GRS-IBS abutment and decreases in all other directions.

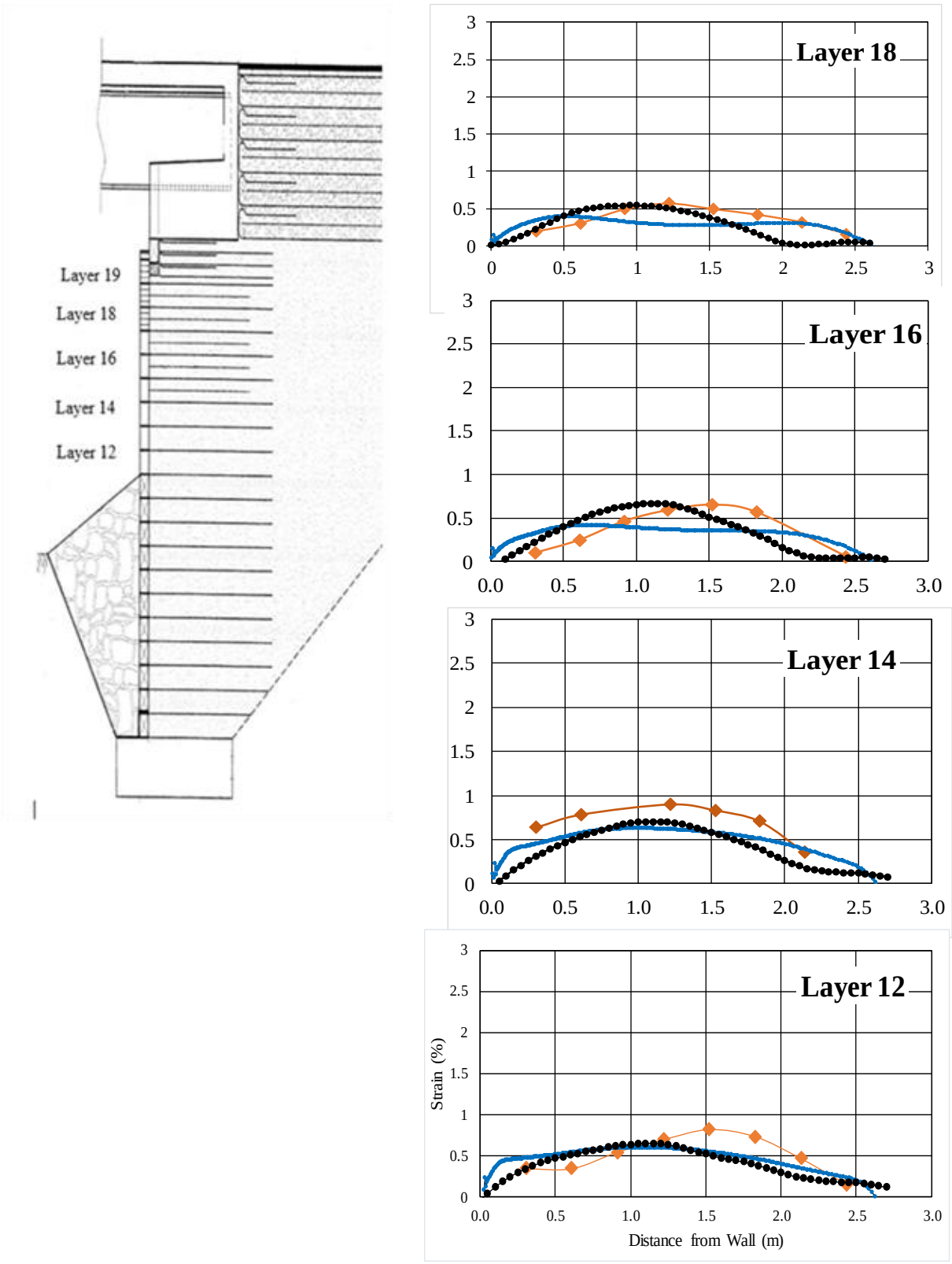

Figure 5.28. Comparison of strain distribution along geosynthetics for Case 1in the transverse direction.

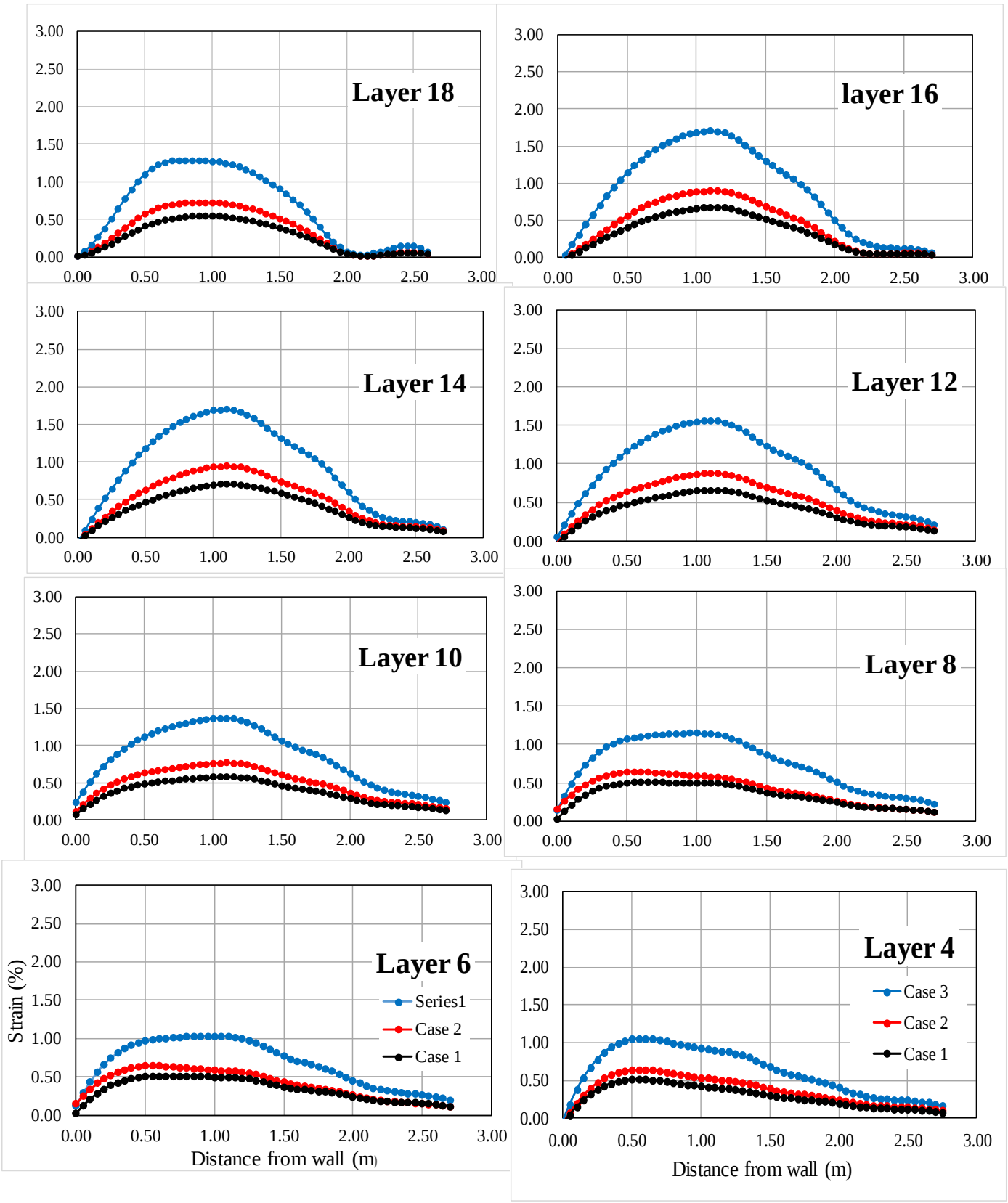

Figure 5.29. Predicted strain distribution along geosynthetics for the three cases of loading in the transverse direction.

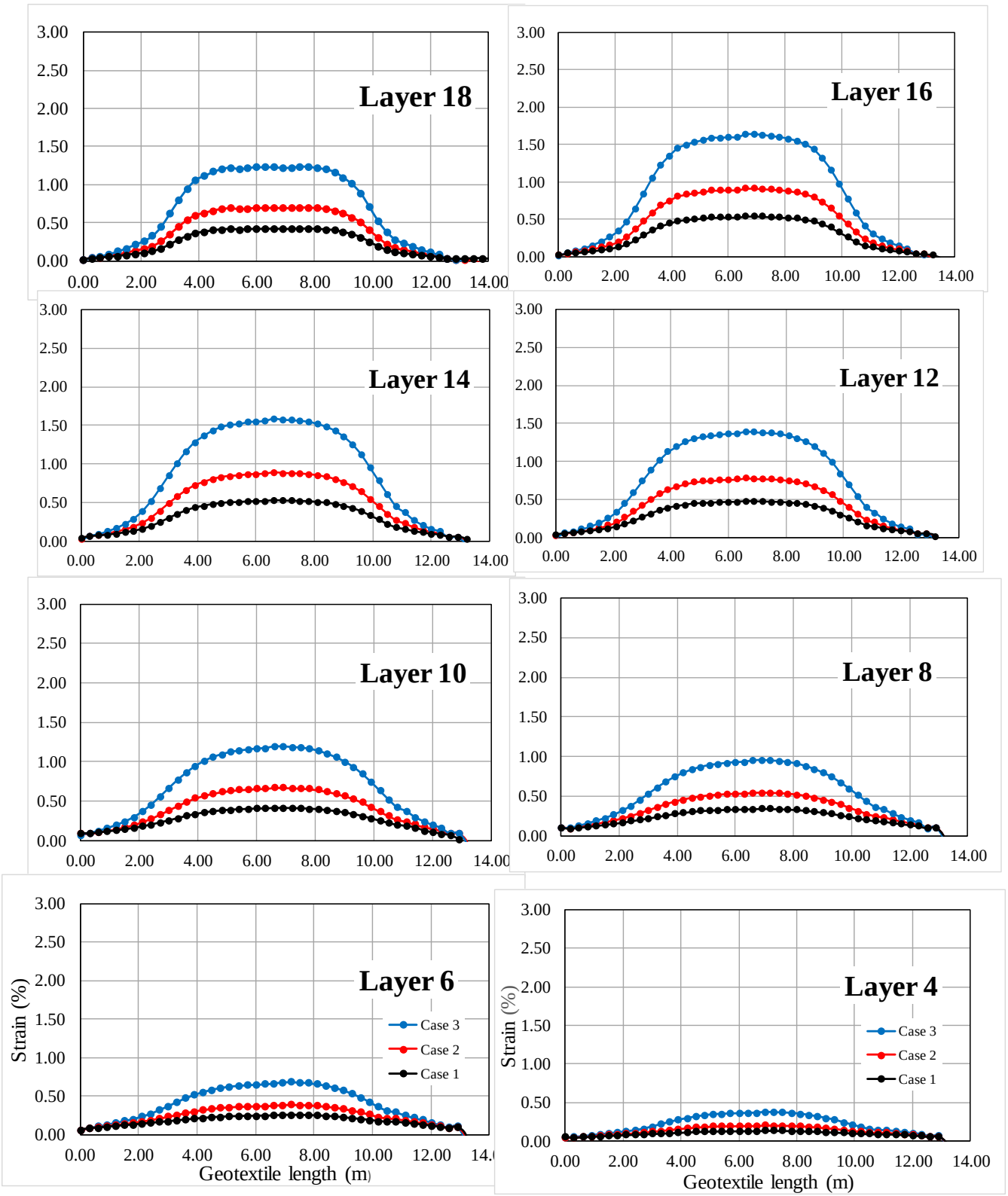

Figure 5.30. Predicted strain distribution along geosynthetics for the three cases of loading in the longitudinal direction.

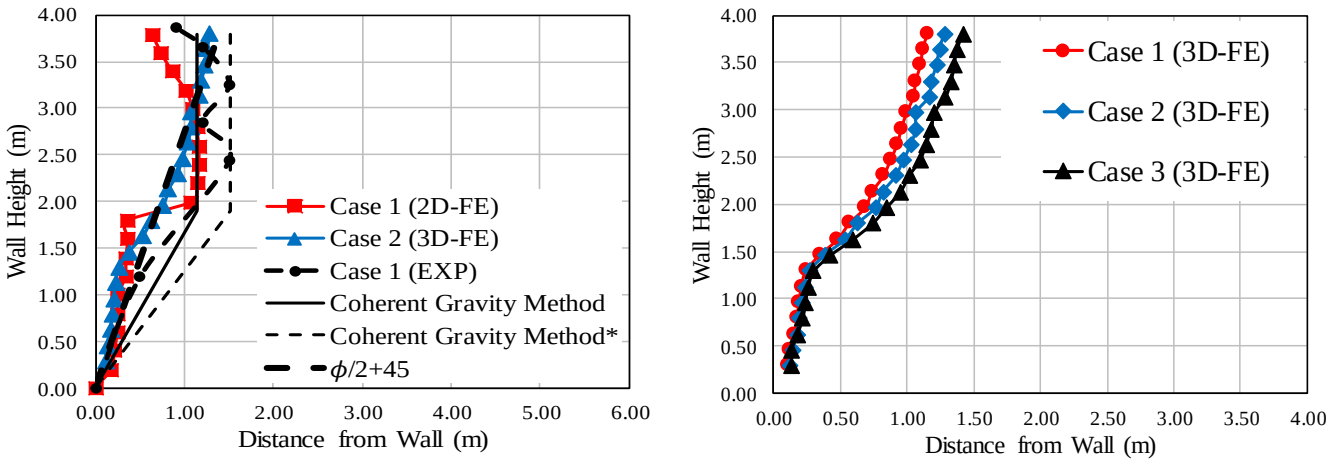

(a) (b)

Figure 5.31. a) Comparison of maximum strain envelope for field and FE results; and b) Maximum strain envelope at different loading conditions.

Table 2. Axial force in the reinforcement and the interface shear stress

Layer #	Case 2						Case 3					
	Axial Force FE-2D (kN/m)	Axial Force FE-3D (kN/m)	Axial Force FHWA (kN/m)	Max Shear Stress FE-2D (kPa)	Max Shear Stress FE-3D (kPa)	Max Shear Stress Analytical (kPa)	Axial Force FE-2D (kN/m)	Axial Force FE-3D (kN/m)	Axial Force FHWA (kN/m)	Max Shear Stress FE-2D (kPa)	Max Shear Stress FE-3D (kPa)	Max Shear Stress Analytical (kPa)
2	4.8	3.6	9.8	272	262	265	9.9	6.3	12.1	529	436	446
3	4.5	3.9	9.8	254	238	248	9.2	5.5	12.2	431	409	411
4	4.3	3.4	9.8	243	234	237	8.9	6.6	12.3	412	383	392
5	4.1	4.1	9.8	235	228	228	8.7	6.3	12.5	398	355	378
6	4	3.9	9.8	230	216	222	8.4	7.1	12.7	388	333	368
7	3.9	4.4	9.9	225	203	216	8.3	6.7	12.9	378	313	358
8	3.8	4.0	9.9	219	192	210	8.2	7.4	13.2	378	298	358
9	3.9	4.4	10.0	214	186	203	8.2	7.7	13.5	367	284	346
10	4.1	4.3	10.2	208	182	196	8.5	8.5	13.9	358	274	336
11	4.2	4.7	10.4	208	171	195	8.9	9.0	14.4	354	269	331
12	4.1	4.9	10.6	209	167	189	8.8	9.6	15.0	356	286	331
13	3.9	5.6	10.9	211	170	194	8.3	8.2	15.7	360	291	332
14	**3.7**	**4.3**	**5.6**	**213**	**175**	**194**	**8.2**	**8.4**	**8.2**	**363**	**333**	**334**
15	**3.5**	**4.5**	**5.9**	**214**	**181**	**193**	**7.6**	**8.4**	**8.7**	**366**	**291**	**335**
16	**3.4**	**4.6**	**6.0**	**212**	**190**	**191**	**7.3**	**8.1**	**9.3**	**368**	**366**	**334**
17	**3.2**	**4.5**	**6.3**	**208**	**200**	**188**	**7.1**	**7.3**	**9.8**	**365**	**350**	**332**
18	**3.0**	**3.9**	**6.3**	**204**	**214**	**185**	**6.7**	**6.3**	**9.8**	**360**	**348**	**328**

Bold: double reinforcement (layer 12-19)

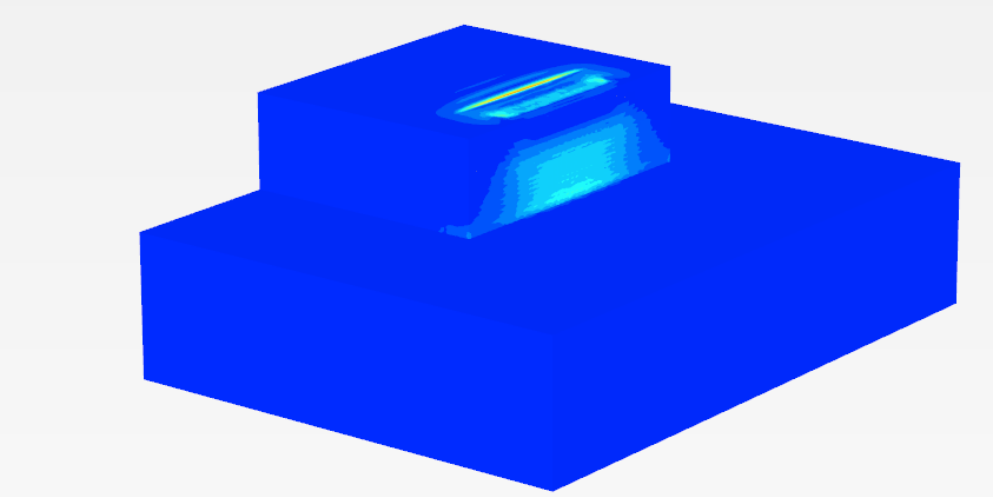

Figure 5.32. Shear strain (Service Load)

Chapter Six
Parametric Study

6.1 Introduction

This chapter presents the evaluation of the performance of the geosynthetic reinforced soil-Integrated Bridge System (GRS-IBS) in terms of lateral facing deformation, settlement of the Reinforced Soil Footing (RSF), strain distribution along geosynthetics, and the location of potential failure zone (locus of maximum strain) subjected to service loading. Simulations were conducted using two-dimensional (2D) PLAXIS 2016 Finite Element (FE) program. The hardening soil model proposed by Schanz et al. (1999) was used to simulate the behavior of the backfill material; the interface between the backfill materials and the reinforcement was simulated using the Mohr-Coulomb frictional model, and the reinforcement and facing block were simulated using the linear elastic model. The numerical model was first verified using the results of field case study conducted at the GRS-IBS of Maree Michel Bridge, Louisiana. A parametric study was then carried out to investigate the effects of abutment height, span length, reinforcement spacing, and reinforcement stiffness on the performance of the GRS-IBS. The results of the FE analyses indicate that the abutment height and span length have significant impact on the maximum strain distribution along the geosynthetic, the lateral facing displacement, and the reinforced soil foundation (RSF) settlement. It was noted that the reinforcement stiffness has a significant impact on the GRS-IBS behavior up to a certain point, beyond which the effect tends to decrease contradictory to the reinforcement spacing that has a consistent relationship between the GRS-IBS behavior and the reinforcement spacing. The results also indicate that the reinforcement spacing has higher influence on the lateral facing displacement than the reinforcement stiffness for the

same reinforcement strength to spacing ratio (T_f/S_v), mainly due to the composite behavior resulted from closely reinforced soil.

6.2 Objective

The main objective of this study is to evaluate the effect of different parameters on the performance of the geosynthetic reinforced soil in terms of lateral facing deformation, settlement of the RSF, reinforcement strain, and location of possible failure zone locus of maximum strain by conducting comprehensive FE analysis parametric study. The FE parametric study includes; effect of abutment height H, span length L_{span}, reinforcement spacing S_v, and reinforcement stiffness, EA, internal friction angle, ϕ, length of reinforcement, Lr, width of reinforcement soil footing, B_{RSF}, secondary reinforcement, setback distance, a_b, subgrade soil conditions, bearing width, b, and effect of differential settlement.the effects of span length, height of GRS abutment, reinforcement spacing, and reinforcement stiffness.

6.3 Numerical Model

The two-dimensional finite element program PLAXIS 2D 2016 (Brinkgreve, 2002) was used in the current study to evaluate the effect of different parameters on the performance of GRS-IBS. The finite element grid and boundary conditions are shown in Figure 6.1. Mesh refinement was first conducted to find the optimum mesh-size where the numerical results are not mesh-size dependent. The dimensions of the model domain were selected far enough to minimize the effect of boundary conditions on the model response. The lateral boundaries were fixed by roller support to prevent the soil movement in the horizontal direction. The bottom of soil foundation was fixed using bin support to prevent the soil from movement in both the horizontal and vertical directions.

In the current study, the configuration of the GRS-IBS numerical model is selected according to the FHWA design criteria recommendation (Adams et al., 2011a). Figure 6.1 presents the configuration of the GRS-IBS model that was adopted to perform the parametric study. The height of bridge abutment H was selected with a minimum span length L_{span} larger than 7.6 m, the minimum base width B_{total} *is* the greater value of 1.83 m or 0.3H. The width of the reinforced soil footing (RSF) B_{rsf} is equal to B_{total} +0.25B_{total}, assuming the bridge span to depth ratio = L_{span}/D = 24 as reported by Zheng and Fox (2017), and the depth of the RSF D_{rsf} is equal to 0.25 B_{total}. The setback distance between the back of the face and the footing a_b is equal to 0.2 m. The minimum clear space d_e, the distance from the top of the facing block to the bottom of the superstructure, is equal to 8 cm or 2% of the abutment height, whichever is greater. The width of the beam seat (strip footing in this study) b was selected equal to 1.2 m with a thickness of 0.6 m (note that the minimum width of the beam seat for a span length greater than 7.6 m is 0.77 m and the minimum thickness is 0.2 m). The minimum reinforcement length L_r at the bottom of the bridge abutment should be 0.3H or B_{total}, whichever is greater, which increases linearly up to 0.7H. The bearing bed reinforcement zone was extended from the top reinforcement layer for six consecutive layers. The length of the bearing bed reinforcement L_{rb} is equal to $2a_b+b$.

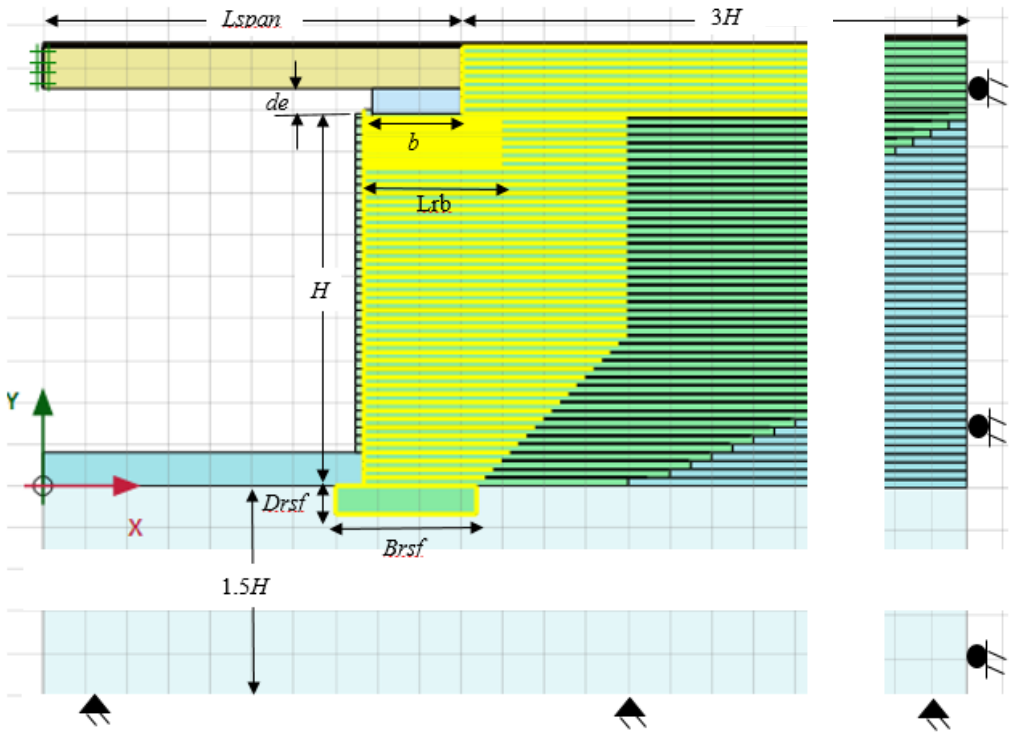

Figure 6.1. GRS-IBS numerical model with geometry and boundaries conditions.

A crushed diabase opened graded backfill materials having maximum particle size D_{max} of 19 mm (3/4 in) was selected in this study similar to the backfill materials used for the construction of the GRS-IBS at Maree Michel bridge site (Ardah et al., 2017). The properties of the backfill materials are listed in Table 1, which were determined and calibrated in a previous study (Ardah et al., 2017).

A review of the recent literature shows that the hardening soil model has been used successfully to simulate the non-linear stress strain behavior of backfill materials (Mirmoradi and Ehrlich, 2014; Wu et al., 2014; Liu, 2015; Zheng and Fox, 2016, 2017; Ardah et al., 2017). The hardening soil model developed by Schanz et al. (1999) is an elasto-plastic type hyperbolic model. An isotropic hardening is assumed with associated plastic flow rule for the cap hardening and a

non-associated flow rule is used for the frictional hardening. The hardening soil can simulate the soil dilation and plastic yielding. It accounts for stress history and stress dependent stiffness, in which the total strains are calculated using a stress-dependent stiffness, which is different for loading and unloading/reloading conditions. The hardening soil model can be used to simulate the behavior of sands and gravels as well as the softer soils (e.g., clay and silt). Formulation and verification of the hardening soil model is well described in Schanz et al. (1999). A total of nine input parameters are required to describe the hardening soil model: the secant stiffness parameter at 50% strain, E_{50}^{ref} obtained from the triaxial test as well as the unloading/reloading stiffness parameter E_{ur}^{ref}, which is assumed to be equal to $3E_{50}^{ref}$ (Lunne et al., 1997); and the stiffness parameter E_{oed}^{ref} is assumed to be equal or less than E_{50}^{ref} as recommended by Schanz et al. (1999). The strength parameters, cohesion *c*, friction angleϕ, and dilation angle Ψ are obtained either from the triaxial test or large direct shear test. The power *m* for stress level dependency of stiffness ranges from 0.5-1.0 (e.g., 0.5 for hard soil such as granular materials and 1.0 for very soft soil) Schanz et al. (1999). The failure ratio R_f, which is equal to the ultimate deviatoric stress divided by the asymptote deviatoric stress, has a default value is 0.9; and the Poisson's ration for the unloading/reloading ν_{ur}, has a default value is 0.2.

The interfaces were simulated using the linear elastic Mohr-Coulomb frictional model. The role of the interface is to transfer the shear and normal stresses from the soil to the structure. The shear strength is governed by the Mohr-Coulomb failure criterion. The properties of the interfaces in PLAXIS can be set by using a reduction factor ($R_i \leq 1.0$) applied to the soil material when defining soil property values (i.e., $R_i = 1.0$, meaning the interface should not have a reduced strength with respect to the strength of the surrounding soil). Hence, the interface property values are directly related to the mechanical properties of the soil forming the interface (e.g. $C_i = R_i * C_{soil}$).

These interfaces have properties of friction angle, cohesion, dilation angle, tensile strength, Young's modulus (E), and Poisson's ratio (ν). For more details about modeling the interfaces in PLAXIS or FLAC, the reader can refer to Yu et al. (2015).

The linear elastic model was selected to simulate the reinforcement, facing blocks, and the strip footing. The Mohr-Coulomb model was selected to simulate the foundation soil. The soil layer was modeled using a 15-noded triangle element, which provides a fourth order interpolation of displacements (note the structure and interface element is automatically taken to be compatible with the soil element). The 5-noded geogrid element was used to simulate the behavior of the geotextile reinforcement, which is composed of line element with two transitional degree of freedom in each node (u_x,u_y). A zero-thickness interface element was selected to simulate the interfaces between the backfill materials and the reinforcement, and the interfaces between the facing blocks and the reinforcement. When using a 15-noded soil element, the corresponding interface elements are defined by 5-pairs of nodes to be compatible with the soil elements.

6.4 Parametric Study

Twelve different parameters were considered in this study to evaluate the performance of the GRS-IBS under service loading condition in terms of lateral displacement of facing, settlement of RSF, reinforcement strain, and location of possible failure locus. The selected parameters are: effect of abutment height H, span length L_{span}, reinforcement spacing S_v, and reinforcement stiffness, EA, internal friction angle, ϕ, length of reinforcement, Lr, width of reinforcement soil footing, B_{RSF}, secondary reinforcement, setback distance, a_b, subgrade soil conditions, bearing width, b, and effect of differential settlement. A 7 m abutment height, 36.6 m span length, 0.2 m reinforcement spacing, and 600 kN/m axial stiffness were considered in this study the reference section subjected to an equivalent

distributed roadway live load of 12 kPa. The bridge girders were modeled as solid blocks ($L_b \times D \times 1$), assuming the bridge span to depth ratio = $L_{span}/D = 24$, composed of elastic elements with an equivalent unit of 11.86 kN/m^3. This procedure was adopted from a previous study by Zheng and Fox (2017).

6.4.1 Effect of Abutment Height (*H*)

Three different abutment heights, *H*, were considered and evaluated in this study: 5.2 m, 7.0 m, and 9.15 m. Figure 6.2 presents the effect of abutment height on the strain distribution along the geosynthetic reinforcement at 40 and 60% of the abutment height as measured from the bottom of the abutment. It can be seen that the maximum strain is affected by abutment height, in which the reinforcement layers at the bottom have higher strains than those in the top layers (e.g. the maximum strain decreases from 1. 1% at 60% of the abutment height to 0.7% at the same location when decreasing the abutment height from 9.15 m to 5.20 m). Figure 6.4a presents the effect of the abutment height on the lateral facing displacement. The lateral facing displacement increases from about 25 mm for abutment height of 5.2 m to around 35 mm for abutment height of 9.15 m, which indicates that increasing the abutment height will increase the lateral facing displacement. However, the location of the maximum lateral displacement unchanged. For the same span length (36.6 m) and the same location under the service loading condition, the figures indicate that the abutment height has a medium impact on the GRS-IBS performance in terms of the strain distribution along the reinforcement and a high impact on the lateral facing displacement.

6.4.2 Effect of Reinforcement Spacing (S_v)

Four different reinforcement spacings, S_v, were considered and evaluated in this study: 0.1 m, 0.2 m, 0.3 m, and 0.4 m. Figure 6.3 presents the strain distribution along the reinforcement at 20 and

80% of the abutment height as measured from the bottom of the abutment. It can be seen that for all cases the maximum strain envelope is located very close to the abutment face at 0.2 *H* of the abutment height and moves to about 1.2 m away from the abutment face at 0.8 *H*. However, the magnitude of maximum strain increases with increasing the reinforcement spacing. The maximum strain increases from 0.62% for a reinforcement spacing of 0.1 m to 1.63% for a reinforcement spacing of 0.4 m at 0.8 *H* from bottom of abutment. Figure 6.4b presents the effect of the reinforcement spacing on the lateral facing displacement. The maximum lateral facing displacement increases from 28 mm for a reinforcement spacing of 0.2 m to about 42 mm for a reinforcement spacing of 0.4 m. The figures indicate that the reinforcement spacing has a significant influence on the strain distribution along the reinforcement and the lateral facing displacement for the same span length (36.6 m) and same abutment height (7.0 m) under the service loading condition.

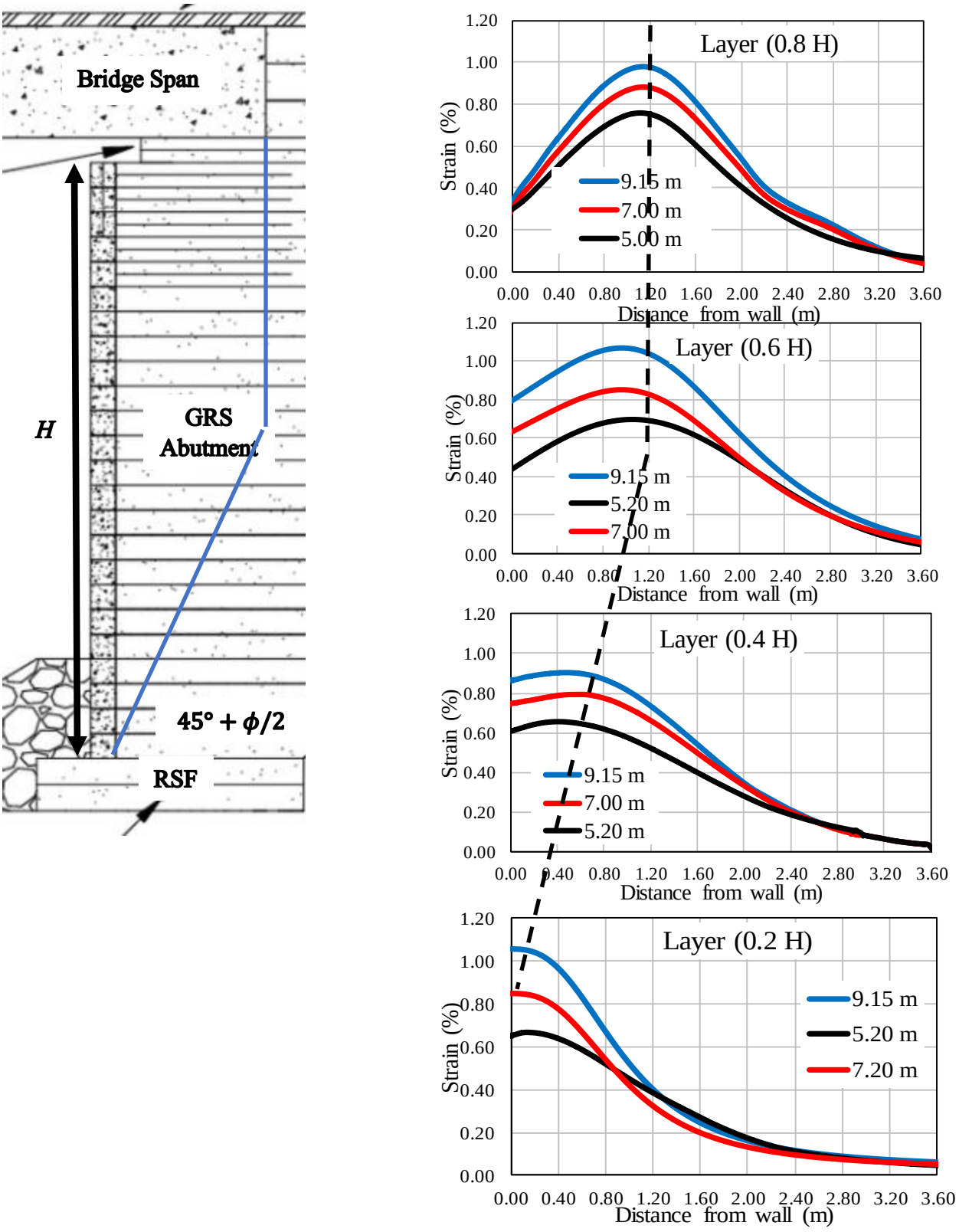

Figure 6.2. Effect of abutment height on the strain distribution along geosynthetics

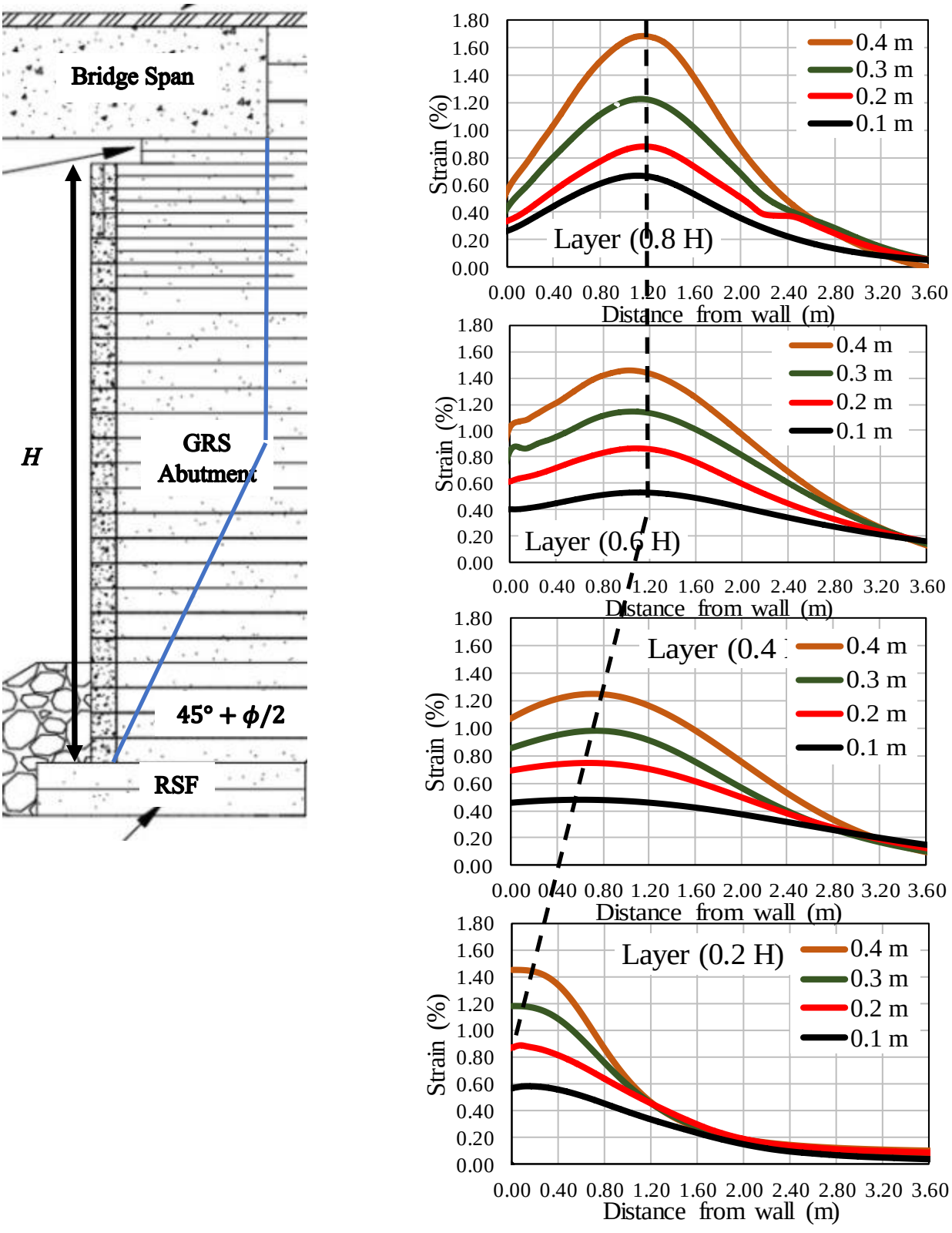

Figure 6.3. Effect of reinforcement spacing on the strain distribution along geosynthetics

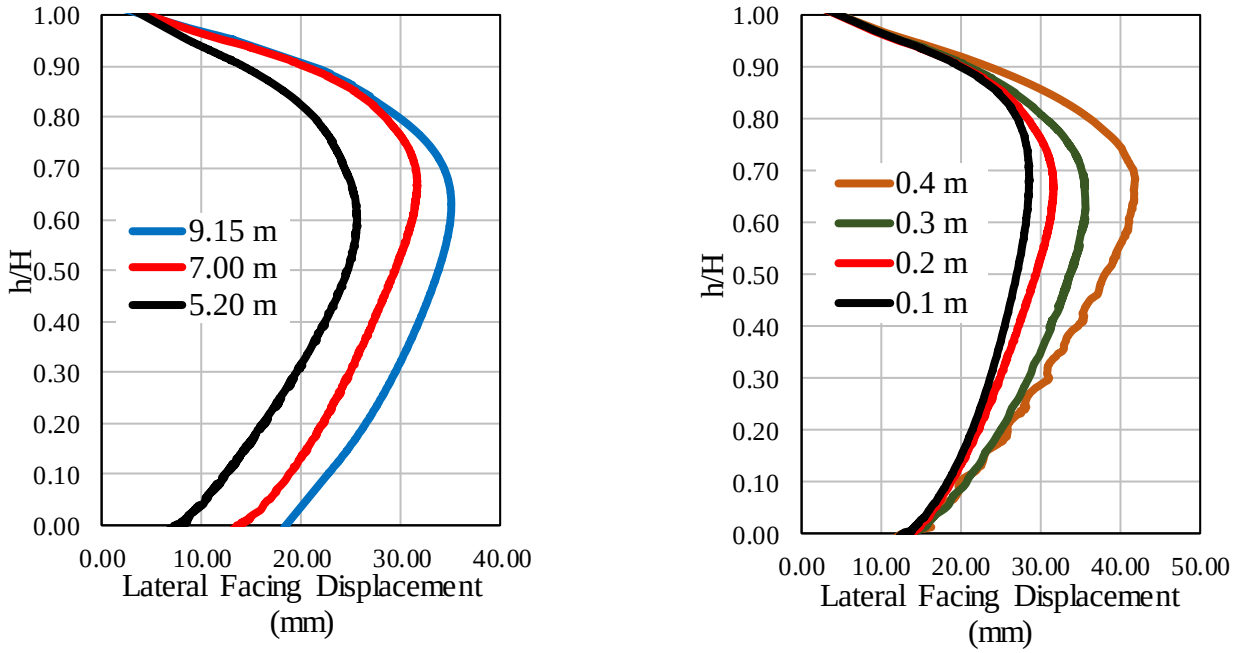

Figure 6.4. Effect of a) abutment height; b) reinforcemnet spacing on the lateral facing displacement

6.4.3 Effect of Span Length (L_{span})

Five different span lengths, L_{span}, were considered and evaluated in this study: 12.2 m, 18.3 m, 24.4 m, 30.5 m, and 36.6 m, which is corresponding to applied loads on top of GRS-IBS equal to 74, 108, 145, 180, and 216 kPa, respectively. Figure 6.5 presents the effect of span length on the strain distribution along the reinforcement at 20, 40, 60, and 80% of the abutment height as measured from the bottom of the abutment. It can be seen that the maximum strain envelope is located near the abutment face at 0.2 *H* and moving about 1.2 m away from the abutment face at 0.8 *H* for all cases. It can be seen that increasing the span length does not affect the shape of the strain distribution, and at the same time slightly shifting the locus of maximum strain to the left. However, increasing the span length results in increasing the magnitude of strain. The maximum strain increases from 0.4% for span length of 12.2 m to around 0.9% for a span length of 36.6 m

at 0.6 *H* and 0.6 *H* above the bottom of the abutment. Figure 6.7a presents the effect of span length on the lateral displacement of wall facing. It can be seen that by increasing the span length, the lateral facing displacement increases, and the location of maximum displacement shifts up. The lateral facing displacement increases from 12 mm for the 12.1 m span length to 30 mm for the 36.6 m span length. The figures indicate that the span length has a significant effect on the GRS-IBS performance in terms of the strain distribution along the reinforcement and the lateral displacement of wall facing for the same abutment height (7.0 m) under service loading condition.

6.4.4 Effect of Reinforcement Stiffness (*EA*)

Five different reinforcement stiffness, *EA*, were considered and evaluated in this study: 300, 600, 900, 1200, and 1500 kN/m. Figure 6.6 presents the strain distribution along the reinforcement at 20, 40, 60, and 80% of the abutment height as measured from the bottom of abutment. Similar to the effect of reinforcement spacing, the reinforcement stiffness affects the magnitude of the strain but does not affect either the shape of the strain distribution or the location of maximum strain. The maximum strain decreases from about 1.3% for a reinforcement stiffness of 300 kN/m to about 0.5% for a reinforcement stiffness of 1500 kN/m. It can be seen that increasing the reinforcement stiffness from 300 kN/m to 900 kN/m has significant effect on the reinforcement strain (e.g., the strain decreases from 1.3% to 0.68% at 0.8 *H*). However, after that, the effect of reinforcement stiffness tends to decrease (e.g., the strain decreases from 0.6% to 0.5% when the reinforcement stiffness increases from 900 kN/m to 1500 kN/m at 0.8 *H*). Figure 6.7b presents the effect of reinforcement stiffness on the lateral displacement of wall facing. The maximum lateral facing displacement decreases from 37 mm for a reinforcement stiffness of 300 kN/m to 26 mm for a reinforcement stiffness of 1500 kN/m.

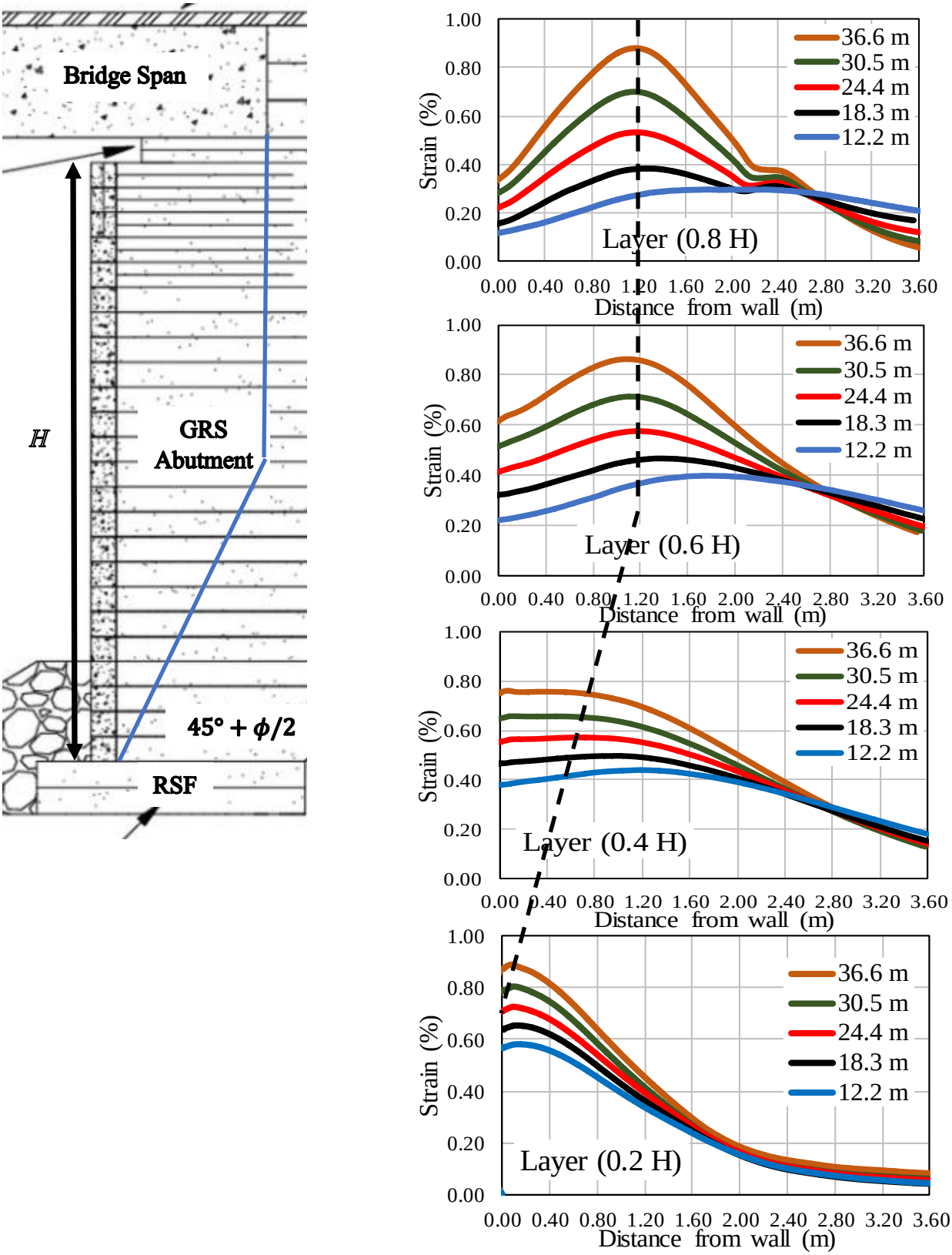

Figure 6.5. Effect of span length on the strain distribution along geosynthetics

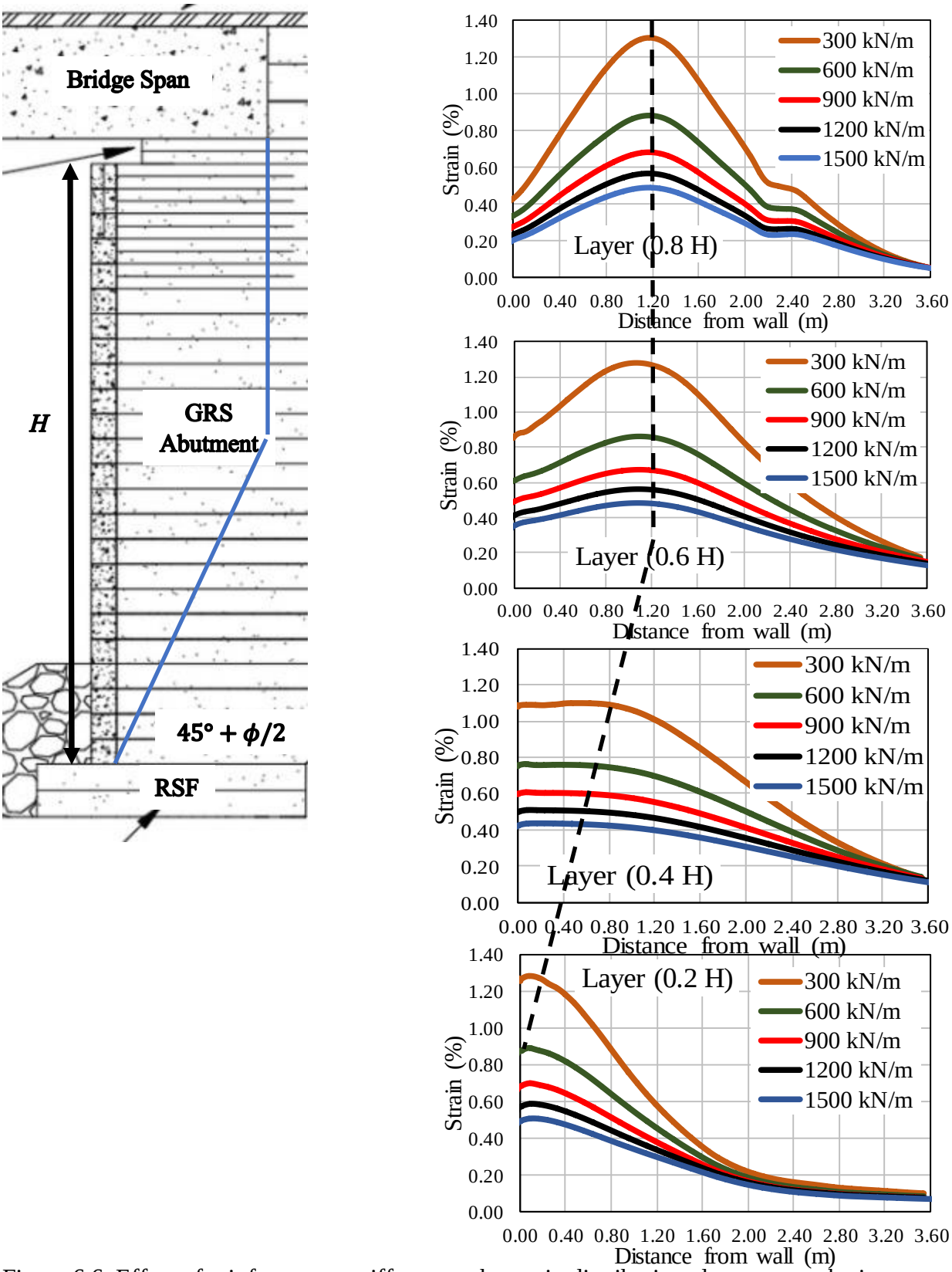

Figure 6.6. Effect of reinforcement stiffness on the strain distribution along geosynthetics

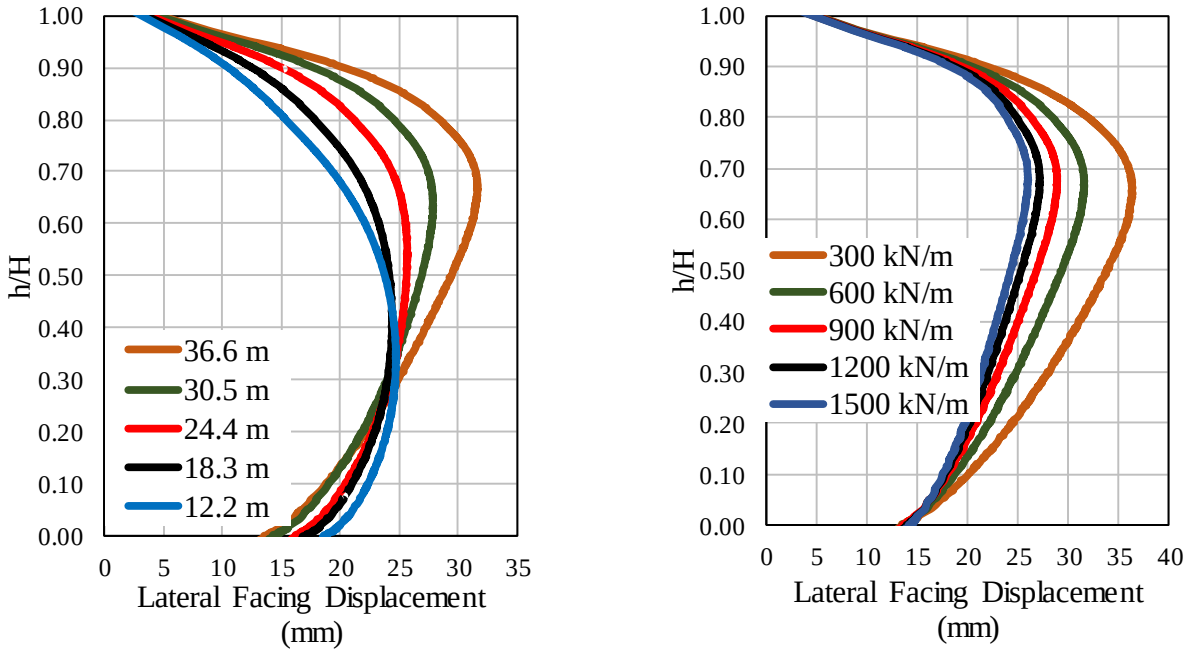

Figure 6.7. Effect of a) span length; b) reinforcement stiffness on the lateral facing displacement

6.4.5 Effect of Internal Friction Angle (ϕ)

Four different internal friction angles of the backfill materials, ϕ, were considered and evaluated in this study: 35°, 40°, 45°, and 50°. Figure 6.9 presents the strain distribution along the reinforcement at 20 and 80% of the abutment height as measured from the bottom of the abutment. It can be seen that for all cases the maximum strain envelope is located very close to the abutment face at 0.2 *H* of the abutment height and moves to about 1.2 m away from the abutment face at 0.8 *H*. However, the magnitude of maximum strain increases with increasing the friction angle. The maximum strain increases from 0.85% for a friction angle of 50° to 1.30% for a friction angle of 35°at 0.8 *H* from bottom of abutment. Figure 6.8a presents the effect of the friction angle on the lateral facing displacement. The maximum lateral facing displacement increases from 32 mm for a friction angle of 50° to about 52 mm for a reinforcement spacing of 35°. The figures indicate that the friction angle has a medium impact on the strain distribution along the reinforcement and

significant impact on the lateral facing displacement for the same span length (36.6 m) and same abutment height (7.0 m) under the service loading condition.

6.4.6 Effect of Length of Reinforcement (*Lr*)

Three different reinforcement lengths, L_r, were considered and evaluated in this study: L_r = 0.3 *H*, 0.5 *H*, 0.7 *H*, and 1.0 *H*. Figure 6.10 presents the effect of reinforcement length on the strain distribution along the geosynthetic reinforcement at 20, 40, 60 and 80% of the abutment height as measured from the bottom of the abutment. It can be seen that the maximum strain is not affected by reinforcement length. Figure 6.8b presents the effect of the reinforcement length on the lateral facing displacement. Reinforcement length has low impact on the lateral facing displacement, especially for $L_r \geq 0.5$ *H*. The lateral facing displacement increases from about 32 mm for L_r = 0.3 *H* to around 35 mm for $L_r \geq 0.5$ *H*, which indicates that increasing the reinforcement length will not decrease the lateral facing displacement.

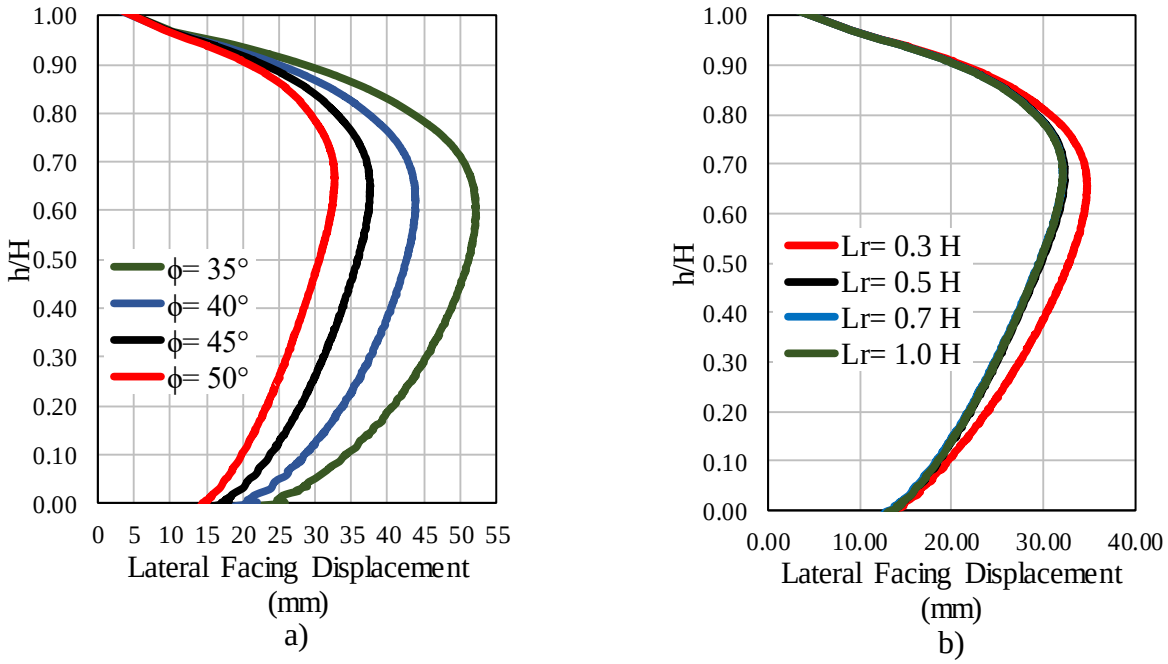

Figure 6.8. Effect of a) internal friction angle; b) reinforcemnet length on the lateral facing displacement

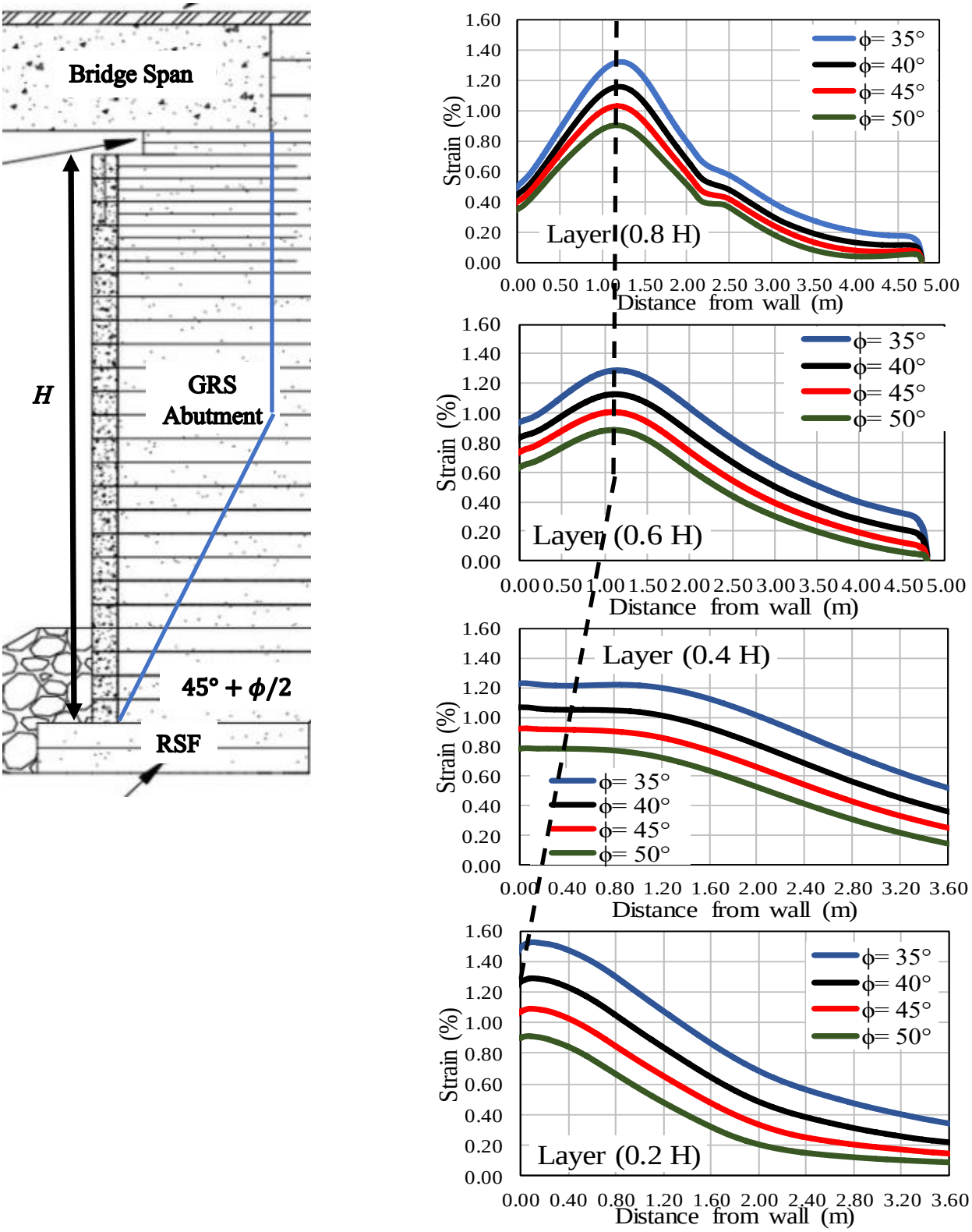

Figure 6.9. Effect of internal friction angle on the strain distribution along geosynthetics

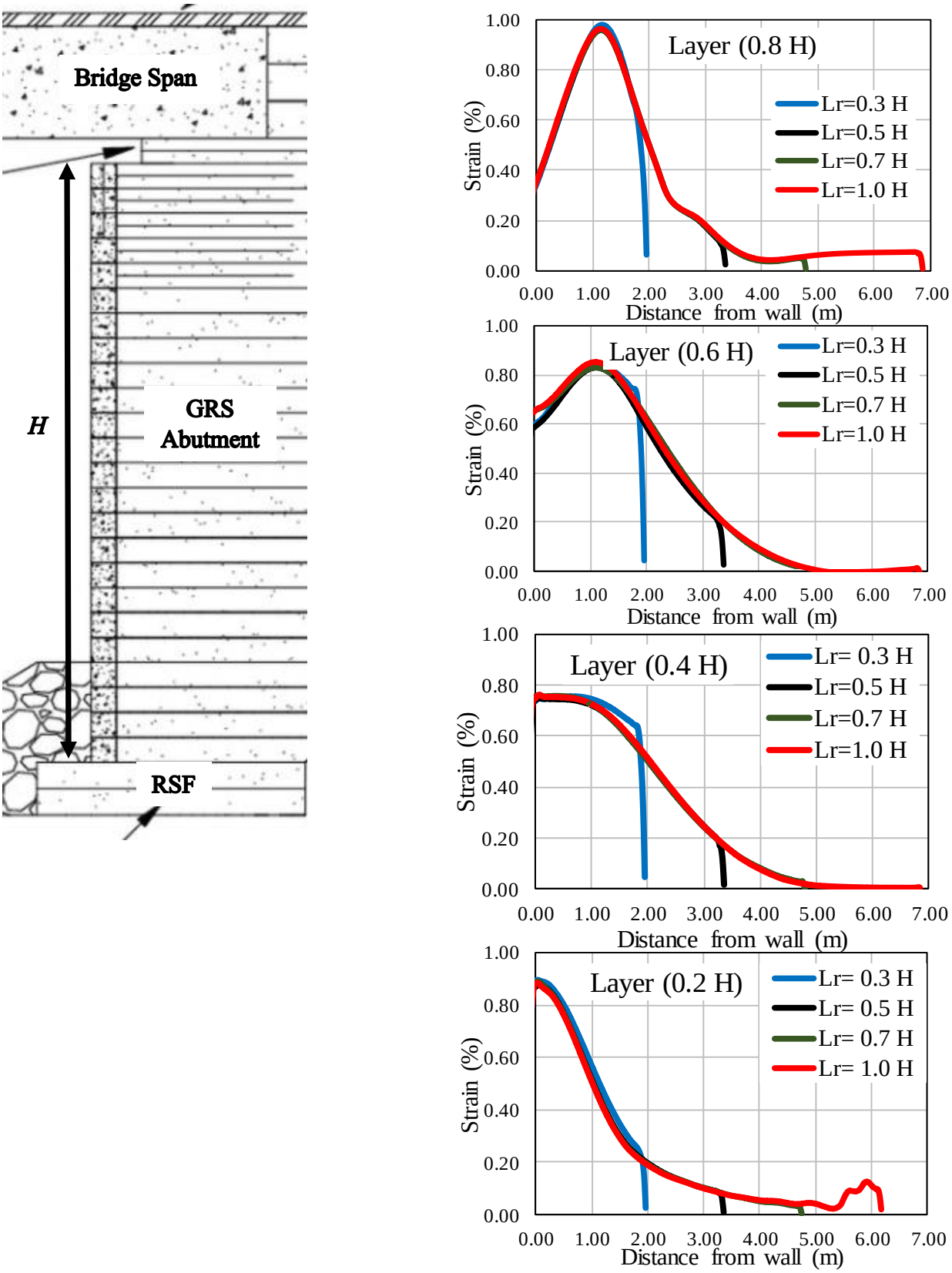

Figure 6.10. Effect of reinforcement length on the strain distribution along geosynthetics

6.4.7 Effect of Width of Reinforced Soil Footing (B_{RSF})

According to the FHWA, the total width of the RSF should extend beyond the base (B) of the GRS abutment by one-fourth the width of the base. In this section, three different widths of RSF, B_{RSF}, were considered and evaluated: B_{RSF} = 1.0 B, 1.25 B, and 1.5 B. Figure 6.12 presents the effect of RSF width on the strain distribution along the geosynthetic reinforcement at 20, 40, 60 and 80% of the abutment height as measured from the bottom of the abutment. It can be seen that the maximum strain is not affected by RSF width. Figure 6.11a presents the effect of the RSF width on the lateral facing displacement. Width of RSF has minimal effect on the lateral facing displacement, which also indicates that increasing the width of RSF will not affect the lateral facing displacement.

6.4.8 Effect of Secondary Reinforcement (Bearing Bed Reinforcement)

Simulations were conducted with bearing and without bed reinforcement layers placed underneath the bridge seat (or strip footing). Figure 6.13 presents the effect of secondary reinforcement on the strain distribution along the reinforcement at 20, 40, 60, and 80% of the abutment height as measured from the bottom of the abutment. It can be seen that the maximum strain envelope is located near the abutment face at 0.2 H and moving about 1.2 m away from the abutment face at 0.8 H for all cases. It can be seen that the maximum strain along the reinforcement at 20, 40, and 60% of the abutment height as measured from the bottom of the abutment decreases slightly when bearing bed reinforcement is included. However, the maximum strain is significantly affected along the reinforcement at 80% of the abutment height as measured from the bottom of the abutment (e.g., the decreasing in the maximum strain when the bearing bed reinforcement is included is equivalent to reducing the span length from 36.6 m to 30.5 m as shown in Figure 6.5).

Figure 6.11b shows that the lateral facing deformation is slightly decreasing when the bearing bed reinforcement is included. The figures indicate that the secondary reinforcement has a significant effect only on the strain distribution along the reinforcement at 80% of the abutment height as measured from the bottom of the abutment.

6.4.9 Effect of Setback Distance (a_b)

Simulations were conducted for five different setback distance a_b = 0.2, 0.4, 0.6, 0.8, and 1.0 m from the abutment face. Figure 6.15 presents the effect of the setback distance on the strain distribution along the reinforcement at 20, 40, 60, and 80% of the abutment height as measured from the bottom of the abutment. It can be seen that the maximum strain along the reinforcement slightly increases by increasing the setback distance away from the abutment face due to increasing the span length associated with increasing the setback distance. Figure 6.14a shows that the lateral facing deformation is slightly increasing when the setback distance is increased. The figures indicate that increasing the setback distance will not necessarily improve the GRS-IBS performance.

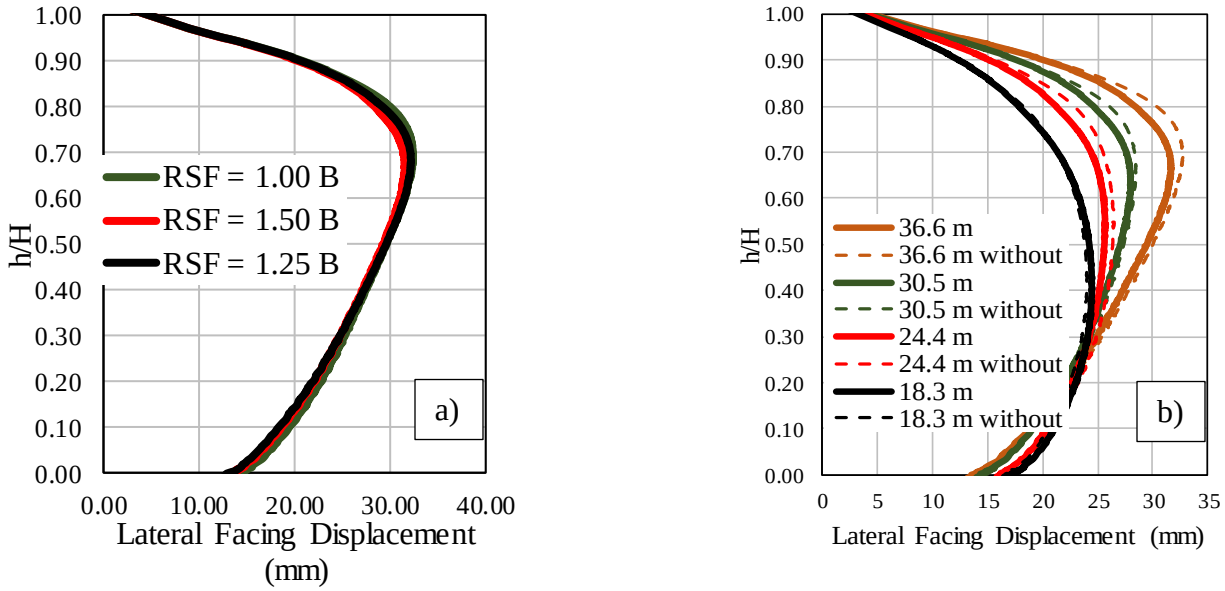

Figure 6.11. Effect of a) footing width; b) secondary reinforcement on the lateral facing displacement.

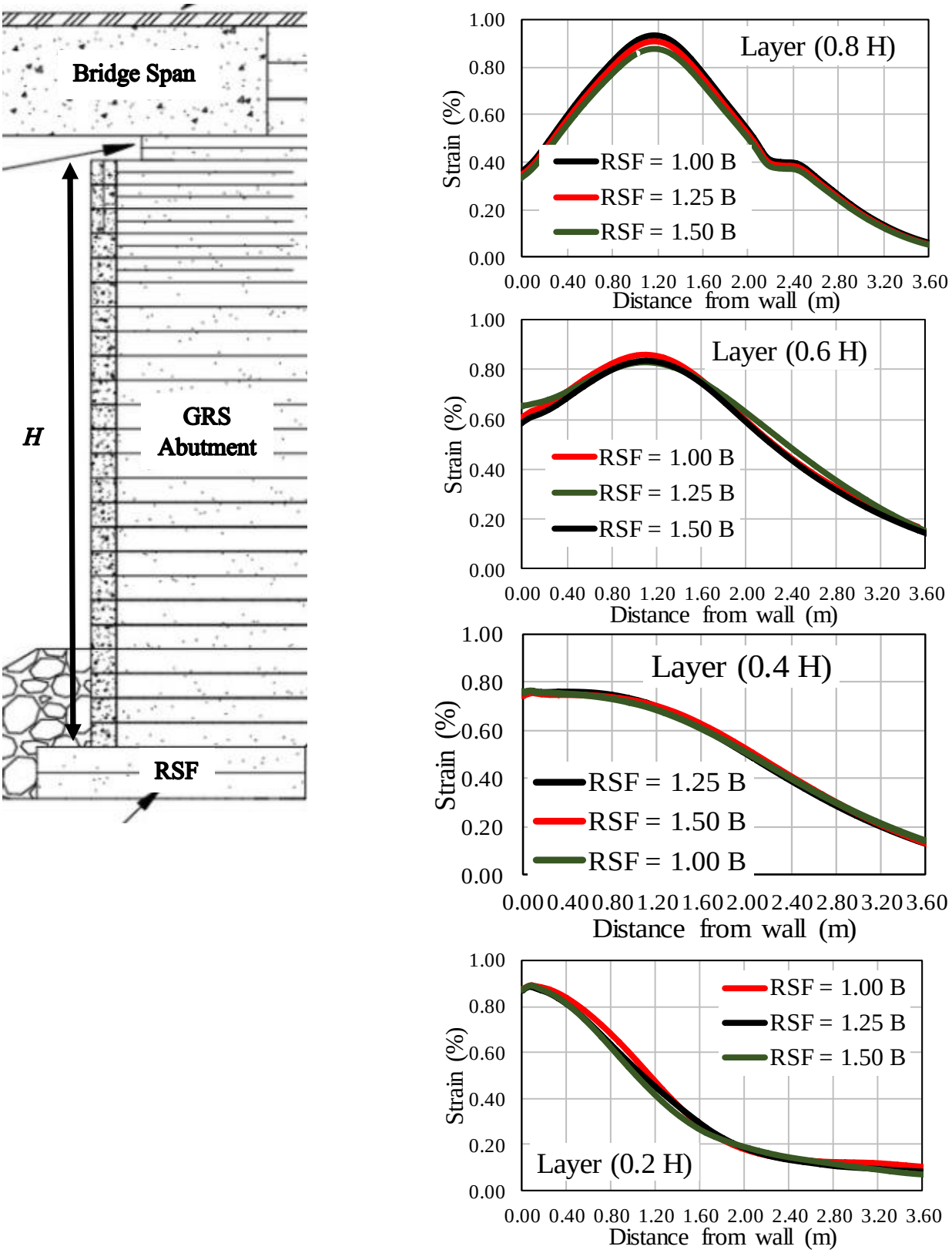

Figure 6.12. Effect of width of footing on the strain distribution along geosynthetics

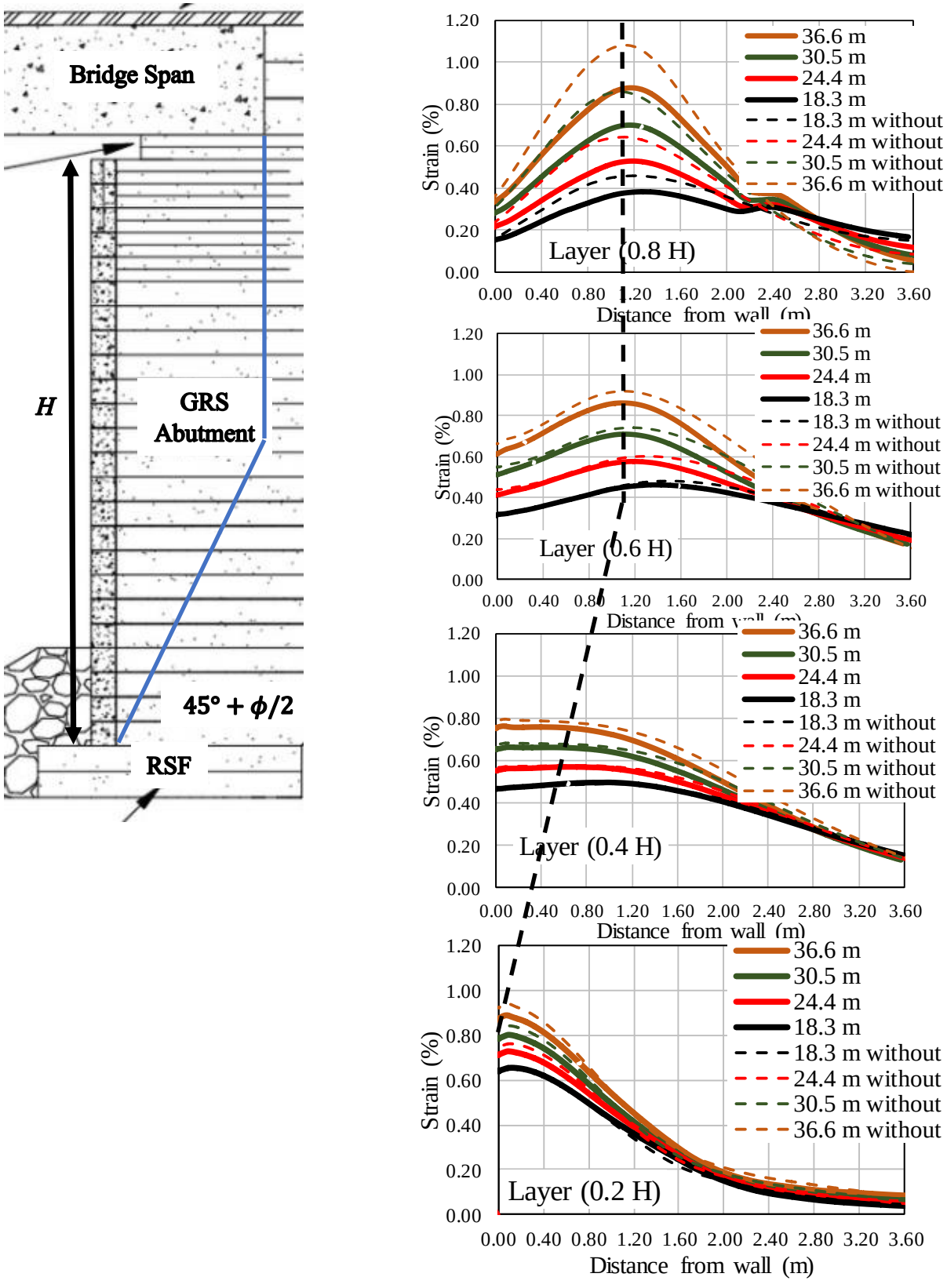

Figure 6.13. Effect of secondary reinforcement on the strain distribution along geosynthetics

6.4.10 Effect of Foundation Type

Three different foundation types were simulated using the Modified Cam clay model. The parameters were selected from previous work by Nazzal (2007) to represent weak, moderate and stiff subgrades. The parameters are presented in Table 6.1. Figure 6.16 presents the effect of foundation type on the strain distribution along the geosynthetic reinforcement at 20, 40, 60 and 80% of the abutment height as measured from the bottom of the abutment. It can be seen that the maximum strain is significantly affected by conditions of subgrade soil. The maximum strain increases from 0.5% for stiff subgrade soil to around 0.9% for a weak soft subgrade soils 0.6 *H* above the bottom of the abutment. Figure 6.14b shows that the lateral facing displacement is highly affected by the subgrade soil conditions. The lateral facing displacement increases from about 26 mm for a soft subgrade soil to around 35 mm for stiff subgrade soil, which indicates that care must be taken when designing a GRS abutment on soft subgrade soils to avoid excessive lateral facing deformation.

Table 1. Modified Cam-Clay Model Parameter for Different Subgrade Soils

Subgrade	G (kPa)	M	λ	κ	e_0	CBR
Soft	5170	0.65	0.225	0.11	1.35	1.5
Medium	20000	1	0.11	0.084	0.95	7
Stiff	35000	1.56	0.022	0.005	0.54	15

6.4.11 Effect of Bearing Width (*b*)

Simulations were conducted for five different bearing width b = 1.2, 1.4, 1.6, 1.8, and 2.0 m to study the effect of bearing width on the GRS-IBS behavior in terms of maximum strain distribution along the reinforcement and lateral facing pressure. Figure 6.17 presents the effect of the bearing width on the strain distribution along the reinforcement at 20, 40, 60, and 80% of the abutment

height as measured from the bottom of the abutment. It can be seen that the maximum strain along the reinforcement slightly decreases by increasing the bearing width, this is most probably due to increasing the area underneath the bridge span which will reduce the pressure on top of the GRS abutment. It was noted that the location of the maximum strain is associated with the bearing width, in which the maximum strain envelope is located right under the inner edge of the bearing width for the reinforcement layer at 0.8 *H* of the abutment height as measured from the bottom of the abutment. This result is very similar to the punching shear failure envelope defined by a previous study conducted by Chen et al. (2009) on reinforced crushed limestone underneath spread footing. Takemura et al. (1992) investigated the failure mechanism of reinforced sand by using centrifuge test. Their results showed that the intensely shear bands were developed from the edges of the footing and is extending vertically downward. Figure 6.14c shows that the lateral facing deformation is increasing by decreasing the bearing width. The figures indicate that increasing the bearing width will improve the GRS-IBS performance in terms of lateral facing displacement and maximum strain distribution especially at the top of GRS abutment.

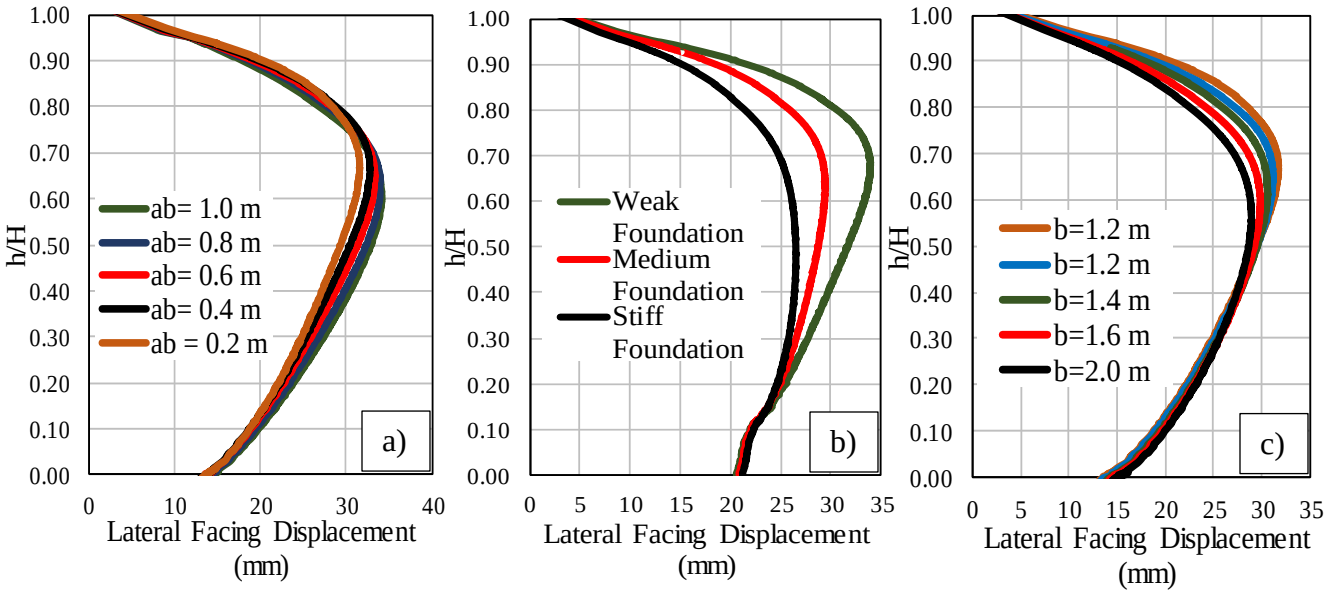

Figure 6.14. Effect of a) setback distance; b) foundation type; width of strip footing on the lateral facing displacement

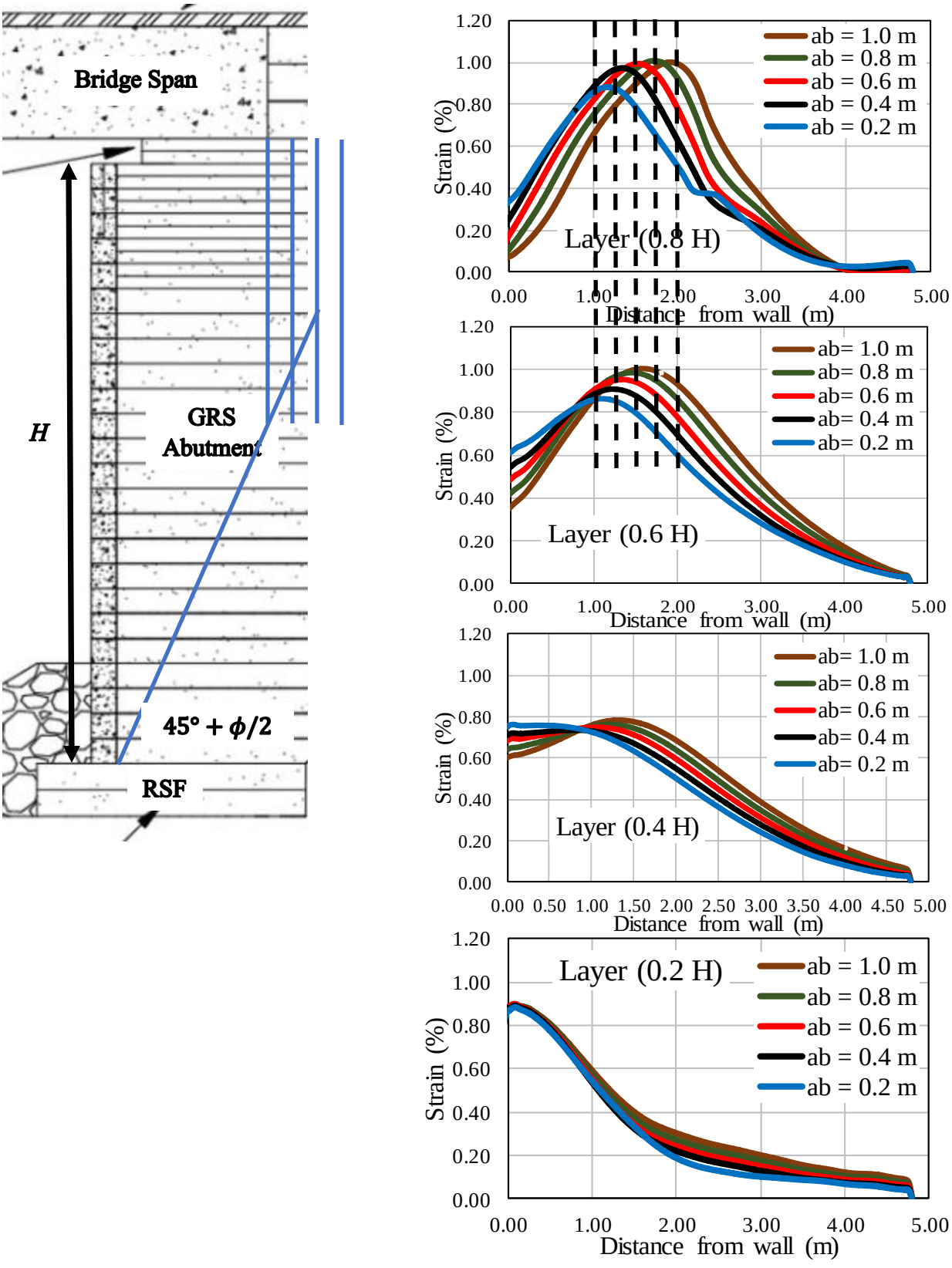

Figure 6.15. Effect of setback distance on the strain distribution along geosynthetics

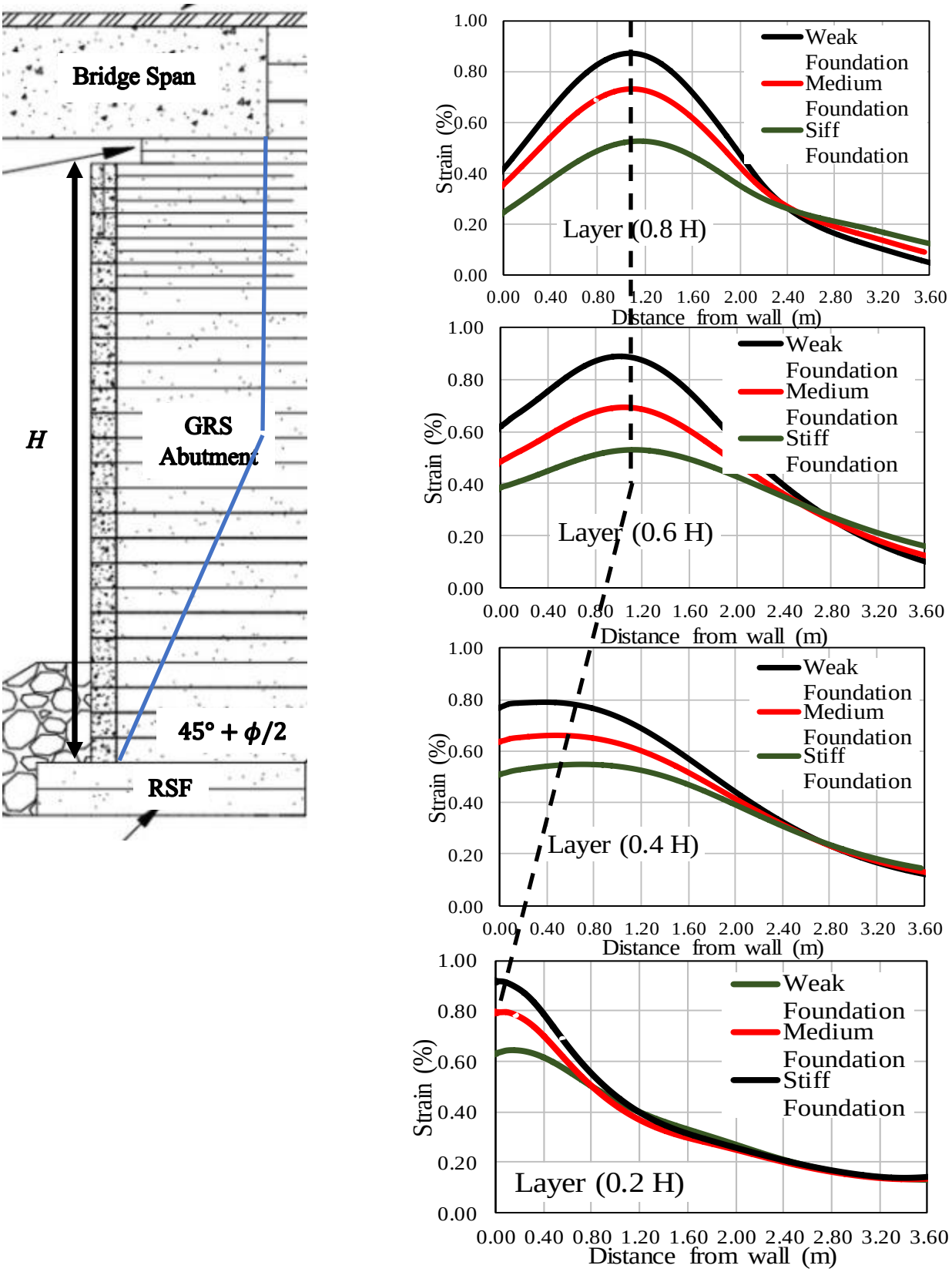

Figure 6.16. Effect of foundation type on the strain distribution along geosynthetics

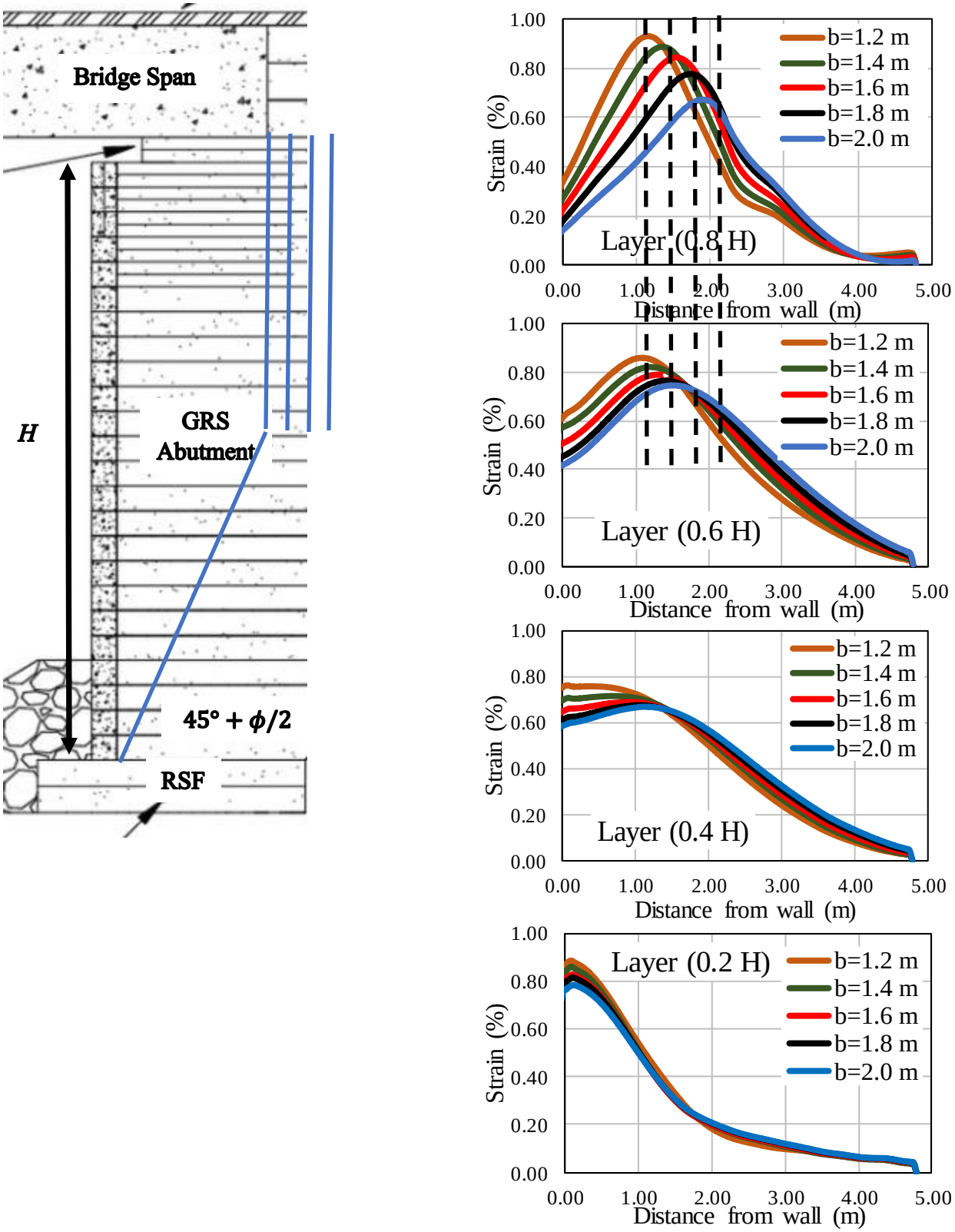

Figure 6.17. Effect of bearing width on the strain distribution along geosynthetics

6.4.12 Effect of Reinforcement stiffness, reinforcement spacing, foundation type, and internal friction angle of backfill materials on the Lateral Earth Pressure

Since the GRS-IBS facing is not considered as a structure element due to the composite behavior of the closely reinforced soil, the lateral facing pressure values are expected to be very small (Adams et al., 2011a; Ardah et al., 2017). The effect of four different reinforcement spacing, five different reinforcement stiffness's, three different subgrade soil types, and four different internal friction angles of the backfill materials on the lateral facing pressure were considered and evaluated in this study. Figure 6.24a presents the effect of reinforcement spacing on the lateral facing pressure. It was noted that the lateral facing pressure increases slightly when the reinforcement spacing increases from 0.1 m to 0.2 m. However, increasing the reinforcement spacing beyond 0.2 m is significantly affecting the lateral facing pressure. For instance, the maximum lateral facing pressure at the bottom of the GRS abutment for a reinforcement spacing of 0.4 m is almost two times higher than a reinforcement spacing of 0.1 m and 0.2 m. Figure 6.18a indicates the importance of closely reinforcement spacing ($Sv \leq 0.2\ m$). Figure 6.18b shows that the lateral facing pressure is slightly increased when the reinforcement stiffness decreases. It can be seen that the reinforcement spacing plays much greater role than reinforcement strength in the performance of the GRS-IBS in terms of lateral facing pressure for reinforcement spacing equal or higher than 0.2 m. Figure 6.18c shows the effect of the subgrade soil conditions on the lateral facing pressure. It can be seen that the subgrade soil conditions have a low impact value on the lateral facing

conditions. Figure 6.18d shows that the lateral facing pressure increases when the internal friction angle of the backfill materials decreases. The lateral facing pressure at the bottom of the GRS abutment increases from about 35° kPa for friction angle of 35 to around 70 kPa for friction angle of 50°, which indicates that increasing the friction angle will certainly decrease the lateral facing pressure as expected.

It was noted that the predicted and measured lateral pressure are much less than the Rankine lateral earth pressure. This is mainly attributed to the composite behavior of closely-spaced reinforced layers. The composite behavior of the GRS-IBS wall plays an important role in reducing the lateral earth pressure at the face as shown in Figure 6.18. The presence of closely reinforcement in a soil mass has proved to reduce the lateral stresses when subjected to vertical loading because the reinforcement is capable of restraining the lateral deformation of the soil around it (Wu, 2007). For instance, the active lateral earth pressure at the facing would be around 80 kPa for backfill material having internal friction angle 51° (using the MSE design criteria where the internal friction angle is capped at 40°) and 216 kPa applied load for a span length of 36.6 m using Rankine method without reinforcement, which is used for MSE wall design criteria.

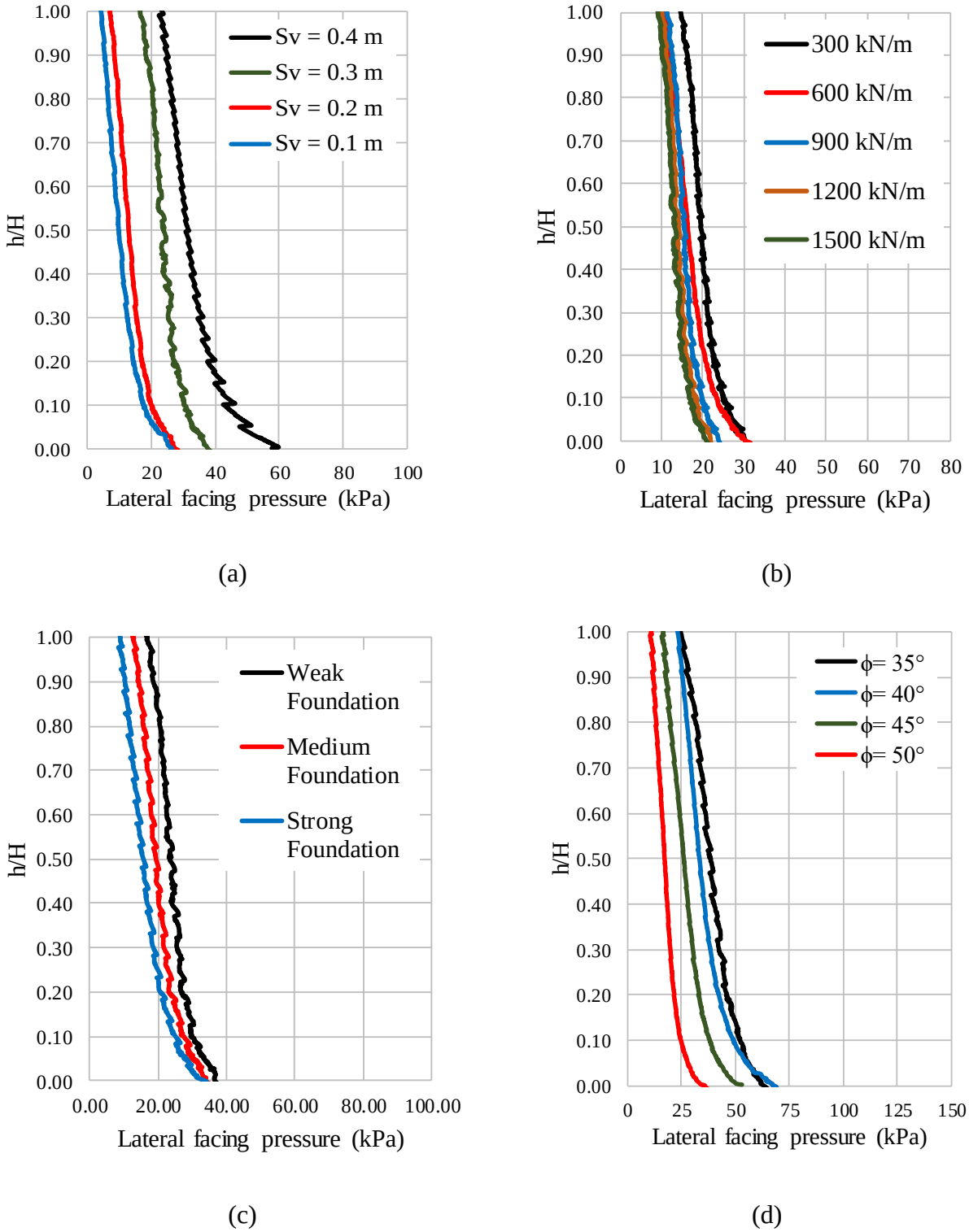

Figure 6.18. Effect of; a) reinforcement spacing; b) reinforcement stiffness; c) foundation type; and d) friction on lateral facing pressure

6.4.13 Effect of Internal Friction Angle (ϕ) Combined with Different Span Lengths (L_{span})

Figures 6.19 & 20 present and compare the effects of changing friction angle under different span lengths (different applied load) on the GRS-IBS performance in terms of maximum strain distribution along the reinforcement and lateral facing displacement. It can be seen that even though increasing the span length changes the magnitude of the maximum strain and lateral facing displacement, the friction angle effect on the maximum strain distribution and lateral facing displacement behavior is independent of increasing or decreasing the span length.

6.4.14 Effect of Reinforcement Spacing (S_v) Combined with Different Span Lengths (L_{span})

Figures 6.21 & 22 present and compare the effects of reinforcement spacing under different span lengths (different applied load) on the GRS-IBS performance in terms of maximum strain distribution along the reinforcement and lateral facing displacement. It can be seen that even though increasing the span length changes the magnitude of the maximum strain and lateral facing displacement, the reinforcement spacing effect on the maximum strain distribution and lateral facing displacement behavior is independent of increasing or decreasing the span length.

6.4.15 Effect of Reinforcement Stiffness (EA) Combined with Different Span Lengths (L_{span})

Figures 6.23 & 24 present and compare the effects of reinforcement stiffness under different span lengths (different applied load) on the GRS-IBS performance in terms of maximum strain distribution along the reinforcement and lateral facing displacement. It can be seen that even though increasing the span length changes the magnitude of the maximum strain and lateral facing displacement, the reinforcement stiffness effect on the maximum strain distribution and lateral facing displacement behavior is independent of increasing or decreasing the span length.

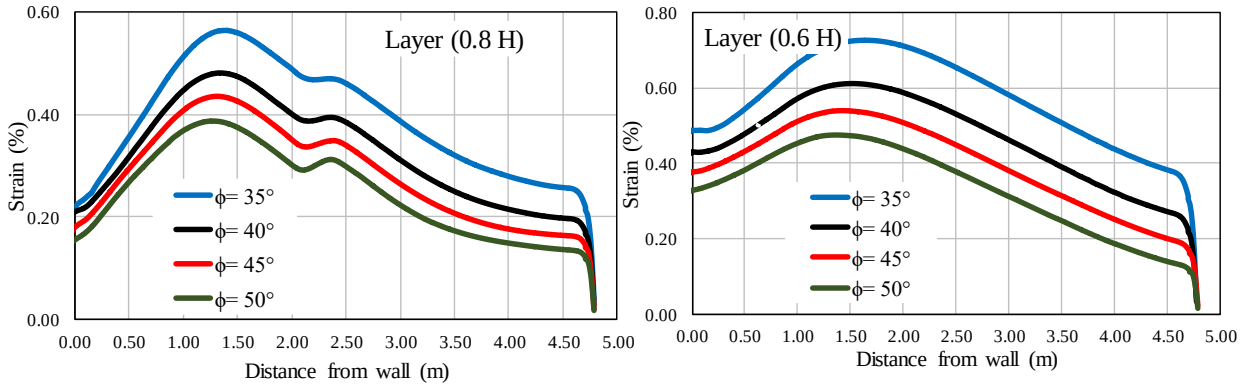

(a)

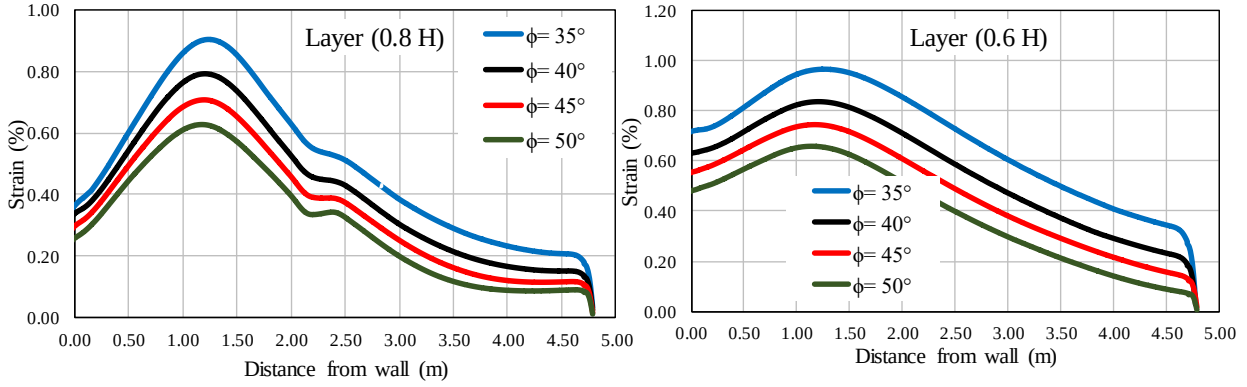

(b)

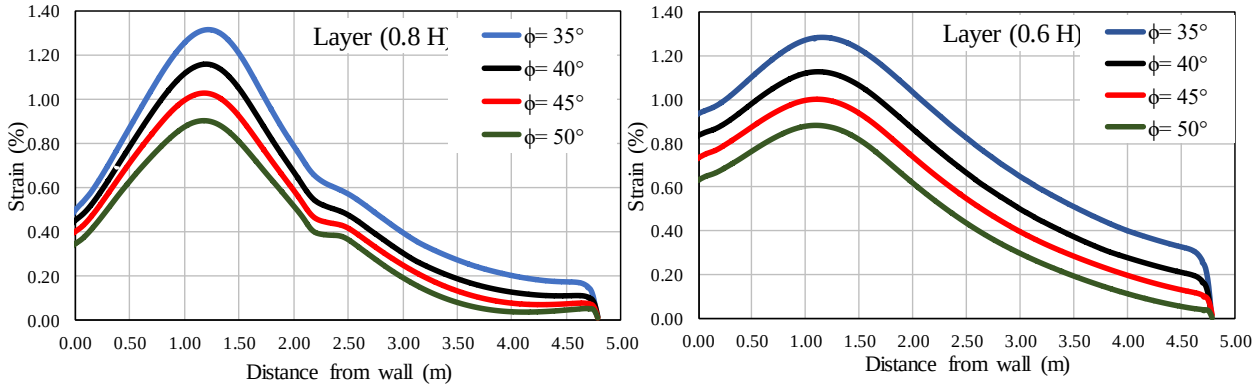

(c)

Figure 6.19. Effect of friction angle on the strain distribution along geosynthetics subjected to different span lengths: a) 18.3 m; b) 27.4 m; and c) 36.6 m

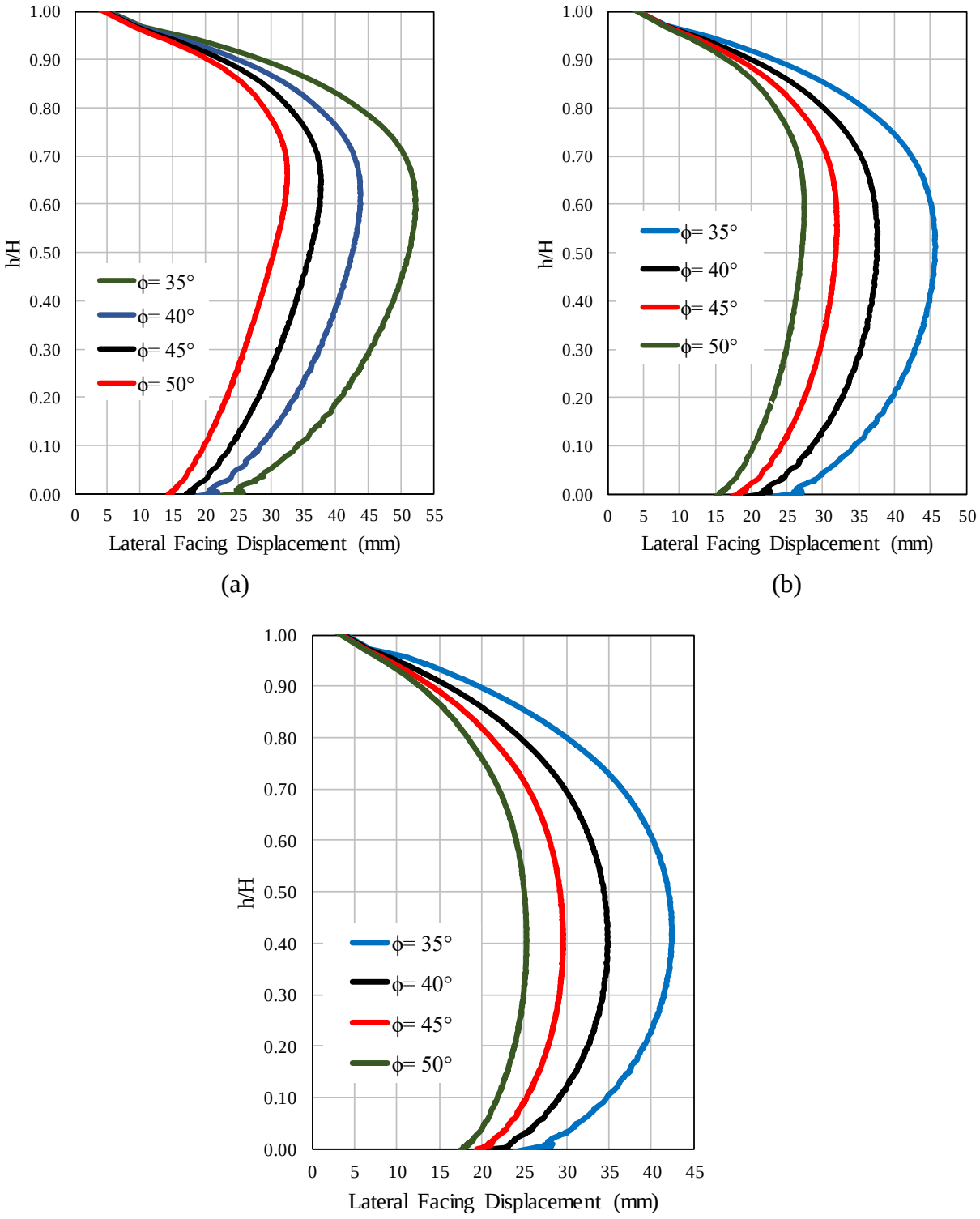

Figure 6.20. Effect friction angle on the lateral facing displacement geosynthetics subjected to different span lengths: a) 18.3 m; b) 27.4 m; and c) 36.6 m

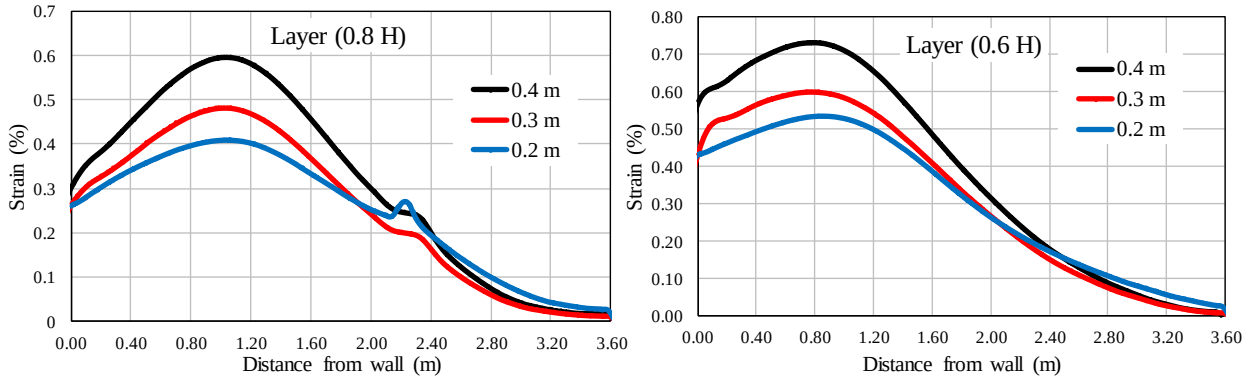

(a)

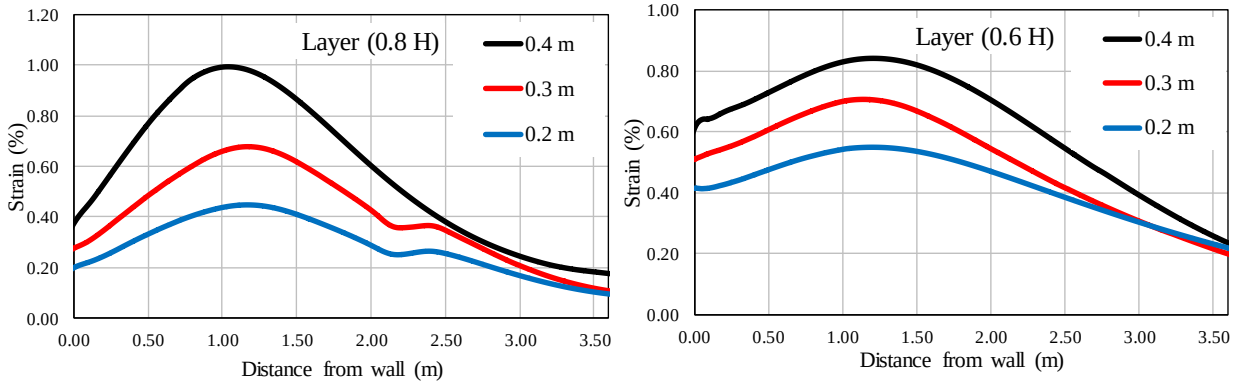

(b)

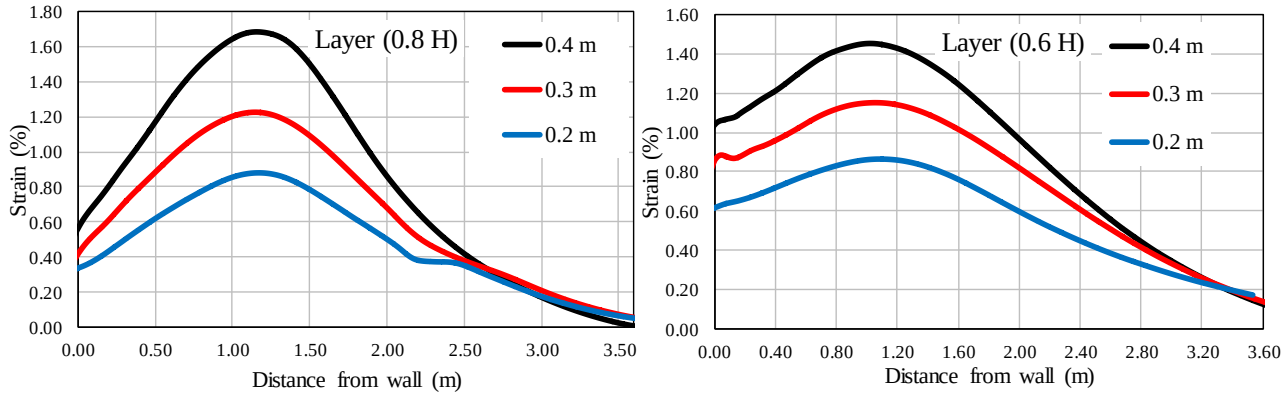

(c)

Figure 6.21. Effect of reinforcement spacing on the strain distribution along geosynthetics subjected to different span lengths: a) 18.3 m; b) 27.4 m; and c) 36.6 m

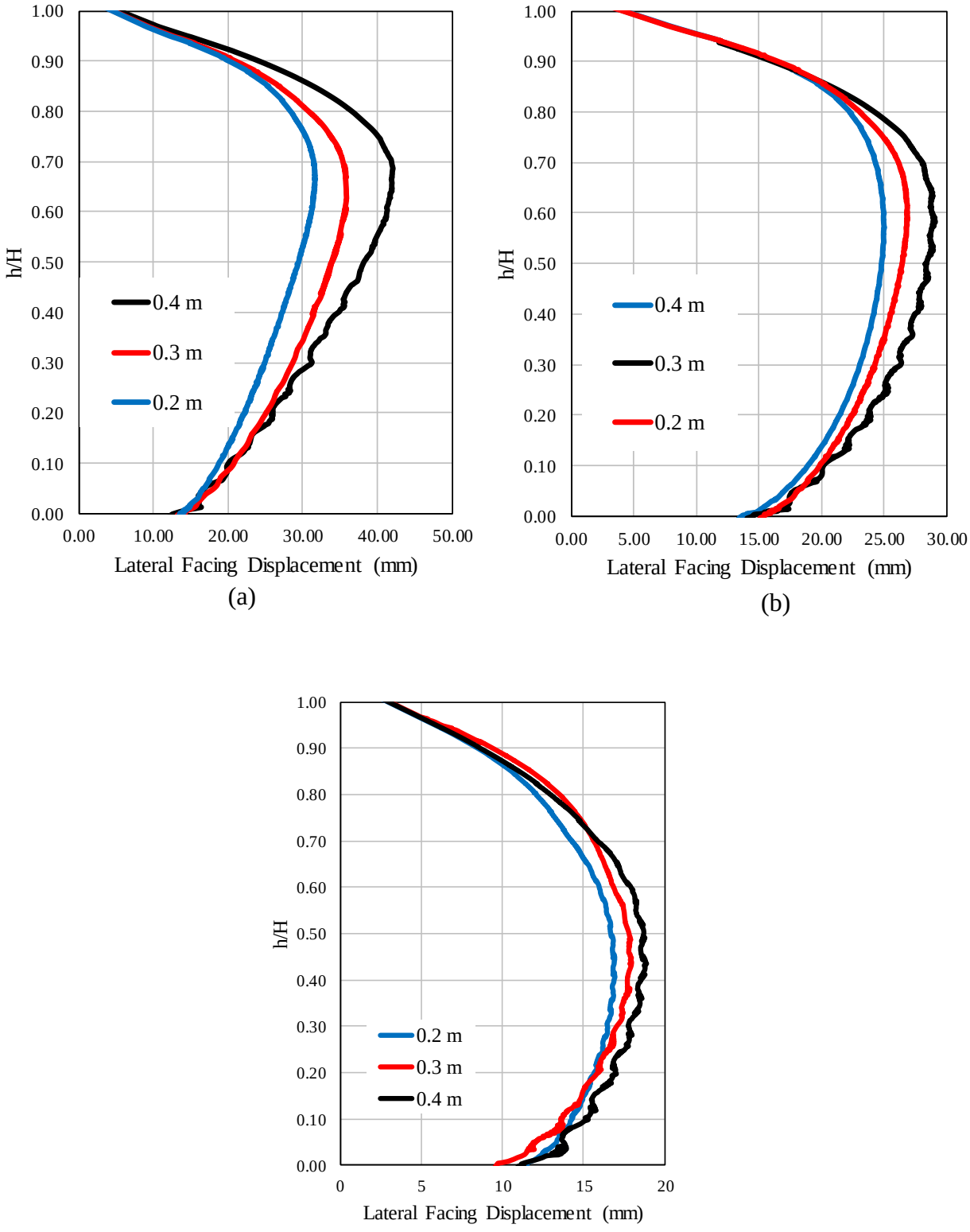

Figure 6.22. Effect reinforcement spacing on the lateral facing displacement geosynthetics subjected to different span lengths: a) 18.3 m; b) 27.4 m; and c) 36.6 m

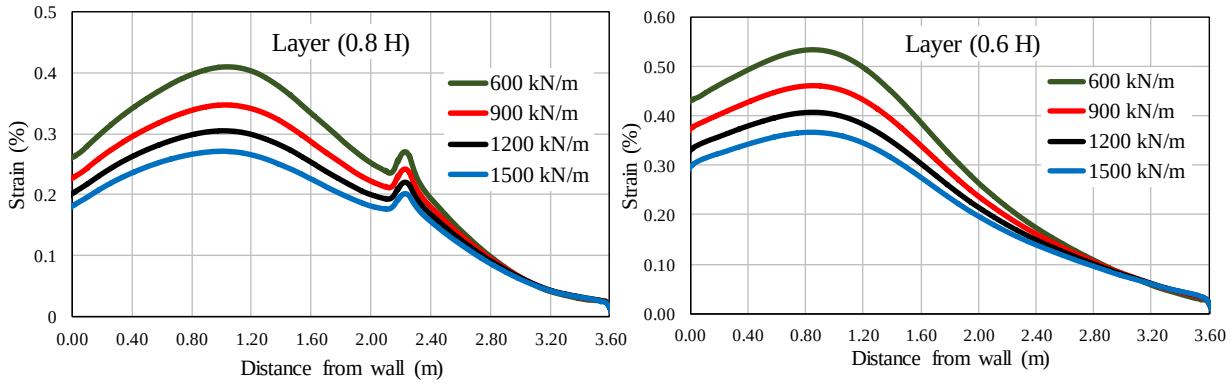

(a)

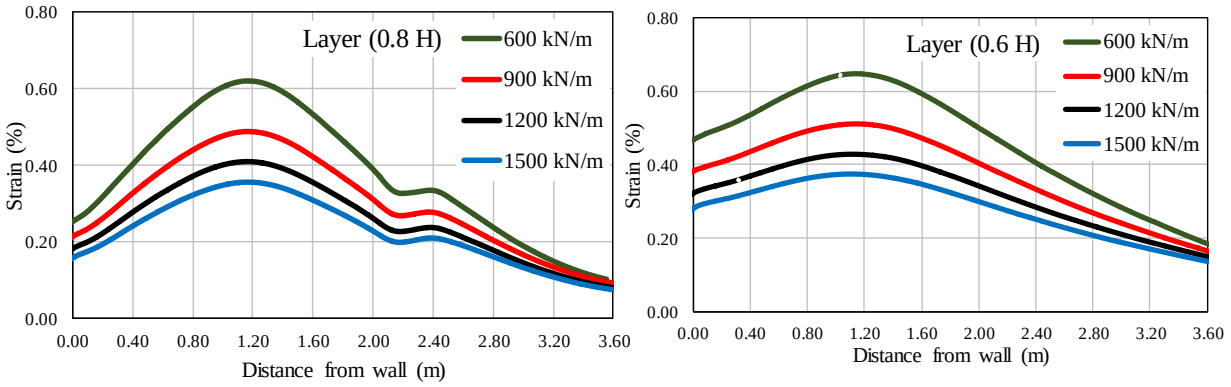

(b)

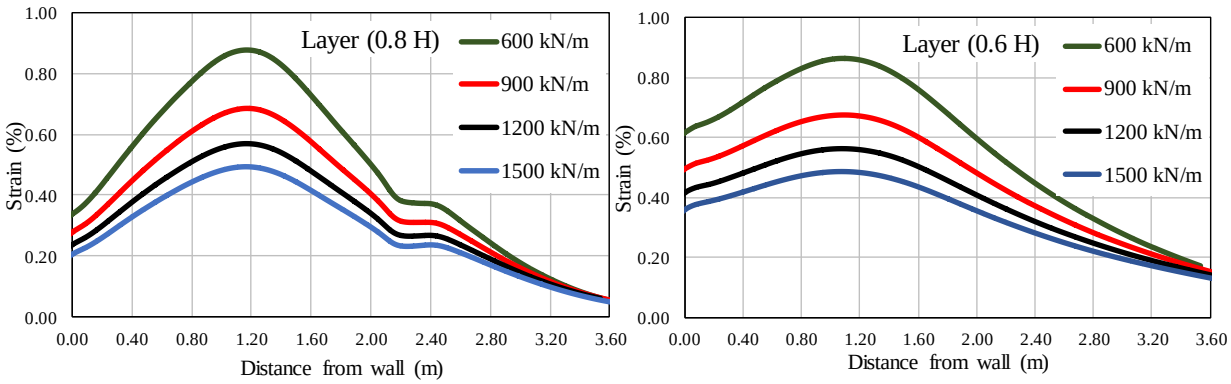

(c)

Figure 6.23. Effect of reinforcement stiffness on the strain distribution along geosynthetics subjected to different span lengths: a) 18.3 m; b) 27.4 m; and c) 36.6 m

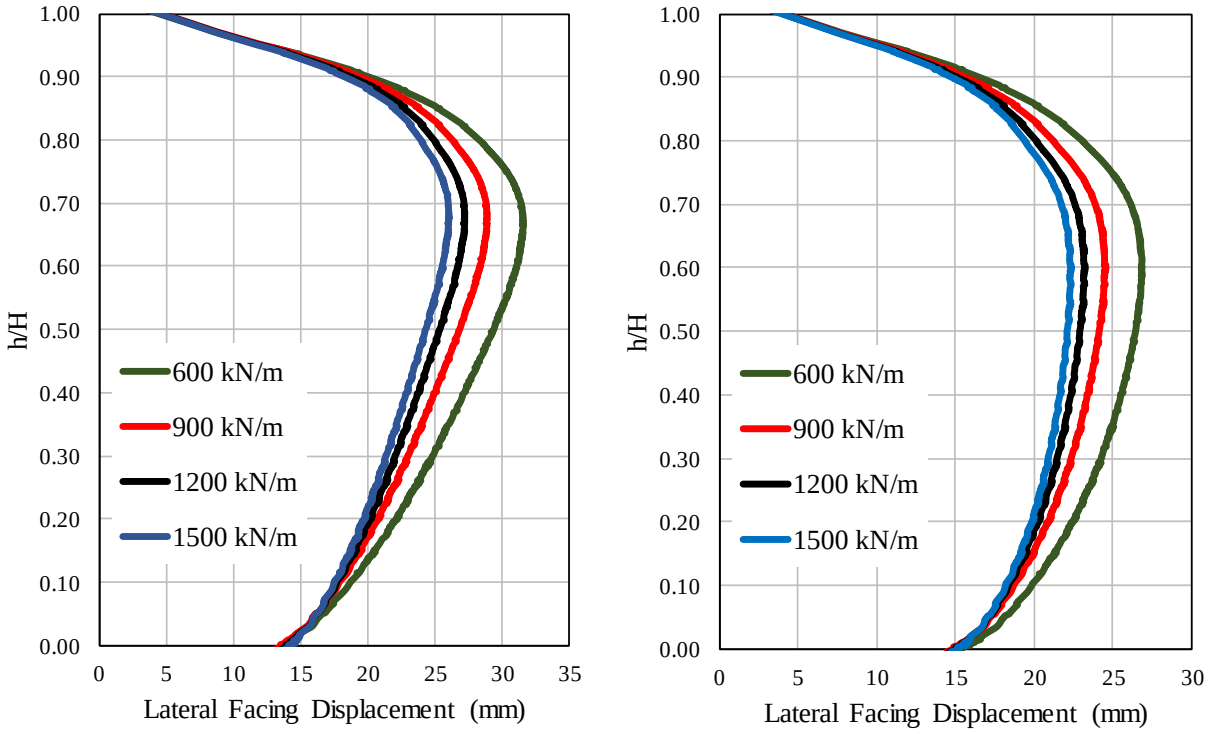

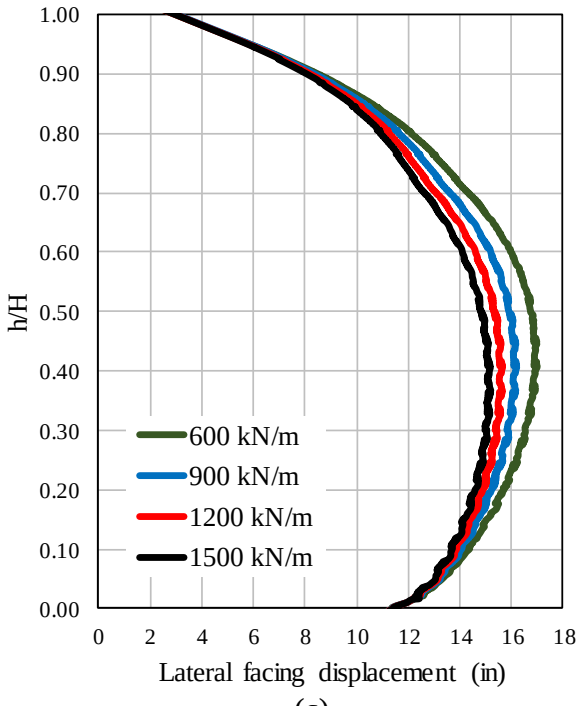

Figure 6.24. Effect reinforcement stiffness on the lateral facing displacement geosynthetics subjected to different span lengths: a) 18.3 m; b) 27.4 m; and c) 36.6 m

6.4.16 Relationship between reinforcement spacing and reinforcement strength

Figure 6.25 presents the effects of changing reinforcement spacing and reinforcement stiffness on the GRS-IBS performance in terms of lateral facing displacement. The results were plotted in terms of reinforcement stiffness/reinforcement spacing ratio in order to evaluate the relationship between the reinforcement stiffness and reinforcement spacing. It can be seen that the reinforcement spacing plays much greater role than reinforcement strength in the performance of the GRS-IBS for reinforcement spacing equal or higher than 0.2 m (e.g., with the same reinforcement stiffness/reinforcement spacing ratio of (=1500 kN/m^2). This is further confirmed by fixing the reinforcement stiffness/reinforcement spacing ratio to a value of 1500 kN/m^2 and changing the reinforcement stiffness and reinforcement spacing accordingly. The lateral facing displacement increased from 33 mm to 42 mm when both reinforcement spacing and reinforcement stiffness increased four times. This behavior is mainly attributed to the composite behavior created by the interface friction between the closely geosynthetic reinforcement layers and backfill materials as defined by Adams et al. (2011a), in which closer spacing results in suppressing dilation of backfill, increasing lateral confinement, and hence increasing the stiffness of backfill material. This means that the relationship between the reinforcement spacing and reinforcement strength is not one-to-one as considered in the GMSE design method, in which increasing the reinforcement strength has the same effect as a proportional decrease in the reinforcement spacing. However, it was noted that the reinforcement stiffness has close or slightly higher impact than the reinforcement spacing on the performance of the GRS-IBS in terms of lateral facing displacement for reinforcement spacing less than 0.2 m, which indicates that 0.2 m reinforcement spacing might be the optimum reinforcement spacing for GRS-IBS.

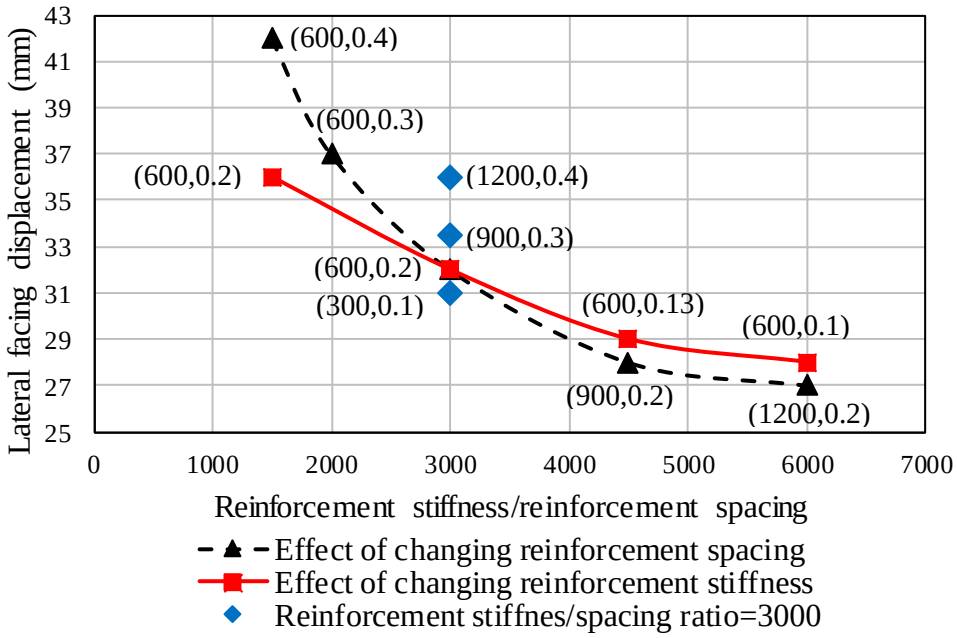

Figure 6.25. Effect of reinforcement stiffness and reinforcement spacing on the lateral facing displacement

6.4.17 Effect of Span Length and Abutment height on RSF settlement

Figure 6.26 presents the effect of the span length and the abutment on the profile settlement of the RSF. The figures indicate that RSF settlement is a function of span length and abutment height, in which the settlement of the RSF increases by increasing the span length and the abutment height. Figure 6.26a presents the effect of span length on the settlement of the RSF. It can be seen that the maximum settlement increases from 30 mm for a 12.2 m span length to around 46 mm for a 36.6 m span length for the same abutment height under the service loading condition. Figure 6.26b presents the effect of abutment height on the settlement of the RSF. The maximum settlement increases from 33 mm for an abutment height of 5.2 m to 43 mm for an abutment height of 9.15 m for the same span length under the service loading condition. Similar analysis was conducted to study the effect of the reinforcement spacing and reinforcement stiffness on the RSF settlement; it

was found that both the reinforcement spacing, and stiffness have a minor influence on the RSF settlement.

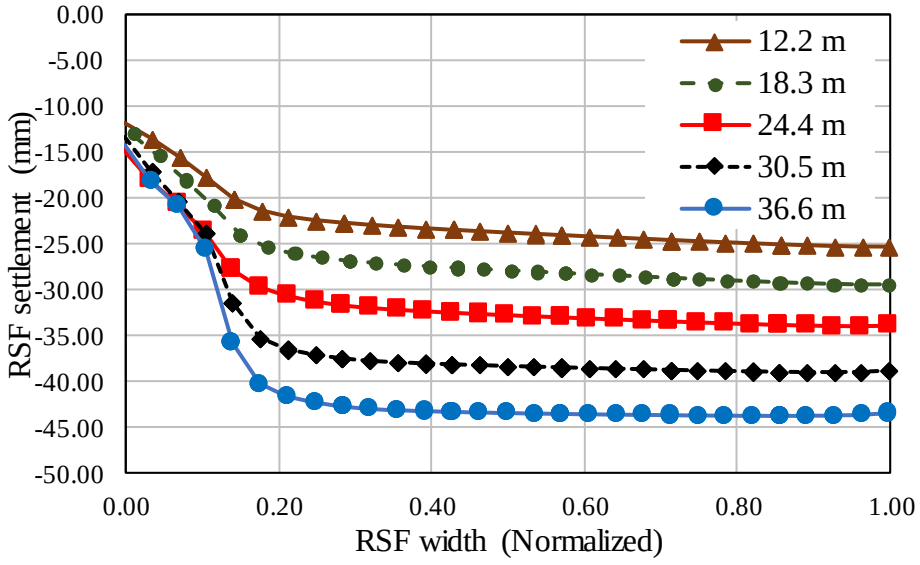

(a)

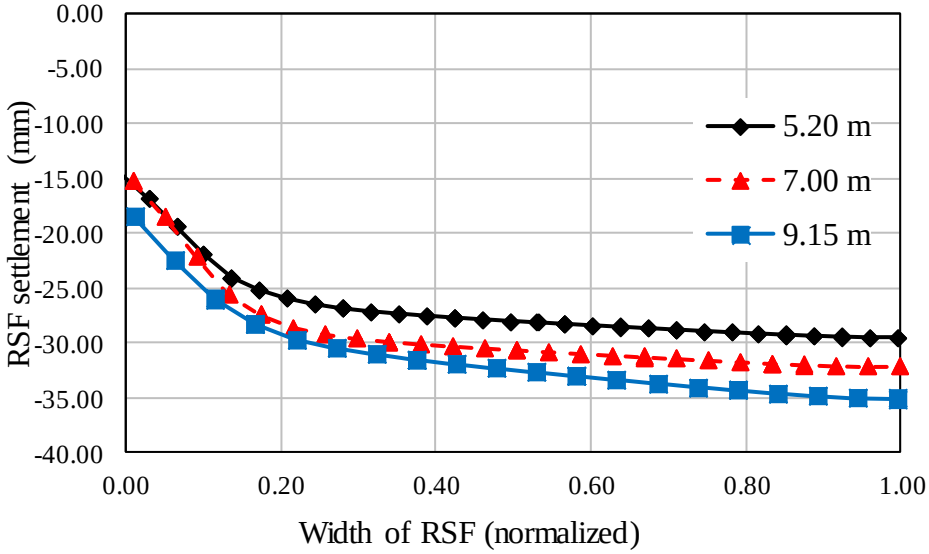

(b)

Figure 26. Effect of: a) span length; and b) abutment height on the RSF settlement

6.4.18 Location of Maximum Strain Envelope

Figure 6.27 presents the location of maximum strain envelope with depth for all cases. The figure depicts the potential failure envelope due to the effect of reinforcement spacing, reinforcement stiffness, and span length for the same height of 7m. It can be seen that the changing in reinforcement spacing, reinforcement stiffness, or span length does not affect the location of possible failure envelope. The location of maximum strain envelope indicates that the possible failure envelope developed from the inner edge of the footing extending vertically downward for the upper half of the bridge abutment and is followed by the general Rankine active failure envelope for the bottom half of the GRS-IBS abutment. This result is very similar to the punching shear failure envelope defined by a previous study conducted by Chen et al. (2009) on reinforced crushed limestone underneath spread footing. Takemura et al. (1992) investigated the failure mechanism of reinforced sand by using centrifuge test. Their results showed that the intensely shear bands were developed from the edges of the footing and is extending vertically downward. For the purpose of comparison and verification, the results were compared with the active Rankine failure envelope as shown in Figure 6.27. It is interesting to note that the results indicate that the failure envelope is a combination of punching shear failure envelope (top) and Rankine failure envelope (bottom), in which the failure envelope is developed under the inner edge of the footing and extending vertically downward to intersect with the Rankine active failure envelope.

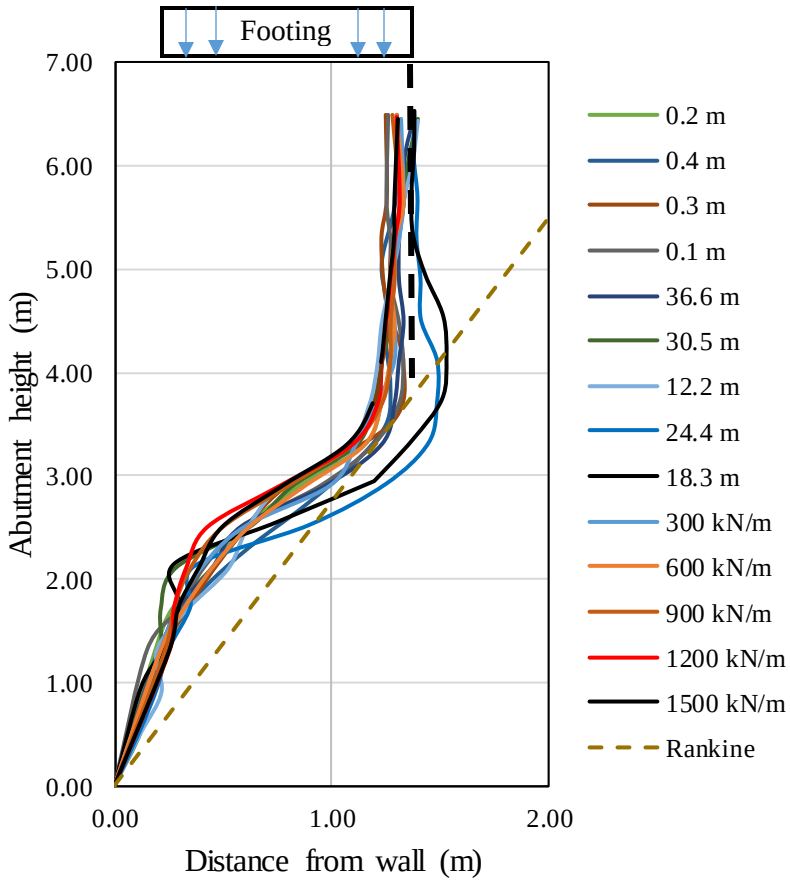

Figure 6.27. Effect of span length, reinforcement spacing, reinforcement stiffness, and abutment height on the maximum strain envelope

6.5 Effect of Differential Settlement

6.5.1 Introduction

Wu et al. (2014) developed a finite element model to investigate the composite behavior of closely spaced reinforcement soil. They conducted a FE parametric study to study the effect of the reinforcement spacing, reinforcement stiffness, and soil stiffness on the volume change behavior (soil dilation). They found that the inclusion of geosynthetic will serve to suppress the soil dilation and lead to a stronger soil and zero volume change assumption, which has been adopted by the FHWA for estimating the lateral deformation of GRS abutment. Zheng and Fox (2017) conducted

another parametric study to investigate the effect of reinforcement stiffness, bearing bed reinforcement, height of the bridge abutment, and bridge load on the lateral deformations and bridge seat settlement. They found that the reinforcement stiffness, bridge load, and the abutment height are the most significant factors on the performance of the GRS-IBS under static loading. It was noticed that the abutment vertical strain decreases with increasing the abutment height due to higher stress conditions and larger soil stiffness for taller abutments.

However; only one case study was conducted by (Kost et al., 2015) to describe the behavior of the GRS-IBS subjected to differential settlements. The differential settlement between the bridge abutment and the approach embankment might be caused by compressible foundation soils or scour. Scour can be defined as the erosion caused by the water of the soil surrounding the bridge abutment or foundation. For more information about the scour causes, design, and evaluation, the reader can refer to (Arneson et al., 2012). A relatively small differential movement produced the common "bump at the end of the bridge," which is unpleasant and often hazardous to the motoring public (Zhang and Hu, 2007). (Kost et al., 2015) conducted a field-scale experiment to examine the response of the GRS abutment to differential settlement. Their experiment lacked integrated approach; instead, a surcharge loading was applied on top of the GRS abutment. The differential settlement was assumed to be located under the edges of the GRS abutment. A 200 mm differential settlement between the edges was assumed under an 83.8 kPa surcharge loading. They found that a GRS abutment can tolerate a relatively large differential settlement under service loading conditions. Review of literature showed that the allowable differential settlement (bump) at the intersection between the bridge span and the approach roadway should range between 15-30 mm (e.g., Zaman et al., 1993). Stark et al. (1995) and Long et al. (1998) considered that a differential settlement of 50-70 mm would create a serious riding comfort issue.

6.5.2 Finite Element Model

The two-dimensional finite element program PLAXIS 2D (Brinkgreve et al., 2014) was used for the current study. Data used for validation of the analysis was obtained from the Maree Michel GRS-IBS Bridge in Louisiana (Figure 6.28) (Saghebfar et al., 2017b). The numerical model was successively developed and verified to simulate the lateral facing displacement, settlement of the RSF, horizontal and vertical stresses, and the strain distribution along the reinforcement under different loading conditions. The simulated results were in good agreement with those obtained from the field measurements (Ardah et al., 2017, 2018). Ardah et al. (2017) concluded that the 2D FE analysis can be used to predict the performance of the GRS-IBS under service loading conditions.

In this study, the configuration of the GRS-IBS numerical model is selected according to the FHWA design criteria recommendation (Adams et al., 2011a). Figure 6.29 presents the configuration of the GRS-IBS model that was adopted for this study. Mesh optimization technique was first conducted, in which the mesh size adopted has no or negligible effect on the predicted results. The dimensions of the model domain were selected far enough to minimize the effect of boundary conditions on the model response. A roller support was selected to prevent the horizontal movement in the x-direction, and bin support was selected to prevent both the horizontal and vertical movement in the x and y-direction.

According to (Adams et al., 2011a), the height of bridge abutment H should be initially selected with a minimum span length, L_{span}, of 7.62 m, and a minimum base width, B_{total}, of 1.83 m or 0.3H. The width of the reinforced soil footing (RSF) $Brsf$ is equal to B_{total} + 0.25B_{total}, and the depth of the RSF D_{rsf} will be equal to 0.25 B_{total}. The setback distance between the back of the face and the footing a_b should be equal to 200 mm. The minimum clear space d_e, the distance from the

top of the facing block to the bottom of the superstructure, should be equal to 76mm or 2% of the abutment height, whichever is greater. The width of the beam seat (strip footing in this study) b was selected equal to 1.22 m with a thickness of 0.61 m (note that the minimum width of the beam seat for a span length greater than 7.62 m is 0.76 m and the minimum thickness is 200 mm). The minimum reinforcement length L_r at the bottom of the bridge abutment should be 0.3H or B_{total}, whichever is greater, and increase linearly up to 0.7H. The bearing bed reinforcement zone was extended from the top reinforcement layer for six consecutive layers. The length of the bearing bed reinforcement is selected to be L_{rb}, equal to $2a_b+b$, assuming the bridge span to depth ratio = L_{span}/D = 24 as reported by (Zheng and Fox, 2017). The finite element mesh with geometry and boundary conditions for the GRS-IBS are presented in Figure 6.29.

Figure 6.28. Maree Michel GRS-IBS Bridge

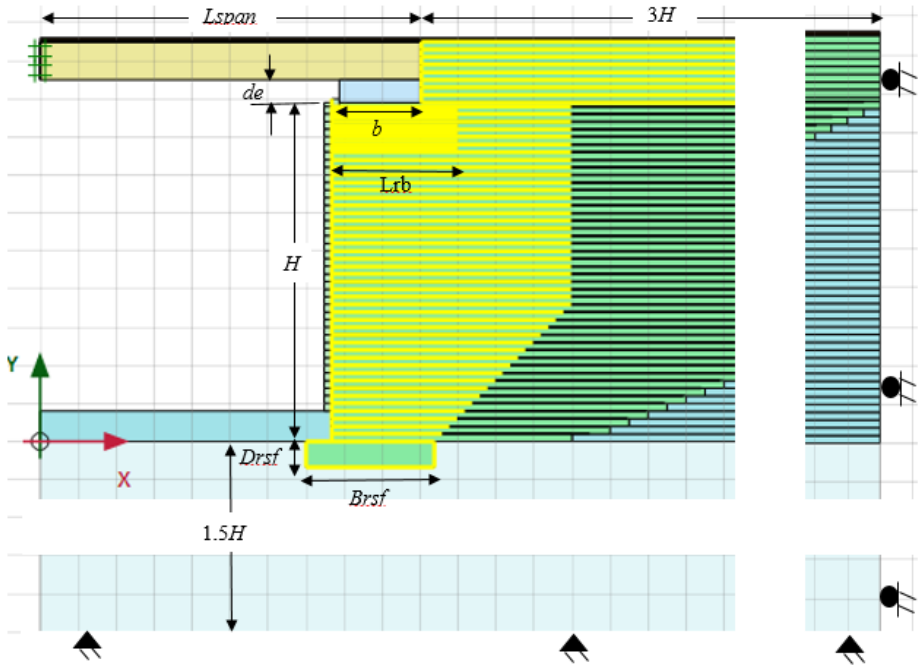

Figure 6.29. GRS-IBS numerical model geometry and boundaries conditions

The selected constitutive model's materials properties are listed in Table 1. The triaxial and large direct shear testing method were conducted to evaluate the strength and stiffness of the backfill materials properties. A total of three triaxial testing were conducted at three different confining pressures of 207, 345, and 483 kPa for a soil specimen size of 15.24 cm diameter and 30.48 cm height. Six large direct shear tests having with dimension size of 30.48 × 30.48 × 15.24 cm were conducted to evaluate the strength properties and the interface friction angle between the geosynthetic and the backfill/facing block materials. The tests were conducted under normal stresses of 48.3, 120, and 191.7 kPa, which results in peak stresses of 83.5, 144, and 260 kPa, respectively. The dilation angle was estimated using the following reference (Bolton, 1986);

$$\phi_p = \phi_{cr} + 0.8\psi$$

where ϕ_p = peak friction angle = 51°; ϕ_{cr} = critical state friction angle = 34°; ψ = dilation angle.

The foundation soil properties were evaluated using the results of in-situ cone penetration test (CPT). The geosynthetic and facing block properties were provided by the manufacturer.

The built-in hardening soil model developed by Schanz et al. (1999) was selected to simulate the backfill materials. The model is capable of simulating the deformation behavior, soil dilation, non-linear stress-strain behavior, and also accounts for stress history under service stresses successively (Wu et al., 2014; Mirmoradi and Ehrlich, 2014a; Zheng and Fox, 2017; Ardah et al., 2017). Formulation and verification of the hardening soil model is well described by Schanz et al. (1999). The zero thickness interface elements with the combination of Mohr-Coulomb frictional criterion model were used to simulate the facing/block backfill-geosynthetic interaction. These interfaces have properties of friction angle, cohesion, dilation angle, tensile strength, Young's modulus (E), and Poisson's ratio (ν). These values were set using a reduction factor (R_i) option available in PLAXIS, in which a reduction factor is applied to the backfill materials (note that a default value of the reduction factor $R_i = 1.0$). In this study, a reduction factor equal to 0.8 was selected similar to a previous study by (Ardah et al., 2017; Abu Farsakh et al., 2017; Abu Farsakh et al., 2018a, b, c). For more details about modeling the interfaces in PLAXIS or FLAC, the reader can refer to (Yu et al., 2015). The linear elastic model was selected to simulate the geosynthetic and the facing block materials and the Mohr-Coulomb model was selected to simulate the foundation soil. The 15-noded triangle element option available in PLAXIS was selected to simulate the soil layer, the facing block, and the bridge span. A compatible 5-noded geogrid element was set by default to represent the geosynthetic reinforcement materials with a correspondent 5-pairs of nodes to represent the zero-interface element. A special feature available in PLAXIS called a prescribed displacement was used in this study to simulate the differential settlement under the RSF, the reinforced-zone, and the retained soil. In this approach, the intended

surface is subjected to a prescribed displacement in the y-direction where the rest of the model remains unchanged which creates a differential settlement.

This feature is used to simulate a special condition that can be imposed to a specific area to control the displacement. The total height of the GRS-IBS wall was divided into subsequent layers to simulate the field construction process by using the staged construction mode in PLAXIS 2D 2016, which allows for simulation of construction and excavation processes. A 63 kPa distribution load at the top and bottom and exposed faces of each soil layer was applied during the staged construction process to simulate the soil compaction. This approach is based on the procedure introduced by Dantas (2004) and Morrison et al. (2006) to consider the induced stress on the backfill soil due to compaction, which was also adopted later by Ehrlich and Mirmoradi (2013), Mirmoradi and Ehrlich (2014 a, b), and Riccio et al. (2014).

6.5.3 Control Sections

For comparison purpose, to evaluate the effect of differential settlement applied at certain locations, a control section was first developed and evaluated without imposing any differential settlement. Three numerical models having span length of 24.4, 30.5, and 36.6 m having a span depth of 110.64, 138.38, and 166.11 cm; bridge abutment height of 5.18 m, and 200 mm reinforcement spacing subjected to a uniformly distributed live load of 12 kPa were considered as the control sections. The girder was modeled as a solid block ($L_{span} \times D \times 1$), assuming the bridge span to depth ratio = L_{span}/D = 24, composed of elastic elements with an equivalent unit of 11.86 kN/m^3. This procedure was adopted from previous work by (Zheng and Fox, 2017). The RSF dimensions are 45.72 by 230.124 cm for all cases.

6.5.4 Effect of Differential Settlement on A 36.6 M Span Length

In this analysis, four differential settlements of 50, 100, 150, and 200 mm were imposed underneath the RSF, underneath the reinforced zone including the RSF, and underneath the retained soil to evaluate the effect of the location on the performance of the GRS-IBS. The results were evaluated in terms of lateral facing displacement and strain distribution value.

6.5.5 Effect of Differential Settlement under the RSF (CASE 1)

Four different values of differential settlement of 50, 100, 150, and 200 mm were considered underneath the RSF, in which only the RSF is subjected to a prescribed displacement while the rest of the model is unchanged. Figure 6.30 presents the effect of the differential settlement on the strain distribution along the geosynthetic at four different locations of 20%, 40%, 60%, and 80% of bridge abutment height (*H*) from the top of the RSF. It can be seen that a differential settlement underneath the RSF has a high impact on the strain distribution. The maximum strain value obtained is 1.4% under 50 mm differential settlement at 40% of bridge abutment height from the top of the RSF and decreases to 0.5% under 150 mm differential settlement at the same location. The lateral facing displacement increases from 28 mm under a differential settlement of 50.8 to 42 mm under 150 mm as shown in Figure 6.33a. It was noted that the lower reinforcement layers are highly affected by the differential settlement underneath the RSF. It can be seen that the at the right edge of the RSF, which is located 18.3 m away from the GRS abutment face, has a high impact on the strain distribution associated with those reinforcement layers located at the bottom of the GRS abutment. It was noted that the maximum strain value increases when the RSF is subjected to a differential settlement of 50 mm and decreases when subjected to a differential

settlement higher than 100 mm. This can be explained by achieving better mobilization of the reinforcements with increasing the settlement (Chen et al., 2009).

6.5.6 Effect of differential settlement under the Reinforced-Zone including the RSF (CASE 2)

The same procedure was followed is this case using the same numerical model and same loading conditions (36.6 m span length) to evaluate the performance of the GRS-IBS subjected to a differential settlement under the reinforced zone including the RSF. It was noted that the strain increases under a 50 mm of differential settlement and decreases when the abutment subjected to a differential settlement higher than 100 mm as shown in Figure 6.31. This is because the reinforcement zone including the RSF is subjected to the same displacement while in case 1 the reinforcement zone was subjected to a partial displacement under the RSF. The lateral facing displacement increases from 28 mm under a differential settlement of 50 mm to 38 mm under a differential settlement of 200 mm as shown in Figure 6.33b.

6.5.7 Effect of differential settlement under the Retained-Soil (CASE 3)

In this case, the retained soil was assumed to be subjected to the differential settlement due to special soil conditions underneath it under the same loading conditions in cases 1 and 2. It can be seen in Figure 6.32 that the differential settlement has a low impact on the strain distribution value and shape as it does on the lateral facing displacement in Figure 6.33c. It was noted that the differential settlement underneath the retained soil caused a rotational behavior for the lateral facing deformation. The lateral facing displacement at the bottom of the GRS abutment increases from 3.5 mm under a differential settlement of 50 mm to 10 mm under a differential settlement of 100 mm and to 29 mm under a differential settlement of 200 mm.

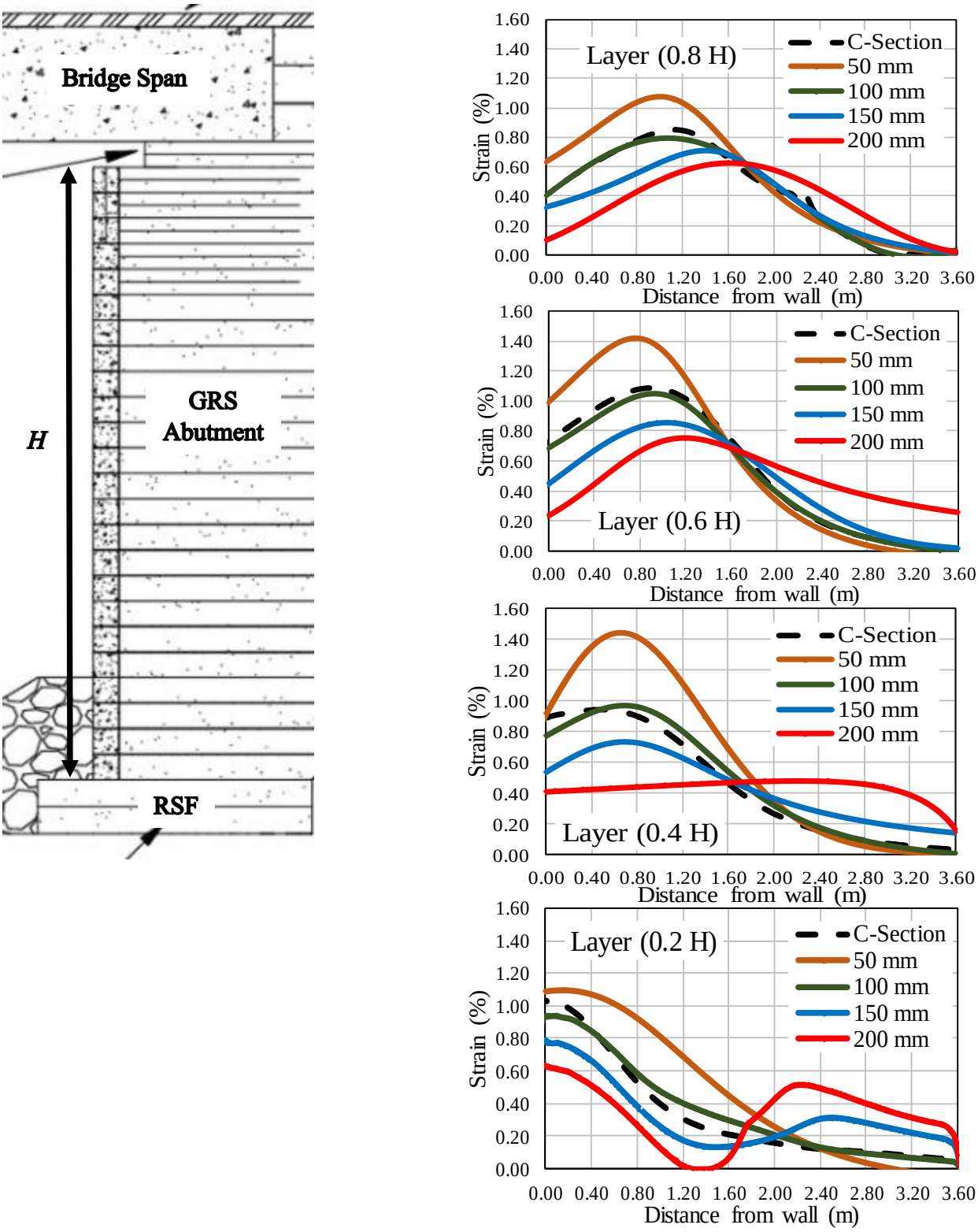

Figure 6.30. Effect of differential-settlement of the RSF on the strain distribution along geosynthetics for a span length of 36.6 m

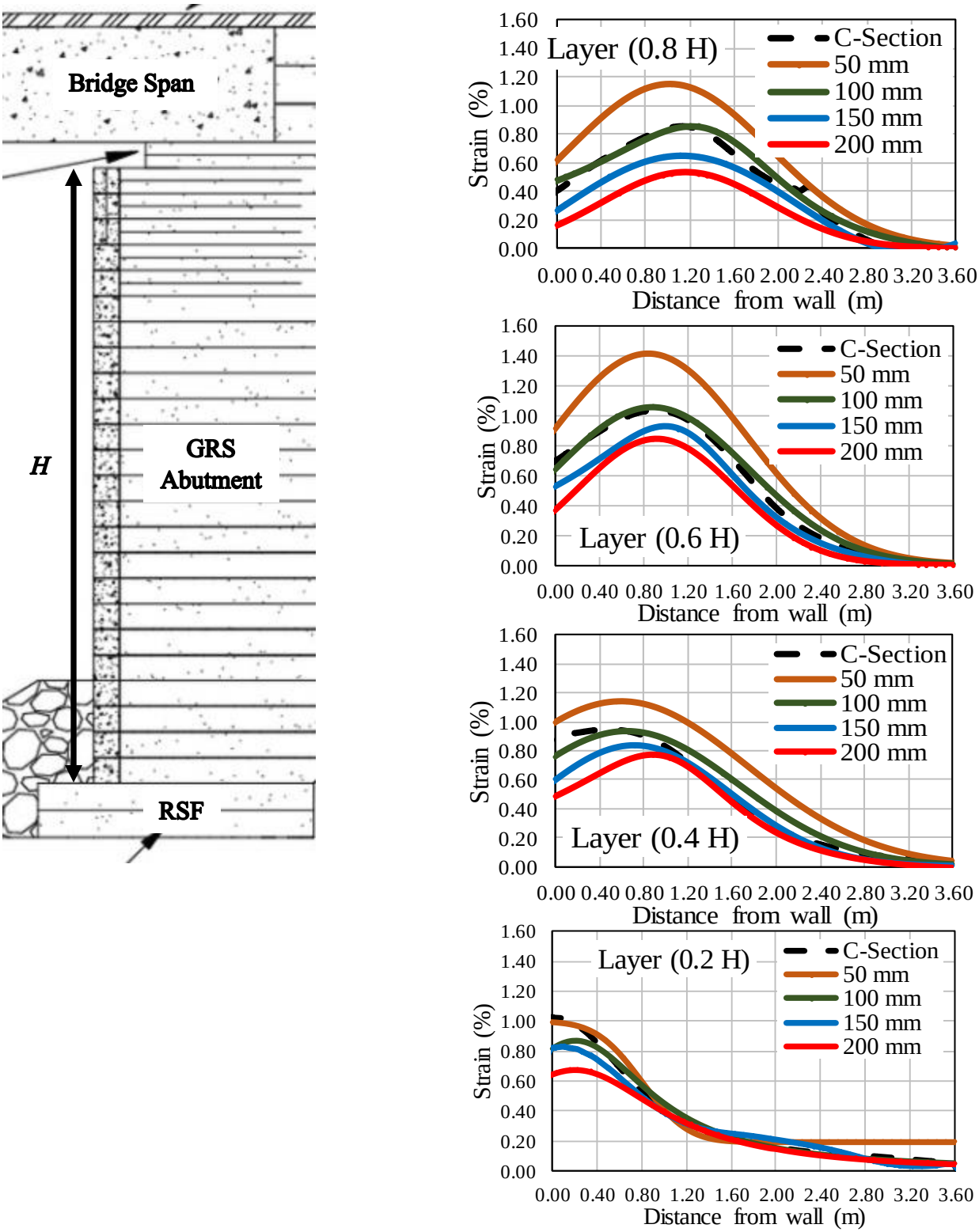

Figure 6.31. Effect of differential-settlement of the reinforced-zone on the strain distribution along geosynthetics for a span length of 36.6 m

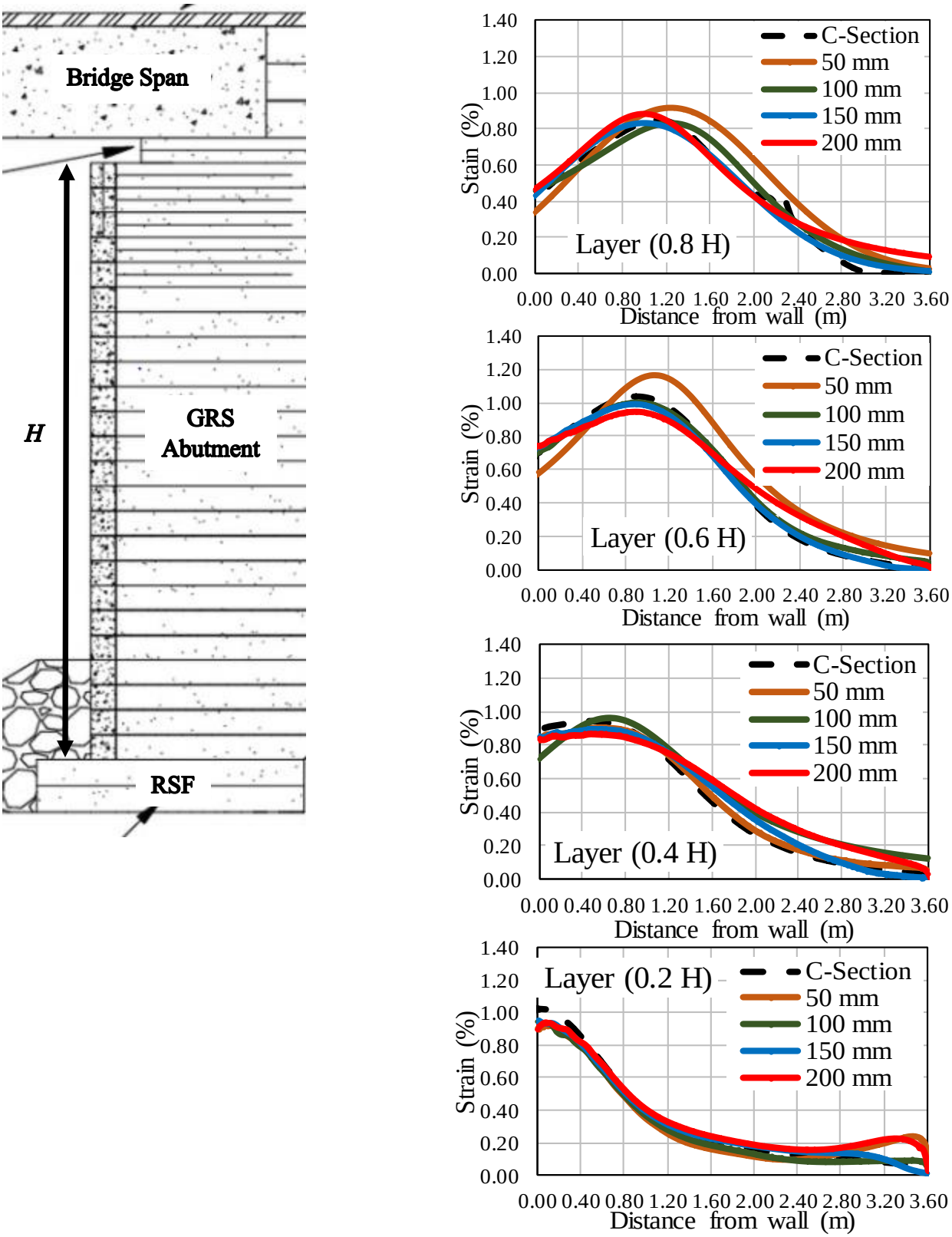

Figure 6.32. Effect of differential-settlement of the retained soil on the strain distribution along geosynthetic for a span length of 36.6 m

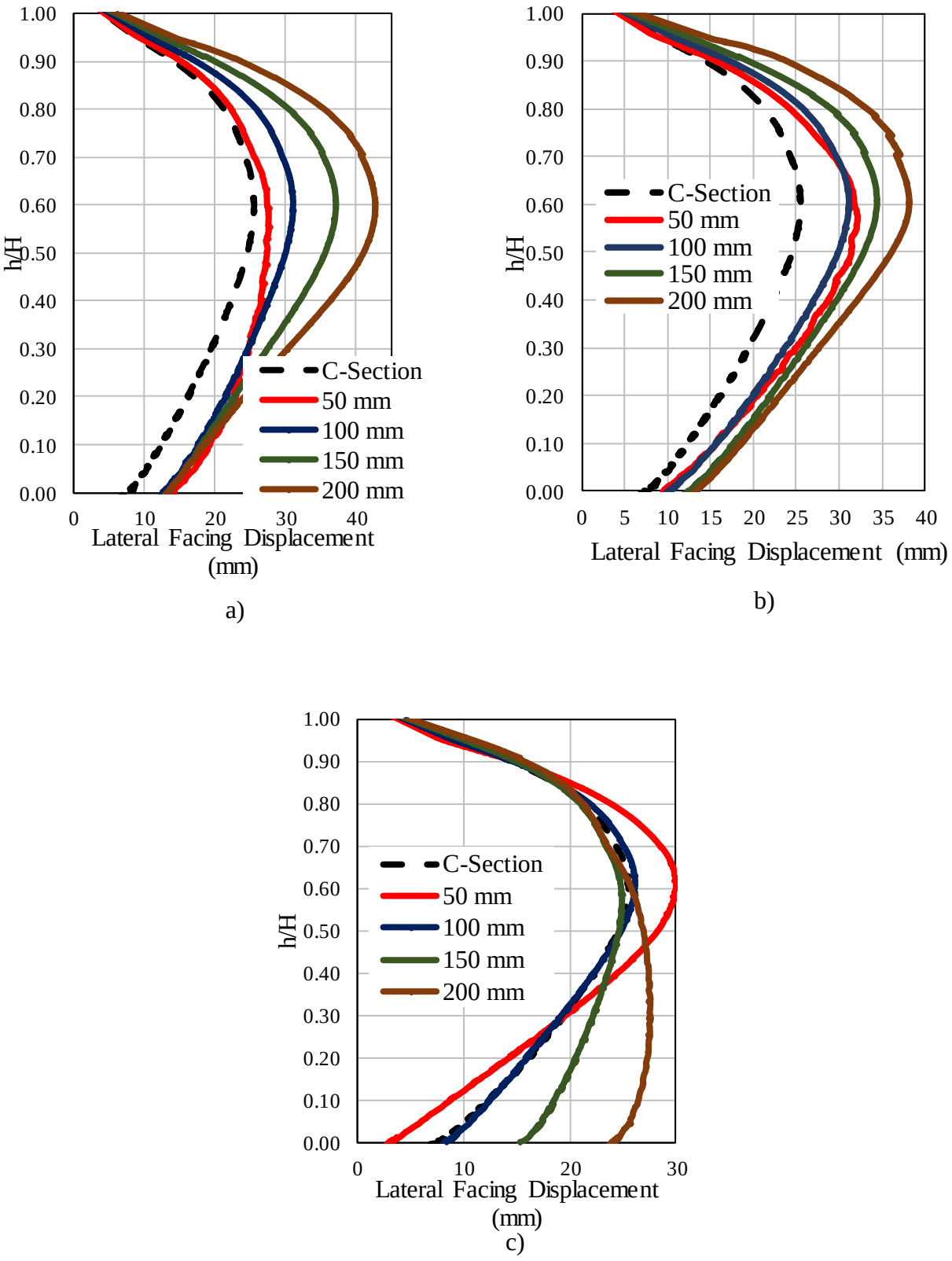

Figure 6.33. Effect of differential-settlement of: a) the RSF; b) the reinforced zone; and c) the retained soil on the lateral facing displacement for a span length of 36.6 m

6.5.8 Effect of Differential Settlement underneath the Reinforced-Zone for Different Span Lengths (Case 2)

The combination effects of differential settlement and span length on geosynthetic strain distribution and lateral facing displacement were investigated for case 2 differential settlement. In this case, the reinforced zone including the RSF was subjected to a differential settlement of 50, 100, 150, and 200 mm, and was analyzed for span lengths of 24.4 m, 30.5m, and 36.6 m.

Similar trend was observed due for all differential settlements, but with different values associated with the span lengths of 24.4, 30.5, and 36.6 m. Figures 6.34 and 6.35 present the strain distribution along the geosynthetic at four different locations at 20, 40, 60, and 80% of the bridge abutment height from the top of the RSF. It can be seen in Figure 6.34 that the maximum strain value increases by applying a 50 mm differential settlement under the reinforced zone and decreases when the differential settlement exceeds 100 mm. The maximum strain value decreases from 1.4% under 50 mm differential settlement at 40% height of the bridge abutment from the top of the RSF for a span length of 36.6 m to 0.9% and 0.7% under the same conditions for the span length of 30.5 and 24.4 m, respectively. Figures 6.36a & b present the effect of the differential settlement for different span lengths on the lateral facing deformation. It can be seen that the differential settlement accompanied with the span length has a high impact on the lateral facing deformation, in which the lateral facing deformation increases by increasing the differential settlement value and the span length. The lateral facing deformation decreases from 38 mm for a span length of 36.6 m to 33 and 28 mm for span lengths of 30.5 and 24.4 m, respectively, under 200 mm differential settlement. It can be concluded that the differential settlement accompanied with the different span lengths have a high impact on the GRS-IBS performance in terms of strain distribution and lateral facing deformation.

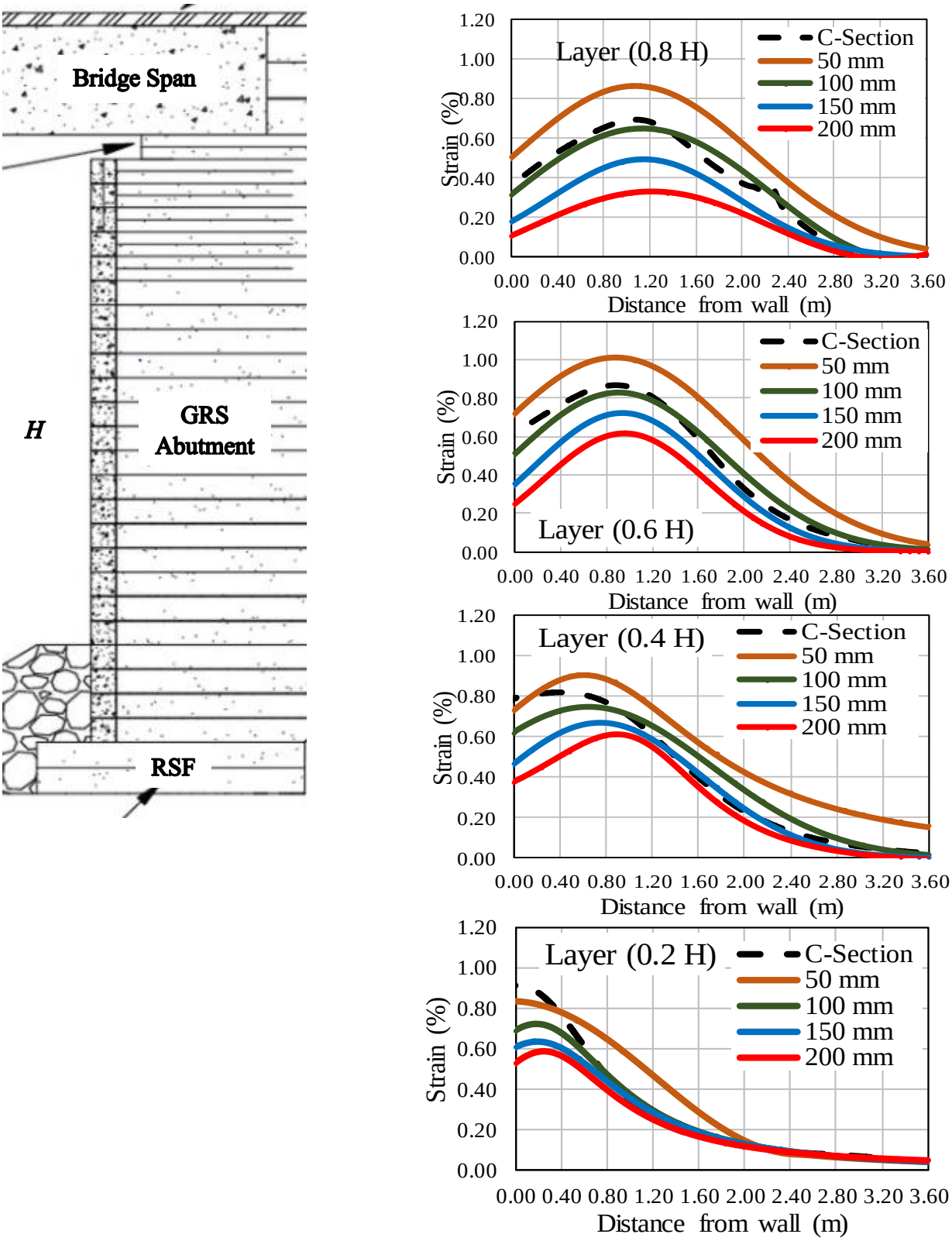

Figure 6.34. Effect of differential-settlement of the reinforced-zone on the strain distribution along geosynthetics for a span length of 30.5 m

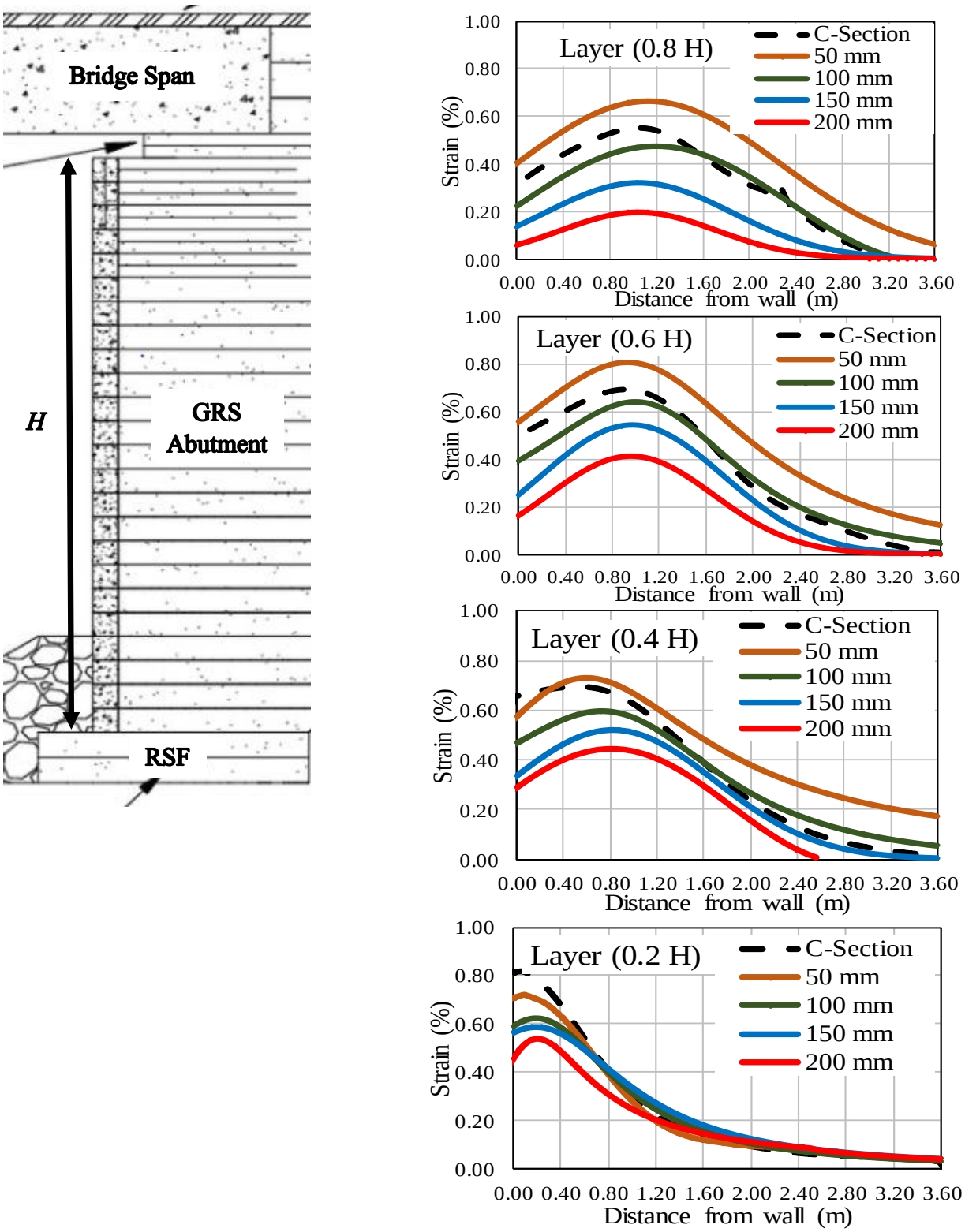

Figure 6.35. Effect of differential-settlement of the reinforced-zone on the strain distribution along geosynthetics for a span length of 24.4 m

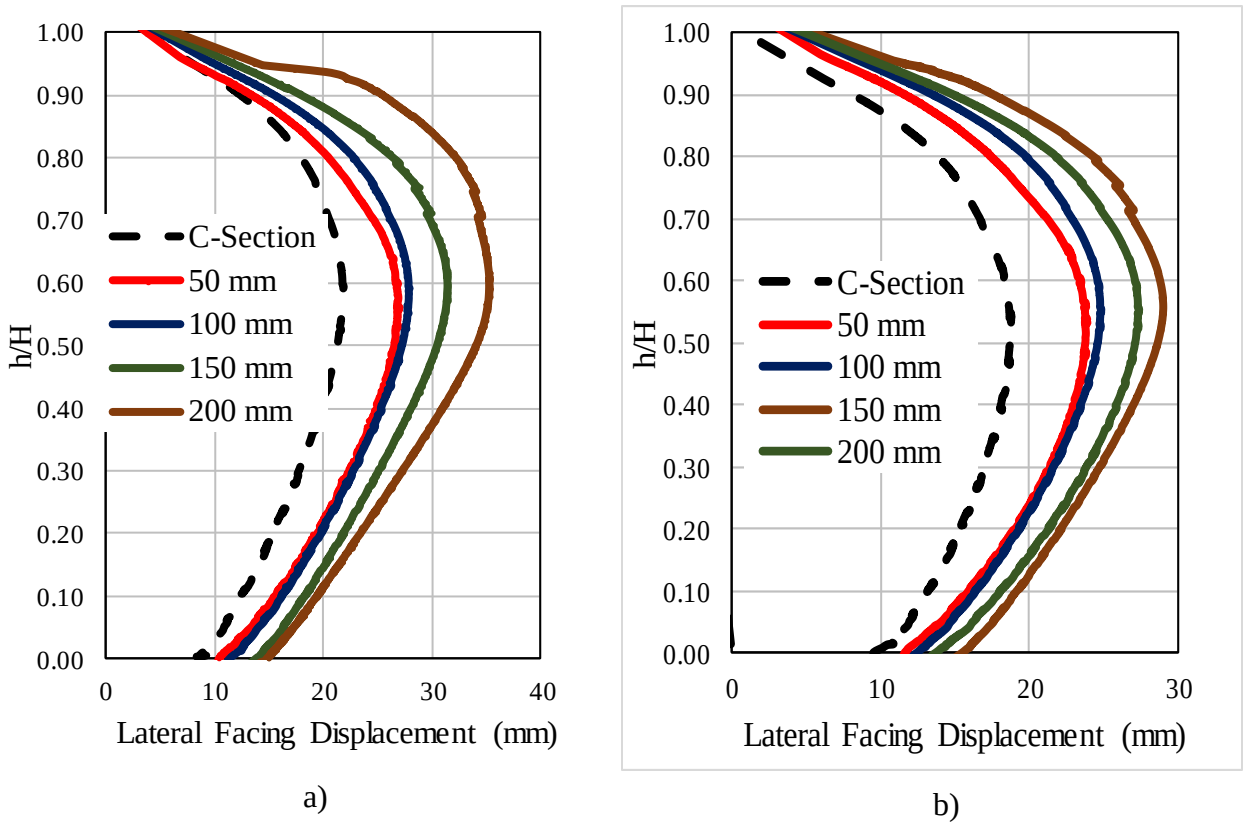

Figure 6.36. Effect of differential-settlement of the retained soil on the lateral facing displacement for a span length of: a) 30.5 m; and b) 24.4 m

6.5.9 Effect of Differential Settlement on the Bump at the Bridge Slab and Approach Roadway Intersection

One of the main advantages of the GRS-IBS is alleviating the bump at the intersection between the bridge span and the approach roadway. Figure 6.37 a and b present the effect of the differential settlement underneath the RSF and underneath the reinforced zone including the RSF on the bump at the bridge slab-approach roadway intersection for three different spans length of 24.4, 30.5, and 36.6 m. It can be seen that the bump at the bridge is proportional to the differential settlement value, in which the bump increases by increasing the differential settlement under both the RSF and the reinforced zone. The maximum bump at the bridge for a span length of 36.6 m under a differential settlement of 200 mm underneath the RSF is 18 mm, which is below the allowable differential settlement of 15-30mm as was documented in previous literature (e.g., Zaman et al.,

1993; Stark et al., 1995; Long et al., 1998). However, the differential settlement underneath the reinforced zone is highly affected the bump value. It can be seen that a 200 mm differential settlement underneath the reinforced zone for a span length of 36.6 m caused 53 mm bump at the intersection of the bridge slab and the approach roadway. This bump value is higher than the allowable bump as documented in the literature. It can be concluded that a differential settlement up to 150 mm accompanied with a bridge span up to 30.5 m underneath the reinforced zone subjected for surface loading will not create a serious riding comfort issue. However, care must be taken in case of a bridge span higher than 30.5 m built on weak or special soils near water as recommended by Adams et al. (2011a) that if the bridge is crossing water, the GRS-IBS should not be considered unless scour effect is properly addressed.

6.5.10 Effect of Differential Settlement on Lateral Facing Pressure

Another issue that must be addressed here is the effect of differential settlement underneath the reinforced including RSF on the lateral facing pressure. Since the GRS-IBS facing is not considered as a structure element due to the composite behavior of the closely reinforced soil, the lateral facing pressure values are expected to be very small (Adams et al., 2011a; Ardah et al., 2017). For the four of differential settlements underneath the reinforced zone considered in this study, the most critical case was found to be for the bridge span length of 36.6 m. Figure 6.38 presents the effect of differential settlement underneath the reinforced zone including the RSF on lateral facing pressure for a bridge span of 36.6 m under service loading condition. It can be seen that the differential settlement has a medium impact on the lateral facing pressure. It was noted that the top of the GRS-IBS abutment is the most effected location, in which the lateral facing pressure decrease by increasing the differential settlement except for 50 mm differential settlement. The lateral facing pressure decreases from 13.8 kPa for the control section to 6.9 kPa

for 200 mm differential settlement and increase to 21 for 51 mm differential settlement. It can be concluded that that the recommendation about inserting pin in the top facing blocks by Adams et al. (2011a) is a must in designing the GRS-IBS bridge abutment.

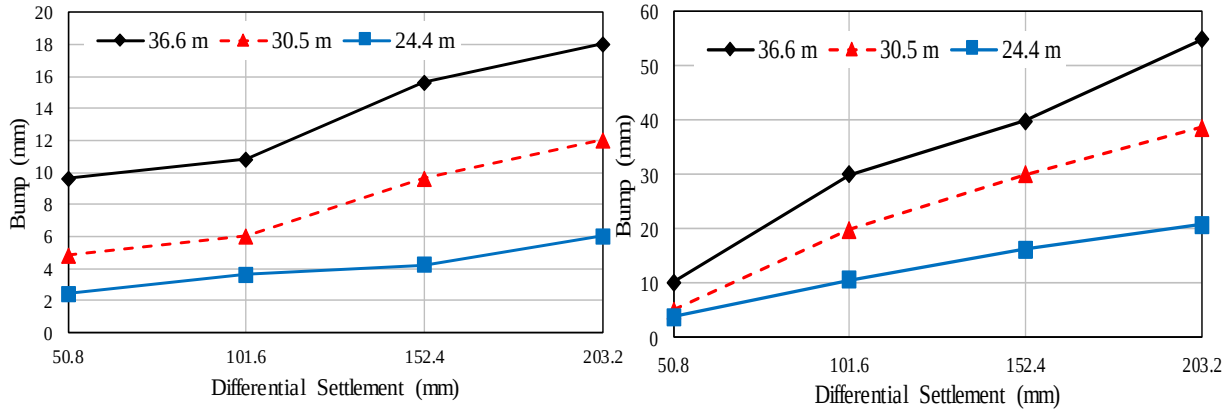

Figure 6.37. Effect of differential settlement on the bump at the intersection between the bridge slab and the approach roadway for different span lengths: a) underneath RSF; b) underneath reinforced zone

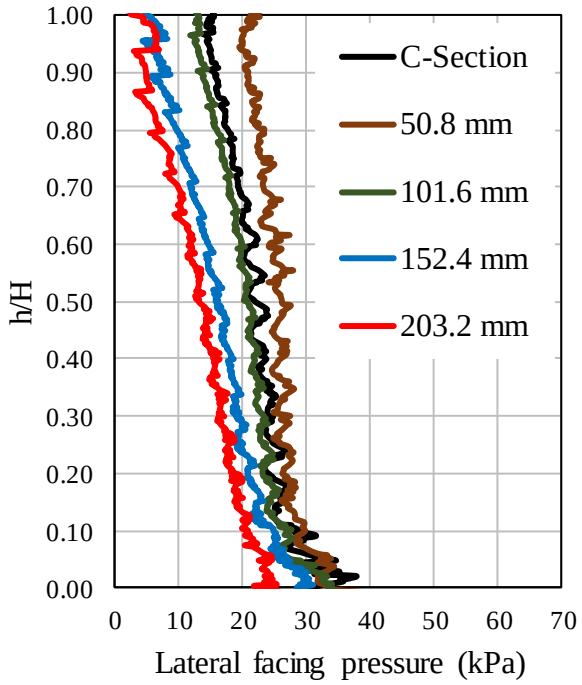

Figure 6.38. Effect of differential settlement on lateral facing pressure for a bridge span of 36.6 m under service loading condition.

Chapter Seven
Analytical Models for Evaluating Composite Strength Properties, And Required Reinforcement Strength

This chapter describes analytical models for evaluating strength properties of a GRS-IBS mass, required tensile strength of reinforcement in the design of GRS structures, and potential failure envelope that can be used for pullout capacity design. The analytical model is for the determination of reinforcement strength in design. This model was developed based on the MSE walls model (Berg et al., 2009). To account for the composite behavior, relationship between reinforcement strength and reinforcement spacing, the active lateral earth pressure coefficient was modified by using the composite friction angle of the reinforced soil instead of using the internal friction angle of the backfill materials only as adopted in MSE walls (Berg et al., 2009).

The lateral pressure at any depth can be divided into two different pressures depending on the applied loads, where σ_{h1} is the lateral pressure as a result of the self-weight of the fill, the surcharge acting on top of the reinforced soil, and the retained soil and σ_{h2} is the lateral pressure as a result of the equivalent dead and live loads from the bridge slab, the lateral pressure is based on Boussinesq theory.

7.1 Calculating the Applied Loads

In this study, we adopted the FHWA's applicable external pressure and loads as defined by Adams et al. (2011a). Figure 7.1 depict the most common pressure which can be (which may be resolved into forces) on GRS-IBS for stability computations (Adams et al.,2011a).

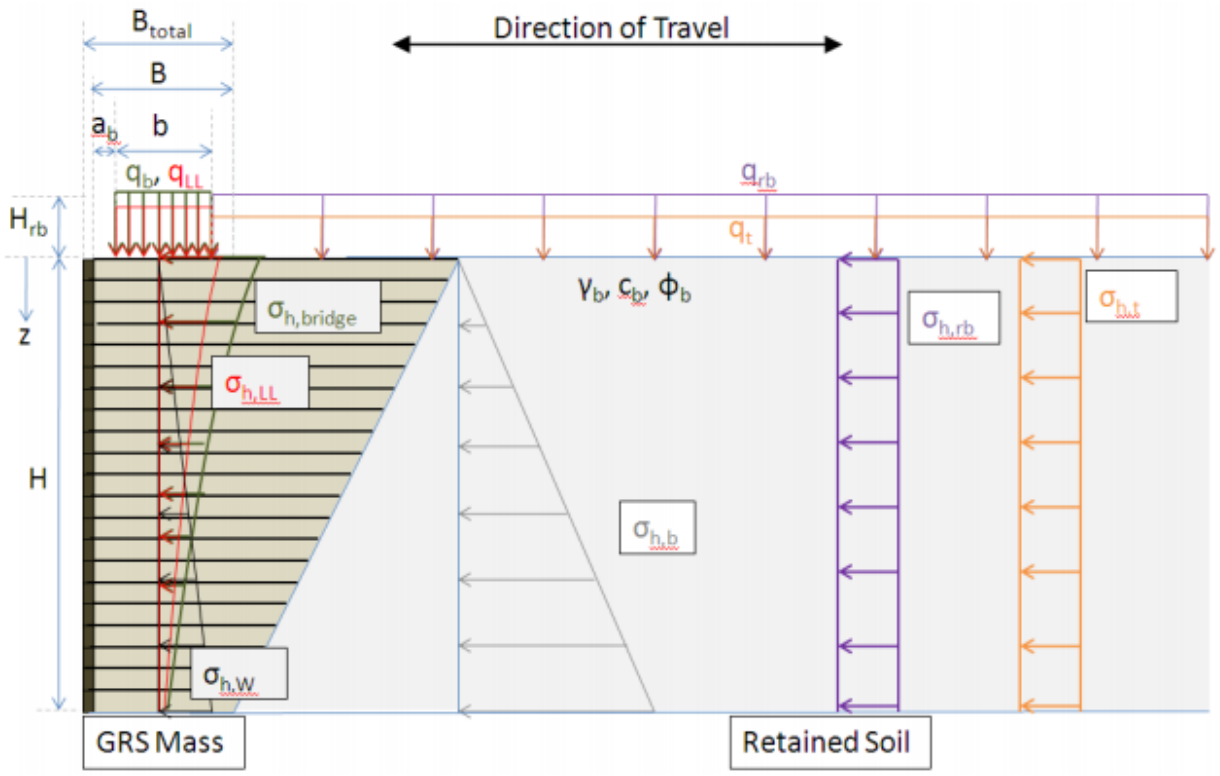

Figure 7.1. Illustration. Vertical and lateral pressures on a GRS abutment (Adams et al., 2011).

Where:

$q_t = equivalent\ roadway\ LL\ surcharge$

$\sigma_{h,t} = lateral\ stress\ distribution\ due\ to\ the\ equivalent\ roadway\ LL\ surcharge$

$q_{rb} = surcharge\ due\ to\ the\ structral\ backfill\ of\ the\ integrated\ approach\ (road\ base)$

$\sigma_{h,rb}$
$= lateral\ stress\ distribution\ due\ to\ the\ structural\ backfill\ of\ the\ integrated\ approach$

$q_b = equivalent\ superstructure\ DL\ pressure$

$\sigma_{h,bridge} = lateral\ stress\ distribution\ due\ to\ equivalent\ superstructure\ DL\ pressure$

$\sigma_{h,b}$
$= equivalent\ lateral\ stress\ distribution\ due\ to\ retained\ soil\ behind\ the\ GRS\ abutment$

$q_{LL} = equivalent\ superstructure\ LL\ pressure$

$\sigma_{h,LL} = lateral\ stress\ distribution\ due\ to\ the\ equivalent\ superstructure\ LL\ pressure$

$\sigma_{h,w} = lateral\ stress\ distribution\ due\ to\ the\ weight\ of\ the\ GRS\ fill$

7.2 Calculating pressure as a result of the self-weight of the fill, the surcharge acting on top of the reinforced soil, and the retained soil:

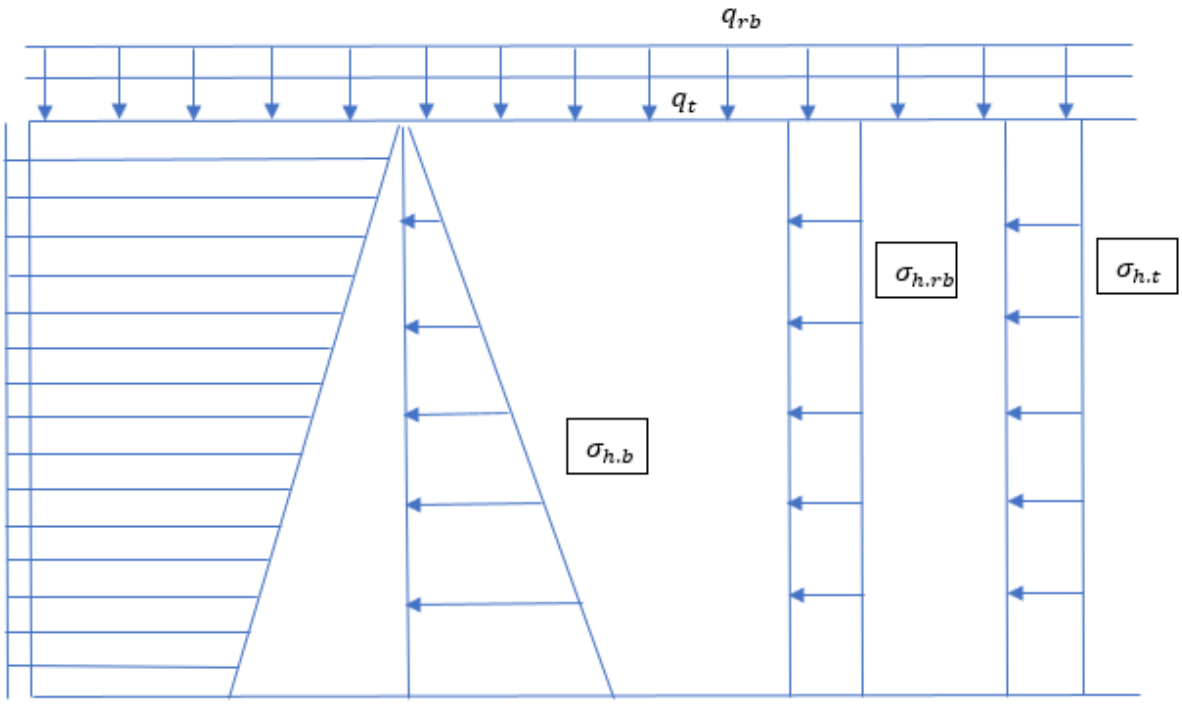

Figure 7.2. pressure as a result of the self-weight of the fill, the surcharge acting on top of the reinforced soil, and the retained soil

In this section, pressure as a result of the self-weight of the fill and the surcharge acting on top of the reinforced soil can be calculated. Assuming a Meyerhof pressure distribution at the base of the structure subjected to an applied moment, M, from the lateral loading (Meyerhof, 1963; Brinch Hansen, 1970). Three different forces that causing moment:

$$F1 = \sigma_{h,t} * H_i * \frac{H_i}{2}$$

$$F2 = \sigma_{h,rb} * H_i * \frac{H_i}{2}$$

$$F3 = 0.5 * \sigma_{h,b} * H_i * \frac{H_i}{3}$$

The vertical loads are:

$$V_{load} = q_b + q_t + \gamma_r H_i$$

The effective length of the footing:

$$L_{effective} = L - 2e$$

Where e: eccentricity

$$e = \frac{M}{V_{load}}$$

$$e_i = \frac{(\sigma_{h,t} * H * \frac{H}{2} + \sigma_{h,rb} * H_i * \frac{H_i}{2} + 0.5 * \sigma_{h,b} * H_i * \frac{H_i}{3})}{(q_b + q_t + \gamma_r H_i) * L}$$

Multiply both sides by 6 and simplify:

$$e_i = \frac{(3\sigma_{h,t} + 3\sigma_{h,rb} + \sigma_{h,b}) * {H_i}^2}{6 * (q_b + q_t + \gamma_r H_i) * L}$$

The effective length, $L_{effective}$, is:

$$L_{effective,i} = L - 2 * \frac{(3\sigma_{h,t} + 3\sigma_{h,rb} + \sigma_{h,b}) * {H_i}^2}{6 * (q_b + q_t + \gamma_r H_i) * L}$$

Simplify,

$$L_{effective,i} = L - \frac{(3\sigma_{h,t} + 3\sigma_{h,rb} + \sigma_{h,b}) * {H_i}^2}{3 * (q_b + q_t + \gamma_r H_i) * L}$$

$$L_{effective,i} = L - \frac{(3\sigma_{h,t} + 3\sigma_{h,rb} + \sigma_{h,b}) * (H_i)^2}{3 * (q_b + q_t + \gamma_r H_i) * L}$$

The vertical pressure,σ_v, is:

$$\sigma_v = \frac{V_{load}}{L_{effective}}$$

$$\sigma_{v,i} = \frac{(q_b + q_t + \gamma_r H_i)}{1 - \frac{(3\sigma_{h,t} + 3\sigma_{h,rb} + \sigma_{h,b}) * \left(\frac{H_i}{L}\right)^2}{3 * (q_b + q_t + \gamma_r H_i)}}$$

Multiply by active pressure coefficient, we find lateral earth pressure, σ_h, equal:

$$\sigma_{h1} = k_a \left[\frac{(q_b + q_t + \gamma_r H_i)}{1 - \frac{(3\sigma_{h,t} + 3\sigma_{h,rb} + \sigma_{h,b}) * \left(\frac{H_i}{L}\right)^2}{3 * (q_b + q_t + \gamma_r H_i)}} \right]$$

7.3 pressure as a result of the equivalent dead and live loads from the bridge slab, the lateral pressure is based on Boussinesq theory

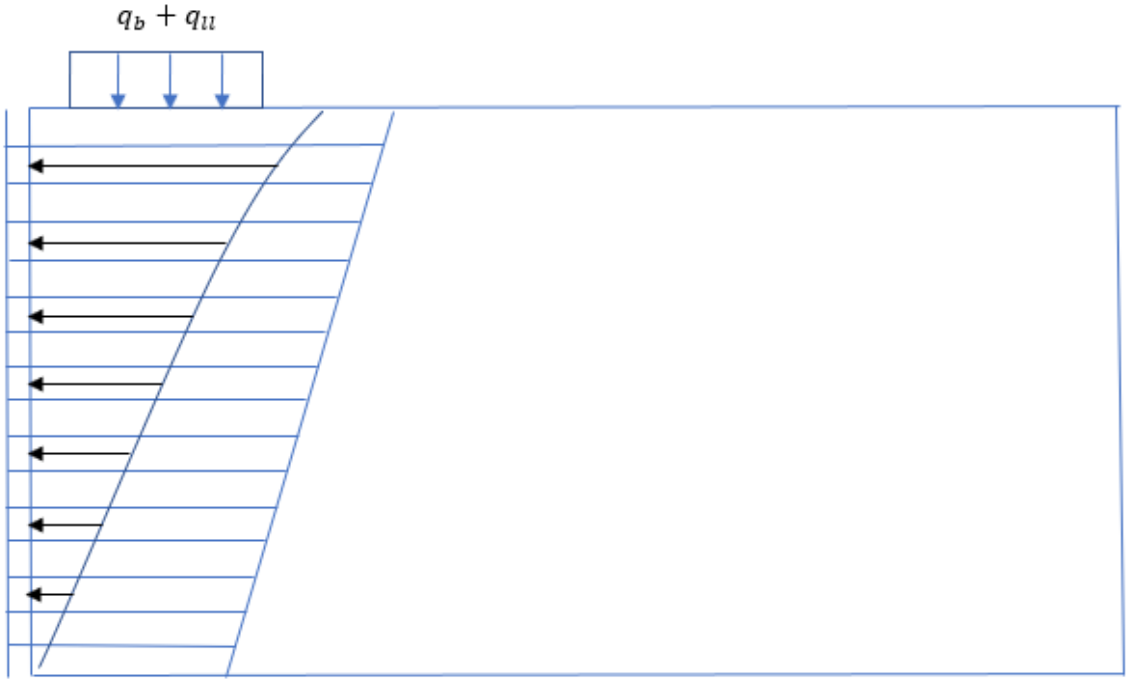

Figure 7.3. pressure as a result of the equivalent dead and live loads from the bridge slab.

In this section, the pressure as a result of the equivalent dead and live loads from the bridge slab can be calculated according to FHWA (Adams et al., 2011a). The lateral pressure can be calculated

based on Boussinesq theory for load distribution through a soil mass for an area transmitting a uniform stress a distance x from the edge of the load (see figure below 7.4) adopted previously by the FWAH (Adams et al., 2011a):

$\sigma_{h,bridge,eq} = \frac{(q_b+q_{ll})-(q_{rb}+q_t)}{\pi}[\alpha_b + sin(\alpha_b)cos(\alpha_b + 2\beta_b)]K_{ar}$ (Adams et al., 2011a)

Where:

$$\alpha_b = tan^{-1}\left(\frac{b}{2z}\right) - \beta_b$$

$$\beta_b = tan^{-1}\left(\frac{-b}{2z}\right)$$

Total lateral pressure equals the summation of σ_{h1} and $\sigma_{h,bridge,eq}$, which is:

$$\sigma_{h,total,i} = \left[k_c\left[\frac{(q_b + q_t + \gamma_r H_i)}{1 - \frac{(3\sigma_{h,t} + 3\sigma_{h,rb} + \sigma_{h,b}) * \left(\frac{H_i}{L}\right)^2}{3 * (q_b + q_t + \gamma_r H_i)}}\right]\right] + \left[\frac{(q_b + q_{ll}) - (q_{rb} + q_t)}{\pi}[\alpha_b + sin(\alpha_b)cos(\alpha_b + 2\beta_b)]K_c\right]$$

The required strength of the reinforcement is:

$$T_{req,i} = \left[\left[k_c \left[\frac{(q_b + q_t + \gamma_r H_i)}{1 - \frac{(3\sigma_{h,t} + 3\sigma_{h,rb} + \sigma_{h,b}) * \left(\frac{H_i}{L}\right)^2}{3 * (q_b + q_t + \gamma_r H_i)}}\right]\right] + \left[\frac{(q_b + q_{ll}) - (q_{rb} + q_t)}{\pi}[\alpha_b + sin(\alpha_b)cos(\alpha_b + 2\beta_b)]K_c\right]\right] * s_v$$

Where

s_v : the reinforcement spacing

K_c : the active earth pressure coefficient for the composite backfill soil

$$K_c = \frac{(1 - sin\phi_c)}{(1 + sin\phi_c)} = tan^2(45° - \frac{\phi_c}{2})$$

Where:

ϕ_c : Internal friction of the composite reinforced soil

If a series of triaxial tests on unreinforced and reinforced soil elements were conducted, the failure envelopes of the unreinforced and reinforced soils would allow the composite friction to be determined, which is certainly would increase the internal friction angle according to the reinforcement spacing and strength. Increasing the internal friction angle is a function increasing the major principle stress at failure from σ_1 to σ_{1R} due to the presence of the reinforcement which is a function of reinforcement spacing (Figure 7.5). Increasing the internal friction angle will decrease the active earth pressure coefficient which will reduce the lateral facing pressure due to the presence of reinforcement as was previously explained by Wu (2007).

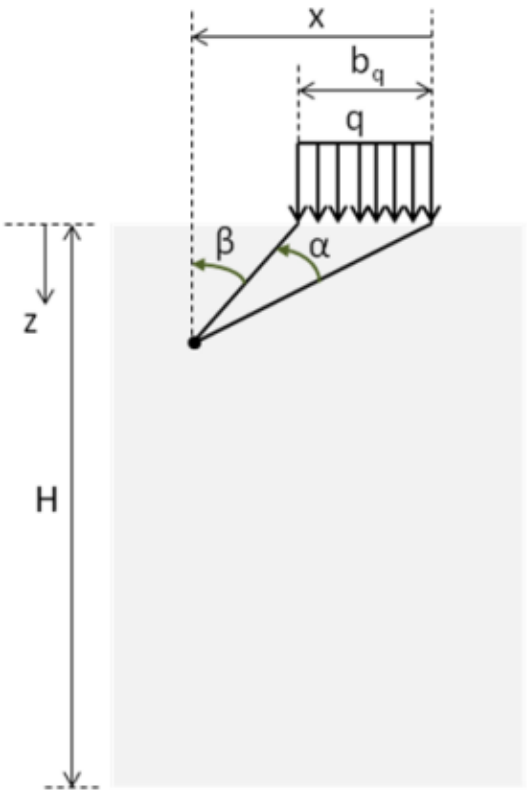

Figure 7.4. Illustration. Boussinesq load distribution with depth for a strip load.

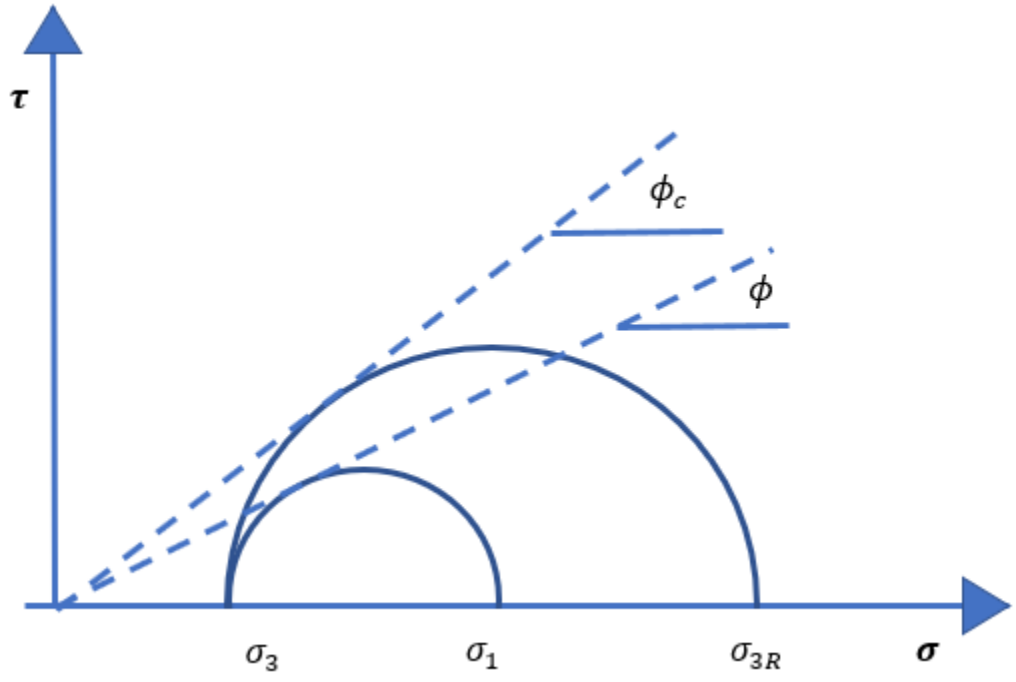

Figure 7.5. Illustration. Concept of increasing major principle stress at failure due to the presence of reinforcement.

7.4 Design Example: Maree Michel Bridge, Vermilion Parish, LA

7.4.1 Project Overview

As a part of the Highways for LIFE (HfL) initiative, the FHWA provided a $376,572 grant to the Louisiana Department of Transportation (LADOTD) to replace two structurally deficient bridges over the Maree Michel Creek & Unnamed Creek. The bridge over Maree Michel Creek was a 23.9-foot by 59-foot treated timber trestle bridge. The project was located on LA 91 in Vermilion Parish, between Gueydan to the north and the White Lake Conservation Area to the south. The small-scale project was intended to eliminate costs from the use of pile foundations by replacing the structurally deficient bridges over the Maree Michel Creek. This project, selected and included into the Preservation Bridge (On System) Program for fiscal year 2012- 2013, was a pilot for geosynthetic reinforced soil-integrated bridge system (GRS-IBS) construction. GRS-IBS and prefabricated bridge elements and systems (PBES) were the two innovations on this project. The project was let on August 14, 2013, and the construction began in November 2014. The project was completed by August 2015.

7.4.2 Project Background and Location

The project was located on LA 91 in Vermilion Parish, between Gueydan to the north and the White Lake Conservation Area to the south. LA 91 is a RC-2 Roadway Design Class with a design speed of 60 mph. The roadway carried average daily traffic (ADT) of 375 in 2013 and is projected to have an ADT of 450 in 2033. The small-scale project was intended to eliminate costs from the use of pile foundations by replacing two structurally deficient bridges over the Maree Michel Creek and Unnamed Creek. The bridges were two lanes, one in each direction. The Maree Michel

Canal Bridge (Structure No. 03572120105611) were respectively located 1.6 miles north of LA 3143. In 2013, the ADT values for the Maree Michel Canal was recorded as 375 vehicles per day.

7.4.3 Maree Michel Bridge Geometry Specification

- Abutment height: 3.8 m (13 ft.)
- Bridge width: 9.14 m (30 ft.)
- Span length: 22 m (72 ft.)
- Lane width: 3.35 m (11 ft.)
- Shoulder width: 1.22 m (4 ft.)

7.4.4 Applicable Loads

The following loads definitions were selected similar to FHWA (Adams et al., 2011a)

$q_t = equivalent\ roadway\ LL\ surcharge$

$q_t = 250\ psf$ (LADOTD)

$\sigma_{h,t} = lateral\ stress\ distribution\ due\ to\ the\ equivalent\ roadway\ LL\ surcharge$

$\sigma_{h,t} = q_t K_{ab} = 250 \times 0.375 = 94\ psf$

K_{ab}*: is the active earth pressure coefficient for the retained backfill soil*

$$K_{ab} = \frac{1 - sin\phi}{1 + sin\phi} = tan^2(45° - \frac{\phi}{2})$$

$Where\ \phi\ is\ the\ interal\ friction\ angle\ of\ the\ retained\ soil$

$q_{rb} = surcharge\ due\ to\ the\ structral\ backfill\ of\ the\ integrated\ approach\ (road\ base)$

$q_{rb} = h_{eq}\gamma_b = 2.8 \times 140 = 392\ lb/ft^3$

$\sigma_{h,rb}$
$= lateral\ stress\ distribution\ due\ to\ the\ structural\ backfill\ of\ the\ integrated\ approach$

$\sigma_{h,rb} = q_{rb}K_{ab} = 392 \times 0.375 = 147\ psf$

$q_b = equivalent\ superstructure\ DL\ pressure$

$q_b = 100\ kPa\ (2100\ lb/ft^2)$

$q_{LL} = equivalent\ superstructure\ LL\ pressure$

$q_{LL} = 77\ kPa\ (1610\ lb/ft^2)$ (LADOTD)

Table 7.1 presents the materials properties that can be used to calculate the pressures on the GRS-IBS abutment. The retained soil having the same properties of the foundation soil.

7.4.5 Calculate the Thrust behind GRS-IBS Abutment

The thrust force from the retained soil can be calculated by using the following equation:

$$F_b = \frac{1}{2}\gamma_b K_{ab} H_i^2$$

The thrust force from the road base can be calculated by using the following equation:

$$F_{rb} = q_{rb} K_{ab} H_i$$

The thrust force from the road way LL surcharge can be calculated by using the following equation:

$$F_t = q_t K_{ab} H_i$$

Where: H_i = Abutment Height at any given level, γ_b = Retained soil Density

Table 7.1. Materials Properties

Category	Description
Geotextile	linear elastic perfectly plastic model; Tensile strength @ 2% = 13×17 kN/m, Tensile strength @ 5% = 35×40 kN/m; Tult = 80 kN/m; reinforcement spacing = 0.2 m; Axial stiffness, EA= 600 kN/m.
Backfill Material	Hardening soil model; dry unit weight, γ_d= 18 kN/m /m^3; wet unit weight, γ_t=19 kN/m /m^3; cohesion, c =20 kPa; friction angle, ϕ =51°; dilation angle Ψ=21°; E_{50}^{ref}=34,000 kPa, E_{ur}^{ref}= 103,200 kPa, E_{oed}^{ref}=26,400, ν= 0.2; power, m = 0.5
Foundation Soil	Soil model, Mohr-Coulomb model; dry unit weight,γ_d= 15.2 kN/m^3; wet unit weight, γ_w=18.65 kN/m^3; cohesion, c=17.7 kPa; ϕ= 27°; E =30000 kPa; ν= 0.2.
Interface (backfill and geotextile)	linear elastic with Mohr-Coulomb failure criterion; adhesion, c=8.6 kPa; interface friction angle δ=40.4°

7.4.6 Calculate the thrust moment, eccentricity, Effective Length, and vertical pressure

Assuming a Meyerhof pressure distribution at the base of the structure subjected to an applied moment, M, from the lateral loading. Three different forces that causing moment:

$$F1 = \sigma_{h,t} * H_i * \frac{H_i}{2}$$

$$F2 = \sigma_{h,rb} * H_i * \frac{H_i}{2}$$

$$F3 = 0.5 * \sigma_{h,b} * H_i * \frac{H_i}{3}$$

The vertical loads are:

$$V_{load} = q_b + q_t + \gamma_r H_i$$

The effective length of the footing:

$$L_{effective,i} = L - 2e$$

Where e: eccentricity

$$e = \frac{M}{V_{load}}$$

$$e_i = \frac{(\sigma_{h,t} * H_i * \frac{H_i}{2} + \sigma_{h,rb} * H_i * \frac{H_i}{2} + 0.5 * \sigma_{h,b} * H_i * \frac{H_i}{3})}{q_b + q_t + \gamma_r H_i}$$

$$L_{effective,i} = L - \frac{(3\sigma_{h,t} + 3\sigma_{h,rb} + \sigma_{h,b}) * (H_i)^2}{3 * (q_b + q_t + \gamma_r H_i) * L}$$

$$\sigma_v = \frac{V_{load}}{L_{effective}}$$

$$\sigma_{v,i} = \frac{(q_b + q_t + \gamma H_i)}{1 - \frac{(3\sigma_{h,t} + 3\sigma_{h,rb} + \sigma_{h,b}) * \left(\frac{H_i}{L}\right)^2}{3 * (q_b + q_t + \gamma H)}}$$

7.4.7 Calculate the Horizontal pressures and required reinforcement strength

the horizontal pressure can be calculated by using the following equation:

$$\sigma_{h,total,i} = \left[k_c \left[\frac{(q_b + q_t + \gamma_r H_i)}{1 - \frac{(3\sigma_{h,t} + 3\sigma_{h,rb} + \sigma_{h,b}) * \left(\frac{H_i}{L}\right)^2}{3 * (q_b + q_t + \gamma_r H_i)}} \right] \right] + \left[\frac{(q_b + q_{ll}) - (q_{rb} + q_t)}{\pi} [\alpha_b + sin(\alpha_b) cos(\alpha_b + 2\beta_b)] K_c \right]$$

$$T_{req,i} = \left[\left[k_c \left[\frac{(q_b + q_t + \gamma_r H_i)}{1 - \frac{(3\sigma_{h,t} + 3\sigma_{h,rb} + \sigma_{h,b}) * \left(\frac{H_i}{L}\right)^2}{3 * (q_b + q_t + \gamma_r H_i)}} \right] \right] + \left[\frac{(q_b + q_{ll}) - (q_{rb} + q_t)}{\pi} [\alpha_b + sin(\alpha_b) cos(\alpha_b + 2\beta_b)] K_c \right] \right] * s_v$$

K_c : the active earth pressure coefficient for the composite backfill soil

$$K_c = \frac{(1 - sin\phi_c)}{(1 + sin\phi_c)} = tan^2(45° - \frac{\phi_c}{2})$$

Where:

ϕ_c : Internal friction of the composite reinforced soil

The lateral stress is calculated for each layer of reinforcement by using the previous equations. Table 7.2 shows the lateral stresses based due to road base DL, the roadway LL, the GRS abutment soil, the retained soil, and an equivalent bridge load. The lateral stresses due to the equivalent bridge load are then calculated according to Boussinesq theory as was described previously by Adams et al. (2011a). Figure 7.6 compares between the maximum reinforcement strength as predicted by the FHWA (Adams et al.,2011a) and the proposed analytical model and compares both model results with the field measurement and finite element analysis. It can be seen that the proposed analytical model results are in a good agreement with both the field measurements and the FE analysis. However, the FHWA model is over predicted the maximum reinforcement strength comparing to the field measurements and FE analysis.

Table 7.2. Depth of bearing bed reinforcement calculations.

Layer #	Depth (m)	Equivalent Bridge Load (kPa)(FHWA)			DL&LL		GRS Fill	T (FHWA)	T (FE)	T (Field)	T (Modify)
		Alpha	Beta	$\sigma_{h,bridge}$	$\sigma_{h,rb}$	$\sigma_{h,t}$					
1	3.80	0.49	-0.24	6.72	6.75	4.50	8.58	9.91	5.30	--	5.05
2	3.60	0.51	-0.26	7.06	6.75	4.50	8.13	9.87	4.80	--	4.95
3	3.40	0.54	-0.27	7.44	6.75	4.50	7.67	9.84	4.50	--	4.86
4	3.20	0.57	-0.29	7.86	6.75	4.50	7.22	9.83	4.30	--	4.79
5	3.00	0.61	-0.30	8.32	6.75	4.50	6.77	9.83	4.10	--	4.75
6	2.80	0.65	-0.32	8.84	6.75	4.50	6.32	9.86	4.00	--	4.72
7	2.60	0.69	-0.35	9.42	6.75	4.50	5.87	9.91	3.90	--	4.72
8	2.40	0.75	-0.37	10.07	6.75	4.50	5.42	9.98	3.80	--	4.74
9	2.20	0.81	-0.40	10.81	6.75	4.50	4.97	10.09	3.90	--	4.78
10	2.00	0.88	-0.44	11.65	6.75	4.50	4.51	10.23	4.10	--	4.85
11	1.80	0.96	-0.48	12.60	6.75	4.50	4.06	10.42	4.20	--	4.95
12	1.60	1.06	-0.53	13.68	6.75	4.50	3.61	10.65	4.10	4.30	5.08
13	1.40	1.18	-0.59	14.89	6.75	4.50	3.16	10.94	3.90	--	5.24
14	1.20	1.33	-0.66	16.25	6.75	4.50	2.71	11.28	3.70	4.20	5.44
15	1.00	1.51	-0.75	17.71	6.75	4.50	2.26	11.65	3.50	--	5.65
16	0.80	1.73	-0.87	19.21	6.75	4.50	1.81	12.04	3.40	3.70	5.88
17	0.60	2.01	-1.00	20.58	6.75	4.50	1.35	12.39	3.20	--	6.09
18	0.40	2.34	-1.17	21.60	6.75	4.50	0.90	12.60	3.00	3.40	6.23

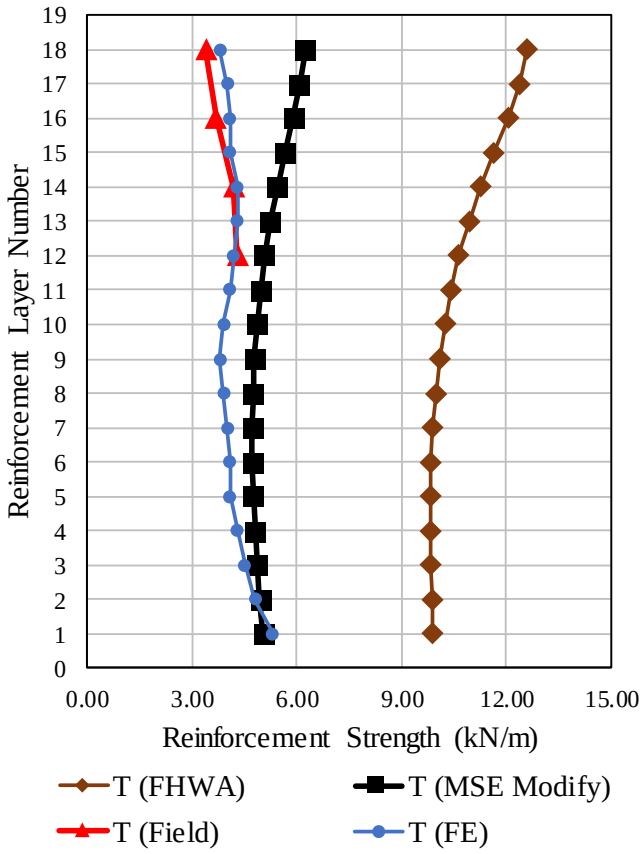

Figure 7.6. Comparison of maximum reinforcement strength using FWHA and proposed analytical model with field measurements and FE analysis

The maximum reinforcement strength at 1.0 m depth from the top of the GRS abutment, layer 15, can be calculated is presented here:

$$\sigma_{v,i} = \frac{(q_b + q_t + \gamma H_i)}{1 - \frac{(3\sigma_{h,t} + 3\sigma_{h,rb} + \sigma_{h,b}) * \left(\frac{H_i}{L}\right)^2}{3 * (q_b + q_t + \gamma H)}}$$

$$\sigma_{v,15} = \frac{(100 + 12 + 18 * 1)}{1 - \frac{(3 * 4.5 + 3 * 7.04 + 5.7 * 1) * \left(\frac{1}{2.6}\right)^2}{3 * (100\ 12 + 18 * 1)}}$$

=132.02 kPa

$$\sigma_{v,15} = 132.02 * 0.1 = 13.2\ kPa$$

$$\sigma_{h,bridge,eq,15} = \frac{(q_b+q_{ll})-(q_{rb}+q_t)}{\pi}[\alpha_b + sin(\alpha_b)cos(\alpha_b + 2\beta_b)]K_{ar}$$

$$\alpha_b = tan^{-1}\left(\frac{b}{2z}\right) - \beta_b$$

$$\alpha_b = tan^{-1}\left(\frac{1.88}{2}\right) - (-0.75) = 1.51$$

$$\beta_b = tan^{-1}\left(\frac{-b}{2z}\right)$$

$$\beta_b = tan^{-1}\left(\frac{-1.88}{2}\right) = -0.75$$

$$\sigma_{h,bridge,eq,15} = \frac{(100 + 77) - (18 + 12)}{\pi}[1.51 + sin(1.51)cos(1.51 + 2(-0.75))]0.1254$$

= 15 kPa

$T_{req,15}$ = (15+13.2) *0.2 = 5.65 kN/m

7.4.8 Define Critical Slip Surface

The potential failure envelope can be defined to coincide with the locus of the maximum strain (maximum tensile force) throughout the reinforcement layers. This critical failure envelope was previously found as a bilinear shape as was shown previously in Figure 6.33 and can be seen in the illustration Figure 7.7 below. The location of maximum strain envelope indicates that the possible failure envelope developed from the inner edge of the footing extending vertically downward for the upper half of the bridge abutment and is followed by the general Rankine active failure envelope for the bottom half of the GRS-IBS abutment. This result is very similar to the punching shear failure envelope defined by a previous study conducted by Chen et al. (2009) on reinforced crushed limestone underneath spread footing. Takemura et al. (1992) investigated the

failure mechanism of reinforced sand by using centrifuge test. Their results showed that the intensely shear bands were developed from the edges of the footing and is extending vertically downward. It is interesting to notice that the results indicate that the failure envelope is a combination punching shear failure envelope (top) and Rankine failure envelope (bottom), in which the failure envelope is developed under the inner edge of the footing and extending vertically downward to intersect with the Rankine active failure envelope.

Having defined the potential failure envelope that coincide with the maximum tensile force throughout the reinforcement layers, the pullout capacity and the required reinforcement length can be evaluated using the conventional MSE walls methods (e.g. Berg et al., 2009).

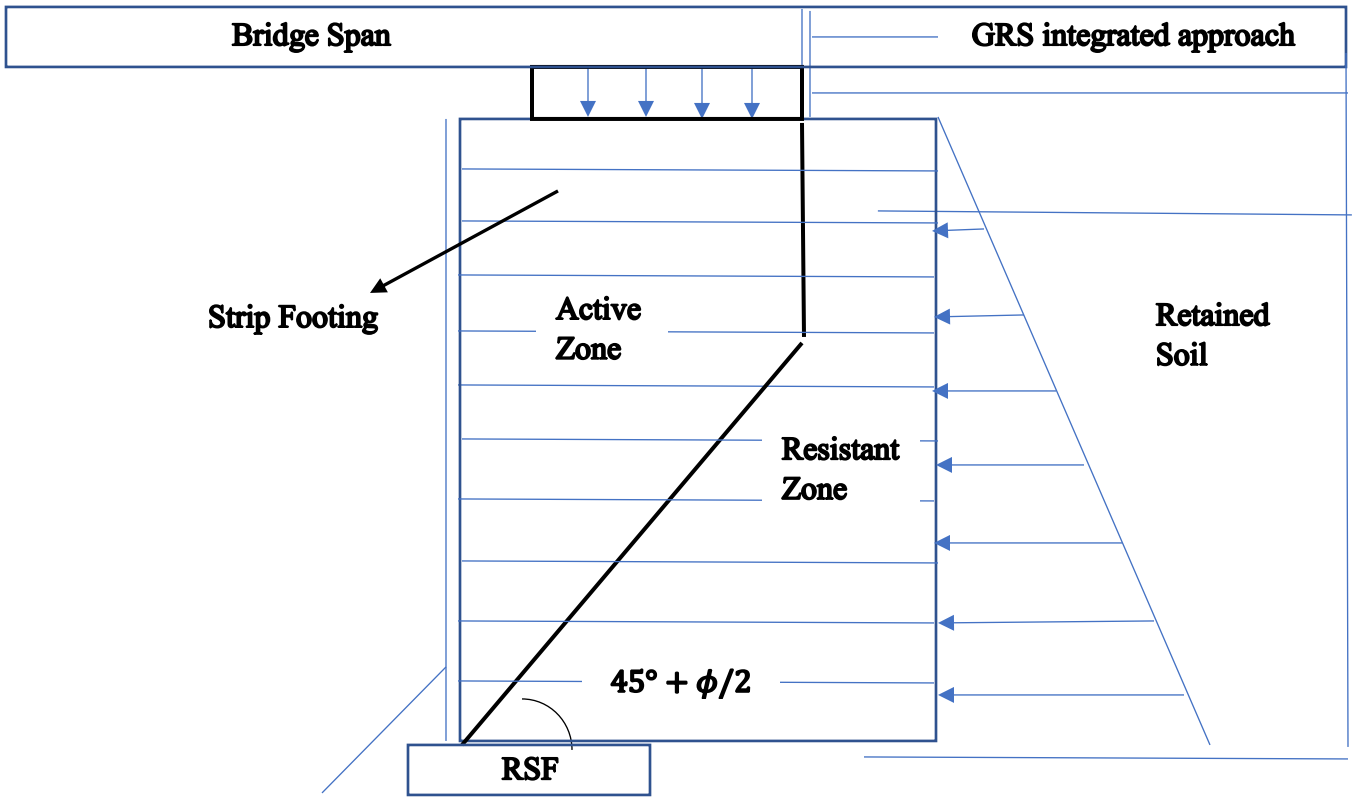

Figure 7.7.
Illustration. Location of potential failure surface for internal stability design of GRS-IBS

Chapter Eight
Conclusions and Recommendations

8.1 Conclusions

This dissertation documents the findings of an extensive research study that was conducted to evaluate the performance of the Geosynthetic Reinforced Soil-Integrated Bridge System (GRS-IBS). The objectives of this study were achieved through conducting an experimental testing and numerical modeling programs. The following sections summarize the findings and conclusions of each of these programs.

8.1.1 Experimental Testing Program

The experimental testing program in this study included fully instrumenting of in-service GRS-IBS abutment at Maree Michel Bridge in Louisiana to monitor and evaluate the performance of the abutment under service loading condition. Various types of instrumentations were installed in the south abutment of the GRS-IBS abutment. The primary measurements were the vertical and horizontal deformations near the front wall, settlements due to the soil foundation and the GRS-IBS backfill, the stresses and distribution of stresses in the GRS-IBS abutments and below reinforced soil foundation, and the distribution of strains along the geosynthetic reinforcements. Six different types of instrumentations were used to monitor the GRS-IBS bridge abutment: Shape Acceleration Array (SAA), earth pressure cells, strain gauges, piezometers, and thermocouples. Additionally, surveying was conducted at the bridge surface upon the completion of the construction. Based on the results of the experimental testing program, the following conclusions can be drawn:

- In general, the satisfactory performance of Maree Michel GRSIBS Bridge and economic benefits, helps LA DOT to gain more confidence in GRS-IBS technology.
- The settlement and deformation measurements of the GRS-IBS exhibited logical and consistent trends. The soil foundation settlement was increased with lift placement, with more movements occurred near the center of the abutment than the corners. The measurements of abutment deformations indicate that the maximum total settlements across the GRS abutment were significantly less than the design value. Majority of this deformation (~70%) was due to settlement of foundation soil, while less than 30% of the total deformation occurred within the abutment and RSF. The maximum vertical strain in the abutment was less than 45% of maximum value specified by the FHWA.
- The maximum lateral movement was observed near the top of the wall. Following the construction of bridge abutment, the facing wall experienced some appreciable outward (away from backfill) lateral deformation. However, after placing the steel girders, the lateral movement close to the wall significantly increased.
- The measured vertical pressure values compared well with the predicted geostatic stresses.
- Measurements from horizontal pressure cells demonstrate that the lateral pressure on the wall face is negligible. In this study, the maximum lateral pressure of 6 kPa was measured in the lower level of the abutment with no secondary reinforcement layer. The addition of secondary reinforcement within the top layers of abutment significantly reduced the lateral pressure. Moreover, no significant change in lateral pressure was observed during the construction stages.

- The observed geotextile strains were within the range specified in the FHWA manual (less than 2%). During the construction, the maximum strain observed along the reinforcement layers was half of the maximum strain specified by FHWA.
- The magnitude and distribution of strain in geosynthetic layers varied in depth of the abutment. Strain measurements showed that the locus of the slip surface changed significantly after placement of the steel girders. Before placement of the girders, the locus of maximum strains formed a bilinear surface with an angle close to theoretical failure surface up to certain height, followed by a vertical surface. However, after placement of the steel girders, the distance of linear surface representing the locus of maximum strains increased with the abutment height at the lower levels and decreased sharply at the top layers of GRS abutment.
- A comparison between the GRS-IBS method and GSME approach shows that GSME approach is more conservative in case of closely-spaced reinforced mass used as a bridge abutment. The calculated lateral pressure on the facing wall based on the GSME approach (Rankine theory) was significantly higher than measurements on the field. In addition, the measured lateral pressures did not change significantly by depth and surcharge load, which contradicts with the classical lateral pressure theory. Small lateral displacement of facing wall verifies the assumption that unlike regular GSME mass, block pull-out and connection force is not an issue in GRS-IBS.

8.1.2 Numerical Modeling Program

2D and 3D-Finite element analyses were conducted to numerically simulate the performance of the GRS-IBS under different loading conditions, which was verified using the results of a fully-instrumented GRS-IBS bridge abutment at the Maree Michel Bridge in Louisiana, and to conduct

a comprehensive parametric study on the effect of different parameters on the performance of GRS-IBS. The FE parametric study included the effects of abutment height H, span length L_{span}, reinforcement spacing S_v, reinforcement stiffness, EA, backfill internal friction angle, ϕ, length of reinforcement, Lr, width of reinforcement soil footing, B_{RSF}, secondary reinforcement, setback distance, a_b, subgrade soil conditions, bearing width, b, and the effect of differential settlement. Different constitutive models were used to describe the behavior of the GRS-IBS abutment. The second order hyperbolic elastoplastic hardening soil model was selected to describe the behavior of the backfill material. The linear elastic model with Mohr–Coulomb failure criterion model was used to simulate the mechanical behavior of the interface between the backfill material and geotextile and the facing blocks. Both the geotextiles and facing blocks were modeled using linear elastic model. An elastic-perfectly plastic models was used to simulate the subgrade soils. Based on the results of the numerical modeling program, the following conclusions can be drawn:

- The maximum lateral deformations of the GRS-IBS wall face were 4 mm (0.11% of the GRS-IBS height) and 9 mm (0.24% of the GRS-IBS height) for the service loading and abnormal loading conditions, respectively.
- The maximum settlement of the GRS-IBS under the service loading as predicted by the FE analysis was 10 mm, which is 0.3% of the GRS-IBS wall height and less than the FHWA recommendations (0.5% of the GRS-IBS wall height) and two times the field measurements (5 mm). This is most probably due to the over consolidated soil caused by the old bridge.
- The maximum reinforcement strain in the GRS-IBS abutment under service loading was 1.2%, which is two times higher than the strain in the RSF and less than the typical design

value of 2%, indicating that the reinforcing is sufficiently stiff to avoid excessive deformation.

- It was shown that the GRS-IBS can be loaded to at least three times the service loading (331 kPa) with satisfactory performance, which is higher than the FHWA recommendations of 190 kPa.

- The 3D-FE analysis shows that the FHWA recommendations underestimate the performance of the GRS-IBS by curbing the allowable bearing pressure to 190 kPa. The results of FE analysis showed that the GRS-IBS can be loaded up to three times the service loading (331 kPa) with satisfactory performance, which indicates that a span longer than 43 m (140 ft.) can be constructed over a GRS-IBS abutment.
- It was shown that the active failure assumption analysis according to the most used methods for MSE wall (i.e., Coherent Gravity Method (AASHTO,1996) and Tie Back Wedge Method (AASHTO, 1996)) is not valid for the case of GRS-IBS abutments and that the failure envelope extends beyond the Coherent Gravity Method assumption up to 33% extra, in which the three points are required to draw the failure envelope; (H, 0.4H), (H/2,0.4H), and (0,0). The difference can be attributed to the fact that in MSE walls we use a tie-back approach where the reinforcements are “attached to” to the rigid face and the function of the reinforcements is to keep the face and soil mass together; however, the reinforcements in GRS walls are “placed in” to internally stabilize the soil by carrying tensile loads due to the interaction between the closely-reinforcement and the soil around it (composite behavior).

- The results of this study clearly demonstrated that the plain strain 2D-FE analysis can be used to simulate the performance of GRS-IBS with good satisfactory, and the results are very close to those predicted by the 3D-FE analyses.
- The magnitude of maximum reinforcement strain is directly related to the location of the reinforcement within the same model, in which the reinforcement layers near the bottom location have higher strains than reinforcement layers near the top location. For example, the maximum strain decreases from about 1.4% at 20% of the abutment height to about 0.7% at 80% of the abutment height for the 7-m abutment height.
- The bridge span length has a significant effect on the GRS-IBS performance such that the magnitude of maximum strain and lateral facing displacement increase with increasing the span length. The maximum reinforcement strain increased from about 0.4% for span length of 12.2 m to about 0.9% for a span length of 36.6 m at 0.6 *H* above the bottom of the abutment, and the lateral facing displacement increased from 12 mm for a 12.1 m span length to 30 mm for a 36.6 m span length. The results indicated that while the magnitude of reinforcement strain is affected by span length and abutment height, the shape of the strain distribution is not affected.
- The reinforcement spacing has significant influence on the strain distribution along the reinforcement and the lateral facing displacement, in which the maximum strain and lateral facing displacement increase with increasing reinforcement spacing. The maximum reinforcement strain increased from about 0.6% for a reinforcement spacing of 0.1 m to about 1.4% for a reinforcement spacing of 0.4 m, and the maximum lateral facing displacement increased from about 28 mm for a reinforcement spacing of 0.2 m to about 42 mm for a reinforcement spacing of 0.4 m.

- The reinforcement stiffness has significant influence on the behavior of GRS-IBS in terms of reducing the lateral facing displacement and the magnitude of strain distribution along the reinforcement with increasing stiffness up to a certain point, after which this impact tends to decrease in contrary to the effect of reinforcement spacing, which shows a constant impact on the performance of GRS-IBS.
- It was noted that the reinforcement spacing has more significant role than the reinforcement stiffness in the performance of the GRS-IBS in terms of lateral facing displacement for reinforcement spacing equal to or higher than 0.2 m. However, the reinforcement stiffness has close or slightly higher impact than the reinforcement spacing reinforcement for reinforcement spacing less than 0.2 m, which indicates that the 0.2 m reinforcement spacing might be the optimum reinforcement spacing for GRS-IBS.
- The FE results indicated that the failure envelope is most likely a combination of punching shear failure envelope (at top) and the Rankine failure envelope (at bottom), in which the failure envelope is developed under the inner edge of the footing and extending vertically downward to intersect with the Rankine active failure envelope.
- The differential settlement under the reinforced zone and RSF and has high impact on the performance of the GRS-IBS in terms of strain distribution along the geosynthetic and the lateral facing displacement. The maximum strain value obtained was 1.4% under 50 mm differential settlement at 40% of bridge abutment height from the top of the RSF and decreased to 0.5% under 150 mm differential settlement at the same location. The lateral facing displacement increased from 28 mm under a differential settlement of 50 mm to 42 mm under 150 mm for abutment height of 36.6 m. However, the maximum reinforcement strain associated with a differential settlement of 200 mm for a span length of 36.6 m under

service loading condition was 1.4%, which is less than the typical design value of 2% as recommended by the FHWA (Adams et al., 2011a).

- The differential settlement under the retained soil has little impact on the reinforcement strain along the geosynthetic but has a high impact on the lateral facing displacement at 50% of the bridge abutment height from the top of the RSF. It was observed that the differential settlement underneath the retained soil caused a rotational behavior for the lateral facing deformation. The lateral facing displacement at the bottom of the GRS abutment increased from 3.5 mm under a differential settlement of 50mm to 10 mm under a differential settlement of 100 mm and to 29 mm under a differential settlement of 200 mm.
- The maximum predicted lateral facing displacement under service loading condition was about 40 mm for a span length of 36.6 m and abutment height of 5.18 m, at a differential settlement of 200 mm. This value is less than the allowable lateral deformation of 50 mm (less than 1% of the abutment height) as recommended by the FHWA (Adams et al., 2011a).
- The maximum predicted bump at the bridge span - approach roadway intersection was 20 mm, which is associated with a 200 mm differential settlement under the RSF for a span length of 36.6 m under service loading. This value is less than the allowable differential settlement values as documented in the literature.
- A differential settlement up to 150 mm accompanied with a bridge span up to 30.5 m underneath the reinforced zone subjected to service loading will not create a serious riding comfort issue. However, care must be taken in case of a bridge span higher than 30.5 m built on weak or special soils near water as recommended by Adams et al. (2011a), and

that if the bridge is crossing water, the GRS-IBS should not be considered unless scour effect is properly addressed.

- It was noted that the differential settlement has moderate effect on the magnitude of lateral facing pressure. The top of the GRS-IBS abutment was the most effected location, in which the lateral facing pressure decreased with increasing the differential settlement except for the 50 mm differential settlement. The lateral facing pressure decreased from 13.8 kPa for the control section to 6.9 kPa for a 200 mm differential settlement and increased to 20.7 kPa for a 50 mm differential settlement. This cdemonstrates that that the recommendation about inserting pin in the top facing blocks by Adams et al. (2011a) is a must in designing the GRS-IBS bridge abutment.
- Based on the concept of apparent cohesion by Schlosser and Long (1974), the apparent internal friction angle for the GRS was modified to account for the increase in major principal stress at failure due to the presence of reinforcement and corresponding composite behavior.

8.2 Recommendations

- Additional research effort is needed to investigate the benefits of geogrid-backfill interlocking on the performance of the GRS-IBS abutment, and the interaction between aggregate size and geogrid aperture when using the geogrid as a reinforcement.
- Additional experimental research effort is required to study the combined effects of reinforcement spacing and reinforcement stiffness on the performance of the GRS-IBS abutment to characterize the reinforcement influenced zone.
- Further experimental investigation is required to study the effects of differential settlement on the performance of the GRS-IBS abutment.

- It is strongly recommended to study the effect of increasing the span length beyond 140 ft.
- It is strongly recommended that the numerical findings of this research are evaluated and verified using large-scale testing.
- Further investigations is needed to study the effects of connection between the facing blocks on the performance of the GRS-IBS abutment to confirm that the facing is not needed as a structurally component especially when the GRS-IBS abutment is subjected to differential settlement.
- Further research effort is recommended to implement the composite concept in the design of GRS-IBS abutment.

References

AASHTO, LRFD Bridge Design Specifications, 2014, seventh ed. American Association of State Highway and Transportation Officials, Washington, D.C.

Abu-Farsakh, M., Ardah, A. and Voyiadjis, G., 2018a. Numerical Investigation of the Performance of Geosynthetic Reinforced Soil–Integrated Bridge System (GRS-IBS) Subjected to Differential Settlement (No. 18-01788).

Abu-Farsakh, M., Saghebfar, M., Ardah, A. and Chen, Q., 2017. A Case Study on Evaluating the Performance of a Geosynthetic Reinforced Soil Integrated Bridge System (GRS-IBS). In: Geotechnical Frontiers, pp. 12-22.

Abu-Farsakh, M., Ardah, A. and Voyiadjis, G., 2018b. 3D Finite element analysis of the geosynthetic reinforced soil-integrated bridge system (GRS-IBS) under different loading conditions. *Transportation Geotechnics*, *15*, pp.70-83.

Abu-Farsakh, M., Ardah, A. and Voyiadjis, G., Numerical Investigation of the Performance of a Geosynthetic Reinforced Soil-Integrated Bridge System (GRS-IBS) under Working Stress Conditions. In *IFCEE 2018c* (pp. 76-87).

Abu-Hejleh, N., Outcalt, W., Wang, T., and Zornberg, J. G. (2000a). "Performance of Geosynthetic Reinforced Walls Supporting the Founders/Meadows Bridge and Approaching Roadway Structures - Report 1: Design, Materials, Construction, Instrumentation, and Preliminary Results." CDOT-DTD-R-2000-5, Colorado Department of Transportation, Denver, CO.

Abu-Hejleh, N., Wang, T., and Zornberg, J. G. (2000b). "Performance of Geosynthetic-Reinforced Walls Supporting Bridge and Approaching Roadway Structures." Advances in Transportation and Geoenvironmental Systems Using Geosynthetics, ASCE, Reston, VA, 218-243

Adams, M. and Nicks, J., 2014. Secondary settlement of geosynthetic-reinforced soil piers: preliminary results. In Geo-Congress 2014: Geo-characterization and Modeling for Sustainability (pp. 4228-4237).

Adams, M. T. (1997). "Performance of a Prestrained Geosynthetic Reinforced Soil Bridge Pier." Proc., International Symposium on Mechanically Stabilized Backfill, J.T.H. Wu (Ed) A.A. Balkema, Rotterdam, 35-53.

Adams, M. T. (2007a). "Mini Pier Experiments Geosynthetic Reinforcement Spacing and Strength as Related to Performance." Proc. of Geo-Denver 2007, ASCE, Denver, CO.

Adams, M. T., Kanop K., and Wu, J. T. H Mini Pier Experiments–Geosynthetic Reinforcement Spacing and Strength as Related to Performance. American Society of Civil Engineers. GSP 165, 2007b, pp. 18-21.

Adams, M. T., Nicks, J., Stabile, T., Wu, J. T. H., Schlatter, W., and Hartmann, J. (2011a). "Geosynthetic Reinforced Soil Integrated Bridge System—Interim Implementation Guide." FHWA-HRT-11-026, Federal Highway Administration, McLean, VA.

Adams, M. T., Schlatter, W., & Stabile, T. (2007c). Geosynthetic reinforced soil integrated abutments at the Bowman Road Bridge in Defiance County, Ohio. In Geosynthetics in Reinforcement and Hydraulic Applications (pp. 1-10).

Adams, M., Nicks, J., Stabile, T., Wu, J., Schlatter, W. and Hartmann, J., 2011b. Geosynthetic Reinforced Soil Integrated Bridge System, Synthesis Report (No. FHWA-HRT-11-027b).

Adams, M.T., Lillis, C., Wu, J.T.H., Ketchart, K., 2002. Vegas GRS mini pier experiment and the postulate of zero volume change. In: 7th International Conference on Geosynthetics, Nice, France, pp. 389e394.

Adams, M.T., Nicks, J.E., Lynch, C., 2015. Lateral deformation of GRS bridge abutments. Geosynthetics 2015. Portland, OR, 15e18 February.

Adib, M., Mitchell, J.K. and Christopher, B., 1990, June. Finite element modeling of reinforced soil walls and embankments. In: Design and Performance of Earth Retaining Structures, pp. 409-423. ASCE.

Allen, T.M., Christopher, B.R. and Holtz, R.D., 1992. Performance of a 41 Foot High Geotextile Wall: Final Report, Experimental Feature WA87-03. Washington State Department of Transportation, Planning, Research and Public Transportation Division.

American Society for Testing and Materials, West Conshohocken, PA, USA. ASTM International, 2011. Standard Test Methods for Tensile Properties of Geotextiles by the Wide-width Strip Method. ASTM D4595.

Ardah, A., Abu-Farsakh, M., & Voyiadjis, G. (2017). Numerical evaluation of the performance of a Geosynthetic Reinforced Soil-Integrated Bridge System (GRS-IBS) under different loading conditions. Geotextiles and Geomembranes, 45(6): 558-569.

Ardah, A., Abu-Farsakh, M.Y. and Voyiadjis, G.Z., 2018. Numerical Evaluation of the Effect of Differential Settlement on the Performance of GRS-IBS. *Geosynthetics International*, pp.1-45.

Arneson, L. A., Zevenbergen, L. W., Lagasse, P. F., & Clopper, P. E. (2012). Evaluating scour at bridges (4th Ed.). Hydraulic Engineering Circular No. 18 (HEC-18). Federal Highway Administration, Washington, DC.

Bathurst, R. J., Allen, T. M., & Walters, D. L. (2005). Reinforcement loads in geosynthetic walls and the case for a new working stress design method. Geotextiles and Geomembranes, 23(4), 287-322.

Bathurst, R. J., Vlachopoulos, N., Walters, D. L., Burgess, P. G., & Allen, T. M. (2006). The influence of facing stiffness on the performance of two geosynthetic reinforced soil retaining walls. Canadian Geotechnical Journal, 43(12): 1225-1237.

Bathurst, R. J., Walters, D. L., Hatami, K., & Allen, T. M. (2001). Full-scale performance testing and numerical modelling of reinforced soil retaining walls. IS Kyushu preprint, 3-28.

Bathurst, R. J., Walters, D., Vlachopoulos, N., Burgess, P., & Allen, T. M. (2000). Full scale testing of geosynthetic reinforced walls. In Advances in transportation and geoenvironmental systems using geosynthetics (pp. 201-217).

Berg, R.R., Allen, T.M. and Bell, J.R., 1998, March. Design procedures for reinforced soil walls-A historical perspective. In Proceedings of the Sixth International Conference on Geosynthetics (pp. 491-496).

Berg, R.R., Christopher, B.R. and Samtani, N.C., 2009. Design of mechanically stabilized earth walls and reinforced soil slopes–Volume I (No. FHWA-NHI-10-024).

Bolton, M. D. (1986). The strength and dilatancy of sands. Geotechnique, 36(1): 65-78.

Brinkgreve, R. B. J. (Ed.). (2002). Plaxis: Finite Element Code for Soil and Rock Analyses: 2D-Version 8:[user's Guide]. Balkema.

Brinkgreve, R. B. J., Engin, E., Swolfs, W. M., Waterman, D., Chesaru, A., Bonnier, P. G., & Galavi, V. (2016). Plaxis 3D 2016. Plaxis bv.

Chen, Q., Abu-Farsakh, M. and Sharma, R., 2009. Experimental and analytical studies of reinforced crushed limestone. Geotextiles and Geomembranes, 27(5), pp.357-367.

Christopher, B.R., Gill, S.A., Giroud, J.P., Juran, I., Mitchell, J.K., Schlosser, F. and Dunnicliff, J., 1990. Reinforced soil structures Volume I. Design and construction guidelines (No. FHWA-RD-89-043).

Dantas, B. T. (2004). Working Stress Analysis Method for Reinforced Cohesive Soil Slopes (Doctoral dissertation, D. Sc. Thesis, COPPE/UFRJ, Rio de Janeiro (in portuguese)).

Duncan, J.M., P. Byrne, K.S. Wong & P. Mabry 1980. Strength, stress-strain and bulk modulus parameters for finite-element analysis of stresses and movements is soil masses. Rep. UCB/GT/80-01, UC Berkeley, CA, USA.

Ehrlich, M. and Mirmoradi, S.H., 2013. Evaluation of the effects of facing stiffness and toe resistance on the behavior of GRS walls. Geotextiles and Geomembranes, 40, pp.28-36.

Elias, V., Christopher, B., and Berg, R. (2001). “Mechanically Stabilized Earth Walls and Reinforced Soil Slopes Design and Construction Guidelines." FHWA-NHI-00-043, ederal Highway Administration, McLean, VA

Elton, D. J. and Patawaran, M. A. B. (2005). "Mechanically Stabilized Earth (MSE) Reinforcement Tensile Strength from Tests of Geotextile Reinforced Soil." A Report to the Alabama Highway Research Center, Auburn University, 77 pages.

Fakharian, K. and Attar, I.H., 2007. Static and seismic numerical modeling of geosynthetic-reinforced soil segmental bridge abutments. *Geosynthetics International*, *14*(4), pp.228-243.

Guler, E., Hamderi, M. and Demirkan, M.M., 2007. Numerical analysis of reinforced soil-retaining wall structures with cohesive and granular backfills. Geosynthetics International, 14(6), pp.330-345.

Hatami, K. & R.J. Bathurst 2000. Effect of structural design on fundamental frequency of reinforced-soil retaining walls. Soil Dyn. Erthq. Eng. 19(3): 137-157.

Hatami, K., & Bathurst, R. J. (2005). Development and verification of a numerical model for the analysis of geosynthetic-reinforced soil segmental walls under working stress conditions. Canadian Geotechnical Journal, 42(4): 1066-1085.

Hatami, K., & Bathurst, R. J. (2006). Numerical model for reinforced soil segmental walls under surcharge loading. Journal of Geotechnical and Geoenvironmental engineering, 132(6), 673-684.

Helwany, S. M. B., Reardon, G., & Wu, J. T. H. (1999). Effects of backfill on the performance of GRS retaining walls. Geotextiles and Geomembranes, 17(1), 1-16.

Helwany, S. M., Wu, J. T., & Froessl, B. (2003). GRS bridge abutments—an effective means to alleviate bridge approach settlement. Geotextiles and Geomembranes, 21(3), 177-196.

Ho, S.K. and Rowe, R.K., 1996. Effect of wall geometry on the behaviour of reinforced soil walls. Geotextiles and Geomembranes, 14(10), pp.521-541.

Hoffman, P. and Wu, J.T., 2015. An analytical model for predicting load–deformation behavior of the FHWA GRS-IBS performance test. International Journal of Geotechnical Engineering, 9(2), pp.150-162.

Holtz, R. D. and Lee, W. F. (2002). "Internal Stability Analyses of Geosynthetic Reinforced Retaining Walls." Report WA-RD 532.1, Washington State Department of Transportation, Washington.

Huang, B., Bathurst, R. J., & Hatami, K. (2007). Numerical study of the influence of block interface stiffness on reinforced soil segmental walls of variable height. In Proceedings of the 60th Canadian Geotechnical Conference, Ottawa, Ont (pp. 21-25).

Huang, B., Bathurst, R. J., & Hatami, K. (2009). Numerical study of reinforced soil segmental walls using three different constitutive soil models. Journal of Geotechnical and Geoenvironmental engineering, 135(10): 1486-1498.

Huang, B., Bathurst, R. J., Hatami, K., & Allen, T. M. (2010). Influence of toe restraint on reinforced soil segmental walls. Canadian Geotechnical Journal, 47(8): 885-904.

Huang, J., Bin-Shafique, S., Han, J. and Rahman, M.S., 2014. Modelling of laterally loaded drilled shaft group in mechanically stabilised earth wall. Proceedings of the Institution of Civil Engineers-Geotechnical Engineering, 167(4), pp.402-414.

Huang, J., Han, J., Parsons, R.L. and Pierson, M.C., 2013. Refined numerical modeling of a laterally-loaded drilled shaft in an MSE wall. Geotextiles and Geomembranes, 37, pp.61-73.

Huang, J., Parsons, R.L., Han, J. and Pierson, M., 2011. Numerical analysis of a laterally loaded shaft constructed within an MSE wall. Geotextiles and Geomembranes, 29(3), pp.233-241.

Ketchart, K., 1997. Performance of geosynthetic-reinforced soil bridge pier and abutment, Denver, Colorado, USA. Mechanically stabilized backfill, pp.101-116.

Ketchart, K., and Wu, J. T. H. (2001). "Performance Test for Geosynthetic Reinforced Soil Including Effects of Preloading", Report FHWA-RD-01-018, Federal Highway Administration, Washington, D.C.

Kost, A., Filz, G. M., & Cousins, T. E. (2015). Differential Settlement of a Geosynthetic Reinforced Soil Abutment: Full-Scale Investigation: Summary Report (No. FHWA/VCTIR 15-R4).

Kost, A., Filz, G., and Cousins, T. (2014). "Differential Settlement of a GRS Abutment: Full-Scale Investigation." Virginia Center for Transportation Innovation and Research Charlottesville, VA.

Leshchinsky, D. and Vulova, C., 2001. Numerical investigation of the effects of geosynthetic spacing on failure mechanisms in MSE block walls. Geosynthetics International, 8(4), pp.343-365.

Ling, H.I., Tatsuoka, F. and Tateyama, M., 1995. Simulating performance of GRS-RW by finite-element procedure. Journal of geotechnical engineering, 121(4), pp.330-340.

Ling, P. and Leshchinsky, D., 1996. Mesa Walls: Field Data Reduction, Finite Element Analysis, and Preliminary Design Recommendations. Report to Tensar Earth Technologies, Inc., Atlanta, GA, February, 1.

Liu, H. (2012). Long-term lateral displacement of geosynthetic-reinforced soil segmental retaining walls. Geotextiles and Geomembranes, 32, 18-27.

Liu, H., 2015. Reinforcement load and compression of reinforced soil mass under surcharge loading. Journal of Geotechnical and Geoenvironmental Engineering, 141(6), p.04015017.

Liu, H., Wang, X., & Song, E. (2011). Reinforcement load and deformation mode of geosynthetic-reinforced soil walls subject to seismic loading during service life. Geotextiles and

Long, J., Olson, S., Stark, T., & Samara, E. (1998). Differential movement at embankment-bridge structure interface in Illinois. Transportation Research Record: Journal of the Transportation Research Board, (1633): 53-60.

Lunne, T., Robertson, P.K. and Powell, J.J.M., 1997. Cone penetration testing. Geotechnical Practice.

Mellas, M., Mabrouki, A., Benmeddour, D. and Rahmouni, O., 2015. Numerical study of geogrid-reinforced segmental earth retaining wall. Journal of Applied Engineering Science & Technology, 1(2), pp.43-49.

Mirmoradi, S. H., & Ehrlich, M. (2014a). Modeling of the compaction-induced stresses in numerical analyses of GRS walls. International Journal of Computational Methods, 11(02): 1342002.

Mirmoradi, S. H., & Ehrlich, M. (2014b). Numerical evaluation of the behavior of GRS walls with segmental block facing under working stress conditions. Journal of Geotechnical and Geoenvironmental Engineering, 141(3): 04014109.

Morrison, K. F., Harrison, F. E., Collin, J. G., Dodds, A. M., & Arndt, B. (2006). Shored mechanically stabilized earth (SMSE) wall systems design guidelines (No. FHWA-CFL/TD-06-001).

Nicks, J. E., Adams, M. T., and Ooi, P. S. K. (2013). Geosynthetic reinforced soil 1 performance testing–axial load deformation relationships. Federal Highway Administration. Report No. FHWA-HRT-13-066, McLean, VA.

Nicks, J.E., Esmaili, D. and Adams, M.T., 2016. Deformations of geosynthetic reinforced soil under bridge service loads. Geotextiles and Geomembranes, 44(4), pp.641-653.

Rahmouni, O., Mabrouki, A., Benmeddour, D. and Mellas, M., 2016. A numerical investigation into the behavior of geosynthetic-reinforced soil segmental retaining walls. International Journal of Geotechnical Engineering, 10(5), pp.435-444.

Riccio, M., Ehrlich, M., & Dias, D. (2014). Field monitoring and analyses of the response of a block-faced geogrid wall using fine-grained tropical soils. Geotextiles and Geomembranes, 42(2): 127-138.

Rowe, R. K., & Ho, S. K. (1998). Horizontal deformation in reinforced soil walls. Canadian Geotechnical Journal, 35(2), 312-327.

Saghebfar, M., Abu-Farsakh, M. Y., Ardah, A., Chen, Q., & Fernandez, B. A. (2017a). Full-Scale Testing of Geosynthetic-Reinforced, Soil-Integrated Bridge System. Transportation Research Record: Journal of the Transportation Research Board, (2656): 40-52.

Saghebfar, M., Abu-Farsakh, M., Ardah, A., Chen, Q., & Fernandez, B. A. (2017b). Performance monitoring of Geosynthetic Reinforced Soil Integrated Bridge System (GRS-IBS) in Louisiana. Geotextiles and Geomembranes, 45(2): 34-47.

Schanz T, Vermeer PA, Bonnier PG. The Hardening Soil model – formulation and verification. In: Proceedings Plaxis Symposium ‘‘Beyond 2000 in Computational Geotechnics, Amsterdam, Balkema; 1999. p. 281–96.

Schlosser, F. and Long, N. T. (1974). “Recent results in French research on reinforced earth,” Journal of Construction Division 100(3), pp 223-237.

Stark, T.D., Olson, S.M. and Long, J.H., 1995. *DIFFERENTIAL MOVEMENT AT THE EMBANKMENT/STRUCTURE INTERFACE-MITIGATION AND REHABILITATION. FINAL REPORT* (No. Project IAB-H1, FY 93).

Takemura, J., 1992. Bearing capacities and deformations of sand reinforced with geogrids. In Proc. of International Symposium on Earth Reinforcement Practic (IS Kyushu'92), Fukuoka, Japan (Vol. 1, pp. 695-700).

Talebi, M., Meehan, C. L., Cacciola, D. V., & Becker, M. L. (2014). Design and Construction of a Geosynthetic Reinforced Soil Integrated Bridge System. In Geo-Congress 2014: Geo-characterization and Modeling for Sustainability (pp. 4176-4190).

VanBuskirk, C. Adoption and implementation of GRS design concepts A consultant's perspective. 19th Vancouver Geotechnical Society Symposium, Geosynthetic Reinforced Walls, Slopes, and Earthworks. 2010.

Wahls, H.E., 1990. Design and construction of bridge approaches (Vol. 159). Transportation Research Board.

Walters, D., K. Hatami, R.J. Bathurst, N. Vlachopoulos, D. Saunders, G.P. Burgess & T.M. Allen 2000. Full-scale testing and modeling of geosynthetic reinforced soil retaining walls. Proc. 53rd Can. Geotech. Conf. Montreal. (in press)

Wu, J. T. (2001). Revising the AASHTO guidelines for design and construction of GRS walls (No. CDOT-DTD-R-2001-16).

Wu, J. T. H. (2007a). "Lateral Earth Pressure against the Facing of Segmental GRS Walls." Geosynthetics in Reinforcement and Hydraulic Applications (GSP 165), Gabr, and Bowders (Eds.). ASCE, Reston, VA, 165-175.

Wu, J. T. H., and Adams, M. (2007). "Myth and Fact on Long-Term Creep of GRS Structures." Geosynthetics in Reinforcement and Hydraulic Applications (GSP 165), Gabr, and Bowders (Eds.). ASCE, Reston, VA, 107-118.

Wu, J. T. H., and Helwany, S. M. B. (1996). A performance test for assessment of long-term creep behavior of soil-geosynthetic composites. Geosynthetics International, 3(1), 107-124.

Wu, J. T. H., Lee, K. Z. Z., Helwany, S. M. B., and Ketchart, K. (2006a). "Design and Construction Guidelines for GRS Bridge Abutment with a Flexible Facing." Report No. 556, National Cooperative Highway Research Program, Washington, D.C.

Wu, J. T., & Pham, T. Q. (2013). Load-carrying capacity and required reinforcement strength of closely spaced soil-geosynthetic composites. Journal of Geotechnical and Geoenvironmental Engineering, 139(9), 1468-1476.

Wu, J. T., Lee, K. Z., & Pham, T. (2006b). Allowable bearing pressures of bridge sills on GRS abutments with flexible facing. Journal of Geotechnical and Geoenvironmental Engineering, 132(7), 830-841.

Wu, J. T., Yang, K. H., Mohamed, S., Pham, T., & Chen, R. H. (2014). Suppression of soil dilation—A reinforcing mechanism of soil-geosynthetic composites. Transportation Infrastructure Geotechnology, 1(1): 68-82.

Wu, J.T., 2007b. Lateral earth pressure against the facing of segmental GRS walls. In Geosynthetics in Reinforcement and Hydraulic Applications (pp. 1-11).

Wu, J.T.H., Ketchart, K., and Adams, M.T. (2001). "GRS Piers and Abutments." Report No. FHWA-RD-00-038, Federal Highway Administration, McLean, VA.

Wu, J.T.H., Pham, T., and Adams, M.T. (2013). "Composite Behavior of Geosynthetic Reinforced Soil Mass." No. FHWA-HRT-10-077.

Yang, Z. (1972). "Strength and Deformation Characteristics of Reinforced Sand." PhD. Thesis, University of California at Los Angeles, Los Angeles, CA.

Yarivand, A., Behnia, C., Bakhtiyari, S. and Ghalandarzadeh, A., 2017. Performance of geosynthetic reinforced soil bridge abutments with modular block facing under fire scenarios. Computers and Geotechnics, 85, pp.28-40.

Yu, Y., Damians, I. P., & Bathurst, R. J. (2015). Influence of choice of FLAC and PLAXIS interface models on reinforced soil–structure interactions. Computers and Geotechnics, 65: 164-174.

Zaman, M., Laguros, J. G., & JHA, R. (1993). STATISTICAL MODELS FOR IDENTIFICATION OF PROBLEMATIC BRIDGE SITES AND ESTIMATION OF APPROACH SETTLEMENTS. PROGRESS REPORT (DRAFT) (No. Study 2188).

Zhang, H. L., & Hu, C. S. (2007). Determination of allowable differential settlement in bridge approach due to vehicle vibrations. Journal of Bridge Engineering, 12(2): 154-163.

Zheng, Y. and Fox, P.J., 2016. Numerical Investigation of Geosynthetic-Reinforced Soil Bridge Abutments under Static Loading. Journal of Geotechnical and Geoenvironmental Engineering, 142(5), p.04016004.

Zheng, Y. and Fox, P.J., 2017. Numerical Investigation of the Geosynthetic Reinforced Soil–Integrated Bridge System under Static Loading. Journal of Geotechnical and Geoenvironmental Engineering, 143(6), p.04017008.

Zheng, Y., Fox, P. J., & Benson Shing, P. (2015a). Numerical study of deformation behavior for a geosynthetic-reinforced soil bridge abutment under static loading. In IFCEE 2015 (pp. 1503-1512).

Zheng, Y., Fox, P. J., & Shing, P. B. (2014). Numerical Simulations for Response of MSE Wall-Supported Bridge Abutments to Vertical Load. In Ground Improvement and Geosynthetics (pp. 493-502).

Zheng, Y., Fox, P. J., & Shing, P. B. (2015b). Verification of numerical model for static analysis of geosynthetic-reinforced soil bridge abutments. Geosynthetics 2015, 152-160.

Zornberg, J. G., Christopher, B., Leshchinsky, D., Han, J., Tanyu, B. F. (2014). “Defining the Boundary Conditions for Composite Behavior of Geosynthetic Reinforced Soil (GRS) Structures.” National Cooperative Highway Research Program (NCHRP) Phase I Interim Report

Appendix
Copyright Information

Please note that, as the author of this Elsevier article, you retain the right to include it in a thesis or dissertation, provided it is not published commercially. Permission is not required, but please ensure that you reference the journal as the original source. For more information on this and on your other retained rights, please visit: https://www.elsevier.com/about/our-business/policies/copyright#Author-rights

BACK CLOSE WINDOW

Vita

Allam Ardah was born on November 14, 1983, in Baqa Algharbia, Israel, to Ismail Ardah and Iqbal Ardah. He finished his high school from Arrabah Secondary Boy School, Jenin, Palestine, in June 2002. He received his bachelor's degree in civil engineering from An-Najah National University, Nablus, Palestine, in May 2007, and went to Dubai in March 2008 and then came to United States October of 2011 to pursue his graduate studies in civil engineering at Louisiana State University, Baton Rouge, Louisiana. In December 2015, he received his master's degree from the civil engineering department. Directly after the completion of his master's degree, he joined the doctoral program in civil engineering. He got married to Amal Adlakh in the summer of 2018, one semester before his graduation right after he passed his defense exam. Allam Ardah is anticipated to fulfill the requirements of the degree of Doctor of Philosophy in civil engineering in December 2018.